

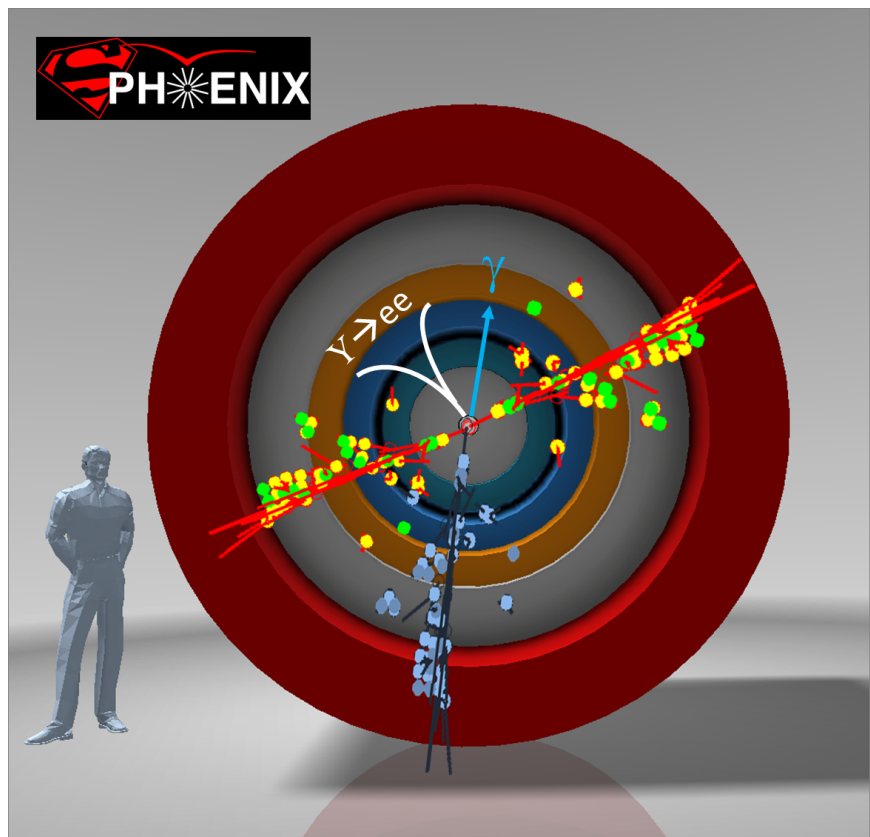


An Upgrade Proposal from the PHENIX Collaboration

Original: July 1, 2012

Updated: October 1, 2013

Updated: June 19, 2014



Executive Summary

The PHENIX collaboration in this document proposes a major upgrade to the PHENIX detector at the Relativistic Heavy Ion Collider. This upgrade, referred to as sPHENIX, enables a compelling jet physics program addressing fundamental questions about the nature of the strongly coupled quark-gluon plasma, discovered experimentally at RHIC to be a perfect fluid. Questions such as how and why the quark-gluon plasma behaves as a perfect fluid in the vicinity of strongest coupling, near $1-2 T_c$, can only be fully addressed with jet, dijet, γ -jet, fragmentation function, and Upsilon observables at RHIC energies, which probe the medium over a variety of length scales. Comparing these measurements with ones probing higher temperature at the Large Hadron Collider will provide invaluable insight into the thermodynamics of QCD. Recent data in $p(d)+A$ collisions renews the question of what are the minimum size, shape, and temperature requirements for the formation of droplets of quark-gluon plasma. Importantly, sPHENIX also provides the foundation for a future detector able to exploit the novel physics opportunities of an electron-ion collider at RHIC.

The sPHENIX upgrade addresses specific questions whose answers are necessary to advance our understanding of the quark-gluon plasma:

- How does a partonic shower develop and propagate in the quark-gluon plasma?
- How does one reconcile the observed strongly coupled quark-gluon plasma with the asymptotically free theory of quarks and gluons?
- What are the dynamical changes in the quark-gluon plasma in terms of quasiparticles and excitations as a function of temperature?
- How sharp is the transition of the quark-gluon plasma from the most strongly coupled regime near T_c to a weakly coupled system of partons known to emerge at asymptotically high temperatures?

The development of the sPHENIX physics program has benefited from very active engagement with the theory community. For current-day questions regarding the perfect fluidity of the quark-gluon plasma, engagement between theorists and experimentalists, fed by increasingly comprehensive data from RHIC and the LHC, has moved the physics discussion beyond merely constraining η/s to exploring its temperature dependence and other properties. In an analogous manner, there is great progress in the theoretical understanding of

jet quenching — see Ref. [1] from the JET Collaboration, for example. We foresee that truly comprehensive jet data from RHIC and the LHC — to which sPHENIX contributes crucially — will move the physics discussion beyond merely constraining the single transport property \hat{q} to a deeper understanding of the dynamics of the quark-gluon plasma.

To pursue these physics questions we are proposing an upgrade consisting of a 1.5 T superconducting magnetic solenoid of inner radius 140 cm with silicon tracking, electromagnetic calorimetry, and hadronic calorimetry providing uniform coverage for $|\eta| < 1$. The sPHENIX solenoid is an existing magnet developed for the BaBar experiment at SLAC, and recently ownership of this key component was officially transferred to BNL. An engineering drawing of the sPHENIX detector and its incorporation into the PHENIX interaction region are shown in the top panel of Figure 1.

The sPHENIX plan has been developed in conjunction with the official timeline from BNL management. The expectation is for RHIC running through 2016, a shutdown in 2017, RHIC running for the increased luminosity beam energy scan in 2018–2019, a shutdown in 2020, and RHIC running in 2021 and 2022. We anticipate installing the magnet, the hadronic calorimeter and portions of the tracking to enable significant commissioning of sPHENIX during the 2019 running period. The sPHENIX detector will be completely integrated during the 2020 shutdown, and it would be available for physics at the start of the 2021 run. With the high luminosity available now, sPHENIX will record over 50 billion and sample over 200 billion Au+Au collisions at $\sqrt{s_{NN}} = 200$ GeV in a 20 week run. The high rate capability of sPHENIX will enable the recording of over 10 million dijet events with $E_T > 20$ GeV, along with a correspondingly large γ +jet sample. We envision a run plan for 2021–2022 consisting of two 30 week physics runs allowing a period for final commissioning, 20 weeks of Au+Au running, and extended periods of $p+p$ and $p(d)+Au$ running.

The design of sPHENIX takes advantage of a number of technological advances to enable a significantly lower cost per unit solid angle than has been previously possible, and we have obtained budgetary guidance from well-regarded vendors for the major components of sPHENIX. Further cost savings are achieved by reusing significant elements of the existing PHENIX mechanical and electrical infrastructure. Thus the sPHENIX physics is delivered in a very cost efficient way.

We have designed sPHENIX so that it could serve as the foundation for a future detector intended to make physics measurements at a future electron ion collider (EIC) at RHIC. The BNL implementation of the EIC, eRHIC, adds a 5–15 GeV electron beam to the current hadron and nuclear beam capabilities of RHIC. The sPHENIX detector, when combined with future upgrades in the backward ($\eta < -1$) and forward ($\eta > 1$) regions enables a full suite of EIC physics measurements as described in Appendix A. The EIC detector concept built around the BaBar solenoid and sPHENIX calorimetry is shown in the bottom panel of Figure 1. There is also the potential, if one can realize appropriate instrumentation in the hadron-going direction while polarized $p+p$ and $p+A$ collisions are still available at RHIC, to pursue a rich program of forward physics measurements.

The document is organized as follows. In Chapter 1, we detail the physics accessible via jet, dijet, γ +jet, fragmentation function, and Upsilon measurements at RHIC to demonstrate the mission need. In Chapter 2, we detail the sPHENIX detector and subsystem requirements needed to achieve the physics goals. In Chapter 3, we detail the specific detector design and GEANT4 simulation results. In Chapter 4, we detail the physics performance with full detector simulations. Finally, Appendix A includes a copy of a Letter of Intent for an EIC detector built around the BaBar magnet and the sPHENIX calorimetry.

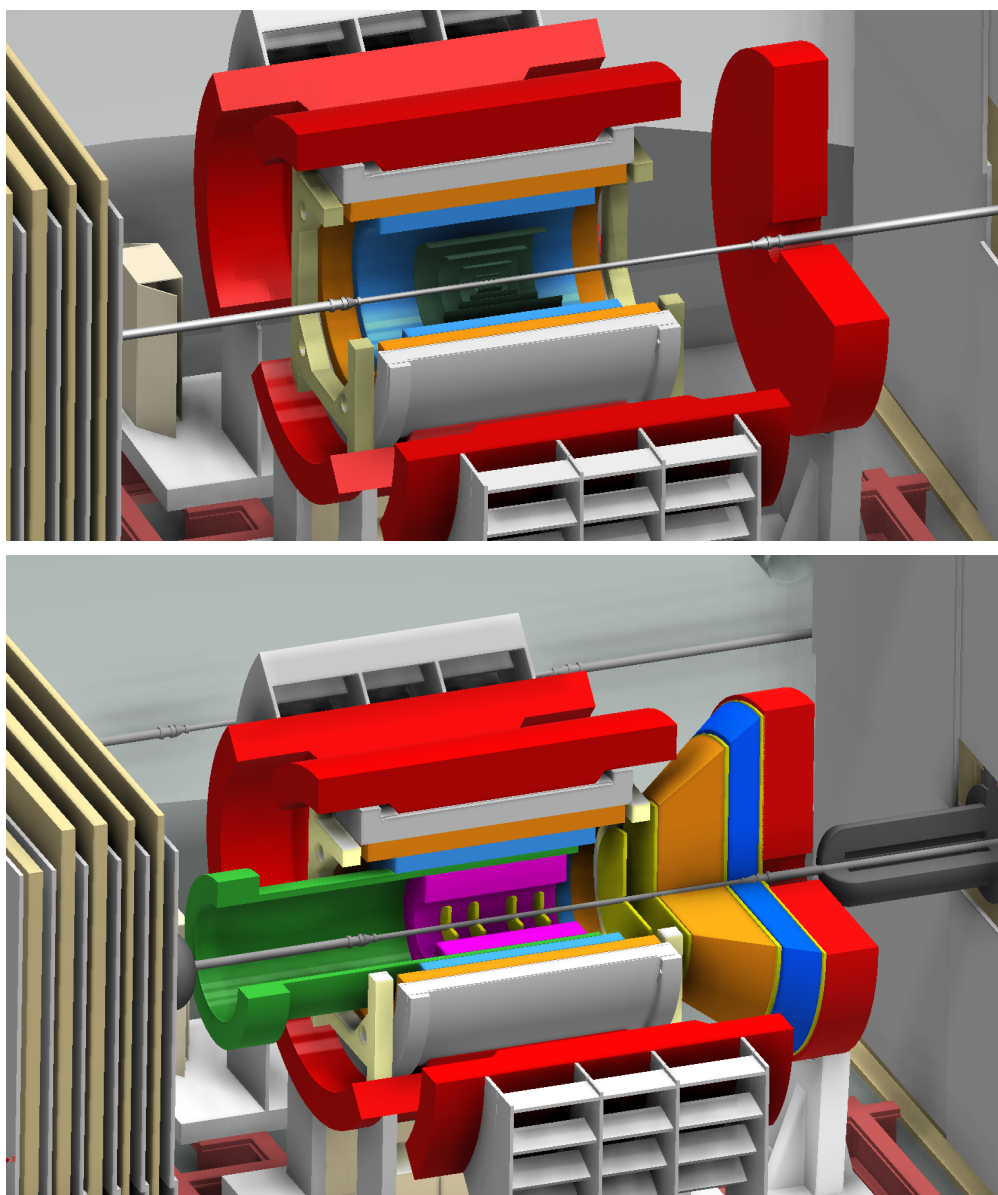


Figure 1: Engineering renderings showing the sPHENIX and future EIC detector concepts. (top) sPHENIX as described in this proposal, showing the all silicon tracking, the electromagnetic calorimeter (in blue), the superconducting solenoid, and the hadronic calorimeter (in red). (bottom) EIC detector concept capable of world-class measurements with an electron collider at RHIC (see Appendix A for details).

Contents

1 The Physics Case for sPHENIX	1
1.1 Pushing and probing the QGP	3
1.2 What is the temperature dependence of the QGP?	5
1.3 What are the inner workings of the QGP?	9
1.4 How does the QGP evolve along with the parton shower?	11
1.5 Current jet probe measurements	12
1.6 Theoretical calculations of jets at RHIC	17
1.7 Fragmentation Functions	26
1.8 Heavy Quark Jets	27
1.9 Jets, dijets, γ -jet and FFs	29
1.10 Beauty Quarkonia Physics	32
1.11 Summary	35
2 Physics-Driven Detector Requirements	37
2.1 Acceptance	40
2.2 Segmentation	41
2.3 Energy Resolution	42
2.4 Tracking	42
2.5 Triggering	43
3 Detector Concept	45
3.1 Magnet	46
3.2 The Electromagnetic Calorimeter	49
3.3 The Hadronic Calorimeter	51
3.4 Calorimeter Simulations	56
3.5 Electronics	59

3.6	Charged Particle Silicon Tracking	71
3.7	sPHENIX Triggering	74
3.8	Mechanical Design and Infrastructure Concept	76
3.9	Detector Development and Testing	79
4	Physics Performance	81
4.1	Jet simulations	82
4.2	Jet finding algorithm	82
4.3	Jet performance in $p+p$ collisions	83
4.4	Jet performance in Au+Au collisions	87
4.5	Jet surface emission engineering	100
4.6	Jet physics at lower RHIC energies	100
4.7	Fragmentation Function and Medium Response Observables	102
4.8	Heavy Quark Jets	106
4.9	Jet Physics Summary.	106
4.10	Beauty Quarkonia Performance	107
A	Evolution to an EIC Detector	111
A.1	EIC Physics.	112
A.2	eRHIC: realizing the Electron-Ion Collider	114
A.3	Physics Deliverables	115
A.4	Detector Requirements	124
A.5	Detector Concept	137
B	The PHENIX Collaboration	157
	References	165

Chapter 1

The Physics Case for sPHENIX

Hadronic matter under conditions of extreme temperature or net baryon density transitions to a new state of matter called the quark-gluon plasma. Lattice QCD calculations at zero net baryon density indicate a smooth crossover transition at $T_c \approx 170$ MeV, though with a rapid change in properties at that temperature as shown in the left panel of Figure 1.1 [2]. This quark-gluon plasma dominated the early universe for the first six microseconds of its existence. Collisions of heavy nuclei at the Relativistic Heavy Ion Collider (RHIC) have sufficient initial kinetic energy that is then converted into heat to create quark-gluon plasma with an initial temperature—measured via the spectrum of directly emitted photons—of greater than 300 MeV [3]. The higher energy collisions at the Large Hadron Collider (LHC) produce an even higher initial temperature $T > 420$ MeV [4].

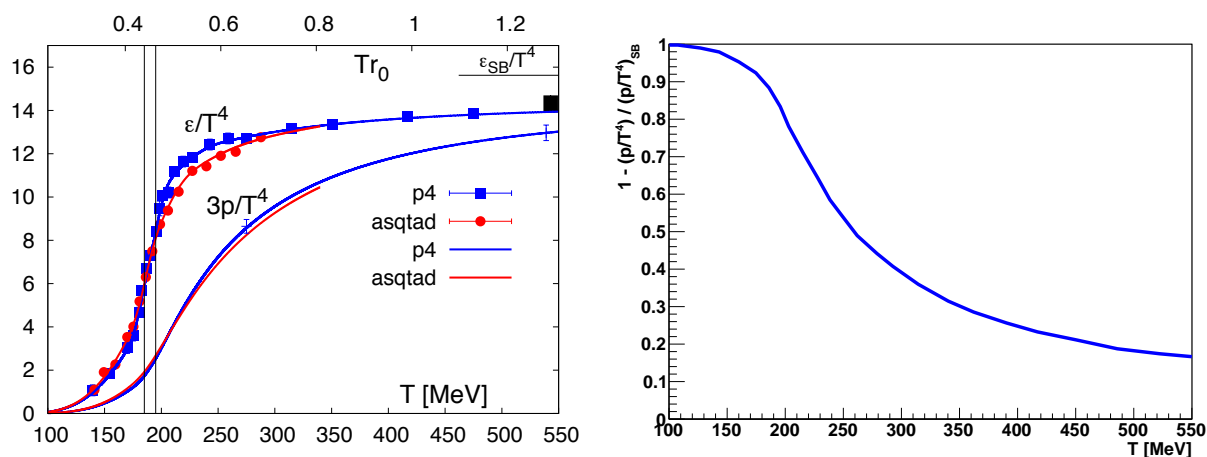


Figure 1.1: (Left) The energy density and three times the pressure normalized by $1/T^4$ as a function of temperature [2]. (Right) Deviation in p/T^4 relative to the Stefan-Boltzmann value as a function of temperature. The deviation from the Stefan-Boltzmann value is 23%, 39%, 53%, and 80% at temperatures of 420, 300, 250, and 200 MeV, respectively.

In materials where the dominant forces are electromagnetic, the coupling α_{em} is always much less than one. Even so, many-body collective effects can render perturbative calculations non-convergent and result in systems with very strong effective coupling [5]. In cases where the nuclear force is dominant, and at temperature scales of order $1\text{--}3 T_c$, the coupling constant α_s is not much less than one and the system is intrinsically non-perturbative. In addition, the many-body collective effects in the quark-gluon plasma and their temperature dependence near T_c are not well understood.

The right panel of Figure 1.1 shows the deviation from the Stefan-Boltzmann limit of Lattice QCD results for the pressure normalized by $1/T^4$. The Stefan-Boltzmann limit holds for a non-interacting gas of massless particles (i.e., the extreme of the weakly coupled limit), and as attractive inter-particle interactions grow stronger the pressure decreases. Thus, one might expect that the quark-gluon plasma would transition from a weakly coupled system at high temperature to a more strongly coupled system near T_c . However, a direct quantitative extraction of the coupling strength warrants caution as string theory calculations provide an example where the coupling is very strong and yet the deviation from the Stefan-Boltzmann limit is only 25% [6, 7]. The change in initial temperature between RHIC and LHC collisions is thus expected to be associated with important changes in the nature of the quark-gluon plasma [8]. If not, the question is why not.

The collisions at RHIC and the LHC involve a time evolution during which the temperature drops as the quark-gluon plasma expands. The real constraint on the temperature dependence of the quark-gluon plasma properties will come from calculations which simultaneously describe observables measured at both energies. Since we are studying a phase transition, it is crucial to do experiments near the phase transition and compare them with experiments done further above T_c . Typically, all the non-scaling behavior is found near the transition.

For many systems the change in coupling strength is related to quasiparticle excitations or strong coherent fields, and to study these phenomena one needs to probe the medium at a variety of length scales. For example, in a superconductor probed at long length scales, one scatters from Cooper pairs; in a superconductor probed at short distance scales one observes the individual electrons. Hard scattered partons generated in heavy ion collisions that traverse the quark-gluon plasma serve as the probes of the medium. Utilizing these partonic probes, measured as reconstructed jets, over the broadest possible energy scale is a key part of unraveling the quasiparticle puzzle in the quark-gluon plasma. Jets at the LHC reach the highest energies, the largest initial virtualities, and large total energy loss to probe the shortest distance scales. The lower backgrounds at RHIC will push the jet probes to lower energies and lower initial virtualities thus probing the important longer distance scales in the medium.

Continued developments in techniques for jet reconstruction in the environment of a heavy ion collision have allowed the LHC experiments to reliably recover jets down to 40 GeV [9, 10], which is well within the range of reconstructed jet energies at RHIC. This overlap opens the possibility of studying the QGP at the same scale but under different

conditions of temperature and coupling strength.

This Chapter is organized into Sections as follows. We first describe the key ways of ‘pushing’ and ‘probing’ the quark-gluon plasma to understand its properties. We then discuss three different aspects in which the RHIC jet results are crucial in terms of (1) the temperature dependence of the QGP, (2) the microscopic inner workings of the QGP, and (3) the QGP time evolution along with the parton shower evolution. We then discuss the current state of jet probe measurements from RHIC and LHC experiments, followed by a review of theoretical calculations for RHIC jet observables. Finally, we review the jet, dijet, and γ -jet rates relevant for measurements at RHIC.

1.1 Pushing and probing the QGP

Results from RHIC and LHC heavy ion experiments have provided a wealth of data for understanding the physics of the quark-gluon plasma. One very surprising result discovered at RHIC was the fluid-like flow of the quark-gluon plasma [11], in stark contrast to some expectations that the quark-gluon plasma would behave as a weakly coupled gas of quarks and gluons. It was originally thought that even at temperatures as low as $2\text{--}5 T_c$, the quark-gluon plasma could be described with a weakly coupled perturbative approach despite being quite far from energy scales typically associated with asymptotic freedom.

The quark-gluon plasma created in heavy ion collisions expands and cools, eventually passing through the phase transition to a state of hadrons, which are then measured by experiment. Extensive measurements of the radial and elliptic flow of hadrons, when compared to hydrodynamics calculations, imply a very small ratio of shear viscosity to entropy density, η/s [12]. In the limit of very weak coupling (i.e., a non-interacting gas), the shear viscosity is quite large as particles can easily diffuse across a velocity gradient in the medium. Stronger inter-particle interactions inhibit diffusion to the limit where the strongest interactions result in a very short mean free path and thus almost no momentum transfer across a velocity gradient, resulting in almost no shear viscosity.

The shortest possible mean free path is of order the de Broglie wavelength, which sets a lower limit on η/s [13]. A more rigorous derivation of the limit $\eta/s \geq 1/4\pi$ has been calculated within string theory for a broad class of strongly coupled gauge theories by Kovtun, Son, and Starinets (KSS) [14]. Viscous hydrodynamic calculations assuming η/s to be temperature independent through the heavy ion collision time evolution are consistent with the experimental data where η/s is within 50% of this lower bound for strongly coupled matter [12, 15, 16, 17, 18, 19]. Even heavy quarks (i.e., charm and beauty) are swept up in the fluid flow and theoretical extractions of the implied η/s are equally small [20].

Other key measures of the coupling strength to the medium are found in the passage of a hard scattered parton through the quark-gluon plasma. As the parton traverses the medium it accumulates transverse momentum as characterized by $\hat{q} = d(\Delta p_T^2)/dt$ and

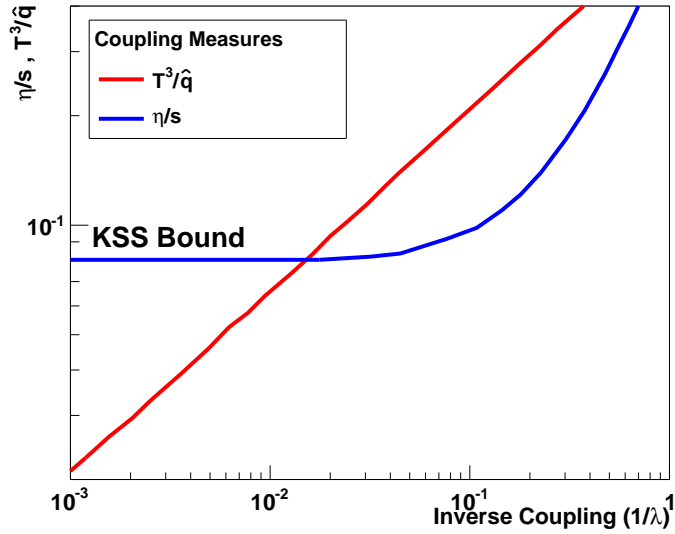


Figure 1.2: η/s (blue) and T^3/\hat{q} (red) as a function of the inverse of the 't Hooft coupling[21]. For large λ (i.e., small $1/\lambda$), η/s approaches the quantum lower bound asymptotically, losing its sensitivity to further changes in the coupling strength.

transfers energy to the medium via collisions as characterized by $\hat{e} = dE/dt$. Ref. [22] has calculated \hat{q}/T^3 in $\mathcal{N} = 4$ supersymmetric Yang-Mills theory to be proportional to the square root of the coupling strength whereas η/s asymptotically approaches the quantum lower bound as the coupling increases. Both of these ratios are shown as a function of the inverse coupling in Figure 1.2. For large 't Hooft coupling (λ), η/s is already quite close to $1/4\pi$, whereas T^3/\hat{q} is still changing. This behavior has caused the authors of Ref. [21] to comment: “The ratio T^3/\hat{q} is a more broadly valid measure of the coupling strength of the medium than η/s .”

In vacuum, the hard scattered parton creates a shower of particles that eventually form a cone of hadrons, referred to as a jet. In the quark-gluon plasma, the lower energy portion of the shower may eventually be equilibrated into the medium, thus giving a window on the rapid thermalization process in heavy ion collisions. This highlights part of the reason for needing to measure the fully reconstructed jet energy and the correlated particle emission with respect to the jet at all energy scales. In particular, coupling parameters such as \hat{q} and \hat{e} are scale dependent and must take on weak coupling values at high enough energies and very strongly coupled values at thermal energies.

The focus of this proposal is the measurement of jet probes of the medium as a way of understanding the coupling of the medium, the origin of this coupling, and the mechanism of rapid equilibration. The quark-gluon plasma is one form of the “condensed matter” of QCD and in any rigorous investigation of condensed matter of any type, it is critical to make measurements as one pushes the system closer to and further from a phase

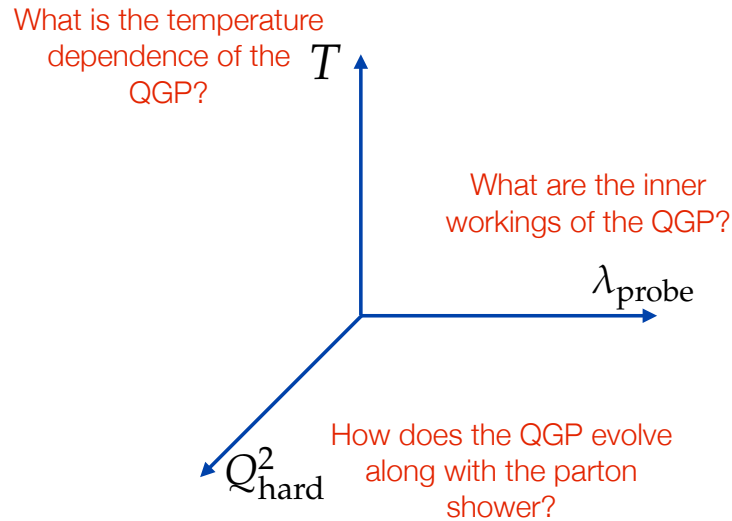


Figure 1.3: Three illustrative axes along which the quark-gluon plasma may be pushed and probed. The axes are the temperature of the quark-gluon plasma, the Q_{hard}^2 of the hard process that sets of the scale for the virtuality evolution of the probe, and the wavelength with which the parton probes the medium λ_{probe} .

transition and with probes at different length scales. Substantially extending these scales with measurements at RHIC, particularly closer to the transition temperature and at longer distance scales, is the unique ability provided by this proposal.

The critical variables to manipulate for this program are the temperature of the quark-gluon plasma, the length scale probed in the medium, and the virtuality of the hard process as shown schematically in Figure 1.3. In the following three sections we detail the physics of each axis.

1.2 What is the temperature dependence of the QGP?

The internal dynamics of more familiar substances—the subjects of study in conventional condensed matter and material physics—are governed by quantum electrodynamics. It is well known that near a phase boundary they demonstrate interesting behaviors, such as the rapid change in the shear viscosity to entropy density ratio, η/s , near the critical temperature, T_c . This is shown in Figure 1.4 for water, nitrogen, and helium [23]. Despite the eventual transition to superfluidity at temperatures below T_c , η/s for these materials remains an order of magnitude above the conjectured quantum bound of Kovtun, Son, and Starinets (KSS) derived from string theory [14]. These observations provide a deeper understanding of the nature of these materials: for example the coupling between the

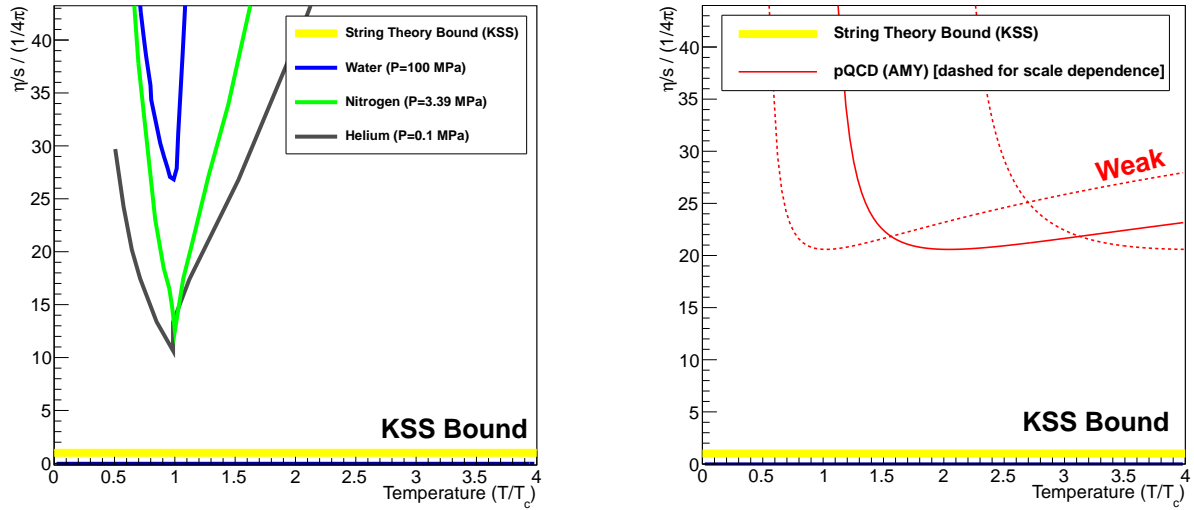


Figure 1.4: (Left) The ratio of shear viscosity to entropy density, η/s , normalized by the conjectured KSS bound as a function of the reduced temperature, T/T_c , for water, Nitrogen, and Helium. The cusp for Helium as shown corresponds to the case at the critical pressure. (Right) Calculation of hot QCD matter (quark-gluon plasma) for a weakly coupled system. Dashed lines show the scale dependence of the perturbative calculation.

fundamental constituents, the degree to which a description in terms of quasiparticles is important, and the description in terms of normal and superfluid components.

The dynamics of the QGP is dominated by quantum chromodynamics and the experimental characterization of the dependence of η/s on temperature will lead to a deeper understanding of strongly coupled QCD near this fundamental phase transition. Theoretically, perturbative calculations in the weakly coupled limit indicate that η/s decreases slowly as one approaches T_c from above, but with a minimum still a factor of 20 above the KSS bound [24] (as shown in the right panel of Figure 1.4). However, as indicated by the dashed lines in the figure, the perturbative calculation has a large renormalization scale dependence and results for different values of the scale parameter ($\mu, \mu/2, 2\mu$) diverge from each other near T_c .

Figure 1.5 (left panel) shows several state-of-the-art calculations for η/s as a function of temperature. Hadron gas calculations show a steep increase in η/s below T_c [25], and similar results using the UrQMD model have also been obtained [26]. Above T_c there is a lattice calculation in the SU(3) pure gauge theory [27] resulting in a value near the KSS bound at $T = 1.65 T_c$. Calculations in the semi-QGP model [28], in which color is not completely ionized, have a factor of five increase in η/s in the region of $1-2 T_c$. Also shown are calculations from a quasiparticle model (QPM) with finite μ_B [29] indicating little change in η/s up to $2 T_c$. There is also an update on the lower limit on η/s from second order relativistic viscous hydrodynamics [30], with values remaining near $1/4\pi$.

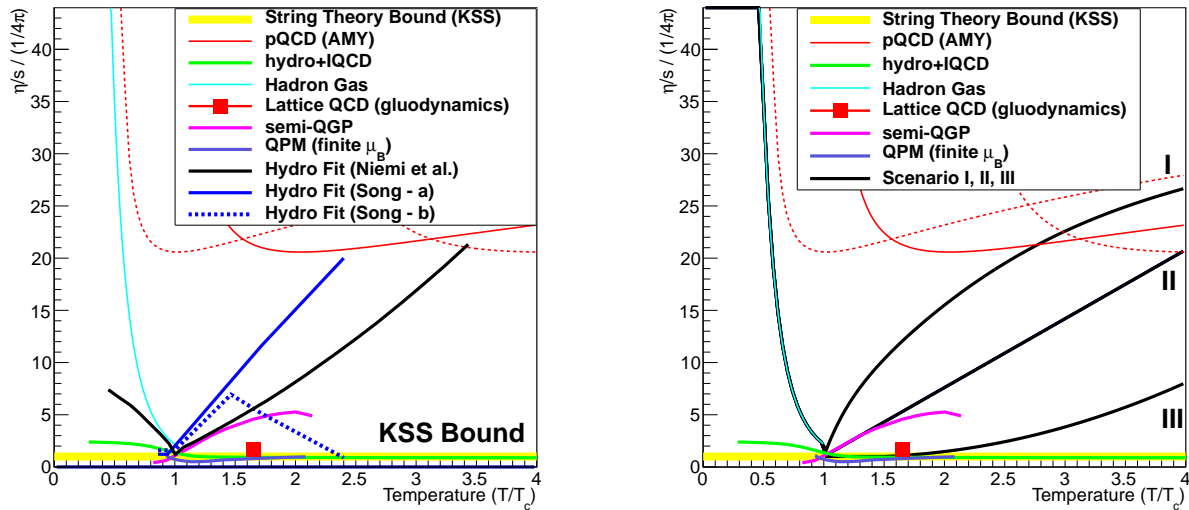


Figure 1.5: (Left) Shear viscosity divided by entropy density, η/s , renormalized by the conjectured KSS bound as a function of the reduced temperature, T/T_c , with various calculations for the quark-gluon plasma case. See text for discussion. (Right) Figure with three conjectured scenarios for the quark-gluon plasma transitioning from the strongly coupled bound (as a near perfect fluid) to the weakly coupled case.

It is safe to say that little is known in a theoretically reliable way about the nature of this transition or the approach to weak-coupling.

Hydrodynamic modeling of the bulk medium does provide constraints on η/s , and recent work has been done to understand the combined constraints on η/s as a function of temperature utilizing both RHIC and LHC flow data sets [31, 32, 33, 34]. The results from [34] as constrained by RHIC and LHC data on hadron transverse momentum spectra and elliptic flow are shown in Figure 1.5 (left panel). These reach the pQCD weak coupled value at $20 \times 1/4\pi$ for $T = 3.4T_c$. Also shown are two scenarios, labeled “Song-a” and “Song-b”, for $\eta/s(T)$ in [32] from which the authors conclude that “one cannot unambiguously determine the functional form of $\eta/s(T)$ and whether the QGP fluid is more viscous or more perfect at LHC energy.”

Shown in Figure 1.5 (right panel) are three possible scenarios for a more or less rapid modification of the medium from the strong to the weak coupling limit. Scenario I has the most rapid change in $\eta/s(T)$ following the “Song-a” parametrization and Scenario III has the least rapid change going through the lattice QCD pure glue result [27]. It is imperative to map out this region in the ‘condensed matter’ physics of QCD and extract the underlying reason for the change.

The above discussion has focused on η/s as the measure of the coupling strength of the quark-gluon plasma. However, both η/s and jet probe parameters such as \hat{q} and \hat{e} are

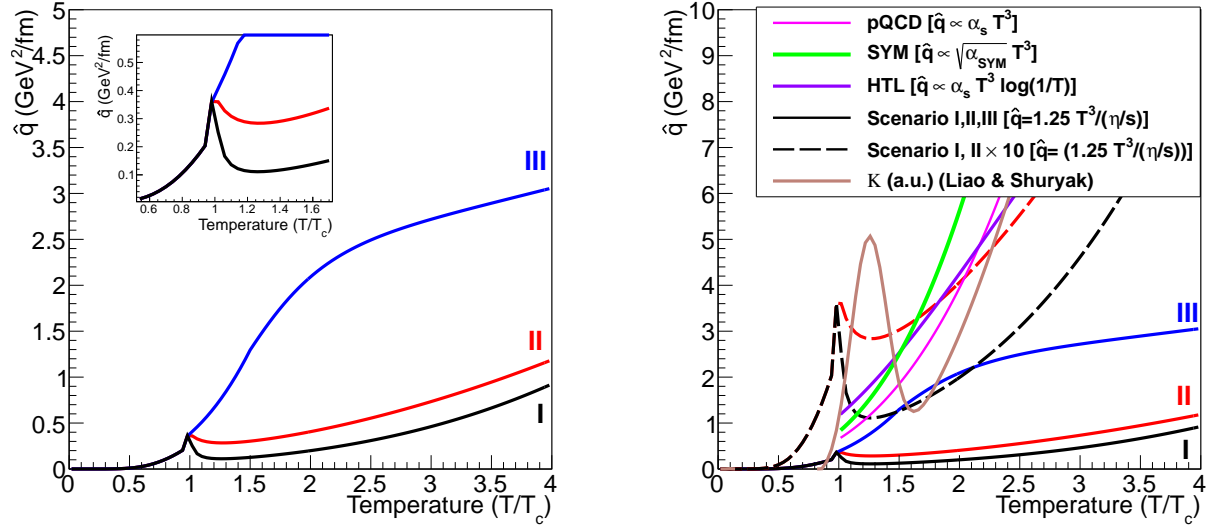


Figure 1.6: (Left) \hat{q} as a function of T/T_c in the three scenarios as related with the weak-coupling calculation. (Right) Different calculations for the scaling of \hat{q} under weak and strong coupling assumptions.

sensitive to the underlying coupling of the matter, but in distinct ways. Establishing for example the behavior of \hat{q} around the critical temperature is therefore essential to a deep understanding of the quark-gluon plasma. Hydrodynamic modeling may eventually constrain $\eta/s(T)$ very precisely, though it will not provide an answer to the question of the microscopic origin of the strong coupling (something naturally available with jet probes).

The authors of Ref [21] propose a test of the strong coupling hypothesis by measuring both η/s and \hat{q} . They derive a relation between the two quantities expected to hold in the weak coupling limit.

$$\hat{q} \stackrel{?}{=} \frac{1.25T^3}{\eta/s} \quad (1.1)$$

The authors conclude that “an unambiguous determination of both sides of [the equation] from experimental data would thus permit a model independent, quantitative assessment of the strongly coupled nature of the quark-gluon plasma produced in heavy ion collisions.” For the three scenarios of $\eta/s(T)$ shown in Figure 1.5 (right panel), we calculate \hat{q} as a function of temperature assuming the equivalence case in Eqn. 1.1 and the result is shown in Figure 1.6 (left panel). The inset in Figure 1.6 shows a magnified view of the region around T_c and a significant local maximum in \hat{q} is observed in scenarios I and II.

Figure 1.6 (right panel) shows that for the equivalence relation of Eqn. 1.1, all three scenarios have a result that differs significantly from the simple perturbative expectation of $\alpha_s T^3$ [35]. Also shown in Figure 1.6 are the predicted temperature dependence of \hat{q} in the strongly coupled AdS/CFT (supersymmetric Yang-Mills) case [22] and the Hard Thermal

Loop (HTL) case [36].

Since the expected scaling of \hat{q} with temperature is such a strong function of temperature, jet quenching measurements should be dominated by the earliest times and highest temperatures. In order to have sensitivity to temperatures around 1–2 T_c , measurements at RHIC are needed in contrast to the LHC where larger initial temperatures are produced. In addition, the ability of RHIC to provide high luminosity heavy-ion collisions at a variety of center of mass energies can be exploited to probe the detailed temperature dependence of quenching right in the vicinity of T_c .

In Ref. [37], Liao and Shuryak use RHIC measurements of single hadron suppression and azimuthal anisotropy to infer that “the jet quenching is a few times stronger near T_c relative to the quark-gluon plasma at $T > T_c$.” This enhancement of \hat{q} is shown in Figure 1.6 (right panel) and is the result of color magnetic monopole excitations in the plasma near T_c . A more detailed discussion of constraints from current experimental measurements is given in Section 1.5. We note that enhancements in \hat{q} above the critical temperature may be a generic feature of many models, as illustrated by the three conjectured evolutions, and so underscore the need for detailed measurements of quark-gluon plasma properties near the transition temperature.

All measurements in heavy ion collisions are the result of emitted particles integrated over the entire time evolution of the reaction, covering a range of temperatures. Similar to the hydrodynamic model constraints, the theory modeling requires a consistent temperature and scale dependent model of the quark-gluon plasma and is only well constrained by precision data through different temperature evolutions, as measured at RHIC and the LHC.

1.3 What are the inner workings of the QGP?

A second axis along which one can investigate the underlying structure of the quark-gluon plasma concerns the question of what length scale of the medium is being probed by jet quenching processes. In electron scattering, the scale is set by the virtuality of the exchanged photon, Q^2 . By varying this virtuality one can obtain information over an enormous range of scales: from pictures of viruses at length scales of 10^{-5} meters, to the partonic make-up of the proton in deep inelastic electron scattering at length scales of less than 10^{-18} meters.

For the case of hard scattered partons in the quark-gluon plasma, the length scale probed is initially set by the virtuality of the hard scattering process. Thus, at the highest LHC jet energies, the parton initially probes a very short length scale. Then as the evolution proceeds, the length scale is set by the virtuality of the gluon exchanged with the color charges in the medium, as shown in the left panel of Figure 1.7. However, if the exchanges are coherent, the total coherent energy loss through the medium sets the length scale.

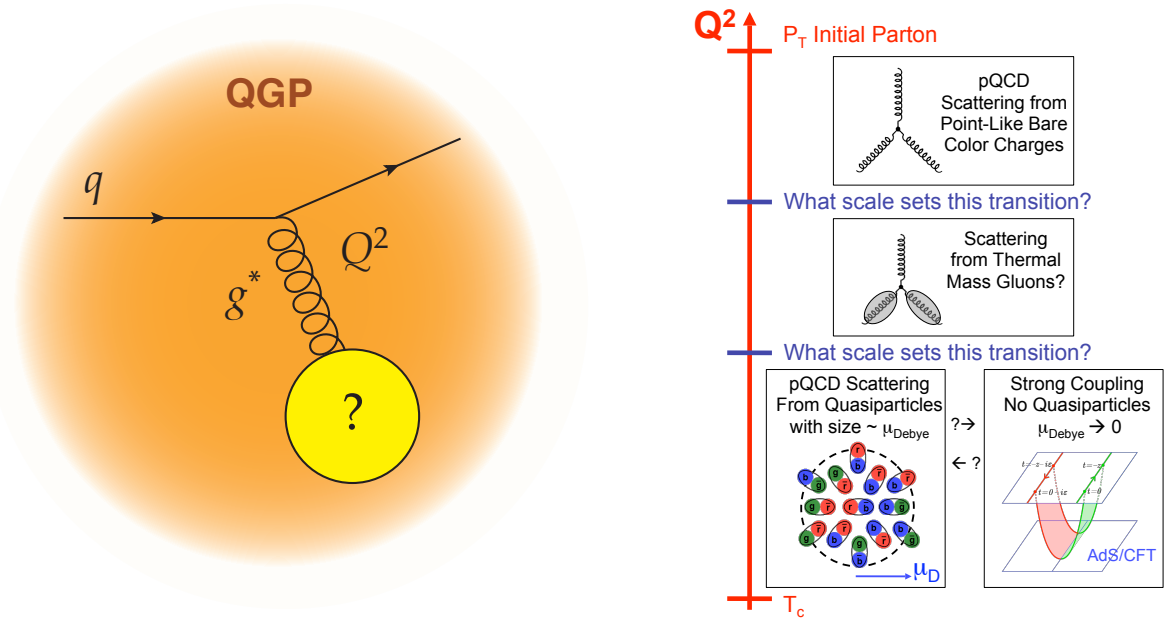


Figure 1.7: (Left) Diagram of a quark exchanging a virtual gluon with an unknown object in the QGP. This highlights the uncertainty for what sets the scale of the interaction and what objects or quasiparticles are recoiling. (Right) Diagram as a function of the Q^2 for the net interaction of the parton with the medium and the range of possibilities for the recoil objects.

Figure 1.7 (right panel) shows that if the length scale probed is very small then one expects scattering directly from point-like bare color charges, most likely without any influence from quasiparticles or deconfinement. As one probes longer length scales, the scattering may be from thermal mass gluons and eventually from possible quasiparticles with size of order the Debye screening length. In Ref. [38], Rajagopal states that “at some length scale, a quasiparticle picture of the QGP must be valid, even though on its natural length scale it is a strongly coupled fluid. It will be a challenge to see and understand how the liquid QGP emerges from short-distance quark and gluon quasiparticles.”

The extension of jet measurements over a wide range of energies and with different medium temperatures again gives one the largest span along this axis. What the parton is scattering from in the medium is tied directly to the balance between radiative energy loss and inelastic collisional energy loss in the medium. In the limit that the scattering centers in the medium are infinitely massive, one only has radiative energy loss—as was assumed for nearly 10 years to be the dominant parton energy loss effect. In the model of Liao and Shuryak [37], the strong coupling near the quark-gluon plasma transition is due to the excitation of color magnetic monopoles, and this should have a significant influence on the collisional energy loss and equilibration of soft partons into the medium.

In a model by Coleman-Smith [39, 40] consisting of parton showers propagating in a medium of deconfined quarks and gluons (see Section 1.6), one can directly vary the mass

of the effective scattering centers and extract the resulting values for \hat{e} and \hat{q} . Figure 1.8 shows $T\hat{e}/\hat{q}$ as a function of the mass of the effective scattering centers in the medium in this model. In the limit of infinitely massive scattering centers, the interactions are elastic and no energy is transferred to the medium.

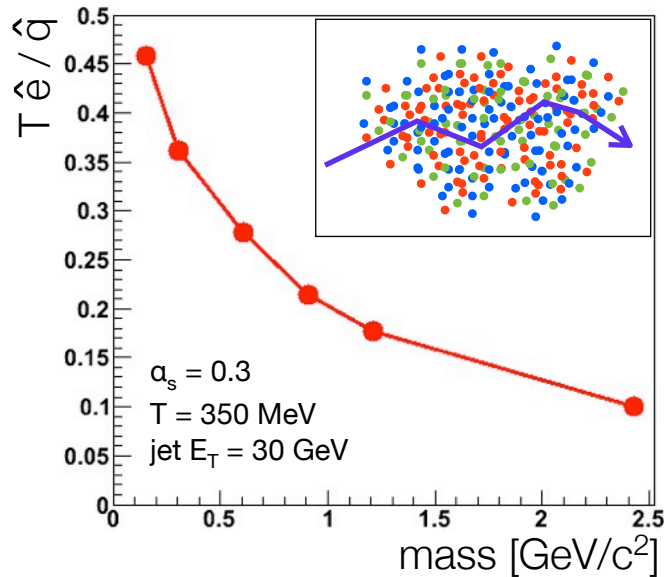


Figure 1.8: $T\hat{e}/\hat{q}$ as a function of the mass of the effective scattering centers in the medium. As the mass increases, the parton is less able to transfer energy to the medium and the ratio drops.

1.4 How does the QGP evolve along with the parton shower?

The initial hard scattered parton starts out very far off-shell and in e^+e^- , $p+p$ or $p+\bar{p}$ collisions the virtuality evolves in vacuum through gluon splitting down to the scale of hadronization. In heavy ion collisions, the vacuum virtuality evolution is interrupted at some scale by scattering with the medium partons which increase the virtuality with respect to the vacuum evolution. Figure 1.9 shows the expected evolution of virtuality in vacuum, from medium contributions, and combined for a quark-gluon plasma at $T_0 = 300$ MeV with the traversal of a 30 GeV parton (left) and at $T_0 = 390$ MeV with the traversal of a 200 GeV parton (right) [41, 42]. If this picture is borne out, it “means that the very energetic parton [in the right picture] hardly notices the medium for the first 3–4 fm of its path length [42].” Spanning the largest possible range of virtuality (initial hard process Q^2) is very important, but complementary measurements at both RHIC and LHC of produced jets at the same virtuality (around 50 GeV) will test the interplay between the vacuum shower and medium scattering contributions.

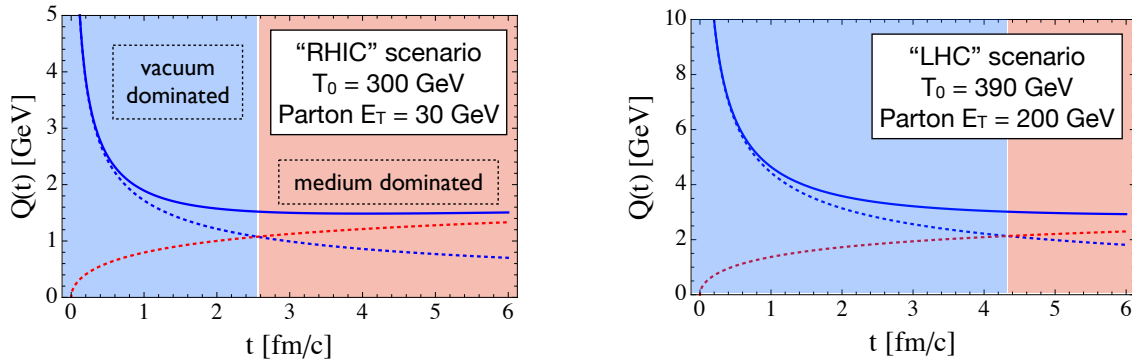


Figure 1.9: Jet virtuality evolution at RHIC (left) and LHC (right). Vacuum contributions to virtuality (blue dashed lines) decrease with time and medium induced contributions (red dashed lines) increase as the parton scatters in the medium. The total virtuality (blue solid lines) is the quadrature sum of the two contributions. At RHIC the medium induced virtuality dominates by 2.5 fm/c while at the LHC the medium term does not dominate until 4.5 fm/c. From Ref. [41].

1.5 Current jet probe measurements

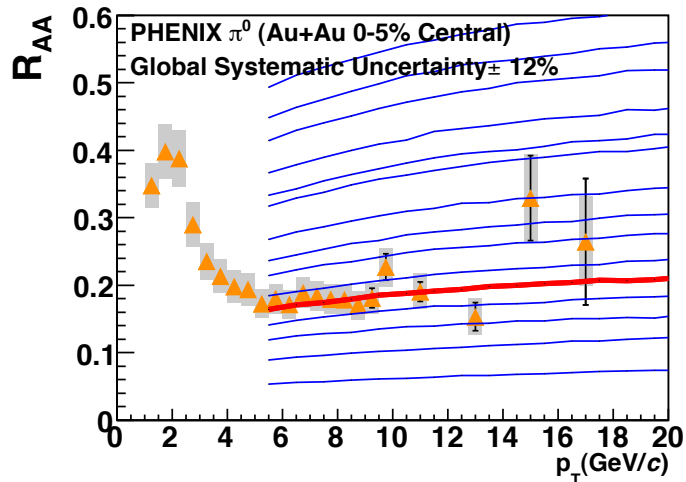


Figure 1.10: $\pi^0 R_{AA}$ for central Au+Au collisions compared to PQM Model calculations [43, 44] for various values of $\langle \hat{q} \rangle$ [45]. The red line corresponds to $\langle \hat{q} \rangle = 13.2 \text{ GeV}^2/\text{fm}$ and is the best fit to the data.

Jet quenching (i.e., the significant loss of energy for partons traversing the QGP) was discovered via measurements at RHIC of the suppression of single hadron yields compared to expectations from $p+p$ collisions [46, 47]. Figure 1.10 [45] shows a comparison between

the PHENIX $\pi^0 R_{AA}$ data and the Parton Quenching Model (PQM) [43, 44] with various values of \hat{q} . This calculation assumes radiative energy loss only in a weakly coupled picture and with no recoil collisional energy loss with partons or quasiparticles in the medium. The coupling parameter value $\hat{q} = 13.2 \text{ GeV}^2/\text{fm}$ implies a very strong coupling and violates the weak coupled assumption of the model formalism.

However, as detailed in Ref. [45, 48], other formalisms also assuming weak coupling are able to achieve an equally good description of the data and with substantially smaller values of \hat{q} . Thus, the single high p_T hadron suppression constrains the \hat{q} value within a model, but is not able to discriminate between different energy loss mechanisms and formalisms for the calculation. Two-hadron correlations measure the correlated fragmentation between hadrons from within the shower of one parton and also between the hadrons from opposing scattered partons. These measurements, often quantified in terms of a nuclear modification I_{AA} [49, 50, 51], are a challenge for models to describe simultaneously [52].

Within the jet quenching model WHDG [53], the authors constrain \hat{q} by the PHENIX π^0 nuclear modification factor. They find the prediction scaled by the expected increase in the color charge density created in higher energy LHC collisions when compared to the ALICE results [54] over-predicts the suppression. This over-prediction based on the assumption of an unchanging probe-medium coupling strength led to title of Ref. [53]: “The surprisingly transparent sQGP at the LHC.” They state that “one possibility is the sQGP produced at the LHC is in fact more transparent than predicted.” Similar conclusions have been reached by other authors [55, 56, 57]. Recently work has been done to incorporate the running of the QCD coupling constant [58].

Theoretical developments constrained simultaneously by data from RHIC and the LHC have been important in discriminating against some models with very large \hat{q} – see Figure 1.11 from Ref. [59] and theory references therein. Models such as PQM and ASW with very large values of \hat{q} have been ruled out by the combined constraint. Shown in Figure 1.12 is a recent compilation of four theoretical calculations with a directly comparable extraction of \hat{q} . Developments on the theory and experimental fronts have significantly narrowed the range of \hat{q} [1]. This theoretical progress lends strength to the case that the tools will be available on the same time scale as sPHENIX data to have precision determinations of \hat{q} and then ask deeper additional questions about the quark-gluon plasma and its underlying properties.

One observable that has been particularly challenging for energy loss models to reproduce is the azimuthal anisotropy of π^0 production with respect to the reaction plane. A weak dependence on the path length in the medium is expected from radiative energy loss. This translates into a small v_2 for high p_T particles (i.e., only a modest difference in parton energy loss when going through a short versus long path through the QGP). Results of $\pi^0 v_2$ are shown in Figure 1.13 [60]. Weakly coupled radiative energy loss models are compared to the R_{AA} (bottom panels) and v_2 (top panels) data. These models reproduce the R_{AA} , but they fall far short of the v_2 data in both p_T ranges measured (6–9 GeV/c and $> 9 \text{ GeV}/c$). This large path length dependence is naturally described by strongly coupled

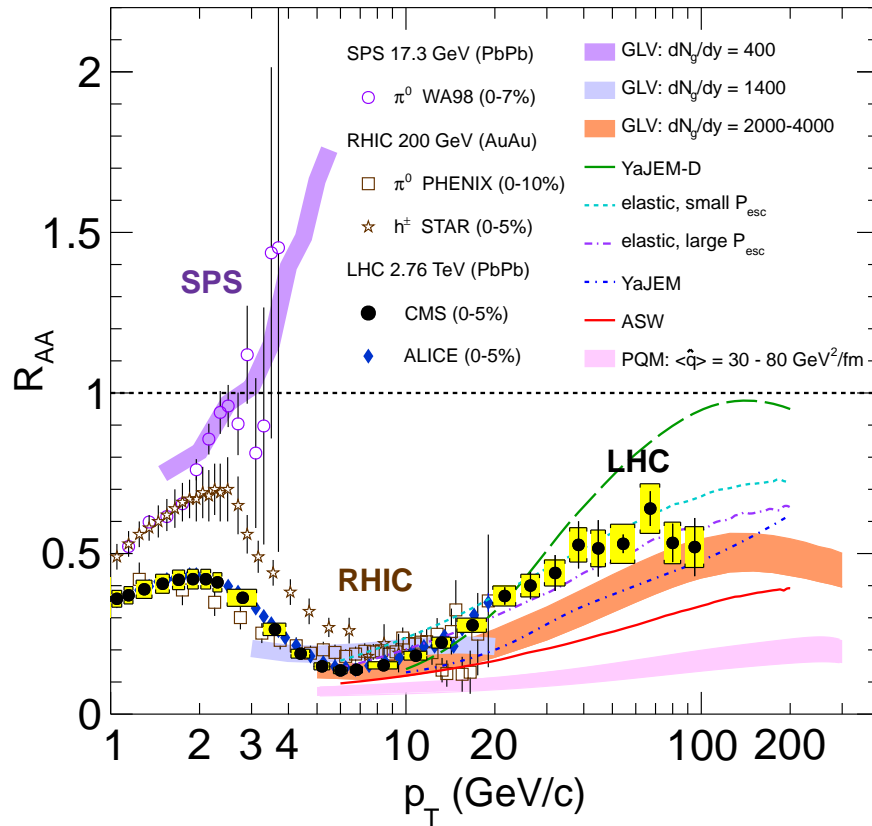


Figure 1.11: The nuclear modification factor R_{AA} as a function of transverse momentum in A+A collisions at the SPS, RHIC, and LHC. Comparisons with various jet quenching calculations as detailed in Ref. [59] and references therein are shown. The simultaneous constraint of RHIC and LHC data is a powerful discriminator.

energy loss models [61, 60]. Note that one can match the v_2 by using a stronger coupling, larger \hat{q} , but at the expense of over-predicting the average level of suppression.

The total energy loss of the leading parton provides information on one part of the parton-medium interaction. Key information on the nature of the particles in the medium being scattered from is contained in how the soft (lower momentum) part of the parton shower approaches equilibrium in the quark-gluon plasma. This information is accessible through full jet reconstruction, jet-hadron correlation, and γ -jet correlation observables. Figure 1.14 shows results from the STAR collaboration [63] on correlations between reconstructed trigger jets and single charged hadrons. The experimental results show the difference in the away-side momentum of hadrons between Au+Au and $p+p$ events. The extent to which this value differs from zero is an indication of the strength of the medium modification of the fragmentation process. The figure also compares these results to calculations obtained using the YaJEM-DE model (see Section 1.6).

There are other preliminary results on fully reconstructed jets from both STAR [64, 65, 66, 67] and PHENIX experiments [68, 69]. However, these results have not proceeded to

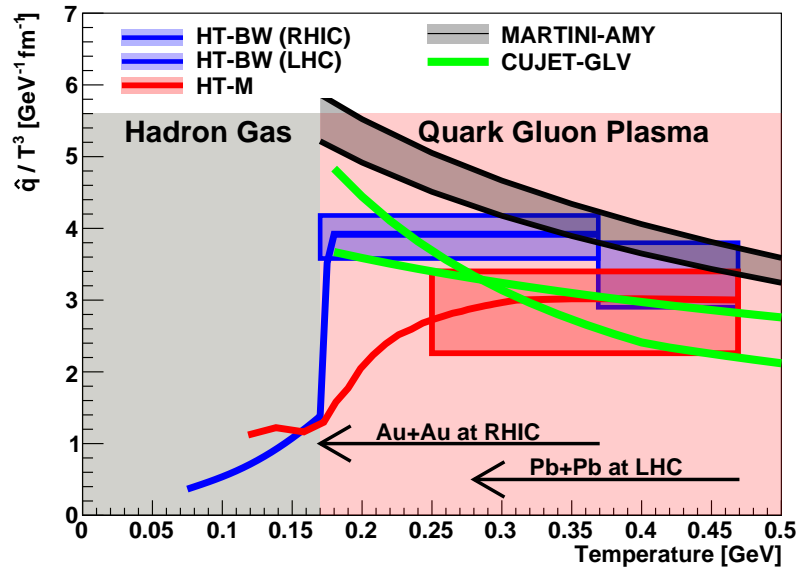


Figure 1.12: Calculations from four jet quenching frameworks constrained by RHIC and LHC R_{AA} data with results for \hat{q}/T^3 as a function of temperature. Details of the calculation are given in Ref. [1].

publication in part due to limitations in the measurement capabilities. In this proposal we demonstrate that a comprehensive jet detector (sPHENIX) with large, uniform acceptance and high rate capability, combined with the now completed RHIC luminosity upgrade can perform these measurements to access this key physics.

The measurements of fully reconstructed jets and the particles correlated with the jet (both inside the jet and outside) are crucial to testing these pictures. Not only does the strong coupling influence the induced radiation from the hard parton (gluon bremsstrahlung) and its inelastic collisions with the medium, but it also influences the way soft partons are transported by the medium outside of the jet cone as they fall into equilibrium with the medium. Thus, the jet observables combined with correlations get directly at the coupling of the hard parton to the medium and the parton-parton coupling for the medium partons themselves.

These jet observables are now available at the LHC. The first results based on reconstructed jets in heavy ion collisions were the centrality dependent dijet asymmetries measured by ATLAS [70]. These results, shown in Figure 1.15, indicate a substantial broadening of dijet asymmetry $A_J = (E_1 - E_2)/(E_1 + E_2)$ distribution for increasingly central Pb+Pb collisions and the lack of modification to the dijet azimuthal correlations. The broadening of the A_J distribution points to substantial energy loss for jets and the unmodified azimuthal distribution shows that the opposing jet $\Delta\phi$ distribution is not broadened as it traverses the matter. Figure 1.16 shows CMS results [71] quantifying the fraction of dijets which are balanced (with $A_J < 0.15$) decreases with increasing centrality.

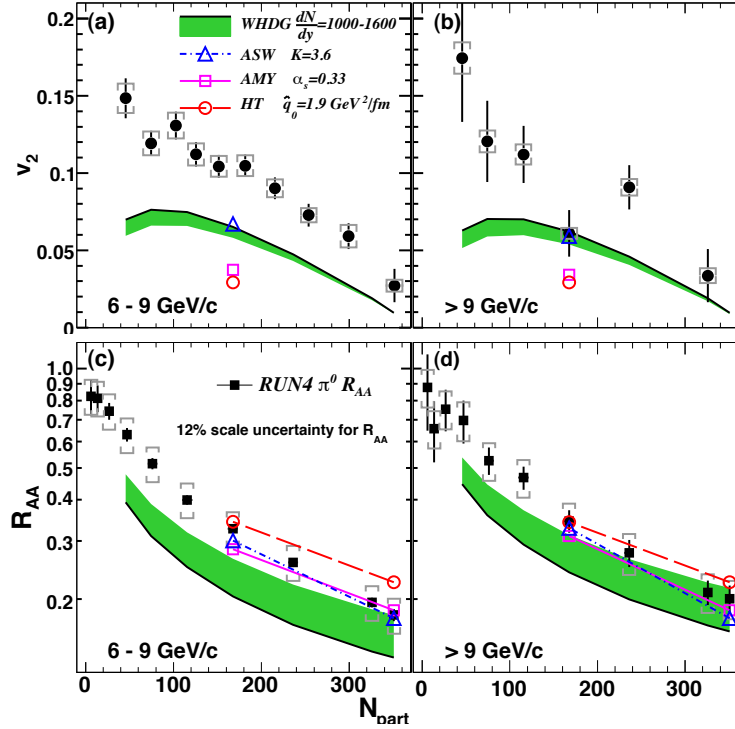


Figure 1.13: π^0 v_2 (top panels) and R_{AA} (bottom panels) for $6 < p_T < 9$ GeV/c (left panels) and $p_T > 9$ GeV/c (right panels). Calculations from four weakly coupled energy loss models are shown as well [48, 62]. From Ref. [60].

Direct photon-jet measurements are also a powerful tool to study jet quenching. Unlike dijet measurements the photon passes through the matter without losing energy, providing a cleaner handle on the expected jet p_T [72]. CMS has results for photons with $p_T > 60$ GeV/c correlated with jets with $p_T > 30$ GeV/c [73]. Though with modest statistical precision, the measurements indicate energy transported outside the $R = 0.3$ jet cone through medium interactions.

These and other reconstructed jet measurements have been complementary to one and two particle measurements at the LHC. Reconstructed jets have significantly extended the kinematic range for jet quenching studies at the LHC, and quenching effects are observed up to the highest reconstructed jet energies (> 300 GeV) [74]. They also provide constraints on the jet modification that are not possible with particle based measurements. For example, measurements from ATLAS constrain jet fragmentation modification from vacuum fragmentation to be small [75] and CMS results on jet-hadron correlations have shown that the lost energy is recovered in low p_T particles far from the jet cone [71]. The lost energy is transported to very large angles and the remaining jet fragments as it would in the vacuum.

Detector upgrades to PHENIX and STAR at RHIC with micro-vertex detectors will allow the separate study of c and b quark probes of the medium, as tagged via displaced vertex

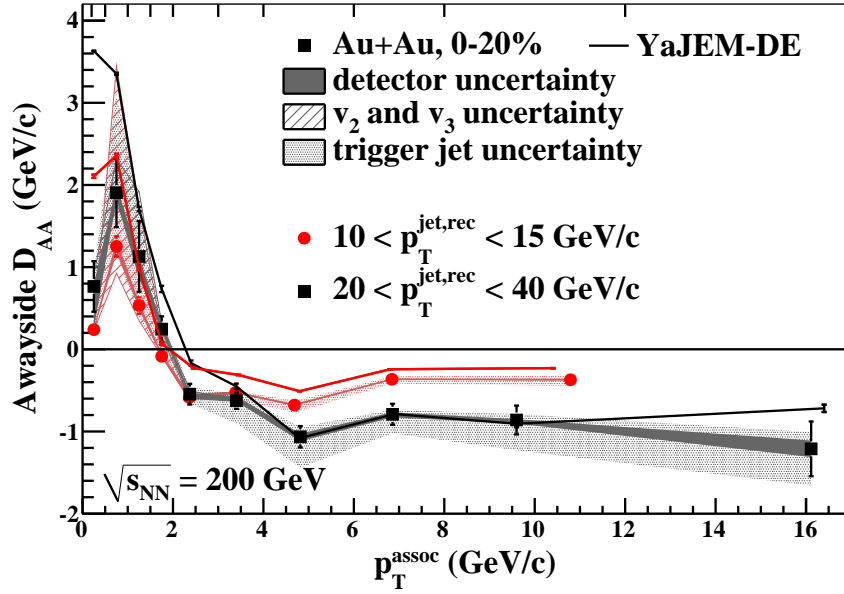


Figure 1.14: The away-side momentum difference, D_{AA} , of hadrons between Au+Au and $p+p$ events, as measured by STAR [63], showing medium modification of jet fragmentation.

single electrons and reconstructed D and Λ_c hadrons. Similar measurements at the LHC provide tagging of heavy flavor probes as well. These measurements will also provide insight on the different energy loss mechanisms, in particular because initial measurements of non-photonic electrons from RHIC challenge the radiative energy loss models.

It is clear that in addition to extending the RHIC observables to include fully reconstructed jets and γ -jet correlations, theoretical development work is required for converging to a coherent 'standard model' of the medium coupling strength and the nature of the probe-medium interaction. In the next section, we detail positive steps in this direction.

1.6 Theoretical calculations of jets at RHIC

Motivated in part by the new information provided by LHC jet results and the comparison of RHIC and LHC single and di-hadron results, the theoretical community is actively working to understand the detailed probe-medium interactions. The challenge is to understand not only the energy loss of the leading parton, but how the parton shower evolves in medium and how much of the lost energy is re-distributed in the quark-gluon plasma. Theoretical calculations attempting to describe the wealth of new data from RHIC and the LHC have not yet reconciled some of the basic features, with some models including large energy transfer to the medium as heat (for example [76]) and others with mostly radiative energy loss (for example [77, 78]). None of the current calculations available has been confronted with the full set of jet probe observables from RHIC and the LHC. Measurements of jets at RHIC energies and with jets over a different kinematic range allow

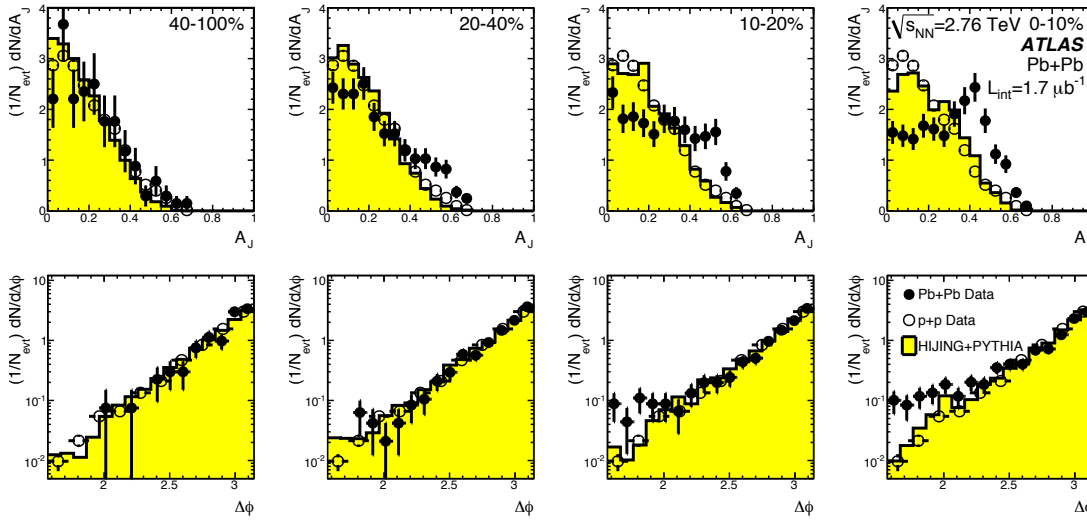


Figure 1.15: A_J (top row) and dijet $\Delta\phi$ distribution from ATLAS [70]. Jets are reconstructed with the anti- k_T algorithm with $R = 0.4$. The leading jet has $E_T > 100$ GeV and the associated jet has $E_T > 25$ GeV. Pb+Pb data (solid points), $p+p$ data at 7 TeV (open points) and PYTHIA embedded in HIJING events and run through the ATLAS Monte Carlo (yellow histograms) are shown. From Ref. [70].

for specific tests of these varying pictures. In this section, we give a brief review of a subset of calculations for jet observables at RHIC enabled by the sPHENIX upgrade and highlight the sensitivity of these observables to the underlying physics.

Much of this work has been carried out under the auspices of the Department of Energy Topical Collaboration on Jet and Electromagnetic Tomography of Extreme Phases of Matter in Heavy-ion Collisions [79]. Workshops held by the JET Collaboration at Duke University in March 2012 and Wayne State University in August 2013 have been dedicated to the topic of jet measurements at RHIC. These workshops were attended by theorists as well as experimentalists from both RHIC and the LHC. This is an active collaborative effort.

In order to overcome specific theoretical hurdles regarding analytic parton energy loss calculations and to couple these calculations with realistic models of the QGP space-time evolution, Monte Carlo approaches have been developed (as examples [80, 81, 82, 40, 83, 84]). Here we describe RHIC energy jet probe results from specific theory groups utilizing different techniques for calculating the jet-medium interactions. These efforts indicate a strong theoretical interest and the potential constraining power of a comprehensive jet physics program at RHIC.

Jets provide a very rich spectrum of physics observables, ranging from single jet observables such as R_{AA} , to correlations of jets with single particles, to correlations of trigger jets with other jets in the event. An example of how one can exploit this variety can be found in recent calculations by Renk [85]. Figure 1.17 is based on calculations using the

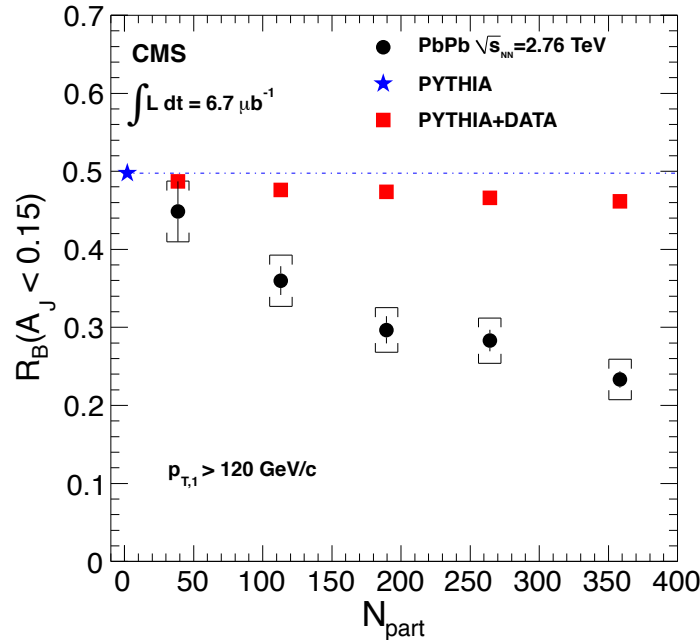


Figure 1.16: Fraction of dijets which have $A_J < 0.15$ in Pb+Pb collisions as a function of centrality. Jets are reconstructed with an iterative cone algorithm with a radius of 0.5. The leading jet is required to have an $E_T > 120$ GeV and the associated jet has $E_T > 50$ GeV. Results are shown for Pb+Pb data (circles), PYTHIA (star) and PYTHIA jets embedded into real data (squares). From Ref. [71].

YaJEM model to illustrate what could be called “jet surface engineering”. Triggers ranging from single hadrons on up to ideally reconstructed jets are used to form correlations with another jet in the event. The different triggers demonstrate different degrees of surface bias in the production point of the “dijet” and this bias itself can be used as a lever to investigate properties of the medium.

We show results are from Coleman-Smith and collaborators [39, 40] where they extract jet parton showers from PYTHIA (turning off hadronization) and then embed the partons into a deconfined quark-gluon plasma, modeled with the VNI parton cascade [87]. For the calculations shown here, the background medium consists of a cylinder of deconfined quarks and gluons at a uniform temperature. One excellent feature of the calculation is that it provides the ability to track each individual parton and thus not only look at the full time evolution of scattered partons from the shower, but also medium partons that are kicked up and can contribute particles to the reconstructed jets.

Calculation results for the dijet asymmetry $A_J = (E_1 - E_2)/(E_1 + E_2)$ in a QGP with a temperature appropriate for LHC collisions and fixed $\alpha_s = 0.3$ are shown in Figure 1.18 (left panel) [39]. The jets in the calculation are reconstructed with the anti- k_T algorithm with radius parameter $R = 0.5$ and then smeared by a simulated jet resolution of $100\%/\sqrt{E}$, and with requirements of $E_{T1} > 120$ GeV and $E_{T2} > 50$ GeV on the leading and sub-leading jet,

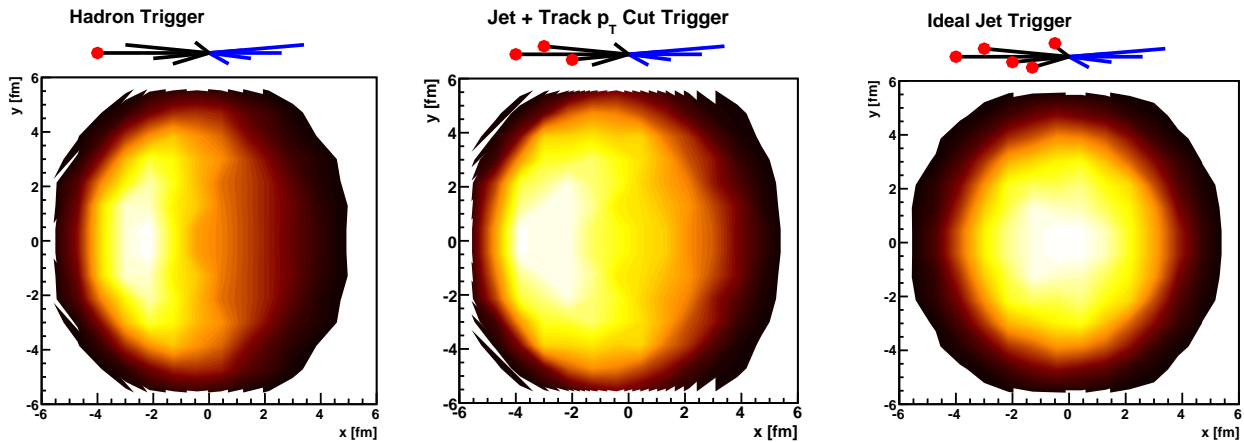


Figure 1.17: Dijet surface bias in YaJEM for various trigger definitions. As the trigger is changed from a single hadron (left) to a reconstructed jet with a minimum p_T selection on charged tracks and electromagnetic clusters (middle) to an ideally reconstructed jet (right), the surface bias in the production point becomes less pronounced. sPHENIX is capable of all three types of measurements. (Based on figure taken from [85].)

respectively. The calculated A_J distributions reproduce the CMS experimental data [71].

In Figure 1.18 (right panel) the calculation is repeated with a medium temperature appropriate for RHIC collisions and with RHIC observable jet energies, $E_{T1} > 20$ GeV and $R = 0.2$. The calculation is carried out for different coupling strengths α_s between partons in the medium themselves and the parton probe and medium partons. The variation in the value of α_s should be viewed as changing the effective coupling in the many-body environment of the QGP. It is interesting to note that in the parton cascade BAMPS, the authors find a coupling of $\alpha_s \approx 0.6$ is required to describe the bulk medium flow [88]. These results indicate sizable modification to the dijet asymmetry and thus excellent sensitivity to the effective coupling to the medium at RHIC energies.

Figure 1.19 demonstrates the determination of the effective coupling in the model of Coleman-Smith. The different curves in the left panel show the distribution of dijet asymmetry for different values of the effective coupling. The data points are generated for a particular value of the coupling strength and the uncertainties are representative of those that sPHENIX would record. By performing a modified χ^2 comparison of the model to the data, one obtains the curve in the right panel. From that curve, one is able to determine the coupling with an uncertainty of about 5%.

Figure 1.20 (left panel) shows the temperature dependence of the dijet asymmetry, now keeping the coupling α_s fixed. One observes a similar sharp drop in the fraction of energy balanced dijets with increasing temperature to that seen for increasing the effective coupling, and so combining these observations with constrained hydrodynamic models and direct photon emission measurements is important. Given that the initial temperatures of the QGP formed at RHIC and the LHC should be significantly different, this plot shows

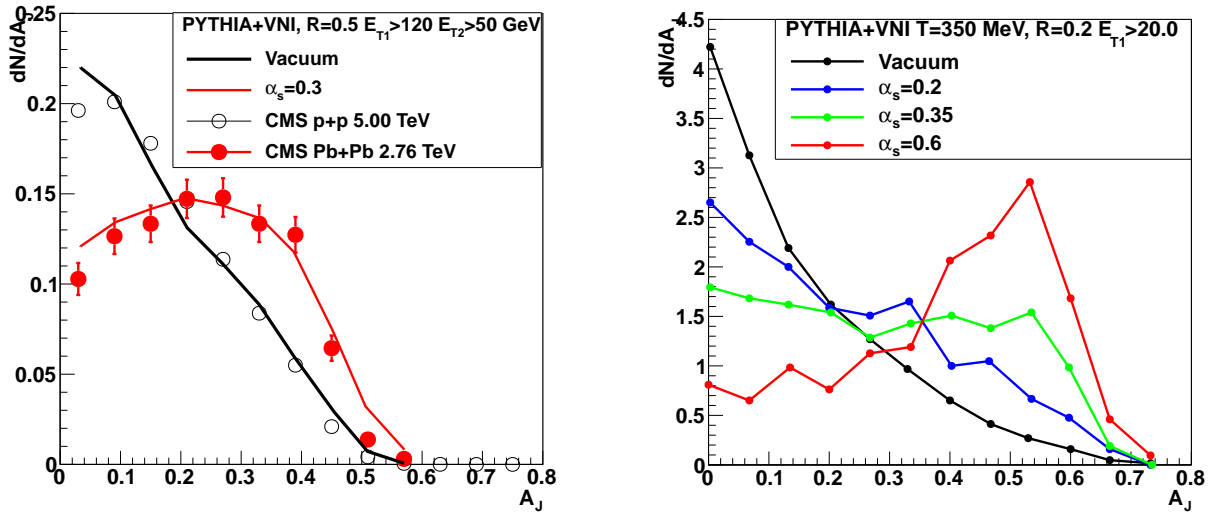


Figure 1.18: (Left) Calculation in VNI parton cascade of dijet A_J with $T = 0.35$ GeV and $\alpha_s = 0.3$ compared to the CMS data [39]. (Right) Calculation for RHIC jet energies, $E_{T,1} > 20$ GeV, for a circular geometry of radius 5 fm of A_J for different values of α_s increasing to $\alpha_s = 0.6$ (red line) [86].

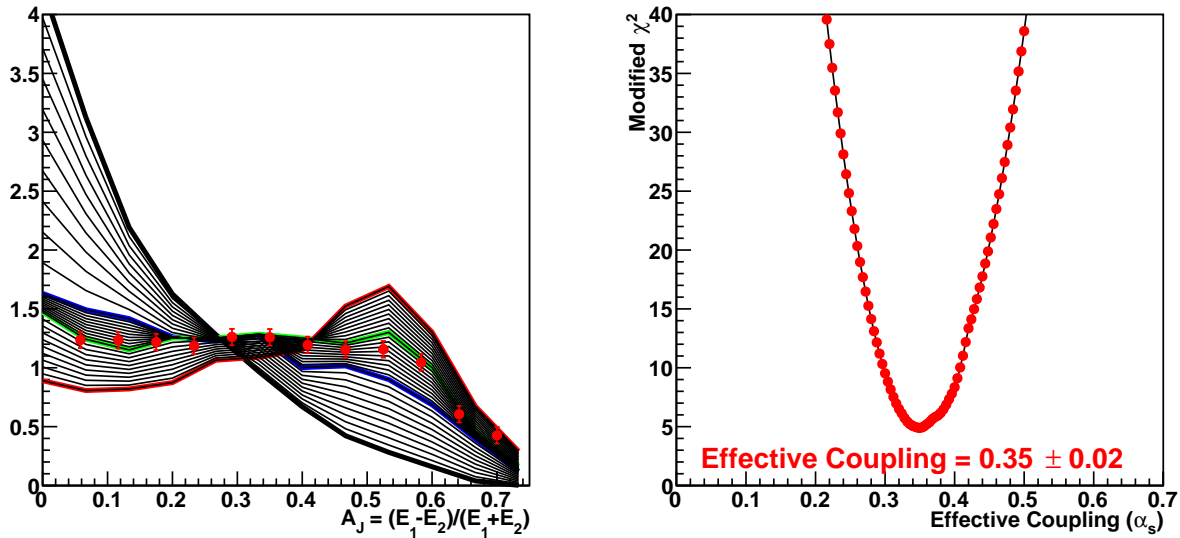


Figure 1.19: Determination of effective coupling strength in the model of Coleman-Smith.

that if RHIC and LHC measure the A_J distribution at the same jet energy there should still be a sensitivity to the temperature which will lead to an observable difference. Thus, having overlap in the measured jet energy range at RHIC and the LHC is important, and this should be available for jet energies of 40–70 GeV. Figure 1.20 (right panel) shows the

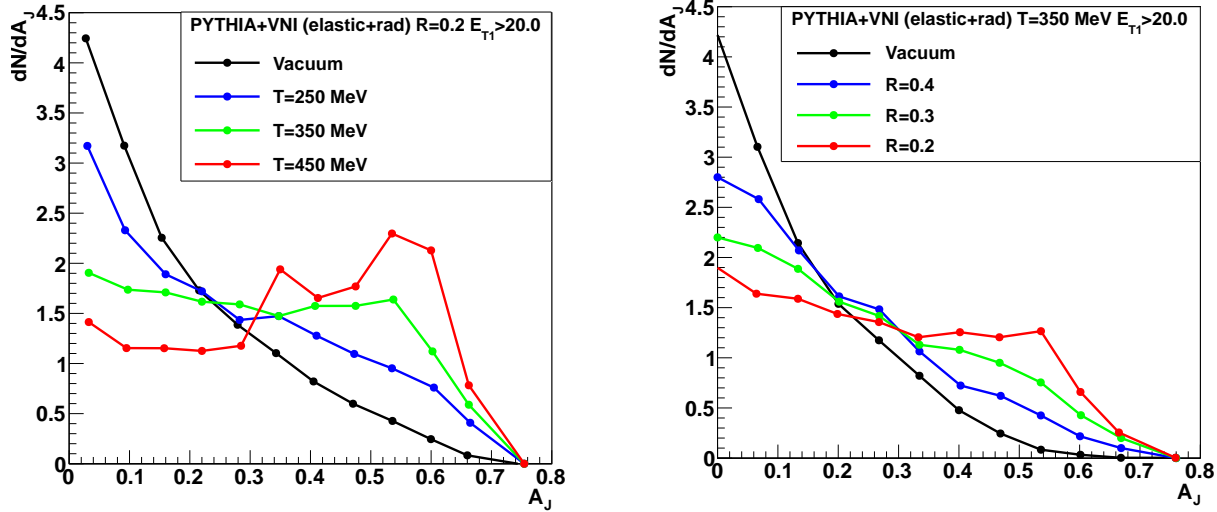


Figure 1.20: Calculations from Coleman-Smith [86] for dijets embedded into the VNI parton cascade. The dijet asymmetry A_J for leading jets with $E_T > 20$ GeV is shown as the medium temperature is varied (left panel) and as the jet cone radius is varied with fixed temperature $T = 350$ MeV (right panel).

jet cone size, R , dependence of A_J at a fixed temperature. The narrowest jet cone $R = 0.2$ has the most modified A_J distribution, as partons are being scattered away by the medium to larger angles.

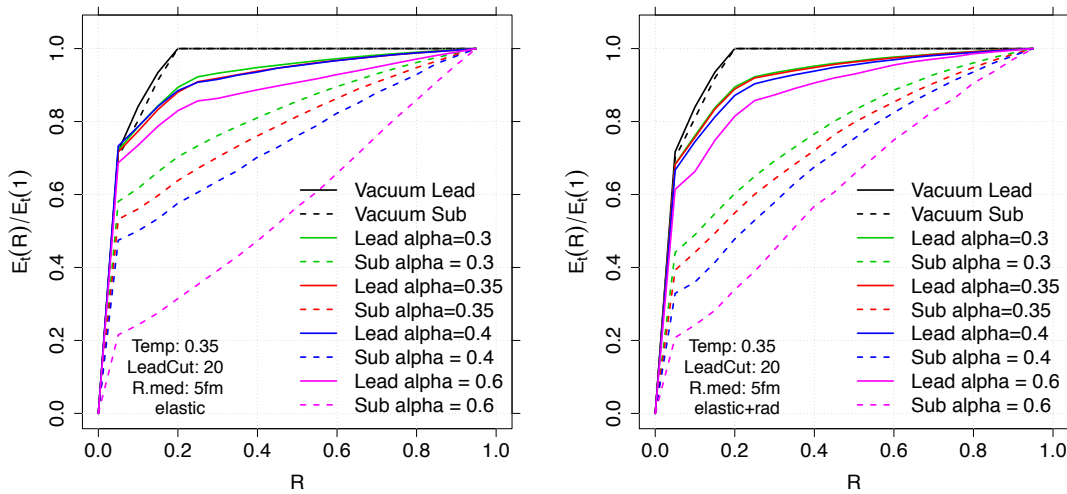


Figure 1.21: Calculations from Coleman-Smith [86] showing the jet energy profile as a function of radius for leading (solid lines) and sub-leading (dashed lines) jets. Leading jets have $E_T > 20$ GeV and sub-leading jets have $E_T > 5$ GeV. The medium temperature is 350 MeV.

Complementary to measuring jets with different radius parameters is to directly examine the profile of energy both within and outside the reconstructed jet. Results on the predicted distribution of energy as a function of radius are shown in Figure 1.21. The solid lines are for the leading jet and for different values of the medium coupling α_s . The dashed lines are for the sub-leading jet. One observes a particularly strong dependence on the coupling in the radial energy profile of the sub-leading jet, as this parton is typically biased to a longer path length through the medium. The left panel is including only elastic collisional interactions and the right panel incorporates additional radiative processes. At coupling $\alpha_s = 0.4$ for example, the fraction of energy in the sub-leading jet within $R < 0.2$ is 60% with elastic collisions only and less than 50% when including radiative energy loss. The experimental extraction of these two contributions is a critical step towards extracting a microscopic picture of the QGP.

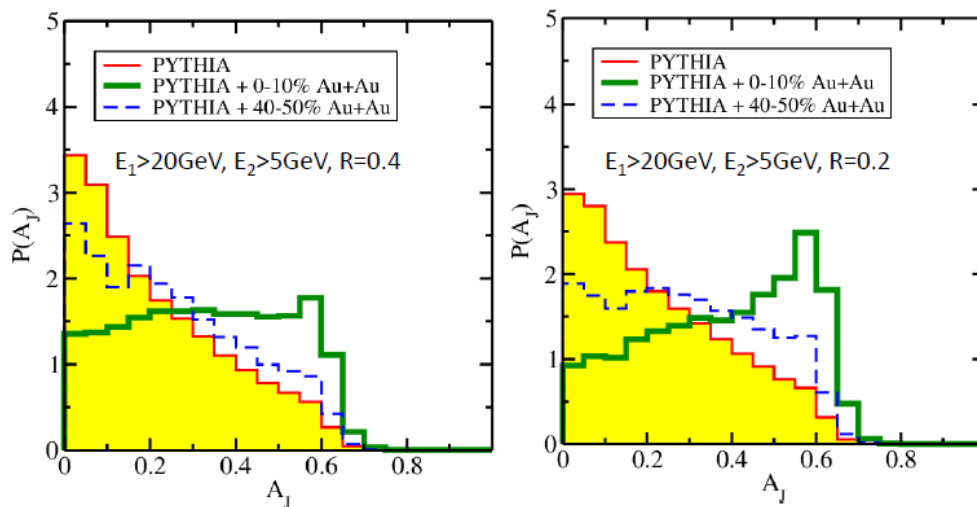


Figure 1.22: Calculations from Qin et al. [89] of dijet A_J for $E_{T,1} > 20 \text{ GeV}$ and $E_{T,2} > 5 \text{ GeV}$ for $R = 0.4$ jets (left) and $R = 0.2$ jets (right). Central (green) and mid-central (blue) distributions are shown along with the initial PYTHIA distributions (red).

The second results are from Qin and collaborators [90, 89] where they solve a differential equation that governs the evolution of the radiated gluon distribution as the jet propagates through the medium. Energy contained inside the jet cone is lost by dissipation through elastic collisions and by scattering of shower partons to larger angles. Their calculation is able to describe the LHC measured dijet asymmetry [90]. Figure 1.22 shows the predicted dijet asymmetry at RHIC for mid-central and central Au+Au collisions for leading jets $E_{T,1} > 20 \text{ GeV}$ and jet radius parameter $R = 0.4$ and $R = 0.2$ in the left and right panels, respectively. Despite the calculation including a rather modest value of \hat{q} and \hat{e} , the modification for $R = 0.2$ is as strong as the result with $\alpha_s = 0.6$ from Coleman-Smith and collaborators shown above in the right panel of Figure 1.18. Calculations of γ -jet correlations indicate similar level modifications. It is also notable that Qin and collaborators have calculated the reaction plane dependence of the dijet A_J distribution and find negligible

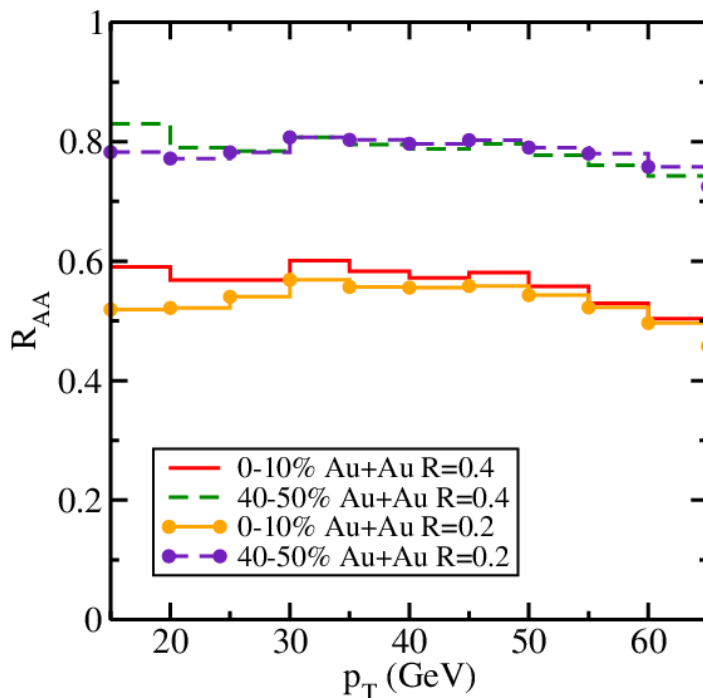


Figure 1.23: Calculations from Qin et al. [89] for jet R_{AA} for central (solid lines) and mid-central collisions (dashed lines) for $R = 0.2$ and 0.4 jets.

differences. This observable will be particularly interesting to measure at RHIC since these calculations have difficulty reproducing the high p_T π^0 reaction plane dependence (v_2) as discussed in the previous section.

Figure 1.23 shows results for the inclusive jet R_{AA} as a function of p_T for jet radius parameters $R = 0.2$ and $R = 0.4$. It is striking that the modification is almost independent of p_T of the jet and there is very little jet radius dependence. The modest suppression, of order 20%, in mid-central Au+Au collisions is of great interest as previous measurements indicate modification of single hadrons and dihadron correlations for this centrality category. Measurements of jets with a broad range of radius parameters are easier in the lower multiplicity mid-central collisions.

The third results are from Young and Schenke and collaborators [82]. These calculations utilize a jet shower Monte Carlo, referred to as MARTINI [91], and embed the shower on top of a hydrodynamic space-time background, using the model referred to as MUSIC [92]. Figure 1.24 shows the jet energy dependence of A_J for RHIC energy dijets, $E_{T1} > 25$ GeV and $E_{T1} > 35$ GeV in the left and right panels, respectively. These results are directly compared to the calculations from Qin and collaborators and indicate a substantially different modification for the higher energy dijets. Interestingly, both of these approaches, when applied at the higher collision energies of the LHC, each reproduce the measured data quite well [93, 90].

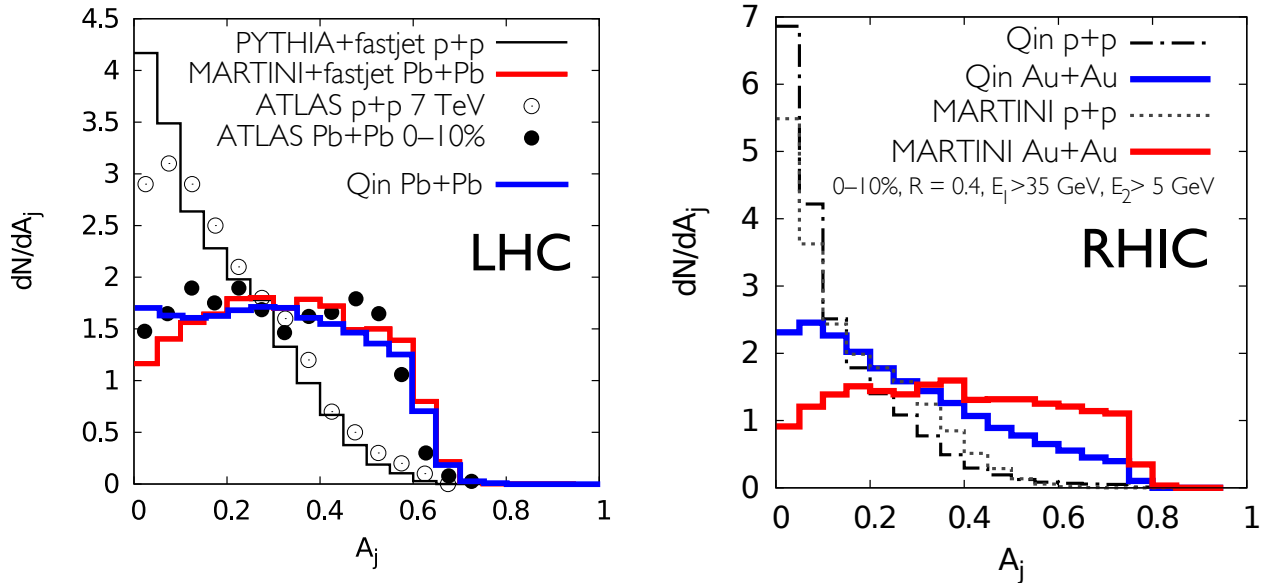


Figure 1.24: A_J distributions in MARTINI+MUSIC [94] and the model of Qin et al. [89]. (Left) Comparison of A_J calculations in MARTINI+MUSIC and by Qin et al for Pb+Pb collisions at 2.76 TeV (red line, Qin et al; blue line, MARTINI+MUSIC). Both calculations show a similar broad A_J distribution. (Right) Same as left panel, but for Au+Au collisions at 200 GeV (with leading jet $E_T > 35$ GeV). Here a difference in shape is observed between the two models with the Qin et al. model developing a peak at small A_J while the MARTINI+MUSIC calculation retains a shape in the calculation at the higher energy.

Our final set of illustrative theory calculations come from Vitev and collaborators [95, 96, 97] where they utilize a Next-to-Leading-Order (NLO) calculation and consider not only final-state inelastic parton interactions in the QGP, but also initial-state cold nuclear matter effects. Figure 1.25 shows the dijet asymmetry A_J for jets with $E_{T1} > 30$ GeV and $R = 0.2$ (left panels) and $E_{T1} > 50$ GeV and $R = 0.6$ (right panels). The upper plots are for radiative energy loss only and the lower plots are including collisional energy loss as well, and then the different colors are varying the probe-medium coupling by $\pm 10\%$. There is sensitivity even to these 10% coupling modifications, and for the higher energy jets there is a dramatic difference predicted from the inclusion of collisional energy loss.

For the inclusive jet suppression, these calculations predict a significant jet radius R dependence to the modification, in contrast to the result from Qin and collaborators. In addition, Vitev and collaborators hypothesize a substantial cold nuclear matter effect of initial state parton energy loss. Because the high energy jets originate from hard scattering of high Bjorken x partons, a modest energy loss of these partons results in a reduction in the inclusive jet yields. At RHIC with d +Au running we will make cold nuclear matter measurements at the same collision energy and determine the strength of these effects as a baseline to heavy ion measurements.

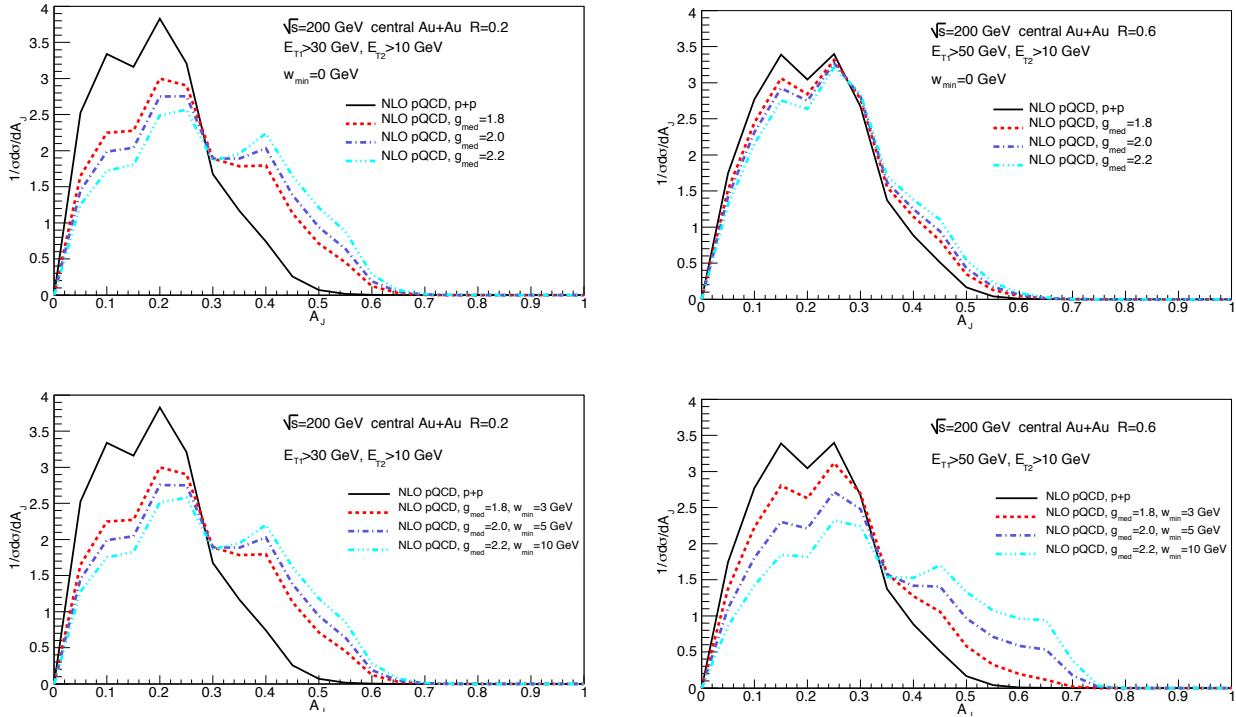


Figure 1.25: A_J distributions calculated by Vitev et al. [95, 96, 97] for two sets of kinematic cuts and jet cone radii. The upper plots are for radiative energy loss only, and the lower plots include collisional energy loss as well.

1.7 Fragmentation Functions

The original predictions of jet quenching in terms of induced forward radiation had the strongest modification in the longitudinal distribution of hadrons from the shower (i.e. a substantial softening of the fragmentation function). One may infer from the nuclear suppression of π^0 in central Au+Au collisions $R_{AA} \approx 0.2$ that the high z (large momentum fraction carried by the hadron) showers are suppressed. However, a direct measurement with reconstructed jets and γ -jet events provides significantly more information. Shown in Figure 1.26 is the fragmentation function for 40 GeV jets in vacuum (PYTHIA) compared with the case of substantial jet quenching (Q-PYTHIA with a quenching factor used to match RHIC single hadron suppression observables). In the sPHENIX upgrade, fragmentation functions via precision charged track measurements are available from high- z where the effects are predicted to be largest to low- z where medium response and equilibration effects are relevant. The independent measurement of jet energy (via calorimetry) and the hadron p_T via tracking is crucial. This independent determination also dramatically reduces the fake track contribution by the required coincidence with a high energy jet.

Measurements of fragmentation functions within reconstructed jets from the CMS and ATLAS experiments in Pb+Pb collisions show very modest modification within uncertainties.

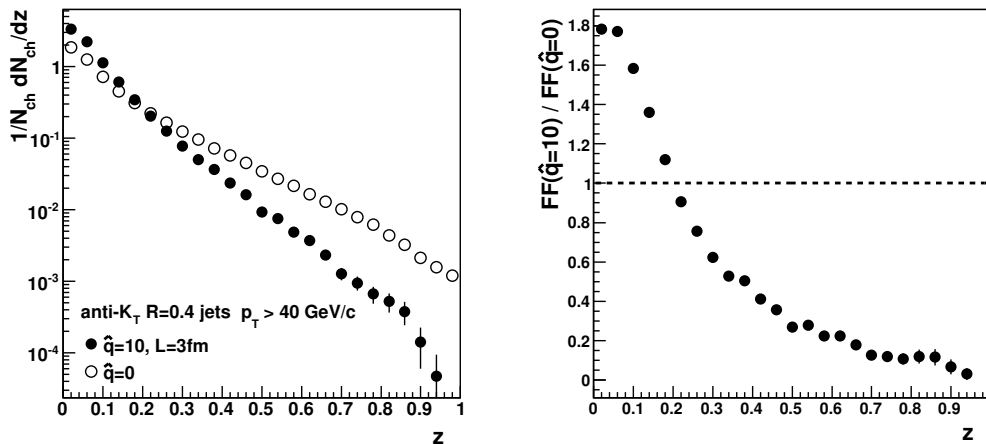


Figure 1.26: Q-PYTHIA simulation with quenching parameter $\hat{q} = 0$ (i.e., in vacuum) and $\hat{q} = 10 \text{ GeV}/c^2$ for the fragmentation function of light quark and gluon jets as a function of z .

Although one explanation is that the jets that are reconstructed are from near the surface and thus not modified, with a nuclear modification factor for inclusive jets $R_{AA} \approx 0.5$ that explanation is challenged. Similar measurements at RHIC energies are crucial to fully map out the re-distribution of energy in the shower and medium response.

1.8 Heavy Quark Jets

A main motivation for studying heavy flavor jets in heavy ion collisions is to understand the mechanism for parton-medium interactions and to further explore the issue of *strong versus weak* coupling [98]. There are crucial measurements of single electrons from semileptonic D and B decays and direct D meson reconstruction with the current PHENIX VTX and the soon to come STAR Heavy Flavor Tracker (HFT) upgrade. The sPHENIX program can significantly expand the experimental acceptance and physics reach by having the ability to reconstruct full jets with a heavy flavor tag. The rates for heavy flavor production from perturbative QCD calculations [99] are shown in Figure 1.27.

One promising tool is the study of heavy flavor jet-shape modification in Au+Au relative to $p+p$ collisions. Different mechanisms of energy loss (radiative versus collisional) predict different re-distributions of the jet fragments both inside and outside the jet cone. There are also scenarios where the heavy meson forms inside the medium and is dissociated in the matter [100, 101]. This would lead to a nearly unmodified jet shape relative to $p+p$ collisions and a much softer fragmentation function for the leading heavy meson. Figure 1.28 shows the D meson fragmentation function in PYTHIA and Q-PYTHIA for 20 GeV charm jets. The peak of the fragmentation function is shifted in Q-PYTHIA from

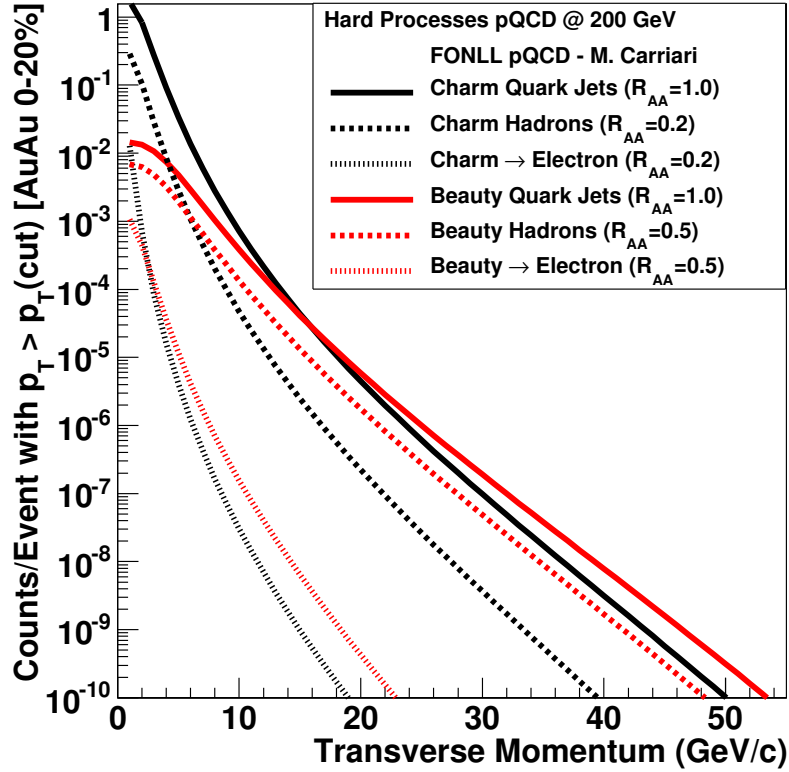


Figure 1.27: FONLL calculations [99] for heavy flavor (charm and beauty) jets, fragmentation hadrons (D , B mesons primarily), and decay electrons as a function of transverse momentum. The rates have been scaled to correspond to counts with $p_T > p_T(\text{cut})$ for Au+Au 0–20% central collisions.

$z \approx 0.7$ to $z \approx 0.5$. Thus, for a given p_T , D mesons are more suppressed than charm jets.

The tagging of charm and beauty jets has an extensive history in particle physics experiments. Detailed studies for this tagging within the sPHENIX upgrade with the additional tracking and electron identification described above are underway. There are three ways to tag heavy flavor jets. First is the method of tagging via the selection of a high p_T electron with a displaced vertex inside the jet. In minimum bias Au+Au collisions at $\sqrt{s_{NN}} = 200$ GeV, the fraction of inclusive electrons from D and B meson decays is already greater than 50% for $p_T > 2$ GeV/c. The VTX in combination with the additional tracking layers can confirm the displaced vertex of the electron from the collision point, further enhancing the signal. Since the semileptonic branching fraction of D and B mesons is approximately 10%, this method provides a reasonable tagging efficiency. Also, the relative angle of the lepton with respect to the jet axis provides a useful discriminator for beauty jets as well, due to the decay kinematics. Second, the direct reconstruction of D and B

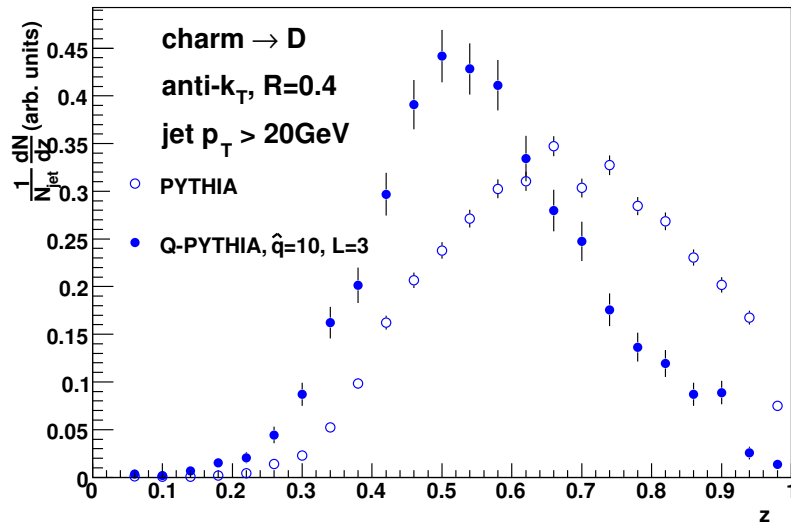


Figure 1.28: D meson fragmentation function in PYTHIA (open points) and Q-PYTHIA (solid points) for anti- k_T jets with $R = 0.4$ and $E_T(\text{jet}) > 20 \text{ GeV}$ as a function of z , the fractional momentum of the D meson relative to the charm quark.

mesons is possible within sPHENIX, with the additional tracking. The current PHENIX VTX is limited in its acceptance for D decays by the need to also reconstruct the track in the existing PHENIX central arm outer spectrometer, which has $|\eta| < 0.35$ and $\Delta\phi = 2 \times \pi/2$. The sPHENIX acceptance will yield a much higher (order of magnitude) yield of D mesons. The third method utilizes jets with many tracks that do not point back to the primary vertex. This technique is used by the $D0$ collaboration to identify beauty jets at the Tevatron [102]. This method exploits the fact that most hadrons with a beauty quark decay into multiple charged particles all with a displaced vertex. The detailed performance metrics for tagged heavy flavor jets are being developed in conjunction with converging on a design for the additional tracking layers.

1.9 Measuring jets, dijets, γ -jet, and fragmentation functions at RHIC

Jet and γ -jet measurements at RHIC are particularly appealing for the reasons previously detailed. In order to make these observations, one requires both sufficient rate and acceptance for jets, dijets, and γ -jet events and a detector with large and uniform acceptance to measure them. The performance of the proposed sPHENIX detector is described in later chapters. Here we highlight the large rate of such events available at RHIC energies.

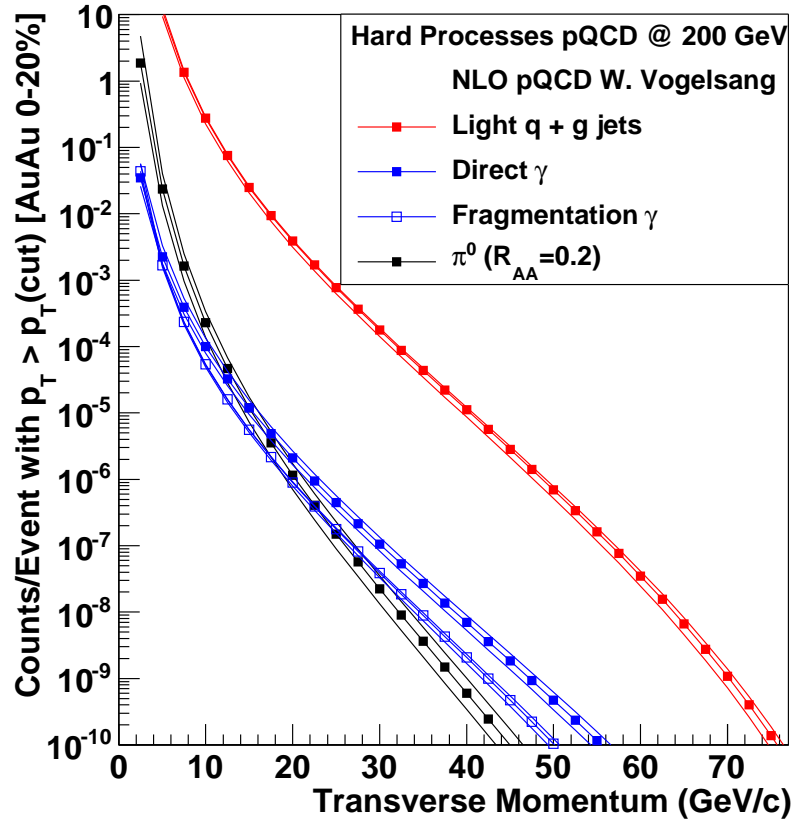


Figure 1.29: Jet, photon and π^0 rates with $|\eta| < 1.0$ from NLO pQCD [103] calculations scaled to Au+Au central collisions for $\sqrt{s_{NN}} = 200$ GeV. The scale uncertainties on the pQCD calculations are shown as additional lines. Ten billion Au+Au central collisions correspond to one count at 10^{-10} at the bottom of the y-axis range. A nominal 20 week RHIC run corresponds to 10 billion central Au+Au events.

The inclusive jet yield within $|\eta| < 1.0$ in 0–20% central Au+Au collisions at 200 GeV has been calculated for $p+p$ collisions by Vogelsang in a Next-to-Leading-Order (NLO) perturbative QCD formalism [103] and then scaled up by the expected number of binary collisions, as shown in Figure 1.29. Also shown are calculation results for π^0 and direct and fragmentation photons. The bands correspond to the renormalization scale uncertainty in the calculation (i.e., $\mu, \mu/2, 2\mu$).

The completion of the stochastic cooling upgrade to the RHIC accelerator [104] has been incorporated into the RHIC beam projections [105]. Utilizing these numbers and accounting for accelerator and experiment uptime and the fraction of collisions within $|z| < 10$ cm, the nominal full acceptance range for the detector, the sPHENIX detector can record 50 billion Au+Au minimum bias collisions in a one-year 20 week run. In fact, in the 2014 Au+Au

run at RHIC, the luminosities have exceeded these projections and for the pure jet and γ -jet observables with modest trigger requirements, one can sample 200 billion Au+Au minimum bias collisions. Note that the PHENIX experiment has a nearly dead-timeless high-speed data acquisition and trigger system that has already sampled tens of billions of Au+Au minimum bias collisions, and maintaining this high rate performance with the additional sPHENIX components is an essential design feature.

Figure 1.29 shows the counts per event with p_T larger than the value on the x-axis for the most central 20% Au+Au collisions at $\sqrt{s_{NN}} = 200$ GeV. With 10 billion events per RHIC year for this centrality selection, this translates into jet samples from 20–70 GeV and direct photon statistics out to 40 GeV. The statistical sample of jets and direct photons measurable in one year with sPHENIX is shown in Table 1.1. It is notable that within the acceptance of the sPHENIX detector, over 80% of the inclusive jets will also be accepted dijet events.

There is a potential future interest, not included in the default run plan for sPHENIX, in extending the jet program to lower energies. Similar NLO calculations have been performed and projected for the most central 20% Au+Au collisions at a lower collision energy of $\sqrt{s_{NN}} = 100$ GeV. The projected luminosity delivered by the collider is lower than in the 200 GeV case, of course, but with 1.7 billion events per RHIC year for this centrality selection, one obtains a substantial sample of jets reaching out to 35 GeV.

Shown in Table 1.1 are the jet and direct photon samples in $p+p$ and $d+Au$ collisions at $\sqrt{s_{NN}} = 200$ GeV. The number of jets expected in the three systems are similar, meaning that good control measurements in $p+p$ and $d+Au$ events will be available on the same timescales to quantify baseline expectations and initial state effects. Additionally, new geometries could be explored with follow up measurements with precision utilizing asymmetric heavy ion reactions, such as Cu+Au, and non-spherical geometries with U+U beams, now available with the RHIC EBIS upgrade [106]. Control measurements with different geometries with high statistics might be particularly interesting since current theoretical calculations are challenged by the path length dependence of the energy lost by the parton probe.

Measurement of direct photons requires them to be separated from the other sources of inclusive photons, largely those from π^0 and η meson decay. The left panel of Figure 1.30 shows the direct photon and π^0 spectra as a function of transverse momentum for both $\sqrt{s} = 200$ GeV and 2.76 TeV $p+p$ collisions. The right panels show the γ/π^0 ratio as a function of p_T for these energies with comparison PHENIX measurements at RHIC. At the LHC, the ratio remains below 10% for $p_T < 50$ GeV while at RHIC the ratio rises sharply and exceeds one at $p_T \approx 30$ GeV/c. In heavy ion collisions the ratio is further enhanced because the π^0 s are significantly suppressed. Taking the suppression into account, the γ/π^0 ratio at RHIC exceeds one for $p_T > 15$ GeV/c. The large signal to background means that it will be possible to measure direct photons with the sPHENIX calorimeter alone, even before applying isolation cuts. Beyond measurements of inclusive direct photons, this enables measurements of γ -jet correlations and γ -hadron correlations.

	Au+Au (central 20%)	$p+p$	$d+Au$
> 20 GeV	10^7 jets	10^6 jets	10^7 jets
	10^4 photons	10^3 photons	10^4 photons
> 30 GeV	10^6 jets	10^5 jets	10^6 jets
	10^3 photons	10^2 photons	10^3 photons
> 40 GeV	10^5 jets	10^4 jets	10^5 jets
> 50 GeV	10^4 jets	10^3 jets	10^4 jets

Table 1.1: Table of jet rates for different systems. Each column shows the number of jets or direct photons that would be measured within $|\eta| < 1$ in 20 week running periods at a collision energy of 200 GeV. These numbers for Au+Au assume only the recorded 50 billion minimum bias event sample, though additional statistics through modest triggering are available.

1.10 Beauty Quarkonia Physics

An extensive program of J/ψ measurements in A+A collisions has been carried out at the SPS ($\sqrt{s_{NN}} = 17.3$ GeV) and RHIC ($\sqrt{s_{NN}} = 200$ GeV) and the LHC ($\sqrt{s_{NN}} = 2.76$ TeV). These measurements were motivated by a desire to observe the suppression of J/ψ production by color screening in the QGP. In fact, strong suppression is observed at all three energies, but it has become clear that the contribution of color screening to the observed modification can not be uniquely determined without a good understanding of two strong competing effects.

The first of these, the modification of the J/ψ production cross section in a nuclear target, has been addressed at RHIC and the SPS using $p(d)+A$ collisions, and is being addressed at the LHC using $p+Pb$ collisions. The second complicating effect arises from the possibility that previously unbound heavy quark pairs could coalesce into bound states due to interactions with the medium. This opens up the possibility that if a high enough density of heavy quark pairs is produced in a single collision, coalescence of heavy quarks formed in different hard interactions might actually increase the production cross section beyond the initial population of bound pairs [109].

Using $p+Pb$ and $d+Au$ data as a baseline, and under the assumption that cold nuclear matter (CNM) effects can be factorized from hot matter effects, the suppression in central

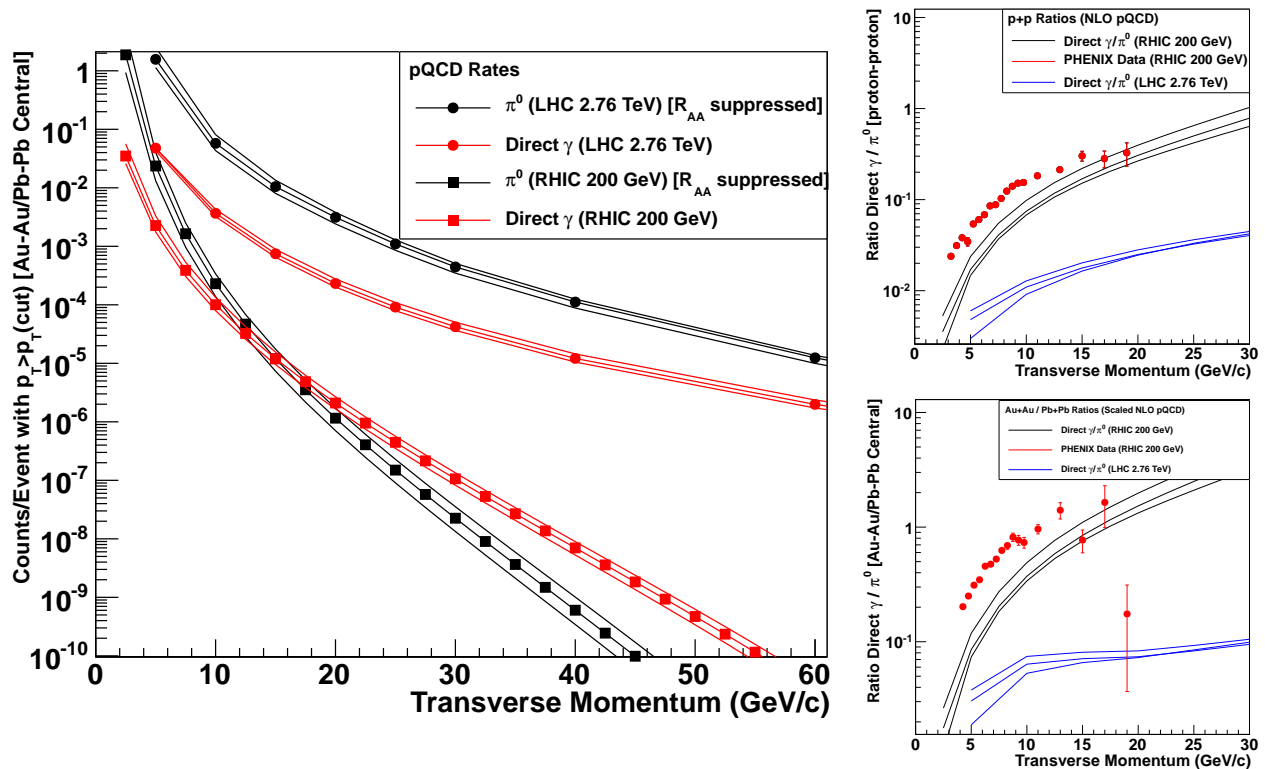


Figure 1.30: NLO pQCD calculations of direct photons and π^0 for RHIC and LHC. The plot on the left shows the counts per event in Au+Au or Pb+Pb collisions (including the measured R_{AA} suppression factor for π^0). The upper (lower) panel on the right shows the direct γ to π^0 ratio in $p+p$ (Au+Au or Pb+Pb) collisions, in comparison with measurements from the PHENIX experiment at RHIC [107, 108].

collisions due to the presence of hot matter in the final state has been estimated to be about 25% for Pb+Pb at the SPS [110], and about 50% for Au+Au at RHIC [111], both measured at midrapidity. The first J/ψ data in Pb+Pb collisions at $\sqrt{s_{NN}} = 2.76$ TeV from ALICE [112], measured at forward rapidity, are shown alongside PHENIX data in Figure 1.31. Interestingly, the suppression in central collisions is far greater at RHIC than at the LHC. This is qualitatively consistent with a predicted [109] strong coalescence component due to the very high $c\bar{c}$ production rate in a central collision at LHC. There is great promise that, once CNM effects are estimated from $p+Pb$ data, comparison of these data at widely spaced collision energies will lead to an understanding of the role of coalescence.

Upsilon measurements have a distinct advantage over charmonium measurements as a probe of deconfinement in the quark-gluon plasma. In contrast the charmonium states appear more sensitive to their thermalization in medium. The $Y(1S)$, $Y(2S)$ and $Y(3S)$ states can all be observed with comparable yields via their dilepton decays. Therefore it is possible to compare the effect of the medium simultaneously on three bottomonium states—all of which have quite different radii and binding energies.

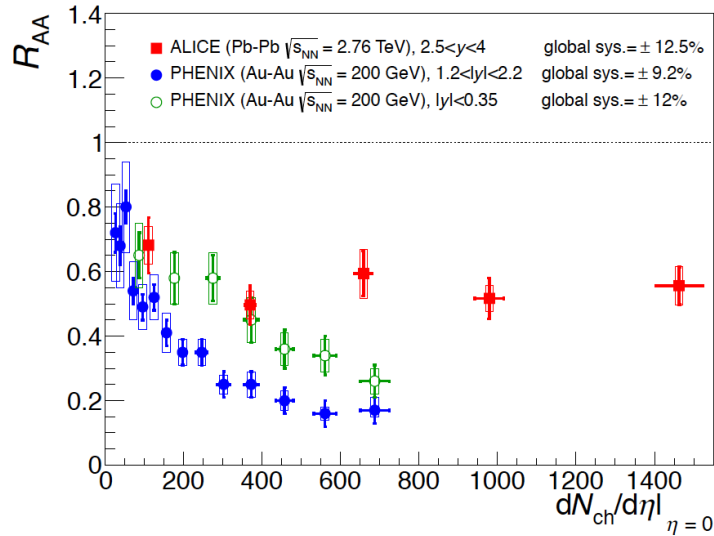


Figure 1.31: Comparison of nuclear modification measured by PHENIX and ALICE, showing that suppression is much stronger at the lower energy [112]. The modification measured by NA50 at low energy is similar to the PHENIX midrapidity result.

CMS has already shown first upilon data from Pb+Pb at 2.76 GeV that strongly suggest differential suppression of the 2S and 3S states relative to the 1S state [113]. With longer Pb+Pb runs, and a p +Pb run to establish a CNM baseline, the LHC measurements will provide an excellent data set within which the suppression of the three upilon states relative to p +Pb can be measured simultaneously at LHC energies.

At RHIC, upilon measurements have been hampered by a combination of low cross sections and acceptance, and insufficient momentum resolution to resolve the three states. So far, there are preliminary measurements of the three states combined by PHENIX [114] and STAR [115], including in the STAR case a measurement for Au+Au. However a mass-resolved measurement of the modifications of the three upilon states at $\sqrt{s_{NN}} = 200$ GeV would be extremely valuable for several reasons.

First, the core QGP temperature is approximately $2T_c$ at RHIC at 1 fm/ c and is at least 30% higher at the LHC (not including the fact that the system may thermalize faster) [116]. This temperature difference results in a different color screening environment. Second, the bottomonium production rate at RHIC is lower than that at the LHC by ~ 100 [111]. As a result, the average number of $b\bar{b}$ pairs in a central Au+Au collision at RHIC is ~ 0.05 versus ~ 5 in central Pb+Pb at the LHC. Qualitatively, one would expect this to effectively remove at RHIC any contributions from coalescence of bottom quarks from different hard processes, making the upilon suppression at RHIC dependent primarily on color screening and CNM effects. This seems to be supported by recent theoretical calculations [117] where, in the favored scenario, coalescence for the upilon is predicted to be significant at the LHC and small at RHIC.

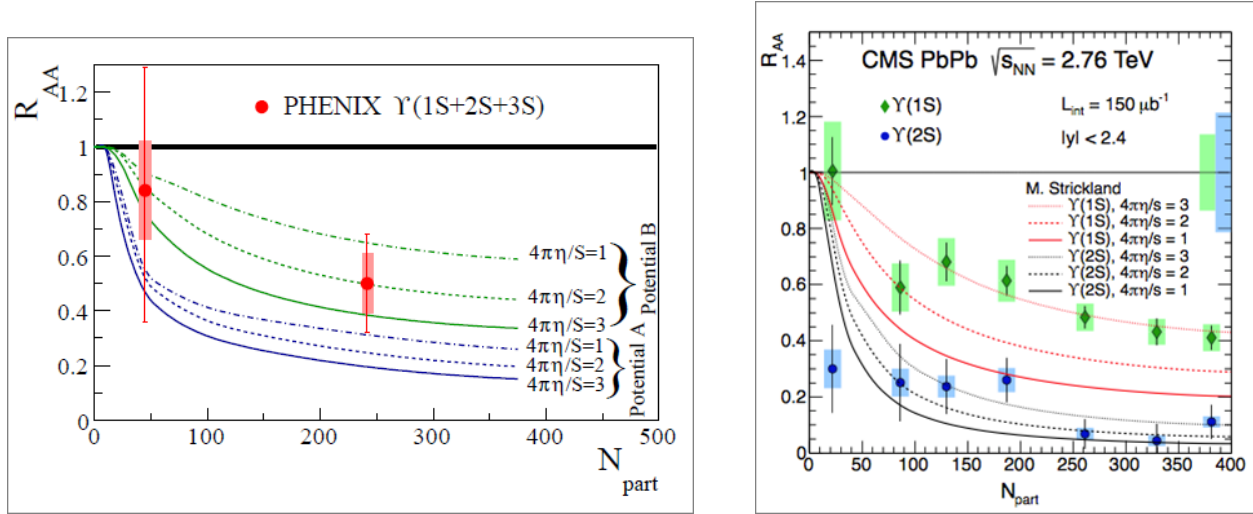


Figure 1.32: Calculations for Upsilon state suppression at RHIC and LHC energies as a function of collision centrality. The current state of measurements are also shown from PHENIX and CMS.

An example theoretical calculation for both RHIC and the LHC is shown in Figure 1.32 indicating the need for substantially improved precision and separation of states in the temperature range probed at RHIC.

STAR has constructed a Muon Telescope Detector (MTD) to measure muons at midrapidity [118]. The MTD construction is now complete and has coverage over $|\eta| < 0.5$, with about 45% effective azimuthal coverage. The MTD will have a muon to pion enhancement factor of 50–100, and the mass resolution will provide a clean separation of the $\Upsilon(1S)$ from the $\Upsilon(2S+3S)$, and likely the ability to separate the $\Upsilon(2S)$ and $\Upsilon(3S)$ by fitting. While STAR will already have made upsilon measurements with the MTD at RHIC before the upgrade to sPHENIX proposed here would be available, the upgrade to sPHENIX would provide better mass resolution and approximately 10 times higher yields per run for upsilon measurements. In concert with the expected higher statistics results from the LHC experiments, sPHENIX data will provide the required precision to discriminate models of breakup in the dense matter and the length scale probed in the medium.

1.11 Summary

Detailed information about the quark-gluon plasma properties, dynamics, time evolution, and structure at $1-2 T_c$ is accessible at RHIC through the extensive set of reconstructed jet measurements proposed here. The theoretical bridgework needed to connect these measurements to the interesting and unknown medium characteristics of deconfined color charges is under active construction by many theorists. Combining this work with the

flexible and high luminosity RHIC accelerator facility can produce new discoveries in heavy ion collisions with an appropriate set of baseline measurements provided a suitable detector apparatus is constructed. Our proposed design for a jet detector at RHIC that is best able to make use of these opportunities is given in the following chapter.

Chapter 2

Physics-Driven Detector Requirements

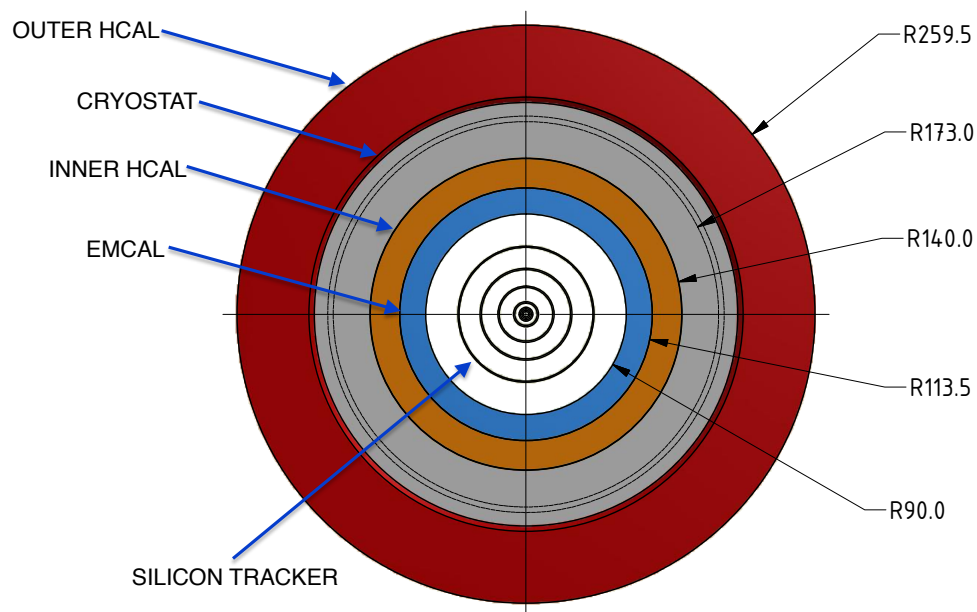


Figure 2.1: End view of the sPHENIX detector with its component subdetectors.

In order to perform the physics measurements outlined in Chapter 1, sPHENIX must satisfy a set of detector requirements. In this Chapter we discuss the physics-driven requirements on the performance of the sPHENIX detector. In addition, as outlined in the Executive Summary, this sPHENIX upgrade serves as the foundation for a future upgrade to a world class Electron-Ion Collider (EIC) detector built around the BaBar magnet and sPHENIX calorimetry, and those requirements are taken into account. The details of specific detector and GEANT4 simulations regarding the physics capability of the sPHENIX reference design are given in Chapter 4. The sPHENIX physics program

rests on several key measurements, and the requirements that drive any particular aspect of the detector performance come from a broad range of considerations related to those measurements. A consideration of the physics requirements has led to the development of the reference design shown in Figure 2.1 and will be described in detail in Chapter 3.

The primary components of the sPHENIX reference design are as follows.

Magnetic Solenoid solenoid built for the BaBar experiment at SLAC which became available after the termination of the BaBar program. The cryostat has an inner radius of 140 cm and is 33 cm thick, and can produce a central field of 1.5 T.

Silicon Tracking six layers of silicon tracking for charged track reconstruction and momentum determination.

Electromagnetic Calorimeter tungsten-scintillating fiber sampling calorimeter inside the magnet bore read out with silicon photo-multipliers. The calorimeter has a small Molière radius and short radiation length, allowing for a compact design.

Inner Hadronic Calorimeter sampling calorimeter of non-magnetic metal and scintillator located inside the magnet bore.

Outer Hadronic Calorimeter sampling calorimeter of steel scintillator located outside the cryostat which doubles as the flux return for the solenoid.

In the following list we provide a high-level mapping between physics aims and various detector requirements. The justification for these requirements are then discussed in more detail in subsequent sections.

Upsilon The key to the physics is high statistics $p+p$, $p+A$, and $A+A$ data sets, with mass resolution and signal-to-background sufficient to separate the three states of the Y family.

- large acceptance ($\Delta\phi = 2\pi$ and $|\eta| < 1$)
- high rate data acquisition (10 kHz)
- trigger for electrons from $Y \rightarrow e^+e^-$ ($> 90\%$ efficiency) in $p+p$ and $p+A$
- track reconstruction efficiency $> 90\%$ and purity $> 90\%$ for $p_T > 3$ GeV/c
- momentum resolution of at least $0.2\% \times p_T$ for $p_T > 3$ GeV/c.
- electron identification with efficiency $> 70\%$ and charged pion rejection of 50:1 or better in central Au+Au at $p_T = 4$ GeV/c.

Jets The key to the physics is to cover jet energies 20–70 GeV, for all centralities, for a range of jet sizes, with high statistics and performance insensitive to the details of jet fragmentation.

Physics-Driven Detector Requirements

- energy resolution $< 120\% / \sqrt{E_{\text{jet}}}$ in $p+p$ for $R = 0.2\text{--}0.4$ jets
 - energy resolution $< 150\% / \sqrt{E_{\text{jet}}}$ in central Au+Au for $R = 0.2$ jets
 - energy scale uncertainty $< 3\%$ for inclusive jets
 - energy resolution, including effect of underlying event, such that scale of unfolding on raw yields is less than a factor of three
 - measure jets down to $R = 0.2$ (segmentation no coarser than $\Delta\eta \times \Delta\phi \sim 0.1 \times 0.1$)
 - underlying event influence event-by-event (large coverage HCal/EMCal) (ATLAS method)
 - energy measurement insensitive to softness of fragmentation (quarks or gluons) — HCal + EMCal
 - jet trigger capability in $p+p$ and $p+A$ without jet bias (HCal and EMCal)
 - rejection ($> 95\%$) of high p_T charged track backgrounds (HCal)
-

Dijets The key to the physics is large acceptance in conjunction with the general requirements for jets as above

- $> 80\%$ containment of opposing jet axis
 - $> 70\%$ full containment for $R = 0.2$ dijets
 - R_{AA} and A_J measured with $< 10\%$ systematic uncertainty (also key in $p+A$, onset of effects)
-

Fragmentation functions The key to the physics is unbiased measurement of jet energy

- excellent tracking resolution out to $> 40 \text{ GeV}/c$ ($dp/p < 0.2\% \times p$)
 - independent measurement of p and E ($z = p/E$)
-

Heavy quark jets The key to the physics is tagging identified jets containing a displaced secondary vertex

- precision DCA (< 100 microns) for electron $p_T > 4 \text{ GeV}/c$
 - electron identification for high $p_T > 4 \text{ GeV}/c$
-

Direct photon The key to the physics is identifying photons

- EMCal resolution for photon ID ($< 15\% / \sqrt{E}$)
 - EMCal cluster trigger capability in $p+p$ and $p+A$ with rejections > 100 for $E_\gamma > 10 \text{ GeV}$
-

High statistics Ability to sample high statistics for $p+p$, $p+A$, $A+A$ at all centralities — requires high rate, high throughput DAQ (10 kHz).

In the following sections, we detail the origin of key requirements.

2.1 Acceptance

The total acceptance of the detector is determined by the requirement of high statistics jet measurements and the need to fully contain both single jets and dijets. To fully contain hadronic showers in the detector requires both large solid angle coverage and a calorimeter deep enough to fully absorb the energy of hadrons up to 70 GeV.

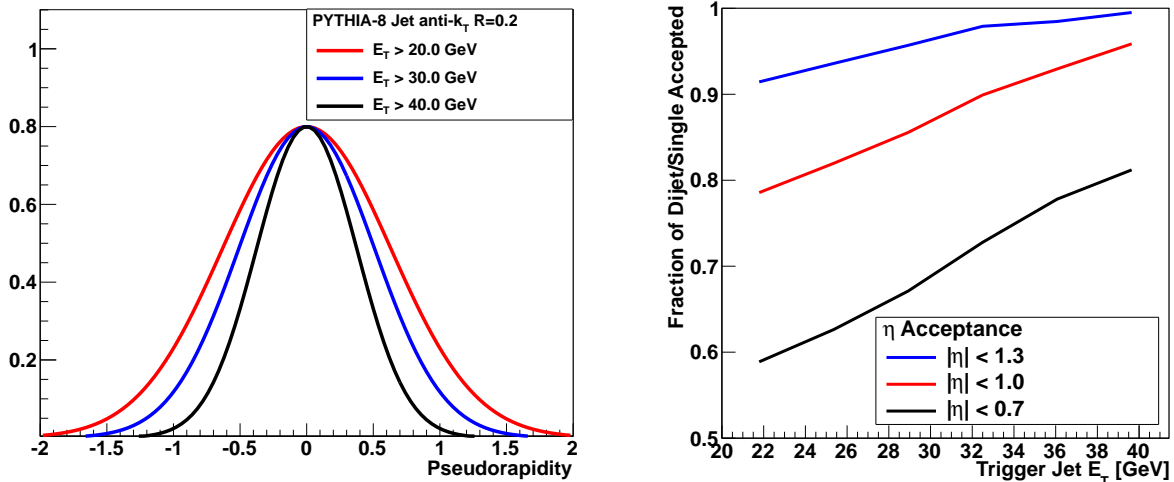


Figure 2.2: (Left) Pseudorapidity distribution of PYTHIA jets reconstructed with the FASTJET anti- k_T and $R=0.2$ for different transverse energy selections. (Right) The fraction of PYTHIA events where the leading jet is accepted into a given pseudorapidity range where the opposite side jet is also within the acceptance. Note that the current PHENIX acceptance of $|\eta| < 0.35$ corresponds to a fraction below 30%.

The PYTHIA event generator has been used to generate a sample of $p+p$ at 200 GeV events which can be used to demonstrate the pseudorapidity distribution of jets. The left panel in Figure 2.2 shows the pseudorapidity distribution of jets with E_T above 20, 30, and 40 GeV. The right panel in Figure 2.2 shows the fraction of events where a trigger jet with E_T greater than a given value within a pseudorapidity range has an away side jet with $E_T > 5$ GeV accepted within the same coverage. In order to efficiently capture the away side jet, the detector should cover $|\eta| < 1$, and in order to fully contain hadronic showers within this fiducial volume, the calorimetry should cover slightly more than that. Given the segmentation to be discussed below, the calorimeters are required to cover $|\eta| < 1.1$.

It should be noted that reduced acceptance for the away-side jet relative to the trigger suffers not only a reduction in statistics for the dijet asymmetry and γ -jet measurements but also results in a higher contribution of low energy fake jets (upward fluctuations in the background) in those events where the away side jet is out of the acceptance. For the latter effect, the key is that both jet axes are contained within the acceptance, and then events can be rejected where the jets are at the edge of the detector and might have partial energy

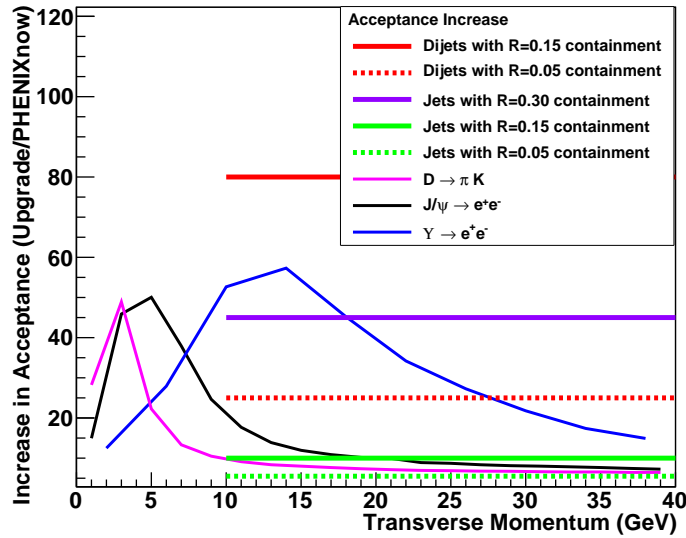


Figure 2.3: Acceptance increase for various processes (as modeled using the PYTHIA event generator) for the proposed sPHENIX barrel detector compared with the current PHENIX central arm spectrometers.

capture.

Compared to the current PHENIX acceptance (the central arms cover $|\eta| < 0.35$ and $\Delta\phi = \pi$), full azimuthal coverage with $|\eta| < 1.1$ results in a very substantial increase in the acceptance of single jets and an even larger increase in the acceptance of dijets for other observables including heavy quarkonia states, as shown in Figure 2.3. The large acceptance and high rate are key enablers of the physics program detailed in Chapter 1.

2.2 Segmentation

Jets are reconstructed from the four-vectors of the particles or measured energies in the event via different algorithms (as described in Chapter 4), and with a typical size $R = \sqrt{\Delta\phi^2 + \Delta\eta^2}$. In order to reconstruct jets down to radius parameters of $R = 0.2$ a segmentation in the hadronic calorimeter of $\Delta\eta \times \Delta\phi = 0.1 \times 0.1$ is required. The electromagnetic calorimeter segmentation should be finer as driven by the measurement of direct photons for γ -jet correlation observables. The compact electromagnetic calorimeter design being considered for sPHENIX has a Molière radius of ~ 15 mm, and with a calorimeter at a radius of about 100 cm, this leads to an optimal segmentation of $\Delta\eta \times \Delta\phi = 0.024 \times 0.024$ in the electromagnetic section.

2.3 Energy Resolution

The requirements on the jet energy resolution are driven by considerations of the ability to reconstruct the inclusive jet spectra and dijet asymmetries and the fluctuations on the fake jet background (as detailed in Chapter 4). The total jet energy resolution is typically driven by the hadronic calorimeter resolution and many other effects including the bending of charged particles in the magnetic field out of the jet radius. Expectations of jet resolutions approximately 1.2 times worse than the hadronic calorimeter resolution alone are typical (see a more detailed discussion in Chapter 4).

In a central Au+Au event, the average energy within a jet cone of radius $R = 0.2$ ($R = 0.4$) is approximately 10 GeV (40 GeV) resulting in an typical RMS fluctuation of 3.5 GeV (7 GeV). This sets the scale for the required reconstructed jet energy resolution, as a much better resolution would be dominated by the underlying event fluctuations regardless. A measurement of the jet energy for $E = 20$ GeV with $\sigma_E = 120\% \times \sqrt{E} = 5.4$ GeV gives a comparable contribution to the underlying event fluctuation. A full study of the jet energy resolution with a GEANT4 simulation of the detector configuration is required and is presented in Chapter 4.

Different considerations set the scale of the energy resolution requirement for the EMCal. The jet physics requirement is easily met by many EMCal designs. For the direct γ -jet physics, the photon energies being considered are $E_\gamma > 10$ GeV where even a modest $\sigma_E/E = 12\%/\sqrt{E}$ represents only a blurring of 400 MeV. In Au+Au central events, the typical energy in a 3×3 tower array is also approximately 400 MeV. These values represent a negligible performance degradation for these rather clean photon showers even in central Au+Au events.

Most of these physics measurements require complete coverage over a large range of rapidity and azimuthal angle ($\Delta\eta \leq 1.1$ and $\Delta\phi = 2\pi$) with good uniformity and minimal dead area. The calorimeter should be projective (at least approximately) in η . For a compact detector design there is a trade-off in terms of thickness of the calorimeter and Molière radius versus the sampling fraction and, therefore, the energy resolution of the device. Further optimization if these effects will be required as we work towards a final design.

2.4 Tracking

The requirements on tracking capabilities are tied to three particular elements of the sPHENIX physics program: fragmentation functions at high and at low z , heavy flavor tagged jets, and the measurement of the upsilon family of quarkonia states.

In order to utilize the available luminosity fully, the tracking systems should have large, uniform acceptance and be capable of fast readout. Measuring fragmentation functions

at low z means looking for possibly wide angle correlations between a trigger jet and a charged hadron. This places only moderate requirements on the momentum resolution ($\Delta p/p \simeq 1\% \cdot p$), but reinforces the requirement of large acceptance.

Fragmentation functions at high z place more stringent requirements on momentum resolution. In order to unfold the full fragmentation function, $f(z)$, the smearing due to momentum uncertainty should be very small compared to the corresponding smearing due to the calorimetric jet measurement for cleanly identified jet. For a 40 GeV jet this condition is satisfied by a tracking momentum resolution of $\Delta p/p \simeq 0.2\% \cdot p$ or better.

The measurement of the Y family places the most stringent requirement on momentum resolution. The large mass of the upsilon means that one can focus primarily on electrons with momenta of ~ 4 GeV/c. The $Y(2S)$ has about 6% higher mass than the $Y(1S)$ state; to distinguish them clearly one needs invariant mass resolution of $\sim 3\%$. This translates into a momentum resolution for the daughter e^\pm of 1.5% at 4 GeV/c.

The Y measurement also generates requirements on the purity and efficiency of electron identification. The identification needs to be efficient because of the low cross section of Y production at RHIC, and it needs to have high purity against the charged pion background to maintain a good signal to background ratio. Translating this need into a detector requirement depends upon detailed simulations and will be discussed in detail in Section 4.10.

Tagging heavy-flavor jets introduces the additional tracking requirement of being able to measure the displaced vertex of a D or B meson decay, as described in Section 4.8. The $c\tau$ for D and B decays is $123 \mu\text{m}$ and $457 \mu\text{m}$, respectively, and displaced vertex would need to be identified with a resolution sufficient to distinguish these decays against backgrounds.

2.5 Triggering

The jet energy should be available at the Level-1 trigger as a standard part of the PHENIX dead-timeless Data Acquisition and Trigger system. This triggering ability is important as one requires high statistics measurements in proton-proton, proton-nucleus, light nucleus-light nucleus, and heavy nucleus-heavy nucleus collisions with a wide range of luminosities. It is important to have combined EMCal and HCal information available so as to avoid a specific bias on the triggered jet sample.

Chapter 3

Detector Concept

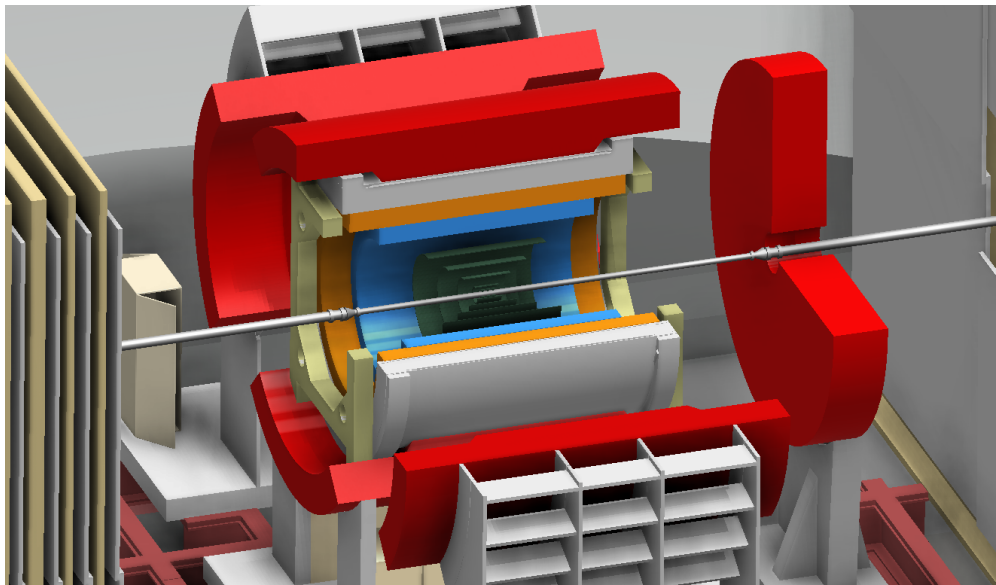


Figure 3.1: An engineering drawing of sPHENIX, showing the superconducting solenoid containing the electromagnetic calorimeter and surrounded by the hadronic calorimeter, with a model of the associated support structure, as it would sit in the PHENIX IR.

In this Chapter we detail the sPHENIX detector design including the magnetic solenoid, electromagnetic and hadronic calorimeters, silicon tracking, and readout electronics. Detector performance specifications are checked using a full GEANT4 simulation of the detector. Full physics performance measures are detailed in Chapter 4.

The sPHENIX detector concept takes advantage of technological developments to enable a compact design with excellent performance. A tungsten-scintillator electromagnetic calorimeter read out with silicon photomultipliers (SiPMs) or avalanche photodiodes (APDs) allows for a physically thin device which can operate in a magnetic field, without the bulk of photomultiplier tubes and the need for high voltage distribution. The thinner

electromagnetic calorimeter allows space for the first longitudinal segment of the hadronic calorimeter to sit inside the bore of the solenoid, with positive implications for electron identification and reducing the overall size of the calorimeter system. The use of solid-state sensors for the hadronic calorimeter allows for nearly identical electronic readout for the two major systems. A superconducting magnet coupled with high resolution tracking detectors provides excellent momentum resolution inside the solenoid. The detector has been designed from the beginning to minimize the number of distinct parts to be simpler to manufacture and assemble. The use of components insensitive to magnetic fields enables the hadronic calorimeter to double as the flux return for the solenoid, reducing both mass and cost. Adapting existing electronic designs for the readout allows for reduced development cost and risk, and leverages a decade and a half of experience at PHENIX. We now detail each subsystem in the following Sections.

A number of alternative designs of both the electromagnetic and hadronic calorimeter have been investigated by means of simulation as well as construction of prototype devices which have demonstrated the feasibility of the approach. Work continues to optimize and simplify the design and manufacture of the calorimeter, but we have chosen a reference design of the technologies used in the calorimeters which has been used to confirm that the design can achieve the physics goals of the experiment. The design discussed in this chapter is identical to the concept used in the simulations shown in this proposal.

3.1 Magnet

The magnet and tracking system should ultimately be capable of order 1% momentum resolution at $10\text{ GeV}/c$, cover the full 2π in azimuth and $|\eta| < 1.1$. The BaBar solenoid is a good match to the requirements, became available in late 2012, and measures were taken to transfer ownership of the coil and related equipment to Brookhaven in early 2013.

The main features of the BaBar solenoid are shown in Table 3.1. The solenoid fits well into the mechanical infrastructure of the existing PHENIX interaction region (IR). The RHIC beamline is 444.8 cm above the tracks that are used to move detectors into the collision hall and 523.2 cm above the floor, and we propose to keep the track system in place for maneuvering detectors in and out. The hadron calorimeter which serves as the flux return for the magnet is 100 cm or less thick, so the outer radius of the hadronic calorimeter is about 150 cm above the tracks which provides adequate clearance for support. Instrumentation in the forward and backward direction is not part of this proposal but the space available is approximately the same as the present muon tracker systems.

The BaBar magnet and related equipment, including the power supply, the quench protection electronics, the dump resistor, rigging fixtures, and some cryogenic components have been removed from the decommissioned BaBar detector and are in staging areas at SLAC. The coil in its transfer frame have been surveyed for residual radiation and have been found to be acceptable to move to Brookhaven. The BaBar solenoid has been prepared for

Table 3.1: Key characteristics of the BaBar solenoid and cryostat.

Central field in BaBar	1.5 T
Cryostat inner radius	140 cm
Cryostat outer radius	173 cm
Cryostat length	385 cm
Mean radius of windings	153 cm
Coil length	351 cm
Material thickness at normal incidence	~ 126 mm Al
Operating current	4596 A
Manufacturer	Ansaldo Energia (now ASG)

**Figure 3.2:** The BaBar solenoid in its transfer frame for shipping at SLAC in May, 2013.

shipping, and is shown in its transfer frame in Figure 3.2.

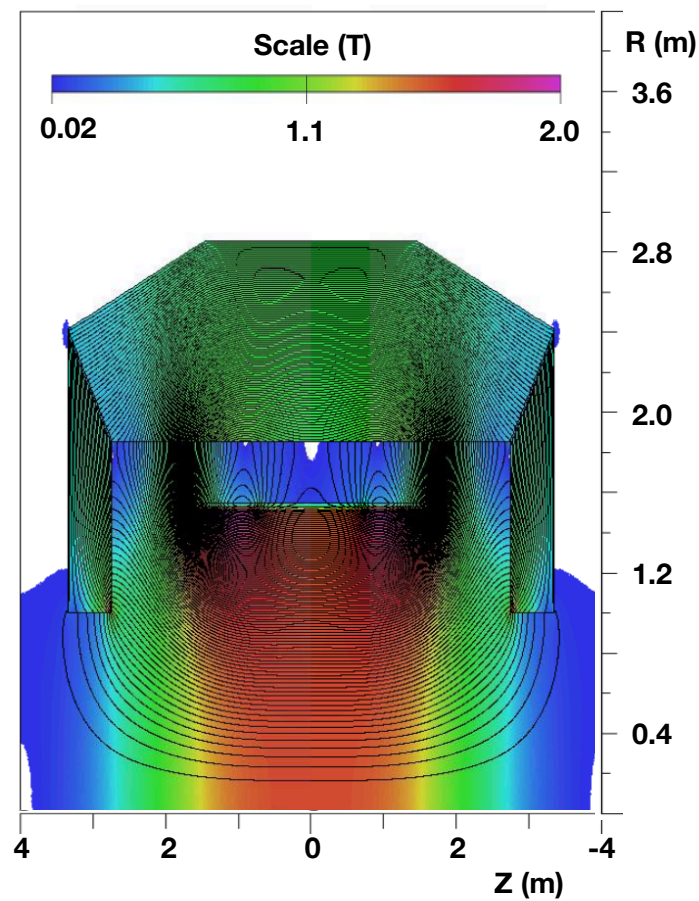


Figure 3.3: Calculation of the magnetic field from the solenoid with the flux returned by the hadronic calorimeter.

3.1.1 Magnetic Field Calculations

Magnetic field calculations of the solenoid coil and a model of the return steel were carried out with the OPERA magnetic field simulation software package. A field map is shown in Figure 3.3. Tools are under development for complete three dimensional field calculations and calculations of the forces on the detector and flux return.

3.2 The Electromagnetic Calorimeter

The concept for the sPHENIX electromagnetic calorimeter follows from the physics requirements outlined earlier in this proposal. These requirements lead to a calorimeter design that is compact (i.e. has a small Molière radius and short radiation length), has a high degree of segmentation (0.024×0.024 in η and ϕ), has small dead area, and can be built at a reasonable cost. Since the calorimeter will be located inside the solenoid cryostat, it will also have to operate in a high magnetic field. A number of alternative designs have been investigated and work continues to optimize and simplify the design and manufacture of the calorimeter, but we have chosen a reference design.

3.2.1 Segmentation and readout

The segmentation of the calorimeter is determined by a number of different requirements. One primary factor is the occupancy of the individual readout towers in heavy ion collisions, which determines the ability to resolve neighboring showers and to measure the energy in the underlying event. In addition, the degree of segmentation also determines the ability to measure the transverse shower shape, which is used in separating electrons from hadrons (e/π rejection). The segmentation chosen for the reference design of the detector will provide the capability to perform the physics program of this proposal.

The calorimeter will be divided into individual towers corresponding to a segmentation in η and ϕ of approximately 0.024×0.024 and would result in about 25,000 readout channels (256 in $\phi \times 96$ in η). The light can be collected at the front or the back of the calorimeter with short light guides forming towers measuring $\sim 2 \times 2$ cm. A design goal is to minimize the radial space required by the light guide, SiPM, readout electronics, and cables.

The reference design for the electromagnetic calorimeter, which satisfies the physics requirements of sPHENIX and the requirements of an experiment at an electron-ion collider is a sampling calorimeter with tungsten powder absorber and scintillating fibers constructed with techniques developed at UCLA.[119] A calorimeter with 0.47 mm diameter fibers on 1 mm centers has a final density of 10.2 g/cm^3 and a radiation length of 7 mm which implies a Molière radius of about 2.3 cm. A calorimeter 18 radiation lengths thick occupies 12.6 cm in radius, and with light collection, sensors, preamps, and cables, the calorimeter is expected to occupy radial space of about 25 cm. Figure 3.4 shows an end view of 4×4 towers with the end of the scintillating fibers visible, before light guides are installed.

A key element of the design of the calorimeter is the light output of the scintillator available to the photodetectors. There must be sufficient light produced by the scintillator at all energies of interest so that photostatistics do not degrade the resolution of the calorimeter. Measured light yields of ~ 500 photoelectrons/GeV of incident energy have been demonstrated with SiPM readout in beam tests. The resulting energy resolution is less



Figure 3.4: View of a prototype calorimeter module with fibers embedded before light guides are installed. (Figure courtesy of Oleg Tsai, EIC-RD1.)

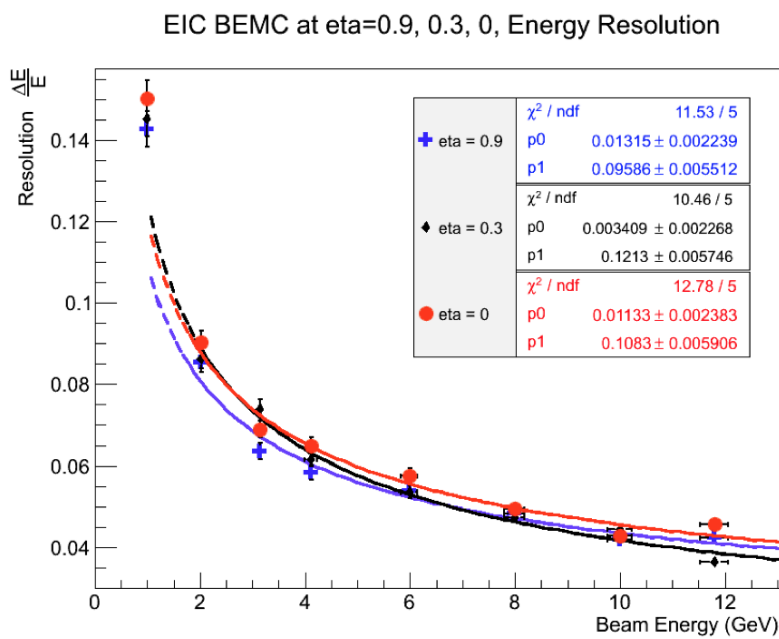


Figure 3.5: Energy resolution achieved in beam tests of a prototype electromagnetic calorimeter compared with GEANT4 Monte Carlo simulation. (Figure courtesy of Oleg Tsai, EIC-RD1.)

than about $12\%/\sqrt{E}$ at the energies and angles relevant to the calorimeter. Figure 3.5 shows the measured resolution of a prototype calorimeter compared with simulation at three incident angles.

The reference design of the electromagnetic calorimeter is projective only in the azimuthal direction; the calorimeter modules are expected to be wedges in ϕ . There are ongoing Monte Carlo studies which aim to confirm that this choice does not introduce problems at large pseudorapidity in the jet reconstruction.

The PHENIX collaboration has worked with the company Tungsten Heavy Powder [120] on the design and fabrication of actual calorimeter components with funding from a Phase I Small Business Innovation Research (SBIR) grant to study and develop materials and components for compact tungsten based calorimeters for nuclear physics applications. Research and development, as part of a broader collaboration, has also been supported by a “Joint Proposal to Develop Calorimeters for the Electron Ion Collider” for EIC research and development funds (EIC-RD1).

3.3 The Hadronic Calorimeter

The hadronic calorimeter is a key element of sPHENIX and many of the overall performance requirements are directly tied to performance requirements of the HCal itself. The focus on measuring jets and dijets in sPHENIX leads to a requirement on the energy resolution of the calorimeter system as a whole—the particular requirement on the HCal is that it have an energy resolution better than $\sigma_E/E = 100\%/\sqrt{E}$.

The jet measurement requirements also lead to a transverse segmentation requirement of $\Delta\eta \times \Delta\phi \approx 0.1 \times 0.1$ over a rapidity range of $|\eta| < 1.1$ with minimal dead area and a longitudinal segmentation satisfactory for electron identification and measurements of the structure of energy flow in underlying event.

The combination of the EMCal and the HCal needs to be at least $\sim 6\lambda_{\text{int}}$ deep—sufficient to absorb $\sim 97\%$ of the energy of impinging hadrons with momenta below $50 \text{ GeV}/c$, as shown in Figure 3.6. The electromagnetic calorimeter is $\sim 1\lambda_{\text{int}}$ thick, so the hadronic calorimeter should be $\sim 5\lambda_{\text{int}}$ deep. Although the thickness of the HCal is driven by physics needs, building it of iron plates and scintillating tiles insures that the hadronic calorimeter can also serve as the return yoke for the solenoid.

The HCal is divided into electromagnetic leakage section integrated with EMCal inside solenoid, and hadronic calorimeter per se outside of the magnet. This design minimizes the overall size of the detector and minimizes the spread of the hadronic shower in the radial space occupied by the cryostat. Detailed mechanical design is needed to determine exactly how much absorber fits in the available space, but about one interaction length is expected to be feasible with the space needed for support, light collection, electronics, and cables.

The outer hadronic calorimeter as shown in Figure 3.7 surrounds the cryostat in an envelope which extends from just outside the cryostat at a radius of about 180 cm to 264.5 cm.

Both the inner and outer longitudinal segments of the calorimeter are constructed of

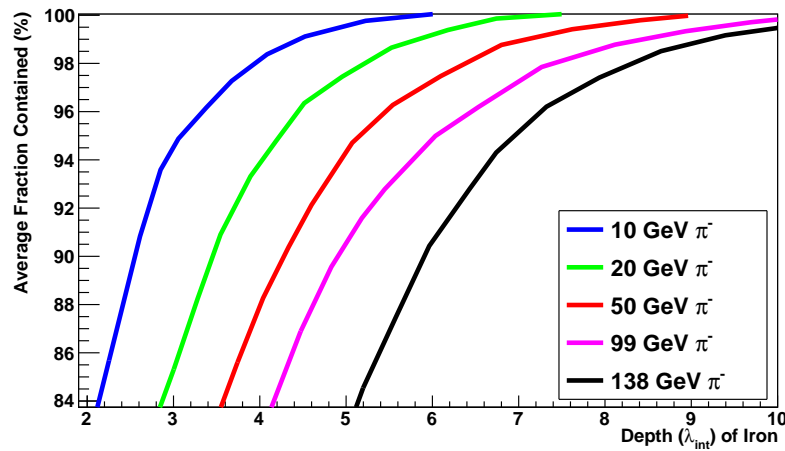


Figure 3.6: Average energy fraction contained in a block of iron with infinite transverse dimensions, as a function of the thickness of the block. Figure adapted from Ref. [121].

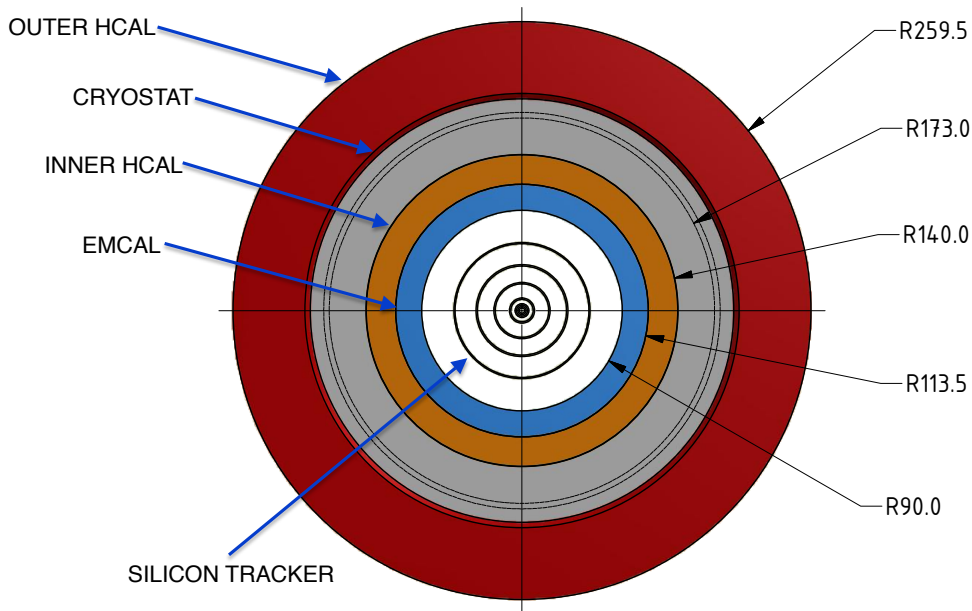


Figure 3.7: Cross section of sPHENIX. The outer hadronic calorimeter surrounds the solenoid cryostat.

tapered absorber plates, creating a finned structure, with each fin oriented at an angle of $\sim \pm 10^\circ$ with respect to a radius vector perpendicular to the beam axis, with the angle chosen so that a radial ray from the interaction point crosses four scintillator layers. There are 384 fins in each of the inner and outer segments. The fins in the inner and outer

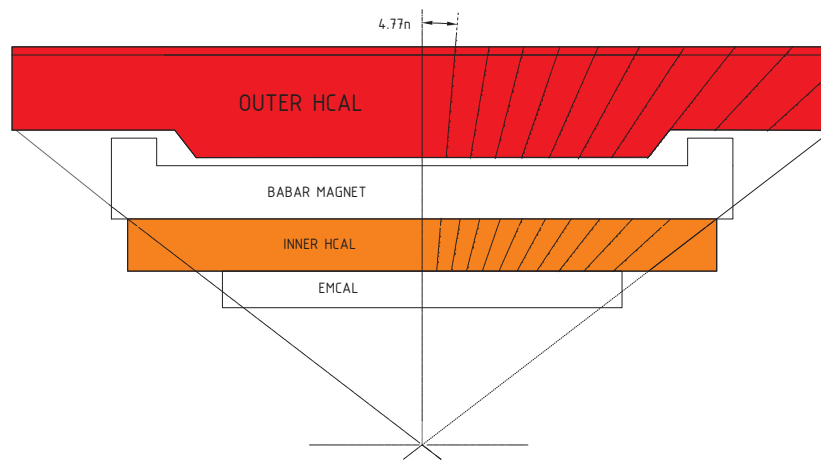


Figure 3.8: Scintillating tiles in the sampling gap of sPHENIX hadronic calorimeter, showing the transverse segmentation into element 0.1 units of pseudorapidity wide.

segments are radially tilted in opposite directions resulting in a $\sim 20^\circ$ angle with respect to each other. They are also staggered by half a fin thickness. The gaps between the iron plates are 8 mm wide and contain individually wrapped 7 mm thick scintillating tiles with a diffuse reflective coating and an embedded wavelength shifting fibers which traverses the entire tile, entering and exiting on the same edge. The slight tilt and the azimuthal staggering of steel fins and scintillating tiles prevents particles from traversing the depth of the calorimeter without encountering the steel absorber (channeling). The benefits of two longitudinal segments include a further reduction in the channeling of particles in the scintillator, shorter scintillators with embedded fibers for collecting the light, shower depth information, and more symmetric response for particles of opposite charge.

With plates oriented as described, particles striking the calorimeter at normal incidence will, on average, traverse about 90 cm of absorber resulting in a probability for the punch through of particles with momenta above $\sim 2 \text{ GeV}/c$ of only 1%. This design has a very small number of distinct components which is designed to make it simple to fabricate, assemble, and to model.

Within each gap, there are 22 separately wrapped scintillator tiles of 11 different shapes, corresponding to a detector segmentation in pseudorapidity of $\Delta\eta \sim 0.1$ (see Figure 3.8). Azimuthally, the hadronic calorimeter is divided into 64 wedges ($\Delta\phi \simeq 0.1$). Each wedge is composed of six sampling cells (steel plate and scintillating tile) with the scintillating tile edges pointing towards the origin. The 22 pseudorapidity slices result in towers about

10 cm \times 10 cm in size at the inner surface of the calorimeter. The total channel count in the calorimeter is 1408×2 .

The light from the scintillating tiles between the steel fins is collected using wavelength shifting fibers laid along a path as shown in Figure 3.9. This arrangement provides relatively uniform light collection efficiency over the whole tile. We have considered two fiber manufacturers: (1) Saint-Gobain (formerly BICRON), product brand name BCF91A [122] and (2) Kuraray, product name Y11 [123]. Both vendors offer single and double clad fibers.

The calorimeter performance is determined by the sampling fraction and the light collection and readout efficiency. The readout contributes mostly to the stochastic term in calorimeter resolution through Poisson fluctuations in the number of photoelectrons on the input to the analog signal processing. Factors contributing to those fluctuations are luminous properties of the scintillator, efficiency of the light collection and transmission, and the photon detection efficiency of the photon detector.

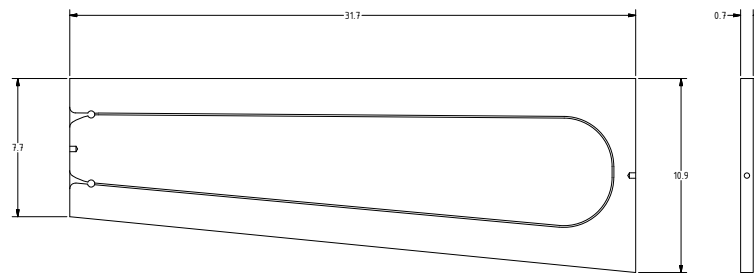


Figure 3.9: Grooved scintillating tiles for inner HCal section, showing the path of the fiber and the uniform thickness of the tiles. This was the design of the tile used in the prototype.

The scintillating tiles are based on the design of scintillators for the T2K experiment by the INR group (Troitzk, Russia) who designed and built 875 mm long scintillation tiles with a serpentine wavelength shifting fiber readout [124]. The T2K tiles are injection molded polystyrene tiles of a geometry similar to those envisioned for sPHENIX, read out with a single serpentine fiber, with each fiber viewed by an SiPM on each end. The measured light yield value was 12 to 20 photoelectrons/MIP at 20°C [125]. With 12 p.e./MIP measured by T2K for 7 mm thick tiles (deposited energy ~ 1.4 MeV) and an average sampling fraction of 4% estimated for the sPHENIX HCal we expect the light yield from the HCal to be about 400 p.e./GeV. A 40 GeV hadron will share its energy nearly equally between the inner and outer HCal segments so the upper limit of the dynamic range of the HCal can be safely set to ~ 30 GeV which corresponds to a yield of 12000 p.e. on the SiPM. To avoid signal

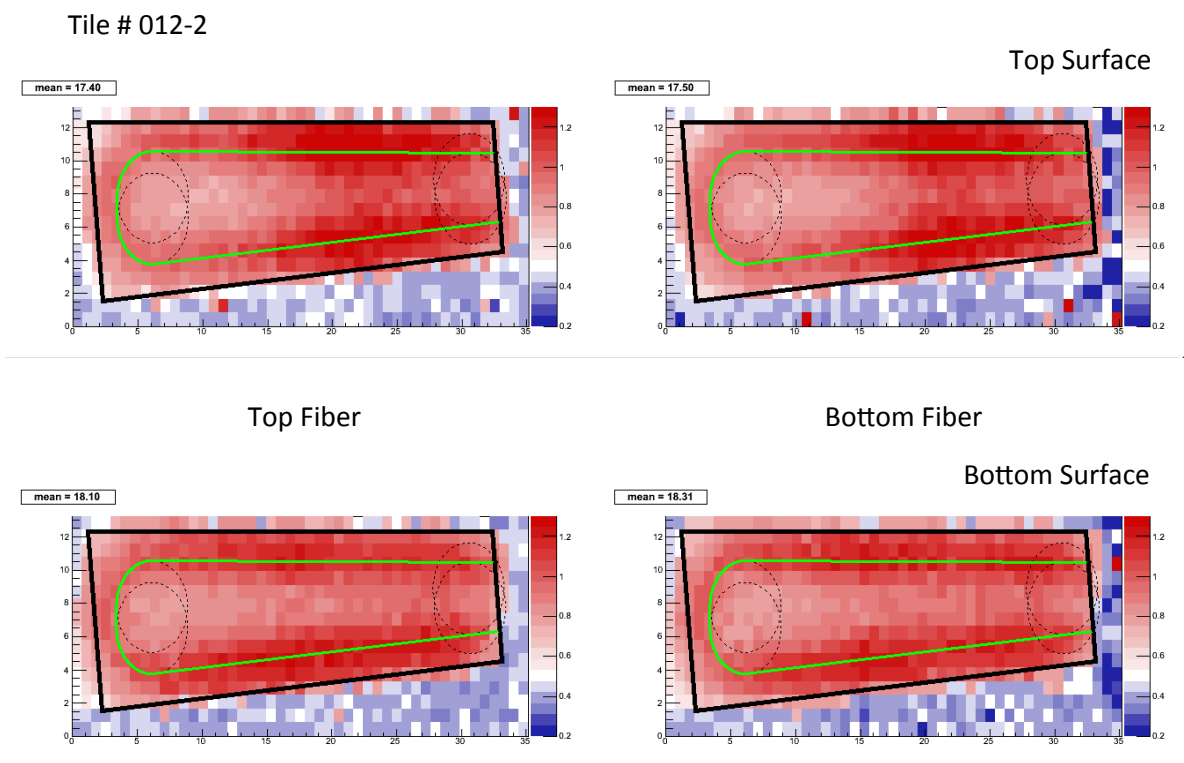


Figure 3.10: Measurement of uniformity of light collection in an sPHENIX prototype tile measured with a ^{90}Sr source at the University of Colorado.

saturation and ensure uniform light collection, care will be required to both calibrate the light yield (possibly requiring some attenuation) and randomize it.

The uniformity of light collection from prototype tiles constructed for the sPHENIX prototype arrangement can be judged from Figure 3.10 with measurements made by scanning a ^{90}Sr source over the surface of a tile. The largest drop in the light yield is along the tile edges and in the corners farthest from the fibers.

We note that this design is optimized for simplicity of manufacturing, good light yield, and to serve as the flux return for the magnet. As such, it has a manifestly non-uniform sampling fraction as a function of depth and is not highly compensated. However, the performance specifications are quite different from particle physics hadronic calorimeters, particularly with a limited energy measurement range (0–60 GeV). GEANT4 simulations described in the next section indicate a performance better than the physics requirements, and test beam results which validate the design.

3.4 Calorimeter Simulations

We have employed the GEANT4 simulation toolkit [126] for our full detector simulations. It provides collections of physics processes suitable for different applications. We selected the QGSP_BERT list which is recommended for high energy detector simulations like the LHC experiments. We have also run additional tests with different physics lists in detailed comparison with test beam data. We have integrated the sPHENIX simulations with the PHENIX software framework, enabling us to use other analysis tools we have developed for PHENIX.

The detectors and readout electronics and support structures are highly configurable in our GEANT4 framework, making it easy to test various geometries and detector concepts. Magnetic field maps for the BaBar magnet have imported from Opera calculations. We keep track of each particle and its descendants so every energy deposition can be traced back to the original particle from the event generator. The detector geometry can be easily configured when events are generated from a number of libraries which simulate concentric cylinders (the simplest idealized geometry), tilted plates, and spaghetti fiber geometries for the electromagnetic and hadronic calorimeters.

The superconducting magnet is simulated with the proper location of the material thickness in the cryostat.

All tracks which reach a layer 10 cm behind the HCal are aborted to prevent particles which are curled up by the field from re-entering the detector. Adding up the energy of those aborted tracks yields an estimate of the energy which is leaked from the back of the hadronic calorimeter.

3.4.1 Electromagnetic Calorimeter Simulation

The electromagnetic calorimeter has been simulated using the GEANT4 tools described above. A detailed description of the SPACAL design is included with fiber locations and orientations as shown in Figure 3.11. This geometry is based on the GEANT4 description developed by Alexander Kiselev for the EIC research and development calorimeter project.

Figure 3.12 shows a typical GEANT4 event in which a 10 GeV/c electron hits the calorimeter. Most of the shower develops in the EMCal. The resolution of the electromagnetic calorimeter for electrons at normal incidence was shown earlier in comparison with the test beam data in Figure 3.5.

The energy deposited in the electromagnetic calorimeter in central HIJING events is shown in Figure 3.13. The mean energy deposited in any single tower is estimated to be approximately 50 MeV. The existing PHENIX electromagnetic calorimeter cluster finding algorithm has been adapted for the sPHENIX EMCal specifications. Initial results indicate that for a 10 GeV photon there is an extra 4% of underlying event energy in the cluster

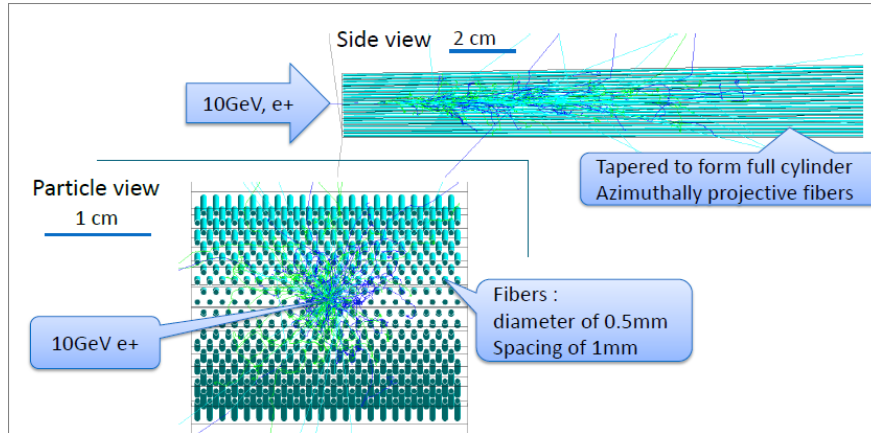


Figure 3.11: GEANT4 event display showing the fiber matrix and an electron shower development in the calorimeter.

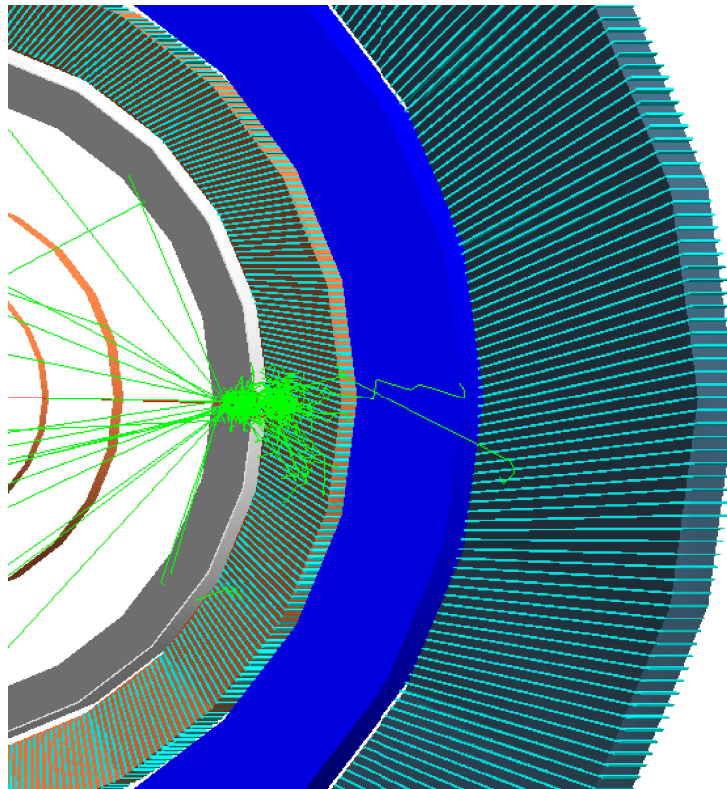


Figure 3.12: Transverse view of a 10 GeV/c electron in sPHENIX. It penetrates the magnet (blue) and showers mainly in the EMCal.

and a degradation of less than 10% in the energy resolution when embedded in a central Au+Au event (simulated with the HIJING event generator).

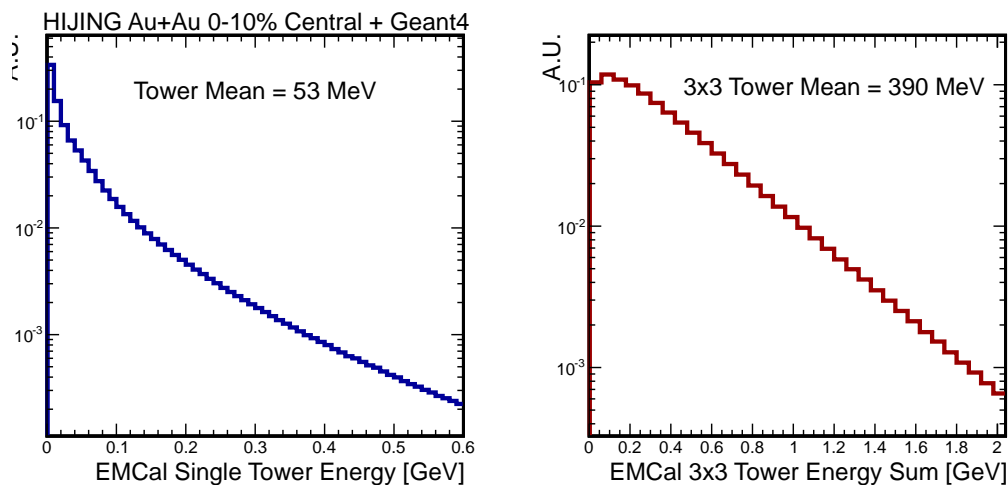


Figure 3.13: Distribution of energy deposited in the electromagnetic calorimeter for single towers (left panel) and in 3×3 arrays of towers (right panel) in central HIJING events.

3.4.2 Hadronic Calorimeter Simulation

The hadronic calorimeter has been simulated using the GEANT4 tools described above. The simulation includes the detailed geometry of the steel plates and interleaved scintillator tiles. Figure 3.14 shows a typical GEANT4 event in which a $10 \text{ GeV}/c \pi^+$ incident on the calorimeter showers in the Hcal.

The average energy deposition in the hadronic calorimeter inner and outer longitudinal segments in a HIJING 10% central Au+Au event is shown in Figure 3.15.

The single particle energy resolution in the HCal has been determined using a full GEANT4 description of the calorimeters. The energy deposition in the scintillator is corrected for the average sampling fraction of the inner and outer sections and electromagnetic calorimeter separately.

The full calorimeter response to single protons and charged pions is shown in Figure 3.16. The mean and standard deviation from a Gaussian fit to the measured energy distribution are used to calculate the nominal detector resolution. These indicate a GEANT4 performance level better than the physics requirements. Note that for jets in the energy range 20–70 GeV, the constant term is not a dominant effect. Detailed comparisons with test beam data are necessary for final optimization of the design.

As mentioned above, the proposed sPHENIX calorimeter system is about $6\lambda_{int}$ deep, and one expects some leakage of energy out of calorimeter. The amount of this leakage and its energy dependence can be estimated from literature Figure 3.6 above or from simulation which is tuned to available experimental data. The probability for a proton to go through the whole depth of calorimeter without an hadronic interaction is about 0.6% (verified

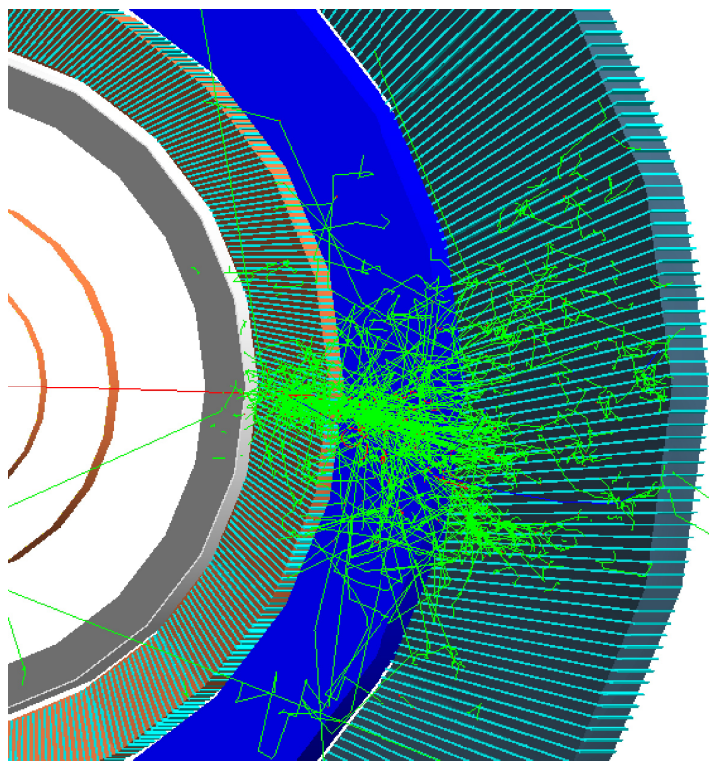


Figure 3.14: Transverse view of a 10 GeV/c π^- in sPHENIX. It penetrates the EMCAL and magnet and showers in the first segment of the HCal.

with full GEANT4 simulations). Energy leakage out the back is thus not expected to be a serious problem for this calorimeter.

3.5 Electronics

For the readout of both the EMCal and HCal a common electronics design will be used to reduce the overall cost and minimize the design time. Two viable alternatives for reading out the sPHENIX calorimeters have been identified. The first approach is based on electronics developed for the PHENIX Hadron Blind Detector (HBD) and Resistive Plate Chambers (RPC), and uses the current PHENIX DAQ as the backend readout. The second approach is based on the BEETLE chip developed for the LHCb experiment and the SRS DAQ developed at CERN. The following sections describe both approaches and how they could be implemented in sPHENIX. Both approaches will be evaluated in terms of performance and cost to enable an eventual selection of a readout system for the sPHENIX calorimeters.

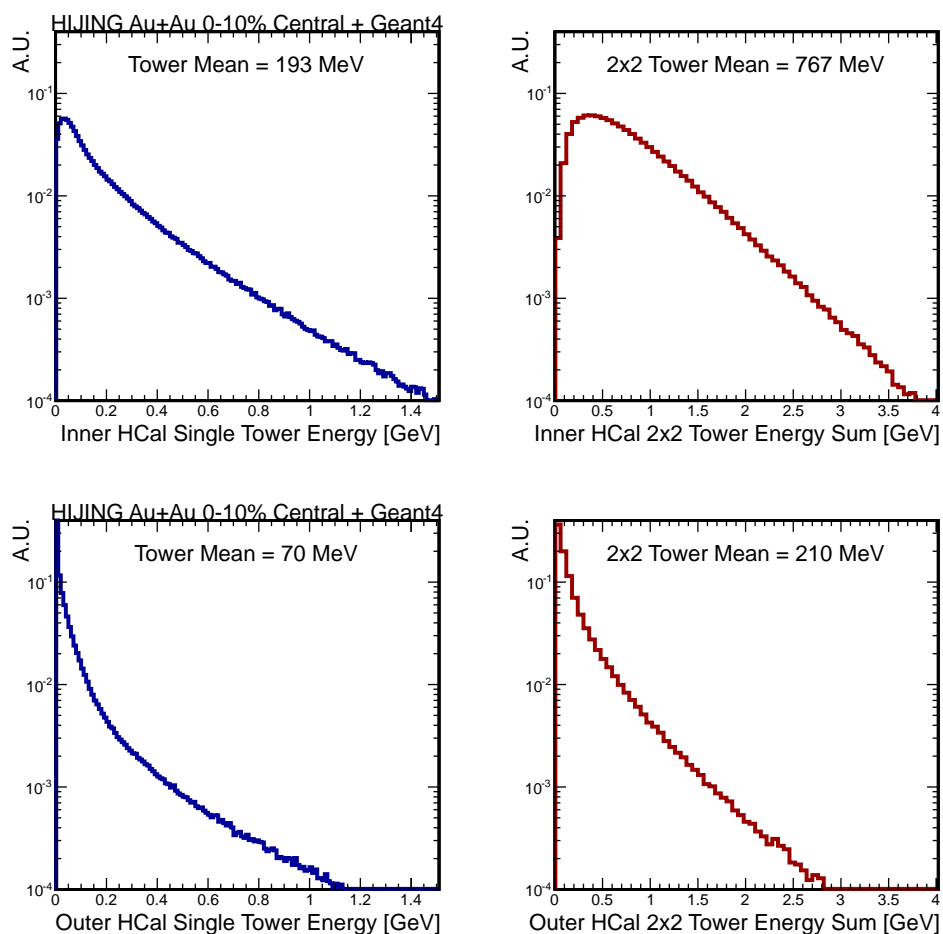


Figure 3.15: Energy occupancy distribution for the inner and outer hadronic calorimeter sections in 10% central Au+Au HIJING events run through the full GEANT4 simulation.

3.5.1 Sensors

For both the electromagnetic and hadronic calorimeters, we are currently considering as sensors $3\text{ mm} \times 3\text{ mm}$ silicon photomultipliers (SiPMs), such as the Hamamatsu S10362-33-25C MultiPixel Photon Counters (MPPC). These devices have 14,400 pixels, each $25\text{ }\mu\text{m} \times 25\text{ }\mu\text{m}$. Any SiPM device will have an intrinsic limitation on its dynamic range due to the finite number of pixels, and with over 14K pixels, this device has a useful dynamic range of over 10^4 . The saturation at the upper end of the range is correctable up to the point where all pixels have fired. The photon detection efficiency is $\sim 36\%$ and it should therefore be possible to adjust the light level to the SiPM using a mixer to place the full energy range for each tower ($\sim 5\text{ MeV} - 50\text{ GeV}$) in its useful operating range. For example, if the light levels were adjusted to give 10,000 photoelectrons for 50 GeV, this would require only 200 photoelectrons/GeV, which should be easily achieved given the light level from the fibers

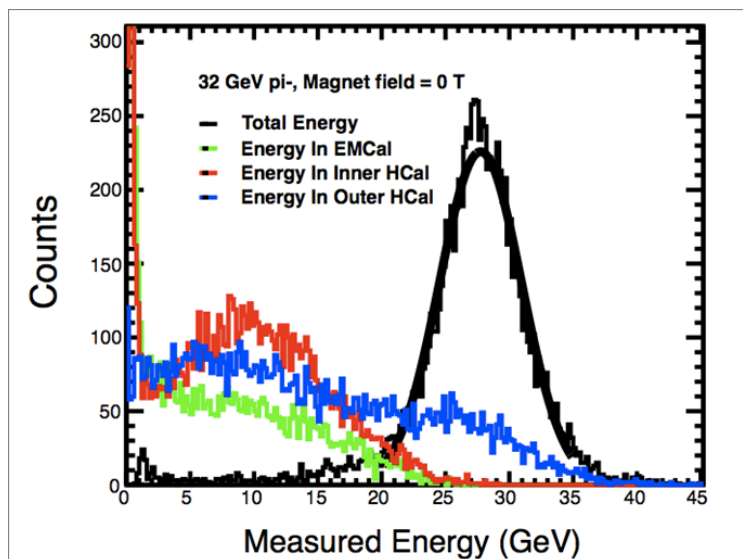


Figure 3.16: Energy deposited in the three longitudinal segments of the calorimetry by 32 GeV/c charged pion, showing the good containment and Gaussian response of the calorimeter.

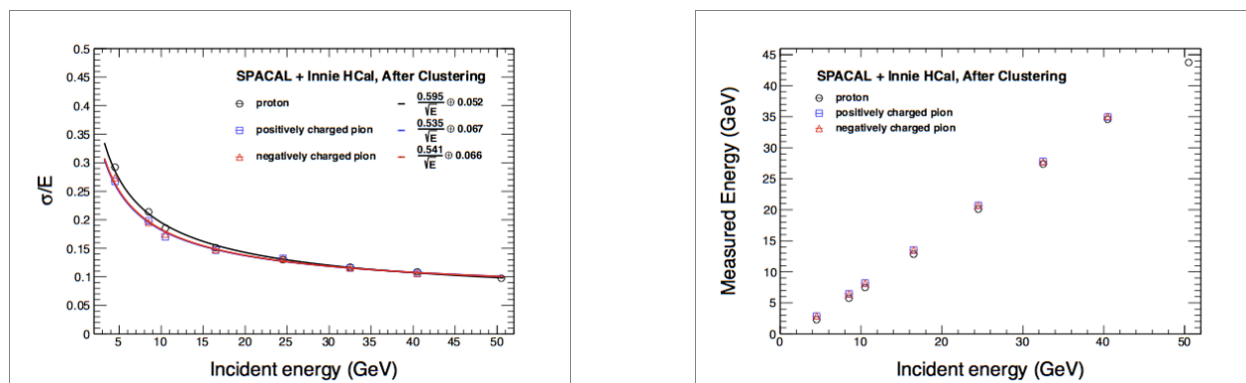


Figure 3.17: Energy resolution of the full calorimeter as a function of incident hadron energy. The left panel shows the Gaussian resolution width and the right panel shows the linearity of the energy response.

entering the mixer.

While we believe that the SiPMs are likely the most suitable sensor for the calorimeters, we are also considering avalanche photodiodes (APDs) as an alternative. They have much lower gain ($\sim 50\text{--}100$ compared to $\sim 10^5$ for SiPMs), and therefore would require lower noise and more demanding readout electronics, but they do provide better linearity over a larger dynamic range. In addition, while the gain of both SiPMs and APDs depend on temperature, SiPMs have a stronger gain variation than APDs (typically $10\%/^{\circ}\text{C}$ for SiPMs

vs $2\%/^{\circ}\text{C}$ for APDs). Thus, we are considering APDs as an alternative solution as readout devices pending further tests with SiPMs and our light mixing scheme.

3.5.2 All Digital Readout [Option 1]

SiPM Preamplifier Circuitry

The requirements of the sPHENIX calorimeter preamplifier circuit board are to provide localized bias/gain control, temperature compensation, signal wave shaping and differential drive of the SiPM signal to an ADC for acquisition. Gain adjustment and temperature compensation are performed as part of the same control circuit. Signal wave shaping is performed by the differential driver to satisfy the sampling requirements of the ADC.

Temperature Compensation

The reverse breakdown voltage V_{br} for the Hamamatsu S10362-33-25C device is nominally 70 Volts. As the bias is increased over the value of V_{br} , the SiPM begins to operate in Geiger mode with a gain of up to 2.75×10^5 . The range of this over-voltage (V_{ov}) is typically 1–2 Volts and represents the useful gain range of the device. The V_{br} increases by $56\text{ mV}/^{\circ}\text{C}$ linearly with temperature and must be compensated to achieve stable gain. This compensation is achieved using a closed feedback loop circuit consisting of a thermistor, ADC, logic and DAC voltage control as shown in Figure 3.18.

The thermistor is fixed to the back of the SiPM and provides a significant voltage variation over temperature when used as part of a voltage divider, thereby easing temperature measurement over a length of cable. The bias supply for an array of SiPMs is fixed nominally at $V_{br} + 2.5\text{V}$. The DAC in each SiPM circuit then outputs a subtraction voltage of 0 V to 5 V to provide a full range of gain control over the device temperature range. The SiPM gain may then be adjusted externally through an interface to the logic.

Preamplifier-Shaper-Driver

The SiPM current develops a voltage across the load resistor R_s proportional to the number of pixels fired. To avoid the region of greatest non-linearity due to saturation of the SiPM, the maximum signal level is optically adjusted to 10K out of 14.4K pixels fired. Simulations of the SiPM indicate that the current could be as much as several tenths of an ampere at this maximum level. Results of a SPICE simulation are shown in Figure 3.19. Such a large current affords the use of a small value for R_s which virtually eliminates the contribution of R_s to non-linearity. This signal voltage is sensed differentially, amplified and filtered by a low power, fully differential amplifier. For sampling by a 65MSPS ADC, a peaking time

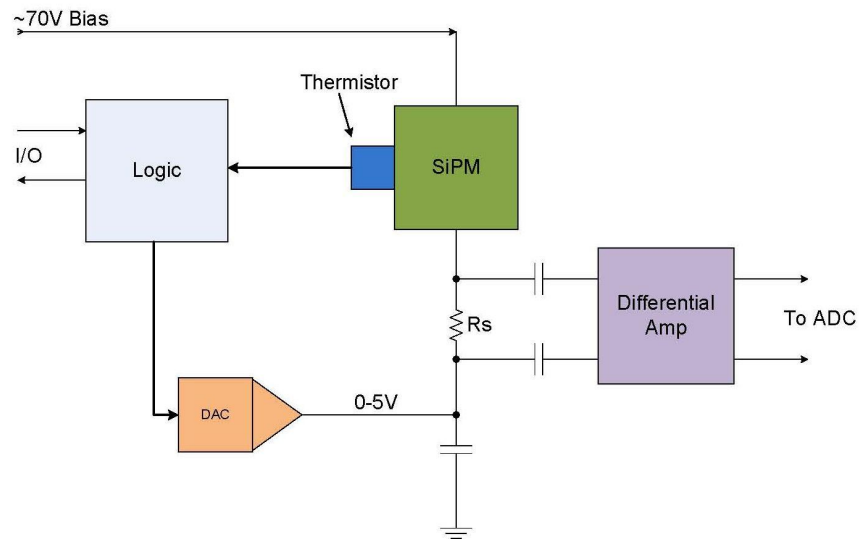


Figure 3.18: Block diagram of a temperature compensating circuit for SiPMs

of approximately 35 ns is achieved through the use of a second order Butterworth filter implemented in the differential driver circuit.

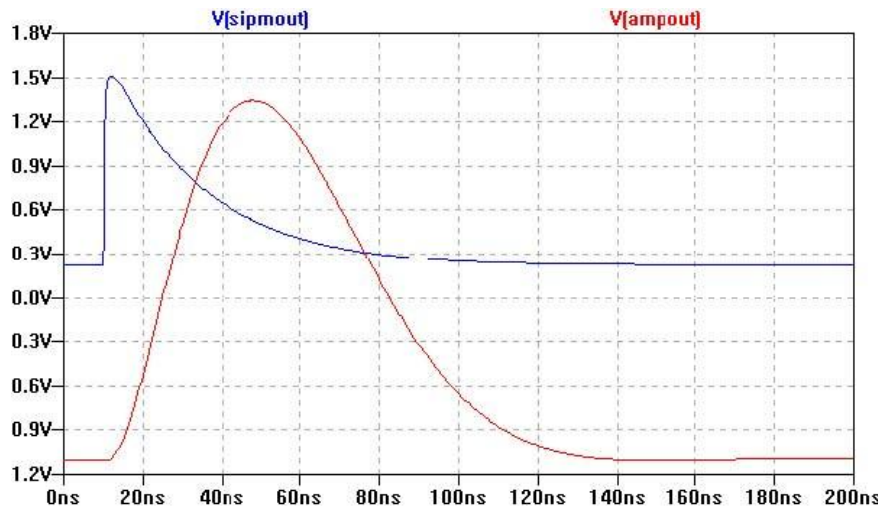


Figure 3.19: SPICE simulation of a prototype temperature compensating circuit for SiPM readout of the sPHENIX EMCAL and HCal.

Signal Digitization

One solution for the readout of the EMCAL and HCal detectors for sPHENIX is the direct digitization of the SiPM signal. The signals from the SiPM are shaped to match the sampling frequency, and digitized using a flash ADC. The data are stored in local memory

pending a Level-1 (L1) trigger decision. After receiving an L1 trigger decision, the data are read out to PHENIX Data Collection Modules (DCM II). These second generation Data Collection Modules would be the identical design as those developed and implemented for reading out the current PHENIX silicon detectors. One advantage of direct digitization is the ability to do data processing prior to sending trigger primitives to the L1 trigger system. The data processing can include channel by channel gain and offset corrections, tower sums, etc. This provides trigger primitives that will have near offline quality, improved trigger efficiency, and provide better trigger selection.

A readout system based on this concept was implemented for the Hadron Blind Detector (HBD) for the PHENIX experiment as shown in Figure 3.20 and subsequently modified for the PHENIX Resistive Plate Chamber (RPC) system. The block diagram of the Front-End Module (FEM) is showed in Figure 3.21. In the HBD system, the discrete preamplifier-shaper is mounted on the detector and the signals are driven out differentially on a 10 meter Hard Metric cable. The signals are received by Analog Device AD8031 differential receivers which also serves as the ADC drivers. Texas Instruments ADS5272 8 channel 12 bit ADCs receive the differential signals from 8 channels and digitize them at 6x the beam crossing clock. The 8 channels of digitized data are received differentially by an Altera Stratix II 60 FPGA which provides a 40 beam crossing L1 delay and a 5 event L1 triggered event buffer.

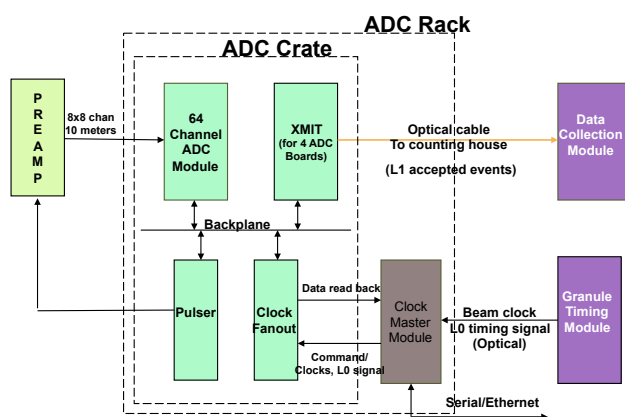


Figure 3.20: Block diagram of read out electronics based on electronics designed for the HBD.

The L1 triggered data from 4 FEMs is received by an XMIT board using token passing to control the readout of the FEMs. The data is then sent by 1.6 GBit optical links to the PHENIX DAQ. A ClockMaster module interfaces to the PHENIX Granulate Timing

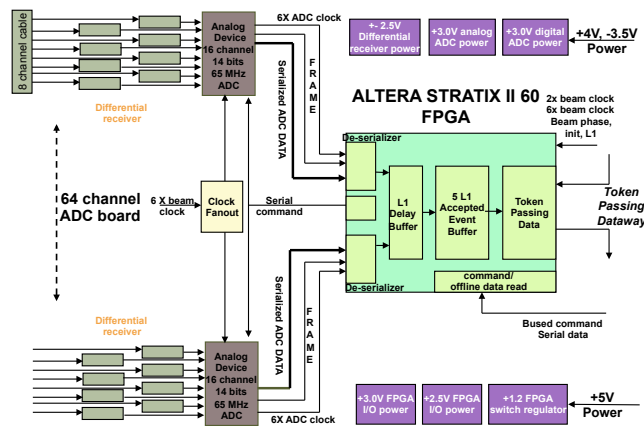


Figure 3.21: Block diagram of ADC system based on design of the HBD system.

Manager (GTM) system and fans out the clocks, L1 triggers and test enable signals to the FEMs and XMIT modules. The ClockMaster module also receives slow control signals for configuring the readout.

Although not shown in the block diagram, the FEM has 4 LVDS outputs that can be used to bring out L1 trigger primitives at 800 Mbits/sec. This feature was not used for the HBD readout, however it has been implemented for the RPC detector. A trigger module for the RPC system based on the Altera Arria FPGA receives the trigger primitives from the FEMs, combines them and sends them to the PHENIX L1 trigger system through two 3.125 Gbit optical links.

For implementation in sPHENIX, two possible implementations are under consideration. The first design would place the analog and digital electronics directly on the detector. All control and clock signals would be brought in and L1 trigger primitives and triggered digital data transmitted out via high-speed optical fibers.

The second approach has the temperature compensating preamplifier mounted on the detectors and the shaped and amplified signals driven differentially to the digital modules located in racks near the detector using shielded differential cables. High speed fiber optic cables bring in all control and clock signals and transmit L1 trigger primitives and triggered data to the PHENIX DAQ.

3.5.3 Mixed-Mode Readout [Option 2]

Preamp ASIC

A preamp ASIC appropriate for readout of sPHENIX calorimeters has been identified. This custom ASIC is being developed at ORNL for front end readout of a new forward calorimeter (FoCal) under consideration as an upgrade for ALICE at CERN. This ASIC, or a very close variant, is appropriate for front end readout of the sPHENIX EMCal and HCal. The ORNL ASIC development is funded as part of a multi-disciplinary DOE SC LAB 11-450 project which is in its first year. The ORNL team is in close communication with colleagues at BNL and are working to coordinate simulation and actual testing of the ORNL ASIC with appropriate Hamamatsu silicon photomultipliers (SiPM) for the sPHENIX EMCal and HCal. The already-funded first year of LAB 11-450 work at ORNL will generate first round ASIC chips this summer for testing.

Traditional charge-sensitive preamplifiers (CSP) are commonly used for readout of capacitive detectors (silicon pads, strips, etc.) for two reasons. First, all the charge generated in a detector due to a radiation event is ultimately collected by the preamplifier irrespective of the detector capacitance. Higher detector capacitance may slow the preamplifier bandwidth such that it takes many microseconds to collect the charge but it will ultimately be collected. Second, the ratio of the output voltage to the input charge (charge gain) is determined by the feedback capacitor used in the CSP and not the detector. Since $Q/C = V$, this will allow a small charge signal to be processed by a small feedback capacitor on the CSP instead of that same small charge on a much larger detector capacitance. This results in a proportionally larger voltage signal for subsequent processing.

Because of the large amount of charge per event available from an SiPM and the need for a fast trigger signal (fast preamplifier response), a traditional CSP is likely not ideal or needed. Therefore, a truly application-specific approach to on-chip readout is proposed. For simplicity, we can utilize a very fast high-speed follower topology similar to that used on a photomultiplier tube. This will allow us to maintain high speed, low noise, and simplicity at the front end detector. With a follower, we will have sufficient bandwidth to provide a fast trigger without having to maintain a high bandwidth closed loop CSP. Processing electronics can be placed away from the detector thus somewhat mitigating heat and power-distribution problems. The follower, shown in Figure 3.22, is very straightforward. Simulations in Figure 3.23 show that if we design the detector/follower such that our input maximum charge results in approximately 1.6 V output, we can develop a circuit which will exhibit noise of approximately 108 μV RMS, a peak/RMS ratio of 14,800. This shows that we will likely not be limited by noise, but by inter-channel crosstalk. The follower requires a buffered output, preferably differential to minimize crosstalk. The output of the differential buffer will drive the signal to an area with more available space, where it will be connected to processing electronics (shaper, trigger processor, ADC), simplifying their requirements.

A block diagram for the proposed preamplifier/driver is shown in Figure 3.24. The

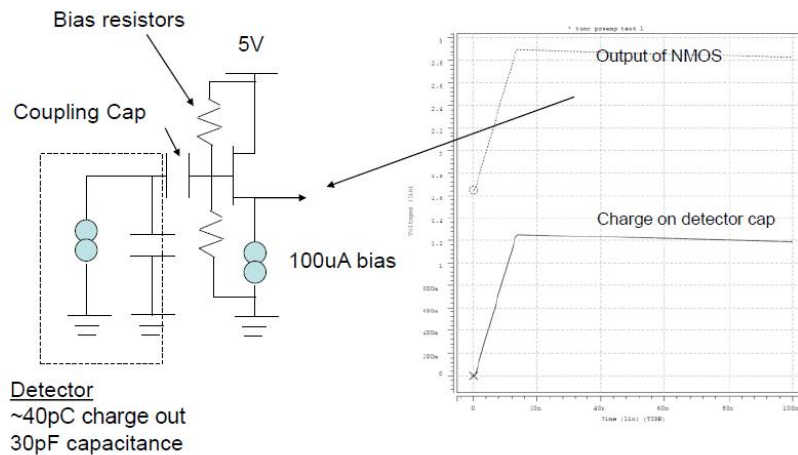


Figure 3.22: ASIC follower schematic and output signal

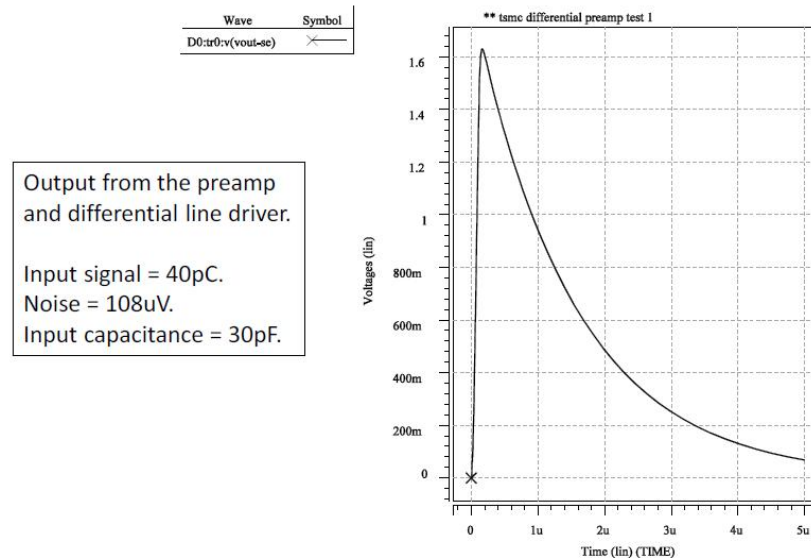


Figure 3.23: Simulation ASIC preamp output voltage versus time.

preamplifier connects to the detector as shown in Figure 3.22 (through a coupling capacitor if needed) and can utilize either polarity of charge input. There are bias setting resistors on the chip that set the quiescent input voltage. When an event occurs, the charge is collected on the detector capacitance and the voltage output is buffered and sent to the single-ended-to-differential driver. This driver is designed to drive a 100-ohm differential line. The power dissipation is currently under 10 mW for the entire circuit which operates on 2.5 V. The preamplifier is presently under design in the TSMC 0.25 μ m CMOS process. A layout estimate results in an expected chip area of under 2 mm \times 2 mm for four channels.

This electrical engineering design and development of the ASIC is undertaken as part of

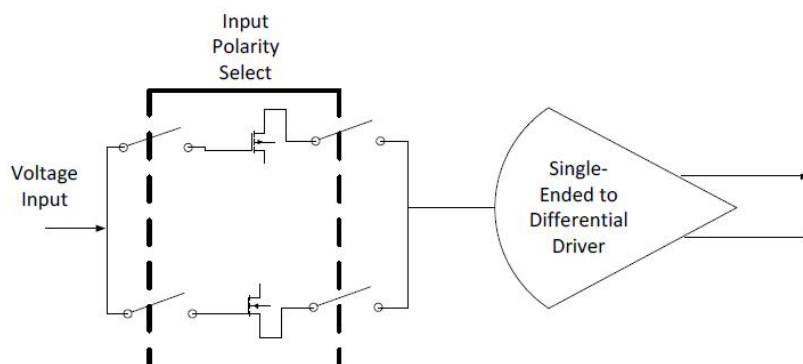


Figure 3.24: A block diagram for the proposed preamplifier/driver.

a separate ongoing DOE LAB 11-450 project. Fabrication and testing of 120 ASIC chips is scheduled for summer 2012. The chip bench testing will be performed at ORNL and include tests of basic functionality to ensure essential operation of the device such as amplification, rise time, power dissipation, channel-to-channel gain variation, noise, and chip-to-chip variations.

We have obtained a MOSIS quotation for fabrication and packaging of a sufficient number of 4-channel preamp ASICs plus spares for the sPHENIX EMCAL and HCal for a cost of \$2.80/channel. This price does not include the testing which can be accomplished very cost effectively by EE and physics graduate students with direct supervision by electrical engineers.

Front-End Readout Design using the CERN SRS

In this Section we present a design outline for sPHENIX calorimeter readout based on the already-existing CERN Scalable Readout System (SRS) which has been developed as part of the CERN RD51 project [127, 128].

The SRS architecture consists of three stages, as shown in Figure 3.25. Signals from the detector elements are conditioned and analog buffered on an analog FEE board (see below for more detail), which also generates trigger primitives. When an event is read out, the FEE board transmits analog levels to the front-end card (FEC), where they are digitized and assembled as sub-events. The transfer from the FEE board to the FEC is carried across commercial standard HDMI-format cables, which can accommodate a separation of several meters from a detector-mounted board to crate-mounted FECs. The FECs receive trigger primitives from the FEE boards along the same HDMI cables.

With existing implementations, each FEC can service eight FEE boards. Continuing hierarchically, up to 40 FECs can be gathered through standard network connections, to one Scalable Readout Unit (SRU) component of the SRS system. The SRU gathers the

real-time trigger information from the whole system and fulfills the same function as the existing PHENIX Local Level-1 (LL1) system. The SRU also serves as the overall controller/director for the FECs and fulfills the same function as the existing the PHENIX Granule Timing Module (GTM) to pass down readout and control instructions. When an event is processed, the FECs can put out sub-event data on standard network connections directly to an Event Builder; and thus the FEC fulfills the function of both the Data Collection Module (DCM II) and Sub-Event Builder (SEB) of the PHENIX architecture.

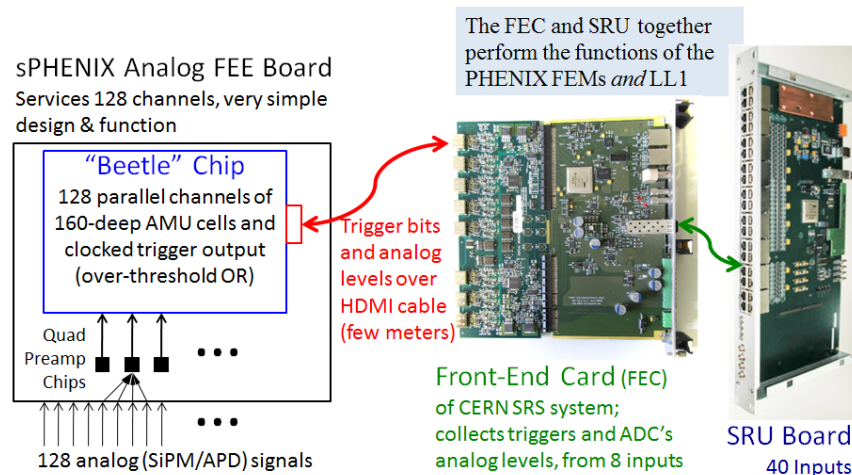


Figure 3.25: The SRS topology: The analog FEE board sits on the detector and buffers analog levels, which are then transferred to, and digitized on, the Front-End Card (FEC); the array of FECs are controlled by a Scalable Readout Unit (SRU) board. Only the analog FEE board is specific to the detector; the FEC and SRU are already-existing components of the SRS.

The sPHENIX Analog FEE Board

The advantage of adopting the SRS, for any large-scale system, is that only the analog FEE board needs to be designed specifically for the detector in question, and its functionality is relatively simple. It only needs to buffer and transmit analog levels; all the ADC and digital processing functions are carried out on existing FECs.

In the SRS-based readout design, we would use an existing circuit for the analog buffering function: the BEETLE chip, designed for use in the LHCb experiment[129]. An SRS FEE card based on the BEETLE chip is being developed by a group from the Weizmann Institute for use in an ATLAS upgrade. The BEETLE has 128 analog input channels, each of which can be buffered at up to 40 MHz in a 160-sample analog ring buffer. On readout, the BEETLE copies the analog level from the appropriate ring cells to an on-chip buffer, so the ring operation is not interrupted; the BEETLE then multiplexes these analog levels over to the FEC for digitization. The entire complement of 128 channels for one event can be transferred and converted in slightly under one microsecond.

Figure 3.26 shows a timing diagram for the processing of one physics event, with the trigger primitive bits coming up through the FECs and the SRU to the PHENIX GL1 system, which returns the LVL-1 accept down to the FECs. Sampling at up to 40 MHz, the BEETLE analog ring has enough depth to accommodate the PHENIX-standard 4 microsecond latency between the crossing of interest and the arrival of the LVL-1 accept instruction.

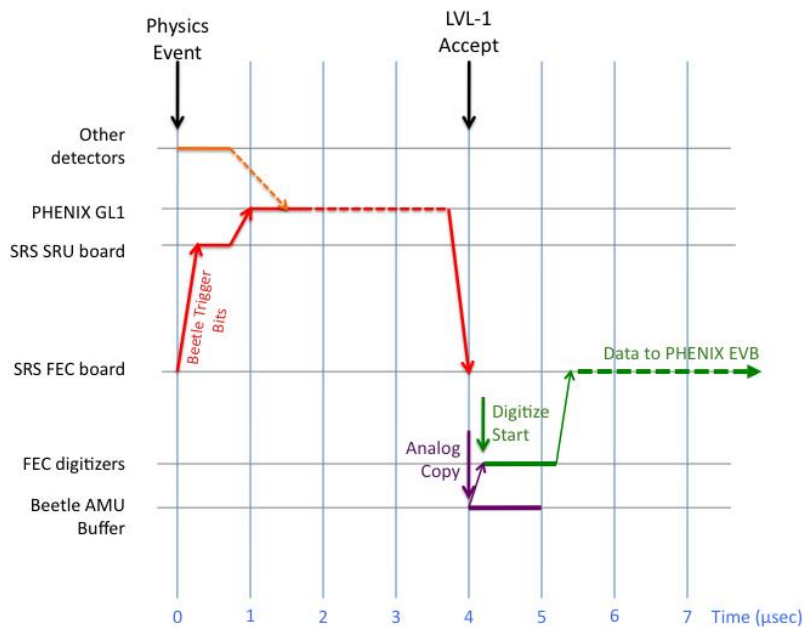


Figure 3.26: Timing diagram for processing one physics event, showing the operation of the BEETLE-based analog FEE board and the FEC and SRU components of the SRS, staying well within the PHENIX specifications for digitization and readout.

Trigger primitive bits are generated within the BEETLE chip, and are continually passed up to the FECs, where they are gathered in the SRU for calorimeter-wide processing. The trigger information provided by each BEETLE chip is essentially a channel-by-channel voltage-over-threshold condition, of which groups of four channels are then OR'ed together. The simplest global condition would be a logical OR of the over-threshold for all the towers in a fiducial portion of either the EMCal or HCal layers of the calorimeter.

One advantage of adapting the SRS system for sPHENIX is the large potential savings in development time and effort and procurement costs. The only component which needs to be specifically designed for the detector is the analog FEE board; and in the scheme outlined here that board is relatively simple, interfacing the ORNL preamp ASIC to the detector and carrying the BEETLE analog buffer chips. The digitization and digital processing are all carried out on the FECs, which use multiplexing of analog levels for higher economy; and the FECs are crate-mounted up to several meters away from the detector, which would simplify the effort of deployment. All together, the FEC/SRU portions of the readout chain are estimated to be available for approximately \$2/channel for large channel count systems, based on the production costs of the first prototype SRS systems including FEC

and SRU modules with power supplies and SRS crates, and including also FEE boards based on the AVX chip.

3.5.4 sPHENIX DAQ

The sPHENIX DAQ will be largely based on the current PHENIX DAQ. In the PHENIX DAQ, trigger primitives from the FEMs are transferred via optical fibers to the Local Level-1 (LL1) trigger system that process the signals and generates an LL1 accept if the event meets the trigger requirements. The trigger operates in a pipeline mode with a 40 beam crossing latency, generating a trigger decisions fro each crossing. The Local Level-1 trigger can be configured to accept events with different signatures and can operate at up to 10 kHz.

The LL1 accept is transmitted to all FEMs, and the corresponding event is transferred to the DCM II modules via optical fibers. The DCM II modules zero suppress the data and transmit the zero suppressed data to the event builder which collects the data and formats it for archiving. The formatted data is buffered locally at the PHENIX experimental hall before being transferred to HPSS for archiving. The PHENIX Online Computing System (ONCS) configures and initializes the DAQ, monitors and controls the data flow, and provides monitoring and control of axillary systems.

For the all digital approach 48 SiPMs are readout by a single FEM and data from 4 FEMs is collected and readout to a single DCM II channel. Each DCM II module has 8 channels, so based on channel count a total of 16 DCM II modules are required for the EMCal and another 2 DCM II modules are required for the HCal.

For the mix-mode approach using the SRS, the SRS replaces the DCM II modules and the data from the SRS would be transmitted directly to the event builder over high speed ethernet.

In either case, raw data manipulation, databases, logging and archiving, controls and monitoring can be adapted from the existing PHENIX architecture with minimal upgrades, taking advantage of a developed system which has been functioning for more than a decade.

3.6 Charged Particle Silicon Tracking

sPHENIX will have very good charged particle tracking with the reference design incorporating six planes of silicon detectors. The current PHENIX silicon vertex tracker (VTX) consists of two inner layers (pixels) at radii 2.5 and 5 cm from the beamline and two outer layers (strip-pixels) at radii of 11.8 and 16.7 cm. The ladders comprising the current PHENIX VTX are shown in the left panel of Figure 3.27. The VTX, combined with the outer PHENIX drift chambers (DC) and pad chambers (PC) provides good track pattern

recognition, high efficiency, and excellent displaced vertex resolution with a specification for the distance of closest approach in the transverse plane better than $100 \mu\text{m}$ for $p_T > 1 \text{ GeV}/c$. This resolution is exceeded even in the high occupancy Au+Au environment as shown later in Figure 4.21.

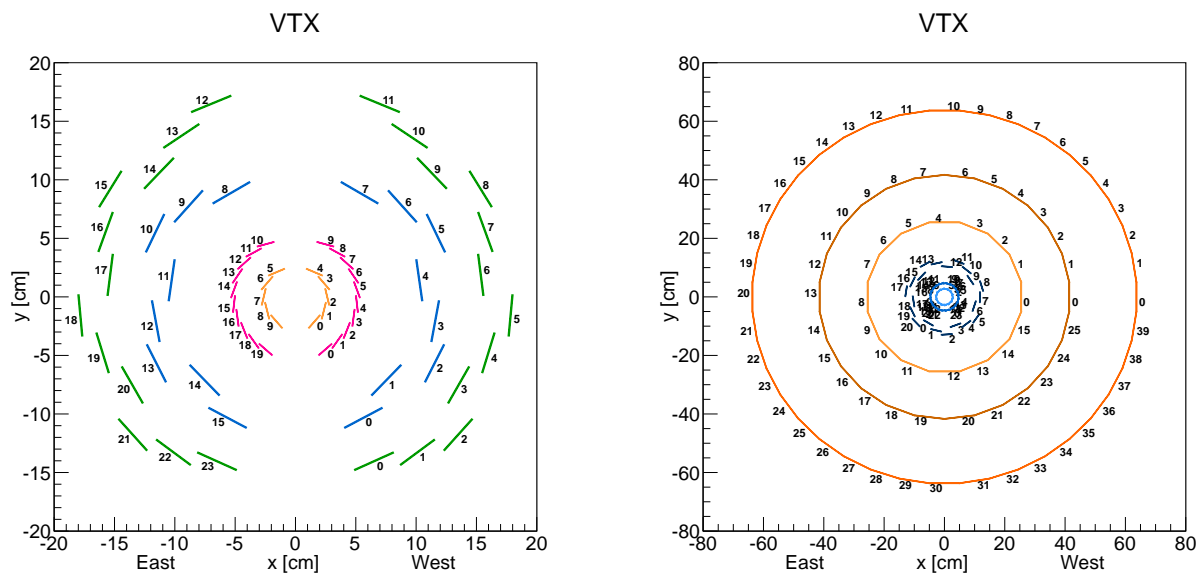


Figure 3.27: Left: Present configuration of silicon tracking layers in the PHENIX VTX detector. Right: Reconfiguration of the VTX layers and additional tracking layers as described in the text.

The reference configuration is to add eight additional ladders to the two inner pixel layers, thus completing azimuthal 2π coverage with the existing $|\eta| < 1.0$ coverage. The strip-pixel layers are combined into one layer with complete azimuthal 2π coverage. These layers have segmentation robust in the highest Au+Au occupancies and with excellent DCA resolution maintained. Radiation exposure for these layers allows for another decade of high efficiency operation, particularly in light of the planned running schedule and beam species over that time period.

For the additional three layers, the reference design is for a simple single-sided strip configuration, utilizing the SVX4 chip which is currently used for the strip-pixels and also the PHENIX MPC-EX pre-shower project. Thus, the collaboration has significant experience with the SVX4. The reference configuration is shown in the right panel of Figure 3.27. The parameters of the reference configuration are shown in Table 3.2. This is still moving towards a final design, and we are optimizing the exact radial positions, strip length and pitch, and total radiation length for the new outer layers. Note that one can improve the momentum resolution by moving the outer layer back to almost $R=80 \text{ cm}$, with the balancing consideration being cost and technical risk.

A full GEANT4 simulation of the tracking performance has been done with a modified

Table 3.2: The parameters of the reference configuration of the tracking layers.

Si tracker reference configuration					
Layer	radius (cm)	sensor pitch (μ m)	sensor length (mm)	sensor depth (μ m)	total thickness % X_0
1	2.7	50	0.425	200	1.3
2	4.6	50	0.425	200	1.3
3	11.8	80	1	625	5
4	24	60	96	320	2
5	40	60	96	320	2
6	60	60	96	320	2

Helix Hough pattern recognition and Kalman fitting. The momentum resolution for protons is shown as a function of momentum in Figure 3.28. The momentum resolution is very good and as detailed later is sufficient to deliver the physics of separate measurements of the Upsilon states and for measuring high- z fragmentation functions.

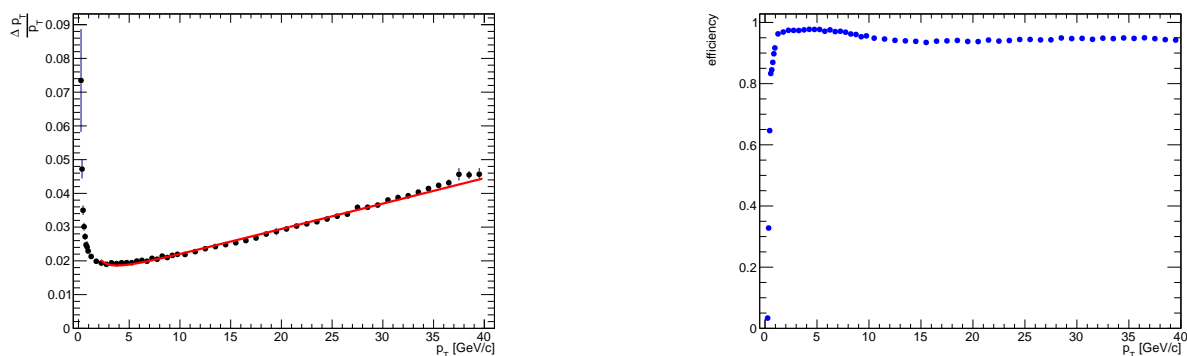


Figure 3.28: GEANT4 and track model evaluation of single particle (proton) momentum resolution (left panel). The fit shown at high momentum follows the form $\Delta p_T/p_T = 1.5 \times 10^{-2} \oplus 7.3 \times 10^{-4} \times p_T/[\text{GeV}/c]$. Also shown is the single particle track reconstruction efficiency as a function of transverse momentum (right panel). The modest drop at the higher p_T is an artifact of incomplete tuning of the Kalman filter and track quality selection cuts.

RIKEN in Japan is planning to make a prototype sensor this year, and the initial layout

from Hamamatsu is shown in Figure 3.29. Integration, cooling, and cabling layout are at an early stage in design modification from the current PHENIX VTX configuration.

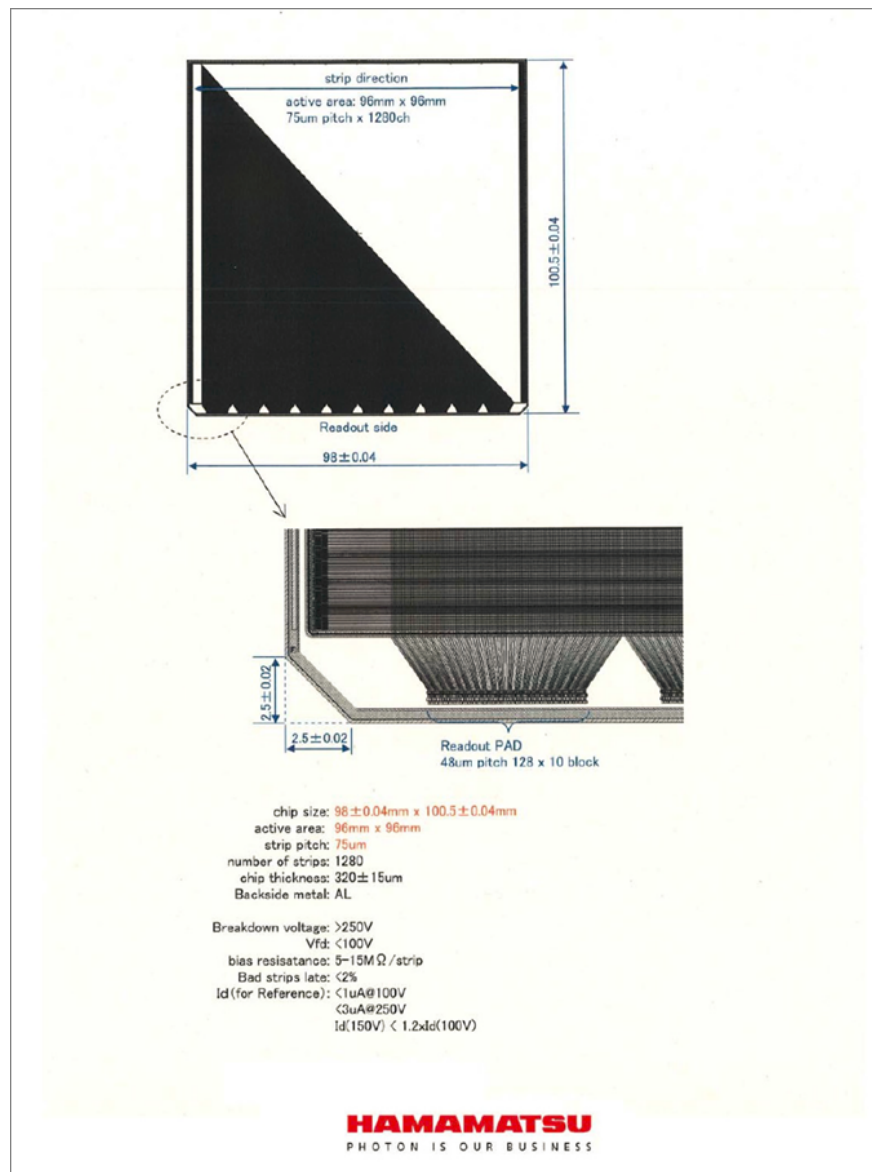


Figure 3.29: Layout for the additional silicon strip layers from Hamamatsu.

3.7 sPHENIX Triggering

Collider experiments typically require rather sophisticated trigger capabilities to sample the rare physics of interest from the large number of “uninteresting” collisions. In the case

of sPHENIX, for many jet observables, selective triggering biases the physics of interest and results in covering only a partial phase space of jets (e.g. jets originating from partons emitted near the surface of the medium). For Au+Au collisions, the high bandwidth and deadtimeless nature of the sPHENIX data acquisition system allows us to record (with only a global Au+Au interaction or minimum bias trigger) a data sample of 50 billion events within a z-vertex $|z| < 10$ cm, corresponding to the optimal acceptance of the silicon tracking system. During that same time period, a total of 200 billion Au+Au interactions over a wider z-vertex range will have taken place that can be sampled with modestly selection triggering. In addition, critical trigger requirements are relevant for $p+p$ and $p(d)+Au$ running, and the lower occupancy environment simplifies the task at hand.

There are three systems where we plan for inputs to the sPHENIX Level-1 trigger system. The current requirement is a modest 4.0 microsecond (i.e. 40 beam clock) latency on the trigger decision. The first two systems with trigger inputs are the electromagnetic and hadronic calorimeters. Both systems utilize a common electronics that digitized the signals at full clock speed, thus removing any need for having separate trigger thresholds applied to split analog signals. The reference design has a set of full digitized energy values with a modest bit number reduction collected into one module from the entire calorimeter systems (of order 25,000 channels). Thus, one has full information in a set of FPGAs to apply a variety of trigger selections:

- Total electromagnetic energy, hadronic energy, and both
- Jet patch energy sums including with average underlying event subtraction
- Cluster energy in the electromagnetic calorimeter, or cluster pairs with geometric configurations

The third detector with input is envisioned utilizing the current PHENIX Beam-Beam Counters (BBC), described in detail in Ref. [130]. The BBC consists of 128 channels of quartz radiators with PMTs on each side in the z-direction of the collision point. The detectors would be moved further back just outside the current design for the magnet flux return. They would thus be moved about one unit further forward in pseudorapidity from their current configuration. In Au+Au collisions, these would provide a precision $\sigma < 1$ cm z-vertex resolution for Level-1 triggering and an independent centrality and event plane determination.

For the jet physics program with observables for single jets, high momentum photons, and high momentum hadrons, the electromagnetic calorimeter cluster trigger inputs and jet patch capabilities are sufficient for sampling the full 200 billion events for the highest energies where the factor of four in Au+Au statistics is particularly beneficially. This triggering also works well in $p+p$ and $p(d)+Au$ collisions, with the interaction rates projected.

3.8 Mechanical Design and Infrastructure Concept

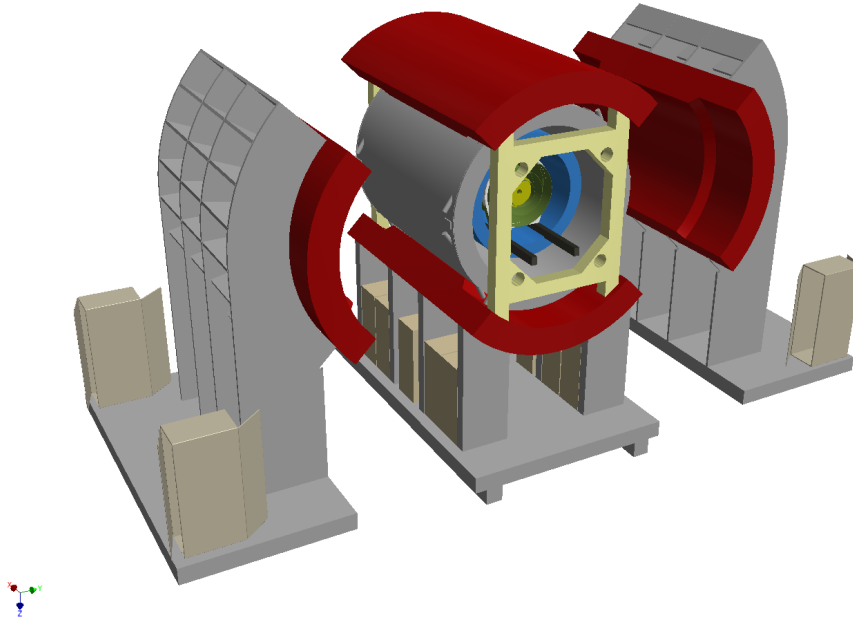


Figure 3.30: Illustration of sPHENIX underlying structural support, support equipment, overall assembly and maintenance concepts

sPHENIX has been designed to be straightforward to manufacture and assemble, but it still requires significant and well thought out infrastructure to support and service it. The overall concept for how sPHENIX will sit in the existing PHENIX IR is shown in Figure 3.30. A set of envelope dimensions and design constraint parameters for each of the major components of sPHENIX has been established and is discussed below.

3.8.1 Beampipe

The existing PHENIX beampipe will be used with minimal modification. The current beampipe has a 40 mm outside diameter in the central area, and connected on either end with transition pipe sections from 40 mm to 75 mm OD and 75 mm OD to 125 mm OD. A new support structure to support the beampipe inside the superconducting solenoid will need to be designed.

3.8.2 Silicon Tracker

The support structure for the VTX, utilities supply and readout design will need to be modified to allow the VTX to fit within the superconducting solenoid cryostat. Existing

VTX and upgrades to detector subassembly will be integrated into a new structural support design and mechanisms which will mount the VTX onto rails supported by the cryostat inner surface, allowing the VTX to be separated laterally then extracted from inside the cryostat longitudinally parallel to the beam pipe for maintenance. The VTX electronics and services inside the cryostat will not be serviceable during runs. The VTX support structure will have a clamshell design to allow the east and west halves to be opened then extracted longitudinally on a rail system during long maintenance shutdowns.

3.8.3 Superconducting solenoid magnet

The BaBar magnet has a 1.5 Tesla solenoid field, 1400 mm inner cryostat radius, 1730 mm outer cryostat radius, 3850 mm cryostat length. The cryostat is not designed to be disassembled. The cryostat incorporates support mounts that will be adapted to the hadronic calorimeter acting as the flux return. The services stack may be modified to exit outside the acceptance beyond the south end of the HCal detector to cryogenic supply lines, power supplies and monitoring equipment. The existing rigging fixtures from SLAC will be adapted for transport, lifting and installation. The Superconducting Magnet Division and Collider-Accelerator Department have the technical expertise to integrate the solenoid into existing RHIC infrastructure.

3.8.4 Electromagnetic calorimeter

The EMCal will have a 130 mm radial thickness with electronics and services on the inner radius and full 2π azimuthal coverage. The EMCal will also incorporate provision for support of itself in the fully assembled configuration, any maintenance configuration, and for assembly/disassembly and integration of component segments. The EMCal is conceived to be built in 2×2 wedges. Details of the mechanical conceptual design of the EMCal is covered in Section 3.2 and more detailed mechanical design is ongoing.

3.8.5 Hadronic calorimeter

The HCal will have full 2π azimuthal coverage, and with the calorimeter divided into an inner radial section inside the solenoid and an outer radial section just outside the solenoid. The inner radial section, which occupied 23 cm in radial thickness in the simulation, will be designed to maximize the absorber inside the magnet while allowing sufficient space for readout electronics and services. The inner HCal was simulated with copper absorber, but brass or non-magnetic stainless steel are options which can be considered in the optimization of the calorimeter design. The outer calorimeter was 67 cm thick in the simulation, making the total HCal about 5.5 nuclear interaction lengths thick. Detailed optimization of the outer HCal will examine the the benefits of dividing

the calorimeter into two longitudinal sections which would reduce the variation of the sampling fraction with depth and allow shorter scintillator tiles. The HCal will provide integral support for the cryostat and/or clearance for support from lower structure. The HCal will also incorporate provision for support of itself in the fully assembled configuration, any maintenance configuration and for assembly/disassembly and integration of component segments. The HCal will be constructed of 384 segments of 7 mm thick scintillator sections with embedded optical fibers which collect the light. The scintillator sections will be sandwiched between tapered steel plates tilted at 10-20 degrees from the radial direction, with the inner steel dividers angled in the opposite direction from the outer steel and offset by a half a segment thickness. Detailed consideration of the mechanical design of the HCal segments is covered in Section 3.3.

3.8.6 Structural support apparatus

Structural support for the sPHENIX major components will provide appropriate structural support for all of the equipment with the following criteria:

- Appropriate structural support will be provided to all components, with integral connections and support interfaces and/or clearances for support structure designed into the comprising detector subassemblies and the superconducting solenoid.
- Components will be able to be completely assembled in the PHENIX Assembly Hall (AH) utilizing existing cranes (40 ton max.). The assembly will be mounted on the existing PHENIX rail system or a modification of the existing rail system.
- Functional tests including pressure, and magnetic tests will be able to be performed in the AH.
- The sPHENIX will have designed-in capabilities to separate into subdivisions to allow maintenance of any electronics, support services and replaceable components. This capability will be available with the full assembly in the AH or the Interaction Region (IR), with full maintenance capabilities during shutdowns between runs and with as much maintenance capabilities during a run as possible.
- The sPHENIX assembly will be relocatable from the AH to the IR using the existing rail system or a modification to the existing rail system. This relocation may be accomplished fully assembled or disassembled into subdivisions which are reassembled in the IR. Disassembly and re-assembly will use existing AH and IR cranes.
- Support equipment for the above components and the utilities supplied to the above structure including provision for electronics racks, cooling services, cryogenics, power and signal cables, and monitoring and control equipment will be provided.

- The assembled sPHENIX will allow partial disassembly during maintenance periods to provide access to all serviceable components, electronics and services. The assembled sPHENIX will provide for electronics racks and all other support components for operation and monitoring of the sPHENIX active components. Safe and efficient access to all service/monitoring components will be integrated into the design of the underlying structural support.
- Infrastructure used successfully for the past fourteen years of PHENIX operation will be adapted and expanded to support sPHENIX. This includes the chilled water system for electronic cooling, air conditioning, and safety systems.

3.9 Detector Development and Testing

Prototype electromagnetic and hadronic calorimeters have been developed for beam tests to validate the design concepts and gain experience with the readout and calibration of silicon photomultipliers in an operating detector. The first prototypes were tested at the Fermilab Test Beam Facility as T-1044 February 5-25, 2014. The EMCal prototype was a 7×7 device with 1 mm tungsten absorber which can be rotated in the beam to study shower development and energy resolution. A beam test of the SPACAL electromagnetic calorimeter was carried out by the UCLA group and collaborators immediately following T-1044. The HCal prototype consists of inner and outer 4×4 sections with machined tapered plates using a mechanical design that is being evaluated for use in building the full detector. Both detectors are read out with Hamamatsu silicon photomultipliers with signal conditioning that allows them to be flash digitized at 60 MHz with existing PHENIX electronics.



Figure 3.31: Top: HCal prototype under construction. The first layers of absorber are being stacked on the lift table for the beam test. Bottom: Calorimeters in MWest beamline of the Fermilab Test Beam Facility.

Chapter 4

Physics Performance

In this Chapter we detail the expected sPHENIX physics performance. The sPHENIX jet, dijet, γ -jet, fragmentation function, and beauty quarkonia performance demonstrates the ability to measure key observables that can test and discriminate different quenching mechanisms, coupling strengths to the medium, and with sensitivity to different length scales in the QGP.

The key aspects of jet performance are the ability to find jets with high efficiency and purity, and to measure the kinematic properties of jet observables with good resolution. It is also necessary to discriminate between jets from parton fragmentation and fake jets caused by fluctuations in the underlying event background. For the sPHENIX physics program, there are four crucial observables that we have simulated in detail to demonstrate the jet performance: single inclusive jet yields, dijet correlations, γ +jet correlations, and modified fragmentation functions. We also find that the combination of full calorimetric reconstructed jets combined with track and electromagnetic cluster jets allows one to engineer the surface emission of the leading jet and thus the path of the partner jet. There are other significant observables such as the participant plane dependence (e.g. v_2 , v_3 , etc.) of jets and jet-hadron correlations that are also enabled by this upgrade.

For beauty quarkonia decaying to e^+e^- , the key aspects of performance are electron identification (particularly in being able to discriminate against charged pions), and good momentum resolution to provide sufficient invariant mass resolution to distinguish clearly the $Y(1s)$, $Y(2s)$, and $Y(3s)$ states..

An important focus will be to demonstrate the capabilities of sPHENIX for central Au+Au collisions at $\sqrt{s_{NN}} = 200$ GeV, where the complications of the underlying event are the most severe. We first detail the physics performance for jet observables and then the performance for the beauty quarkonia physics.

4.1 Jet simulations

sPHENIX is able to record 50 billion Au+Au minimum bias interactions in 20 weeks of running at $\sqrt{s_{NN}} = 200$ GeV. With the currently achieved RHIC luminosities in 2014, for the calorimetric observables, sPHENIX can sample 200 billion such interactions. It is not possible to simulate with full GEANT4 [126] the equivalent data sample. Thus, we perform three different levels of simulations described in detail below. The most sophisticated and computationally intensive are full GEANT4 simulations with PYTHIA [131] or HIJING [132] events where all particles are traced through the magnetic field, energy deposits in the calorimeters recorded, clustering applied, and jets are reconstructed via the FASTJET package [133]. We utilize this method to determine the jet resolution in $p+p$ and Au+Au collisions from the combined electromagnetic and hadronic calorimeter information. We have also performed a full GEANT4 study of the reconstruction of PYTHIA jets embedded in central Au+Au HIJING events to gauge the effect of the underlying event on jet observables.

For studies of fake jets in Au+Au central collisions, one needs to simulate hundreds of millions of events and for this we utilize a fast simulation where the particles from the event generator are parsed by their particle type, smeared by the appropriate detector resolution parametrization from GEANT4 simulations, and segmented into detector cells. As described in detail below, a full underlying event subtraction procedure is applied, and then jets are reconstructed using FASTJET. This method is also utilized for embedding events from PYTHIA or PYQUEN [134] (a jet quenching parton shower model) into Au+Au HIJING events to study dijet and γ +jet observables. Finally, in order to gain a more intuitive understanding of the various effects, we run a very fast simulation where PYTHIA particles are run directly through FASTJET and then the reconstructed jet energies smeared by the parametrized resolutions and underlying event fluctuations.

This Section is organized as follows. First we describe the jet reconstruction and evaluate its performance in $p+p$ collisions for both an idealized detector as well as a fully simulated version. Then we describe our study of fake jet contamination, which has been published in Physical Review C [135]. We show the expected performance for sPHENIX measurements of inclusive single jet, dijet and γ +jet correlations, and modified fragmentation functions.

4.2 Jet finding algorithm

For all of the studies presented here we use the anti- k_T jet algorithm [136] implemented as part of the FASTJET package [133]. The anti- k_T algorithm is well suited to heavy ion collisions and produces cone-like jets in an infrared and collinear safe procedure. The parameter that controls the size of the jet in this algorithm is the jet radius, R . While this is not strictly a cone size it does specify the typical extent of the jet in η - ϕ space. High energy experiments typically use large R values of 0.4–0.7 in order to come as close as possible

to capturing the initial parton energy. In heavy ion collisions, the desire to measure the quenching effects on the jet profile and to minimize the effects of background fluctuations on jets has led to the use of a range of R values. Values from 0.2 to 0.5 have been used to date in Pb+Pb collisions at 2.76 TeV at the LHC [70, 74]. We note that looking at the jet properties as a function of the radius parameter is very interesting and potentially sensitive to modifications to the jet energy distribution in the medium. For the studies presented here we use R values of 0.2, 0.3, and 0.4. Larger values of R are achievable with track jet matching and also in non-central Au+Au centralities.

4.3 Jet performance in $p+p$ collisions

We begin by exploring the performance of the detector in $p+p$ collisions. This allows us to investigate the effects of detector resolution and how well the process of unfolding these effects in simpler collisions works before considering the additional effects of the underlying event and jet quenching in heavy-ion collisions.

The most realistic understanding of the sPHENIX jet reconstruction performance comes from a full GEANT4 simulation of the detector response. In this case, PYTHIA particles are run through a GEANT4 description of sPHENIX, the resulting energy deposition is corrected for by the sampling fraction of the relevant calorimeter, binned in cells of η - ϕ (0.024×0.024 for the EMCal and 0.1×0.1 for the HCal) and the resulting cells are used as input to FASTJET. Particles from PYTHIA events are put through FASTJET to determine the truth jets.

We then calculate the difference between the energy of the reconstructed calorimeter jets, E_{reco} , and the particle-level truth jets, E_{true} . The width of this distribution, $\sigma(E)$, is fit with a functional form

$$\frac{\sigma(E)}{E} = \frac{a}{\sqrt{E}} + b \quad (4.1)$$

Full GEANT4 calculations of the energy resolutions for jets in $p+p$ collisions reconstructed with anti- k_T and $R = 0.2$ and $R = 0.4$ are shown in Figure 4.1. The resolutions are relatively independent of R and in simulation are substantially better than the required specification detailed in Chapter 2.

The jet energy resolution in collider experiments is often found to be a factor of 1.2–1.3 worse than the quoted single particle resolution of the hadronic calorimeter. This factor is a balance of many effects including the better resolution for the electromagnetic part of the shower, soft particles that deflect out of the jet cone in the magnetic field, some lost energy, etc. The CMS quoted jet resolution in $p+p$ collisions at 7.0 TeV is approximately $120\%/\sqrt{E}$ which is roughly 1.2 times worse than the quoted single particle hadronic calorimeter resolution [137]. The sPHENIX jet energy resolution and hadronic calorimeter resolution from GEANT4 are consistent with this expectation, and both are within our performance specifications.

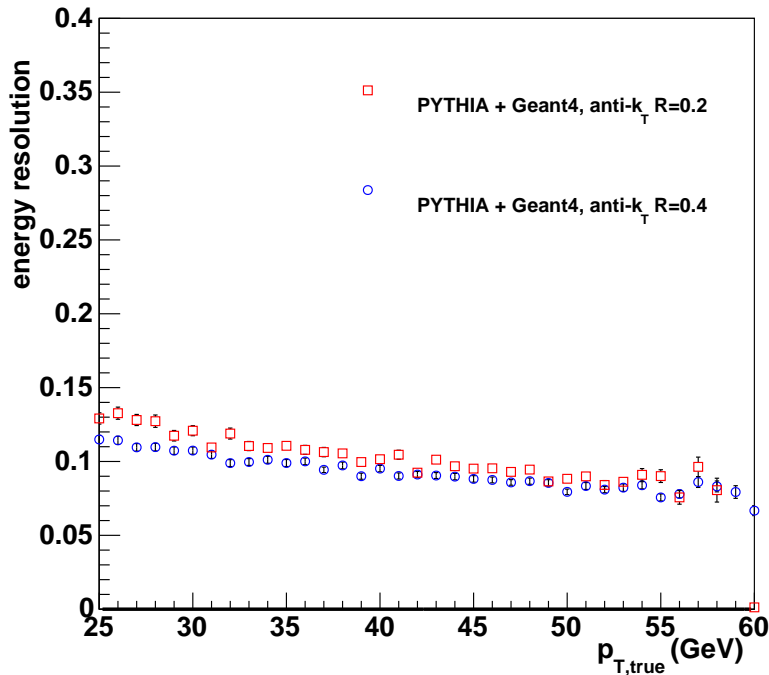


Figure 4.1: The GEANT4 calculated energy resolution of single jets in $p+p$ collisions reconstructed with the FASTJET anti- k_T algorithm with $R = 0.2$ and $R = 0.4$.

4.3.1 $p+p$ Inclusive Jet Spectra

In order to model the jet resolution effects described above on the inclusive jet spectra in $p+p$ collisions at $\sqrt{s_{NN}} = 200$ GeV, we have used the very fast simulation. This method entails running PYTHIA, sending the resulting final state particles through FASTJET to find jets, and then blurring the energy of the reconstructed jets with values obtained from the full GEANT4 simulation.

The truth spectrum of jets is obtained by using FASTJET to cluster the PYTHIA [131] event with the anti- k_T algorithm. Figure 4.2 shows the true jet p_T spectrum as the solid histogram. The convolution of the hard parton-parton scattering cross section and the high- x parton distribution function results in a jet cross section that falls nearly exponentially over the range 20–60 GeV, before turning steeply downward as it approaches the kinematic limit, $x = 1$.

Figure 4.2 also shows the very fast simulation result for the measured jet E_T spectrum. The main effects of the jet resolution on the jet energy spectrum are to shift it to higher energy and stiffen the slope slightly. Both of these effects can be undone reliably by a process of unfolding. We have employed the ROOUNFOLD [138] package and for this demonstration utilize the Iterative Bayes method with 4 iterations. The results of the unfolding are shown in Figure 4.2, along with the ratio of the unfolded to the true E_T spectrum, in the lower

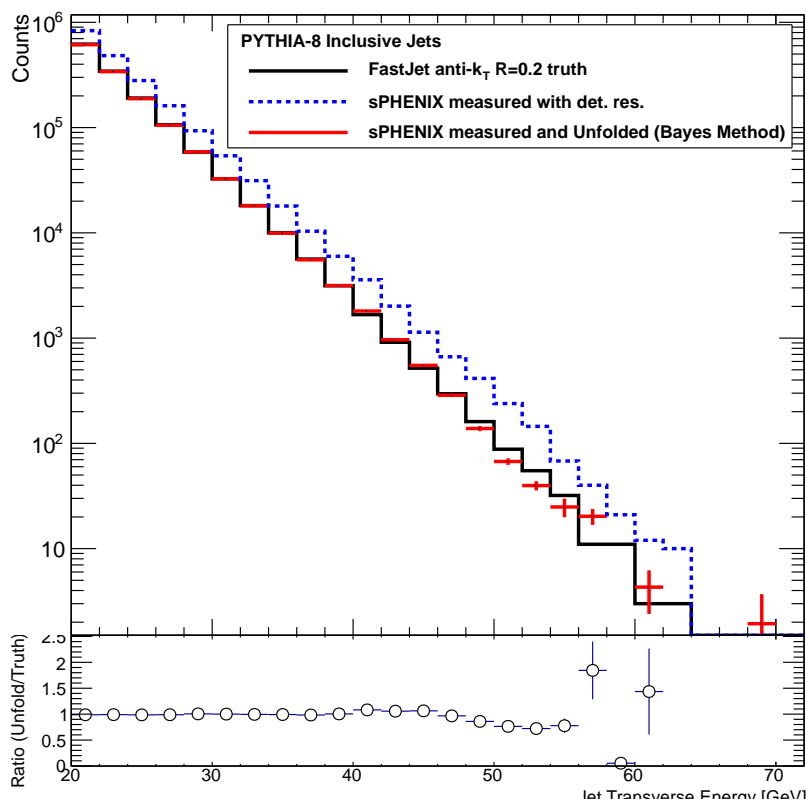


Figure 4.2: Unfolding the effect of finite detector resolution on jet reconstruction in $p+p$ events. The black histogram is the truth spectrum of jets from PYTHIA, the blue dotted histogram is the spectrum after smearing by the jet energy resolution and the red histogram shows the result of using ROOUNFOLD Iterative Bayes method to unfold the detector effects. The lower panel shows the ratio of the unfolded to the true E_T spectrum.

panel. The ratio of the two distributions demonstrates that the measurement provides an accurate reproduction of the true jet energy spectrum.

4.3.2 $p+p$ Dijet Asymmetry

The very fast simulation is also used to establish expectations for dijet correlations. Figure 4.3 shows the dijet correlation for PYTHIA events reconstructed using the anti- k_T algorithm with $R = 0.2$. The highest energy jet in the event is taken as the trigger jet and its transverse energy is compared to the transverse energy of the highest energy jet in the opposite hemisphere.

The jet asymmetry $A_J = (E_{T1} - E_{T2}) / (E_{T1} + E_{T2})$ for the true jets, reconstructed at the particle level, is shown for leading jets with $E_{T1} > 30$ GeV in Figure 4.3. Also shown is the simulated measurement with the jet resolution included. The resolution results in a reduction in the fraction of events observed with balanced jet energies (i.e. near

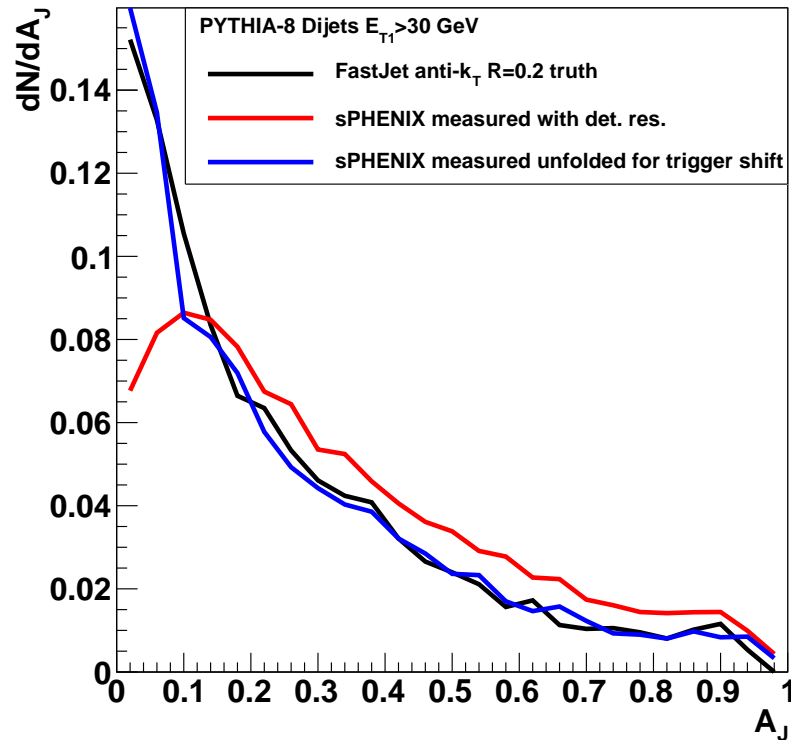


Figure 4.3: Dijet asymmetry, A_J , in $p+p$ collisions. The truth spectrum is shown in black; the spectrum measured in PYTHIA and smeared by the jet energy resolution is shown in red. The effect of the unfolding of the trigger jet bias is also shown in blue.

$A_J \approx 0$). ATLAS and CMS dijet asymmetries in Pb+Pb collisions [70, 71] are shown without unfolding for these detector or underlying event effects. A simultaneous two-dimensional unfolding of both the jet energies (i.e., $E_{T1}(\text{meas}), E_{T2}(\text{meas}) \rightarrow E_{T1}(\text{true}), E_{T2}(\text{true})$) is required in this case. Both ATLAS and CMS collaborations are actively working on this two-dimensional unfold, and the sPHENIX group is as well. At RHIC energies, the largest effect is that the trigger jet is being selected from a steeply falling spectrum and is biased by the resolution to be reconstructed higher than the true energy. If one simply shifts the trigger jet down by this average bias (and inverts the identity of trigger and associated jet if the trigger jet energy is then below that of the associated jet), the original dijet asymmetry distribution is recovered, as shown in Figure 4.3. This procedure is not a replacement for the eventual two-dimensional unfolding, but demonstrates the dominant effect.

4.4 Jet performance in Au+Au collisions

Here we simulate the performance of inclusive jet and dijet observables in heavy ion collisions. The sPHENIX trigger and data acquisition will sample jets from the full Au+Au minimum bias centrality range, resulting in key measurements of the full centrality dependence of jet quenching effects. Finding jets and dealing with the rate of fake jets become much easier as the multiplicity due to the underlying event drops, and so we have concentrated on showing that we have excellent performance in central Au+Au collisions (i.e., in the most challenging case).

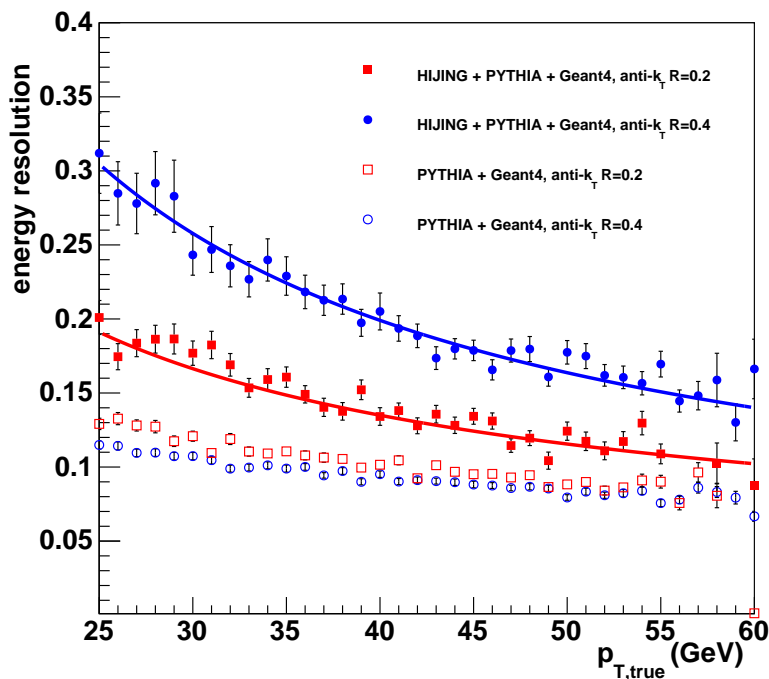


Figure 4.4: The GEANT4 calculated energy resolution of PYTHIA jets embedded in a Au+Au HIJING event, reconstructed using the anti- k_T algorithm with $R = 0.2$ and $R = 0.4$. The points, showing the result of the full simulation, are compared to the dotted lines, showing the result obtained using the fast simulation.

The effective jet resolution also has an important contribution from fluctuations in the underlying event in the same angular space as the reconstructed jet. We have carried out a full GEANT4 simulation embedding PYTHIA jets into 0–10% central Au+Au HIJING events. The true PYTHIA reconstructed jets are then compared with the Au+Au extracted jets (as detailed below) to determine the jet energy resolution, as shown in Figure 4.4. Also shown in the figure as dotted lines are the parametrized electromagnetic and hadronic calorimeter resolution contributions used in the fast simulation. Again, the GEANT4 resolutions are well below our physics performance specifications.

In addition to the resolution effects, fluctuations in the underlying event can create local maxima in energy that mimic jets, and are often referred to as fake jets. While resolution effects can be accounted for in a response matrix and unfolded, significant contributions of fake jets cannot be since they appear only in the measured distribution and not in the distribution of jets from real hard processes. Thus, we first need to establish the range of jet transverse energies and jet radius parameters for which fake jet contributions are minimal. Then within that range one can benchmark measurements of the jet and dijet physics observables.

4.4.1 Jet and Fake Jet Contributions

In this section we discuss both the performance for finding true jets and estimations based on HIJING simulations for determining the contribution from fake jets. It is important to simulate very large event samples in order to evaluate the relative probabilities for reconstructing fake jets compared to the rate of true high E_T jets. Thus, we employ the fast simulation method and the HIJING simulation model for Au+Au collisions. The ATLAS collaboration has found that the energy fluctuations in the heavy ion data are well matched by HIJING at $\sqrt{s_{NN}} = 2.76$ TeV [139]. We have also added elliptic flow to the HIJING events used here. The fast simulation takes the particles from the event generator and parses them by their particle type. The calorimeter energies are summed into cells based on the detector segmentation and each tower is considered as a four-vector for input into FASTJET.

Any jet measurements in heavy ion collisions must remove the uncorrelated energy inside the jet cone from the underlying event. The approach developed in our studies is described in detail in Ref. [135]. A schematic diagram of the algorithm (based on the ATLAS heavy ion method) is shown in Figure 4.5. Candidate jets are found and temporarily masked out of the event. The remaining event background is then characterized by the strength of its v_2 and the overall background level in individual slices in pseudorapidity. Higher order flow harmonics were not included in this study. New candidate jets are determined and the background and v_2 are recalculated. The jet finding algorithm is then re-run on the background subtracted event to determine the collection of final reconstructed jets. This process is then run iteratively to a convergent result.

In order to distinguish true jets from fake jets we have augmented the HIJING code to run the FASTJET anti- k_T algorithm with the output of each call to the fragmentation routine (HIJFRG). In this way the true jets are identified from a single parton fragmentation without contamination from the rest of the simulated event. The reconstructed jets can then be compared to these true jets. Reconstructed jets which are within $\Delta R = \sqrt{\Delta\eta^2 + \Delta\phi^2} < 0.25$ of a true jet with $E_T > 5$ GeV are considered to be matched and those which are not are classified as fake jets.

Other estimates of fake jet rates in heavy ion collisions have failed to take into account how the structure of the background fluctuations and the detector granularity affects the

probability of any particular fluctuation being reconstructed as a jet. Note that simply blurring individual particles by a Gaussian with an underlying event fluctuation energy results in a substantial overestimate of the fake jet rate, and is not a replacement for a complete event simulation incorporating FASTJET reconstruction with a full jet and underlying event algorithm implementation. Thus, we believe these studies provide an accurate assessment of the effect of fake jets.

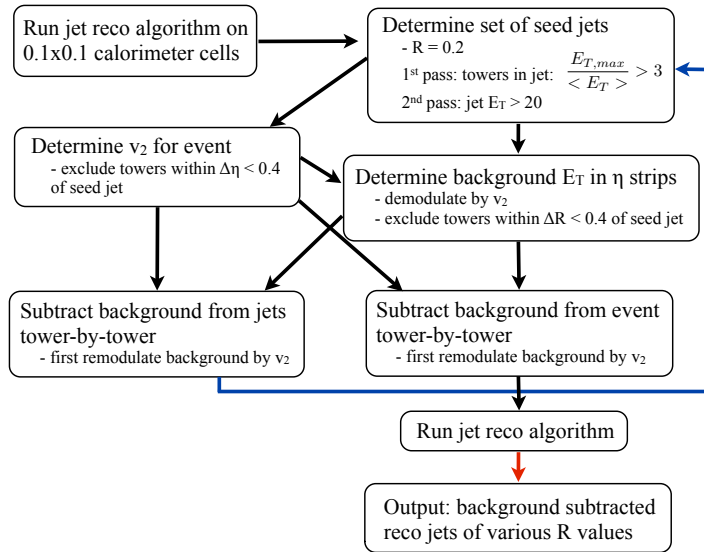


Figure 4.5: Schematic diagram for the jet reconstruction algorithm.

As an illustration of true and fake jets we show two calorimeter event displays in Figure 4.6. True jets at high E_T are a rare occurrence. A large energy background fluctuation at high E_T that mimics a jet is also a rare occurrence. Thus the only way to quantify the impact of fake jets on the jet performance is to run a large sample of untriggered simulated events and assess the relative probability of true and fake jets as a function of E_T and R .

A sample of over 750 million minimum bias Au+Au HIJING events at $\sqrt{s_{NN}} = 200$ GeV with quenching turned off was used in these studies. The observable particles are binned in η - ϕ cells of size $\Delta\eta \times \Delta\phi = 0.1 \times 0.1$. In these studies, we have not included smearing due to detector resolution as it is expected to be a sub-dominant effect and we want to isolate the effects of the underlying event. At the end of this Section we present results including detector resolution that do not change the key conclusions of these studies.

The fast simulation result for $R = 0.2$ jets without including detector-level smearing of the jet energies is shown in Figure 4.7. The full spectrum is shown on the left as solid points. The spectrum of those jets that are successfully matched to true jets is shown as a blue curve. That curve compares very well with the spectrum of true jets taken directly from HIJING. The fake jet, those not matched with a true jet, spectrum is shown as the dashed curve. For $R = 0.2$, real jets begin to dominate over fake jets above 20 GeV. The panels on the right of Figure 4.7 are slices in reconstructed jet energy showing the distribution and make up

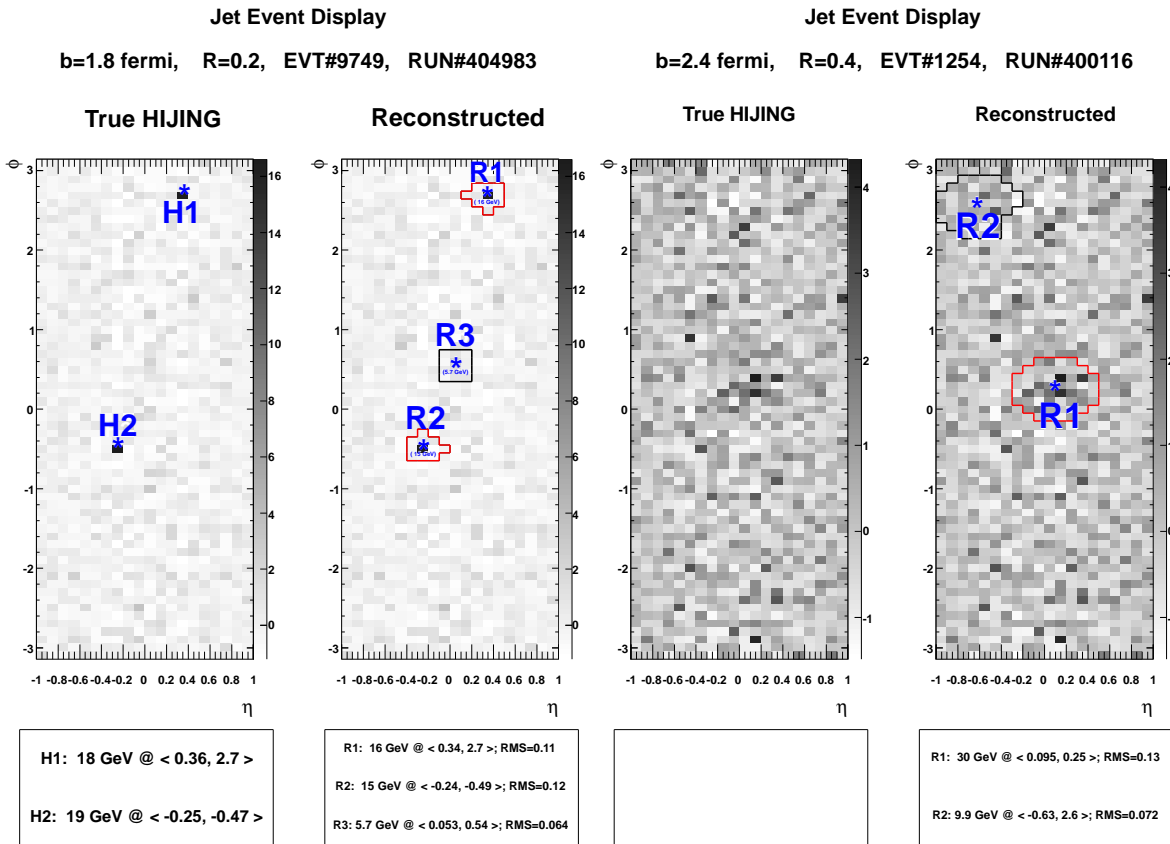


Figure 4.6: Event displays of true and reconstructed jets shown overlaid on background subtracted calorimeter towers from fast simulation. The left event shows a HIJING dijet event where both dijets (labeled H1 and H2) are reconstructed and matched (R1 and R2). A third jet, not matched to a true jet, is also reconstructed (R3). The right event shows a HIJING event with no true jets with $E_T > 5$ GeV. Two fake jets are reconstructed, one with $E_T = 30$ GeV.

of the true jet energy. For reconstructed jets with $E_T = 25\text{--}30$ GeV, a contribution of fake jets can be seen encroaching on the low energy side of the distribution. For $E_{\text{reco}} > 25$ GeV fake jets are at the 10% level and for $E_{\text{reco}} > 30$ GeV fake jets are negligible. Contributions from fake jets for larger jet cones are shown in Fig 4.8. The true jet rate becomes large compared to the fake jet rate at 30 GeV for $R = 0.3$ and 40 GeV for $R = 0.4$. We note that in one year of RHIC running, sPHENIX would measure 10^5 jets with $E_T > 30$ GeV and 10^4 jets with $E_T > 40$ GeV.

There are various algorithms for rejecting fake jets based on the jet profile or the particles within the jet. These methods applied by the ATLAS experiment significantly reduce the fake rate by an order of magnitude or more, increasing the energy and R values over which it is possible to measure jets [10]. A detailed study of this fake jet rejection method and its utility is enabling new physics is discussed later in Section 4.5.

The efficiency of finding true jets is shown in Figure 4.9. We find $> 95\%$ efficiency for

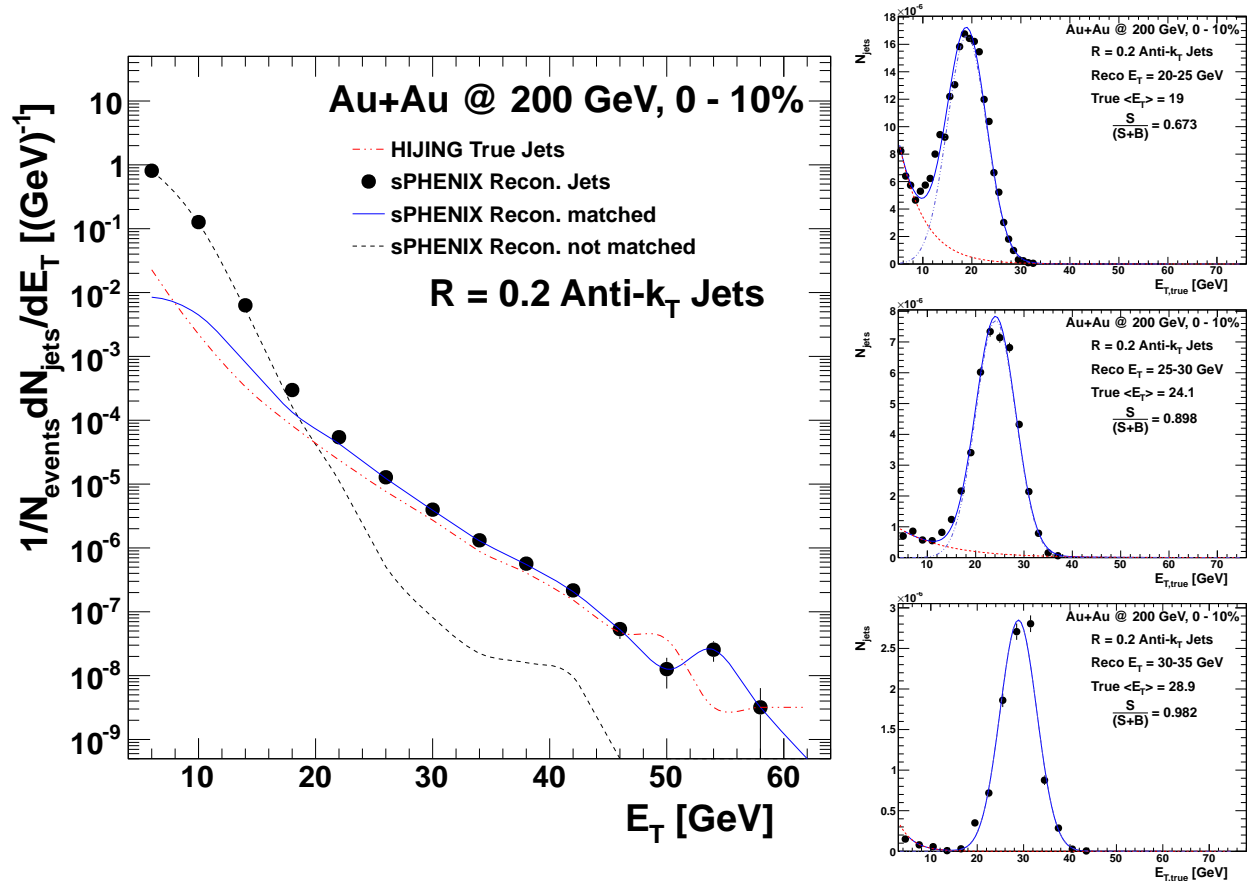


Figure 4.7: The composition of the jet spectrum in central 0–10% Au+Au based on 750M HIJING events. The full spectrum is shown in the left plot as solid points. The spectrum of those jets that are successfully matched to known real jets is shown as a blue curve. That curve compares very well with the spectrum of true jets taken directly from HIJING. The jets which are not matched with known jets are the fake jets, and the spectrum of those jets is shown as the dashed curve. For $R = 0.2$, real jets begin to dominate over fake jets above 20 GeV. The panels on the right are slices in true jet energy showing the distribution and make up of the reconstructed jet energy. At low E_{true} , fake jets can be seen encroaching on the low energy side of the distribution. For higher E_{true} the fake jets are negligible.

finding jets above 20 GeV reconstructed with $R = 0.2$ or 0.3 and above 25 GeV for jets reconstructed using $R = 0.4$.

Having found the jets in Au+Au with good efficiency and having established that the rate of fake jets coming as a result of background fluctuations are understood and under control, we also need to show that we can reconstruct the kinematics of jets accurately and precisely. This is quantified by the jet energy scale, the average shift of the jet energy between reconstructed and true jets and the jet energy resolution which shows the relative width of the difference between the true and reconstructed jet energies. Results from $R = 0.2$ and 0.4 are shown in Figure 4.10. For both jet radii the jets are reconstructed within

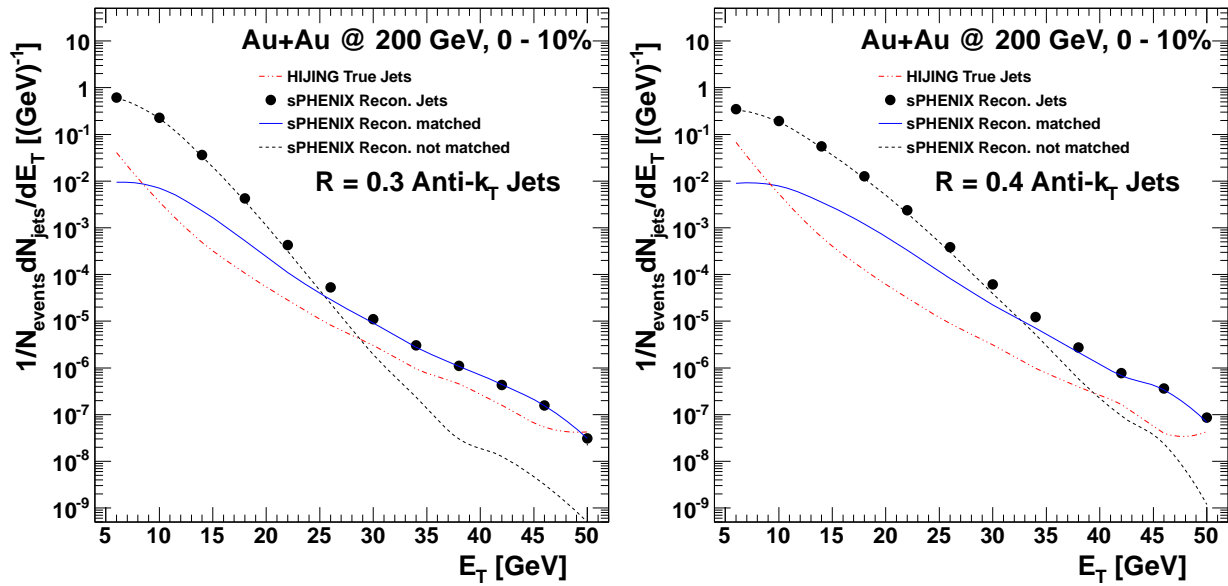


Figure 4.8: Composition of the jet spectra in central 0–10% Au+Au based on 750 million HIJING events for $R = 0.3$ (left) and $R = 0.4$ (right) jets.

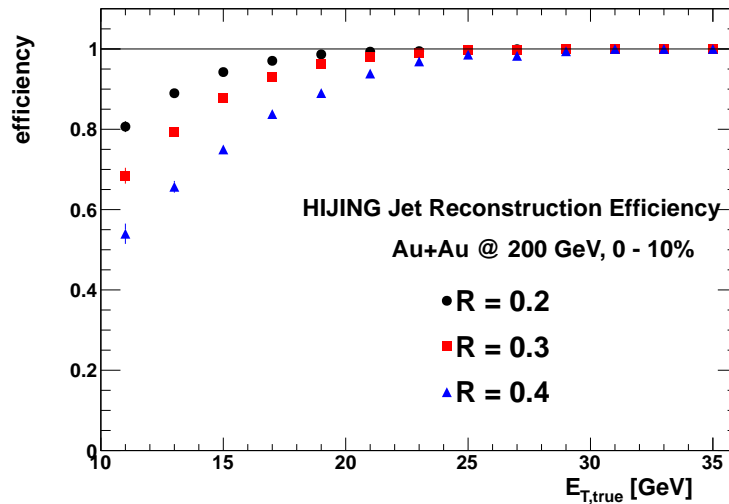


Figure 4.9: The efficiency for finding jets in central Au+Au collisions as a function of true jet energy and for $R = 0.2, 0.3$ and 0.4 .

4% of the true energy over the measured range. Note that this is just a first step energy scale determination. The jet energy resolution shown in the right panel only includes effects due to the detector segmentation applied and the underlying event resolution. In $p+p$ collisions the resolution for $R = 0.4$ jets is better than for $R = 0.2$ jets because the segmentation can cause jet splitting with the smaller jet cones. In Au+Au collisions the order is swapped because the dominant effect is the additional smearing due to the underlying event.

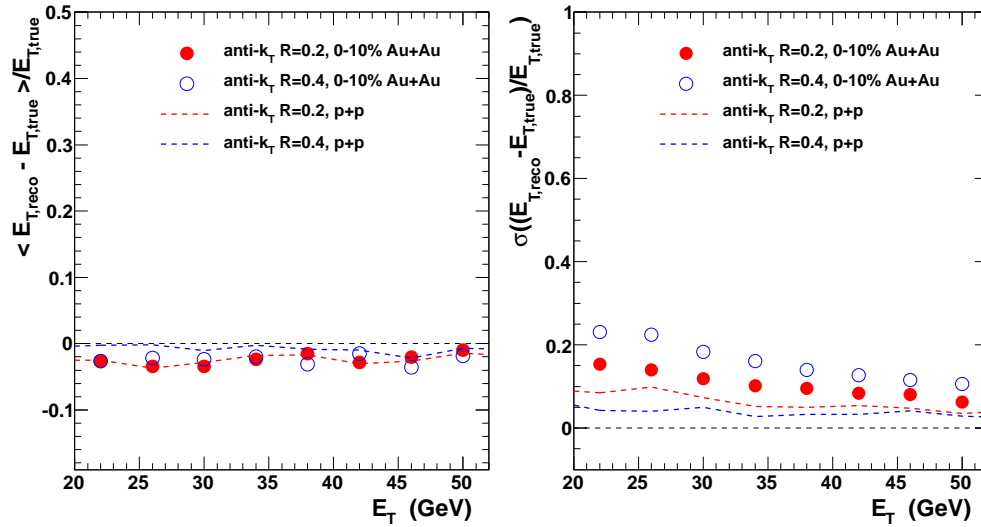


Figure 4.10: The energy scale of reconstructed jets in Au+Au collisions. The left plot shows the shift in the mean energy of the reconstructed jets compared to the true value. There is only a few percent shift in the energy and no apparent dependence on jet cone size. The right plot shows the jet energy resolution.

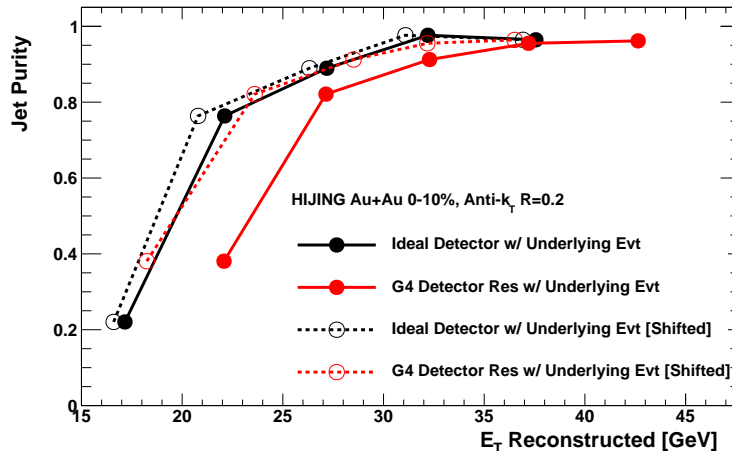


Figure 4.11: Results for the jet purity ($S/(S + B)$) in terms of matched true and fake jets in 0–10% Au+Au collisions from HIJING. The purity values are for an ideal detector (i.e. sPHENIX segmentation with perfect resolution) and then including the GEANT4 parametrized EMCal and HCal resolutions. Both results are then shifted down in E_T by the reconstructed energy bias.

The fast simulation results described above have been re-run with the inclusion of the detector resolutions as parametrized from the single particle GEANT4 results — detailed in Section 3.4. The results shown in Figures 4.7 and 4.8 remain quite similar with the detector resolution included, though with an overall shift of all the distributions to higher E_T due to the additional blurring on falling spectra. For $R = 0.2$ jets, the smearing due to detector resolution is comparable to the effect of the underlying event and for larger jet

cones the effect of the underlying event is found to be much larger than detector resolution effects. Figure 4.11 shows the jet purity for $R = 0.2$ jets as a function of reconstructed E_T . The solid black (red) points correspond to the cases without (with) detector resolution effects. Also shown as open points are both results shifted down in energy by the average reconstructed energy bias as determined from the reconstructed matched jet sample. One observes that the relative true and fake jet contributions are the same for the equivalent true jet energy ranges.

4.4.2 Inclusive Jet Yield in Au+Au Collisions

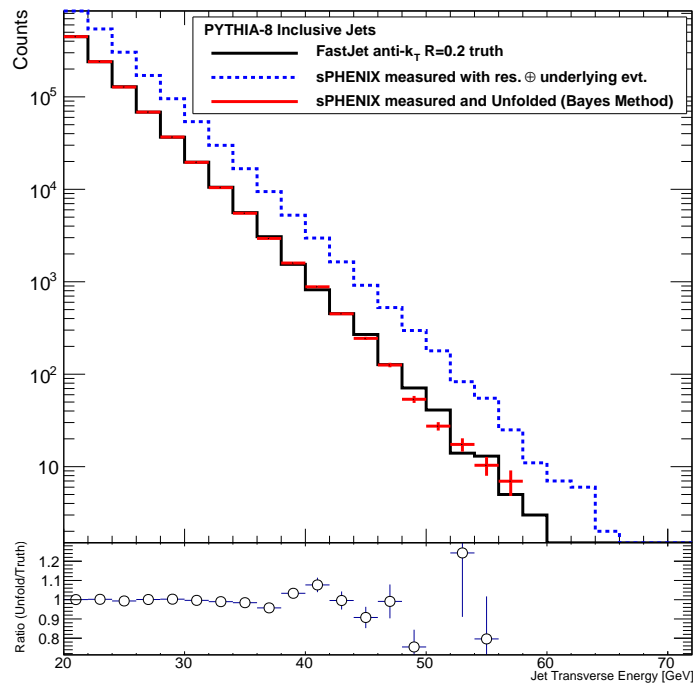


Figure 4.12: Effect of smearing the inclusive jet spectrum in Au+Au collisions. The jets found by FASTJET are smeared by the jet resolution contributions from the detector and the underlying event fluctuations. The unfolded spectrum from the Iterative Bayes method is shown and the ratio of the unfolded to the true p_T spectrum (lower panel).

The inclusive jet spectrum is the most important first measurement to assess the overall level of jet quenching in RHIC collisions. The results shown in Figure 4.12 were obtained by the very fast simulation approach described above. PYTHIA was used to generate events and the final state particles were sent to FASTJET in order to reconstruct jets. The resulting jet energy spectrum was smeared by the jet resolution determined for $p+p$ collisions from GEANT4, and an additional smearing by the underlying event fluctuations (determined from the full 0–10% central HIJING fast simulation). Finally, an unfolding procedure was used to recover the truth spectrum. The ratio shown at the bottom of the plot shows that the unfolding is very effective.

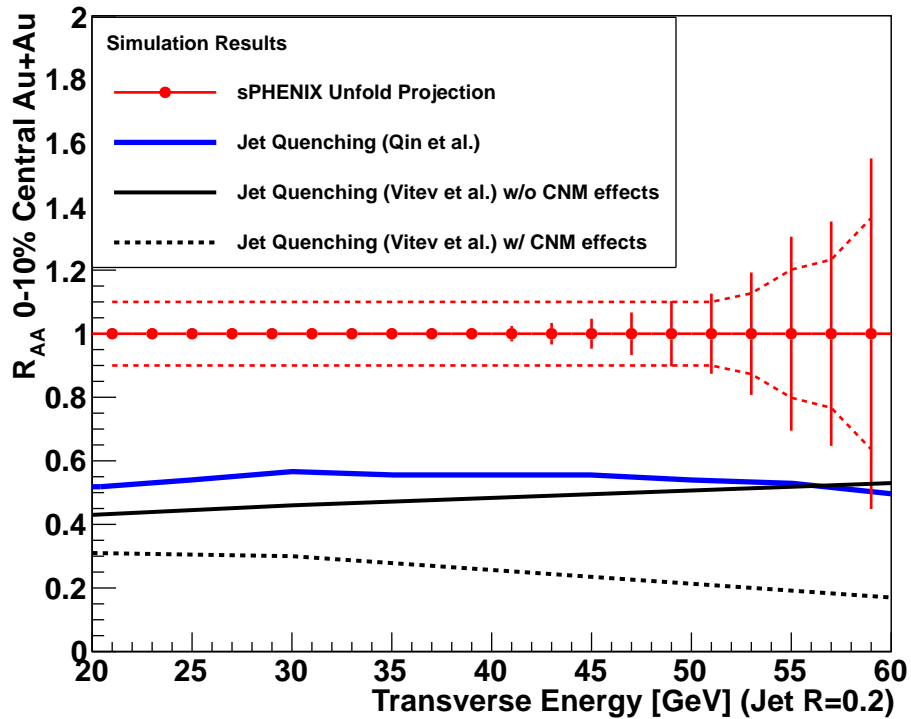


Figure 4.13: Single inclusive jet R_{AA} with $R = 0.2$ for Au+Au central events from the unfolding of the $p+p$ and Au+Au spectra with an estimated systematic uncertainty as a multiplicative factor of approximately $\pm 10\%$. Also shown are the predictions from a calculation including radiation and collisional energy loss and broadening [89] and another with and without cold nuclear matter effects [95, 96, 97] (as discussed in Section 1.6).

As an estimate of the uncertainties on a jet R_{AA} measurement from one year of RHIC running, the uncertainties from Figures 4.3 and 4.12 are propagated and shown in Figure 4.13. For $E_T < 50$ GeV the point to point uncertainties are very small. Also shown is an estimated systematic uncertainty including the effects from unfolding. All points are shown projected at $R_{AA} = 1$, and we show for comparison the predicted jet R_{AA} including radiative and collisional energy loss and broadening from Ref. [89].

4.4.3 Dijets in Au+Au collisions

Fake jets contaminate dijet observables much less than they do the inclusive jet measurement. In the case of inclusive jets, one is working with a sample of 10^{10} central Au+Au events in a typical RHIC year, so even if it is only a rare fluctuation in the background that will be reconstructed as a real jet, there is a huge sample of events in which to look for such fluctuations.

The case of dijet correlations is very different. There are 10^6 clean trigger jets above $E_T = 30$ GeV in central Au+Au collisions in a RHIC year – detailed in Figure 1.1. This means there is a factor of 10^4 fewer chances to find the rare background fluctuation that appears to be a true jet in the opposite hemisphere. Also, the presence of a high energy jet, for which the fake rate is known to be low, tags the presence of a hard process occurring in the event, and thus dramatically reduces the probability of a jet in the opposite hemisphere being a fake. Because of these considerations, one can go to much lower p_T for the away side partner of a dijet pair. Studies presented here include away side jets down to 5 GeV, and we have found that the fake jet rate remains small for the associated jets, even at these low jet energies.

In order to address the sensitivity to modifications of the A_J distributions that might be expected at RHIC here we compare PYTHIA simulations with those from PYQUEN [134] (a jet quenching parton shower model with parameters tuned to RHIC data). All the PYQUEN events generated are for central Au+Au events with $b = 2$ fm. Figure 4.14 shows the particle level (i.e truth) A_J distributions and how they are reconstructed after being embedded in a central Au+Au event with a parametrized detector smearing and segmentation applied. As described above, the full iterative underlying event subtraction method is applied. The simulated measured distributions (middle panel of Figure 4.14) show the effects of the smearing; and the distinction between the PYTHIA and PYQUEN distributions remain large. An unfolding procedure can be applied to these embedded distributions to regain the true distributions. However, as in the $p+p$ case discussed in Section 4.3.2 this should involve a full two-dimensional unfolding. Applying the same “unfolding” applied to the $p+p$ case where the smearing of the trigger jet is taken as the dominant effect recovers most of the original distribution, as shown in the lower panel of Figure 4.14. Again, this does not replace a full unfolding procedure, but it does show that the reconstruction is well under control and unfolding will be possible despite the presence of a large fluctuations in the underlying event, after baseline and flow subtraction.

4.4.4 γ +jets in Au+Au collisions

The rate for γ +jet events is lower than the rate for dijet events by approximately α_{EM}/α_s . In a 20 week RHIC run of Au+Au at $\sqrt{s_{NN}} = 200$ GeV, one would expect more than 2×10^4 direct photons above 20 GeV/c. As shown earlier in Figure 1.30, at $p_T = 20$ GeV the fraction of direct photons in the inclusive photon sample is large and γ -jet measurements will be possible without employing isolation cuts. The γ measurement is very clean as fake jets are not an issue for trigger photons. We show fast simulation results for high p_T γ triggers embedded in central Au+Au events.

In contrast to the dijet case studied above, the γ -jet measurements do not compare two similar objects with the same effects from the underlying event. The γ is always the trigger. In this case it makes sense to measure $x \equiv E_{\text{jet}}/E_\gamma$ rather than A_J . While in a leading order QCD picture the γ and the jet should exactly balance in energy, in reality this is not the

case, especially when higher-order diagrams are taken into account. For small jet sizes there is a significant probability that the away side parton shower is split into more than one jet by the reconstruction procedure, with each carrying a fraction of the energy needed to balance that of the γ . This can be seen in the PYTHIA truth curves in the top panels of Figure 4.15. The smeared and embedded results are shown in the middle panel. Again the smearing has a significant effect, but the distinction between the PYTHIA and PYQUEN results is retained.

In the γ -jet case, the unfolding is to a very good approximation one-dimensional. This is because the dominant smearing effect is on the jet energy since the γ is measured in the EMCal which has a very good energy resolution compared to the jet. We have applied a one dimensional Iterative Bayes unfolding procedure to the γ -jet x distributions for the $R = 0.3$ jets in the bottom panel of Figure 4.15. The unfolded results compare well with the particle level distributions for both PYTHIA and PYQUEN.

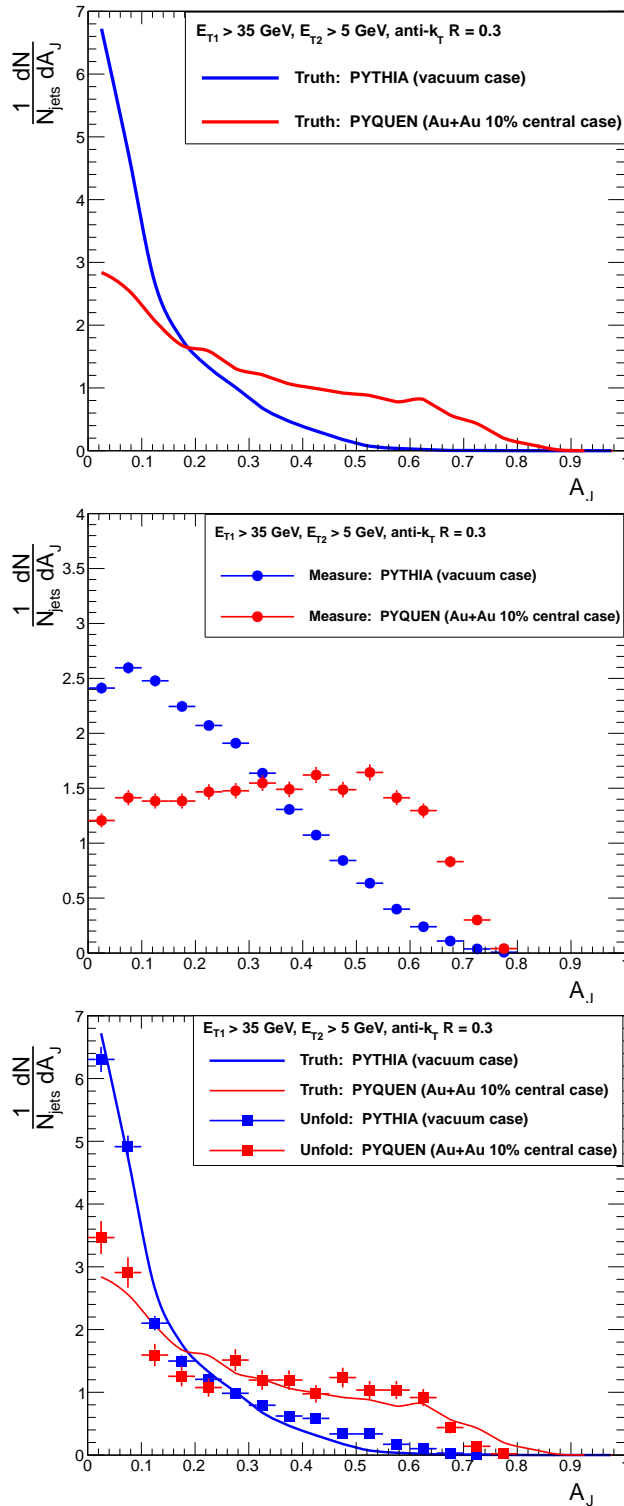


Figure 4.14: The effect of smearing on A_J for $R = 0.3$ jets. The upper panel shows the ratio expected in PYTHIA and PYQUEN, showing the effect of quenching. The middle panel shows the effect of smearing on the ratio determined from jets reconstructed after embedding in Au+Au events. Although smeared, the reconstructed data still show a distinct difference between the quenched and unquenched results. The bottom panel shows the results of the “unfolding” procedure discussed in Section 4.3.2.

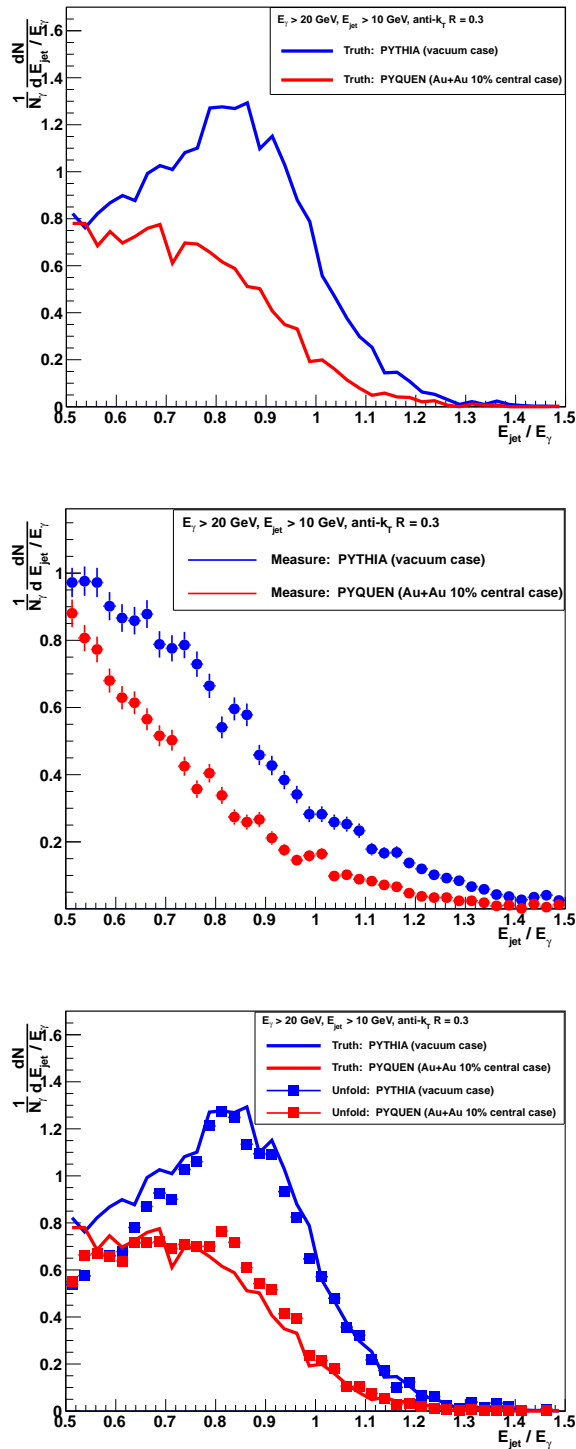


Figure 4.15: The effect of smearing on energy ratio E_{jet}/E_γ for $R = 0.3$ jets. The upper panel shows the ratio expected in PYTHIA and PYQUEN, showing the effect of quenching. The middle panel shows the effect of smearing on the ratio determined from jets reconstructed after embedding in Au+Au events. Although smeared, the reconstructed data still show a distinct difference between the quenched and unquenched results. Results of a one dimensional unfolding are compared with the truth particle level distributions in the bottom panel.

4.5 Jet surface emission engineering

Experiments have employed fake jet rejection cuts to substantially extend the high purity jet energy range accessible in central heavy ion collisions – for example see Refs. [10, 63]. We are able with the sPHENIX detector to utilize track + electromagnetic jets matched to fully calorimetric jets in a similar fashion. In addition to extending the measurable jet energy range to lower energies, for energies with high purity without any selection one can turn this method into a powerful tool to engineer the degree jet surface emission. For example, in the sample of 10^5 jets with $R = 0.4$ and $E_T > 40$ GeV, we can measure a high purity sample of reconstructed jets in central Au+Au collisions. We can then dial in the required track + electromagnetic cluster jet characteristics to achieve a particular surface bias - as proposed by Renk [85] and shown earlier in Figure 1.17.

We first examine track jets, which are determined by running the FASTJET algorithm on all charged particle tracks above a minimum p_T selection. These track jets are then subject to a minimum total E_T cut and matched to fully calorimetric jets within $\Delta R < 0.25$. The results are run on full HIJING events with the full background subtraction procedure detailed earlier. We have run a grid of single track p_T selections (1, 2, 3, 4 GeV) and track jet energy selections (5, 7, 9 GeV). The resulting jet efficiencies, with the additional track jet match requirement, are shown in the upper panel of Figure 4.16. Also shown in the lower panel are the calorimetric jet purities after the match requirement is applied. The dominant effect for increasing the jet purity is the minimum p_T selection on the tracks contributing to the track jet. With appropriate selections, one might extend the $R = 0.4$ measurable energy range from $E_T > 40$ GeV to $E_T > 20 - 25$ GeV. In addition, for 40 GeV jets, one can dial the entire range of cuts thus slowly eliminating the soft portion of the parton shower.

One can also incorporate electromagnetic clusters, which provide additional input to the alternate jet reconstruction. The electromagnetic clusters and tracks have the same minimum energy cut and are then input to the FASTJET algorithm. Figure 4.17 shows in the upper panel the jet purity for different jet radii $R = 0.2, 0.3, 0.4, 0.5$ with a nominal track + electromagnetic jet match requirement ($E_T > 7$ GeV for the match jet, $E_T > 3$ GeV for the electromagnetic cluster and charged track). The results are very good and indicate that even $R = 0.5$ jets can be reconstructed in the most central Au+Au events. Figure 4.17 shows in the lower panel the results for $R = 0.4$ for various Au+Au centralities. The results demonstrate the dramatically increased range for jet reconstruction in mid-central Au+Au collisions, where significant jet quenching effects have already been measured including the theoretically challenging high p_T hadron azimuthal anisotropy.

4.6 Jet physics at lower RHIC energies

If additional running time becomes available and if physics investigations indicate interest in this direction, there is the potential for extending sPHENIX jet measurements to lower

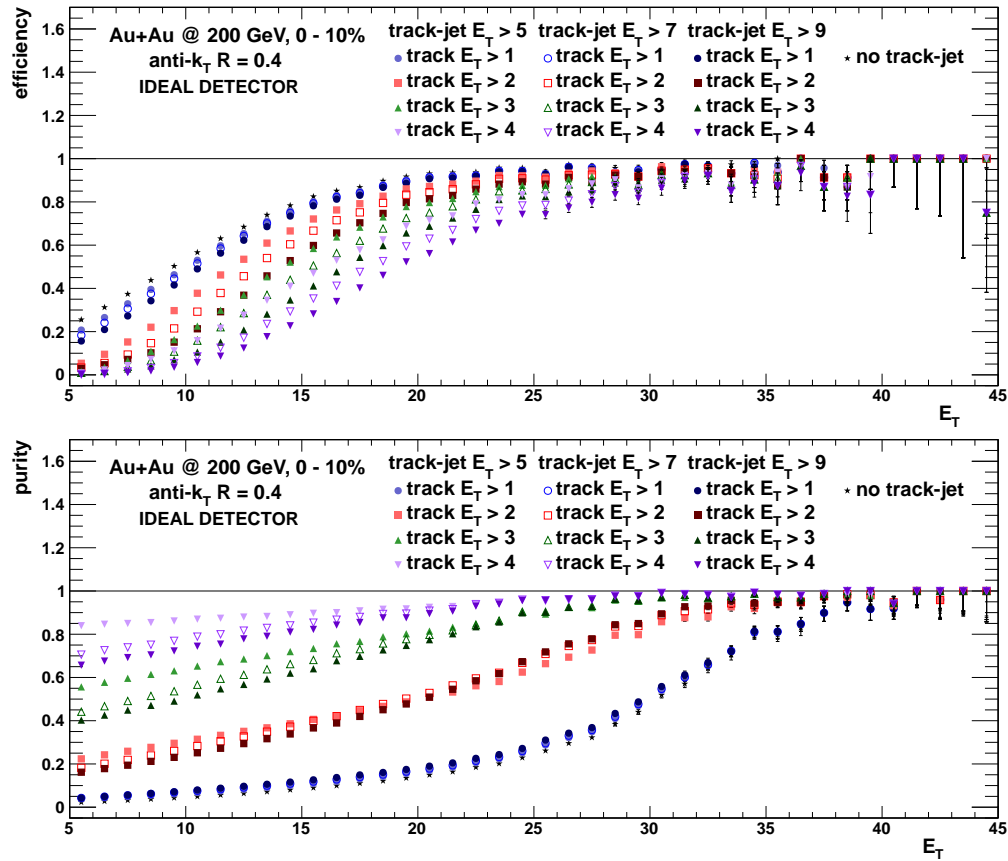


Figure 4.16: Shown are results for $R = 0.4$ anti- k_T fully calorimetric jets reconstructed in 0-10% central Au+Au HIJING events. The upper panel shows the efficiency when requiring a match within $\Delta R < 0.25$ of a track jet with the minimum track energy and minimum track jet energy as shown. The lower panels shows the improvement in jet purity for different requirements on the match track jet. For comparison the results with no track jet matching requirement are shown as stars.

energies at RHIC. In a 20 week running period, one can sample 10 billions Au+Au events at $\sqrt{s_{NN}} = 100$ GeV. Although the background multiplicity in these events is lower than in corresponding collisions at $\sqrt{s_{NN}} = 200$ GeV, the true jet spectrum at the lower collision energy is steeper. We have performed simulations to demonstrate that we can reconstruct jets in this environment.

A procedure identical to that used for evaluating the jet finding performance at the top RHIC energy was followed to evaluate the jet finding performance for Au+Au collisions at $\sqrt{s_{NN}} = 100$ GeV. A sample of 400 million HIJING events at the lower collision energy was generated and the procedure of Section 4.4.1 was employed. The results are shown in Figure 4.18. The effects of the steeper jet spectrum and of the reduced multiplicity at the lower collision energy largely negate one another, and the true jet signal dominates over the background at transverse energies quite similar to that seen for $\sqrt{s_{NN}} = 200$ GeV.

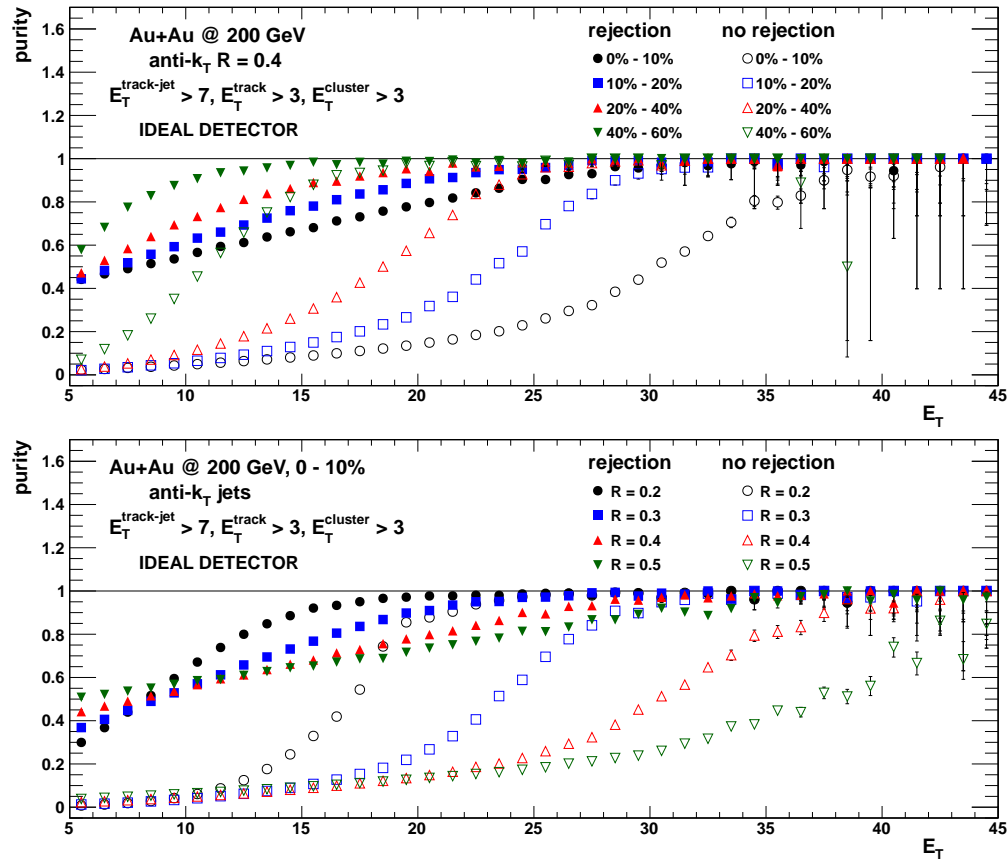


Figure 4.17: (Upper) Shown are purity results for $R = 0.2, 0.3, 0.4, 0.5$ anti- k_T calorimetric reconstructed jets in 0-10% central Au+Au HIJING events. The open points are without any track + electromagnetic cluster jet match requirement and the closed points are with the match requirement. (Lower) Shown are purity results for $R = 0.4$ anti- k_T calorimetric jets with and without track + electromagnetic cluster jet match requirements for different Au+Au event centralities. The purities are significant higher for mid-central collision geometries.

4.7 Fragmentation Function and Medium Response Observables

One of the most important classes of observables is to measure the re-distribution of energy within the parton shower directly. This re-distribution takes place both along the parton direction, i.e. fragmentation function modification, and transverse to the parton direction, i.e. relative azimuthal correlations. The sPHENIX capabilities and statistics allow for the eventual measurement of the two-dimensional distribution of energy to be measured and compared between $p+p$, $p(d)+Au$, and Au+Au. Again, this highlights the necessity of fully calorimetric jet measurements and direct photons coupled with excellent charge track capabilities.

Figure 4.19 shows the results of a fast simulation of the sPHENIX measurement capabilities

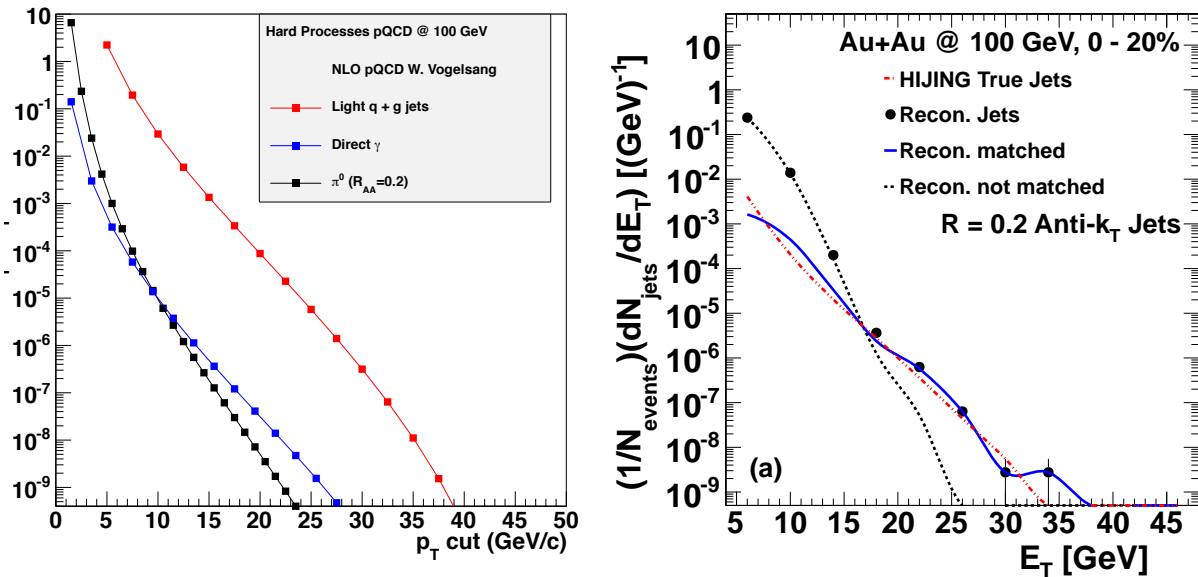


Figure 4.18: (left) Jet, photon and π^0 rates with $|\eta| < 1.0$ from NLO pQCD [103]. A nominal 20 week RHIC run corresponds to 1.7 billion central Au+Au events at $\sqrt{s_{NN}} = 100$ GeV. (right) Results of a fake jet study at $\sqrt{s_{NN}} = 100$ GeV for the most central 20% of the cross section. The anti- k_T algorithm with $R = 0.2$ was used to reconstruct jets. True jets dominate over fake jets for $E_T > 20$ GeV.

for the fragmentation function for jets with energy greater than 40 GeV. Shown is the expected unmodified fragmentation function truth parameterized from PYTHIA and then the projected measurement implementing the energy response for jets with the calorimetry and the charge tracking resolution from the independent silicon detector. Resolution and underlying event effects on the jet measurement cause a net shift in the measured energy to higher values as detailed earlier. Similar resolution effects on the track momentum can cause a net shift towards higher momentum. However, the tracking resolution is very good up to high momentum and thus this effect is quite small and subdominant. The measured fragmentation function is thus shifted down in z and the unfold correction shown in the figure works very well to recover the original truth distribution. The statistics shown in the figure correspond to the projected event sample for jets measured above 40 GeV in 20-weeks of Au+Au running in central events. A comparable statistical sample will also be measured in $p+p$ and $p(d)+Au$ at the same energy.

sPHENIX will also have excellent γ -h fragmentation function measurements. Given the potential loss of energy from the jet cone, it is critical to compare these two measurements and confront them with full Monte Carlo parton shower calculations. The γ is measured with much better resolution and thus the shifting downward in z is much less pronounced and thus the unfold is simplified. The statistics for direct photons with energy above 20 GeV will be approximately an order of magnitude smaller than in the above Figure, which still provides coverage over the full z range with good statistics and slightly coarser binning.

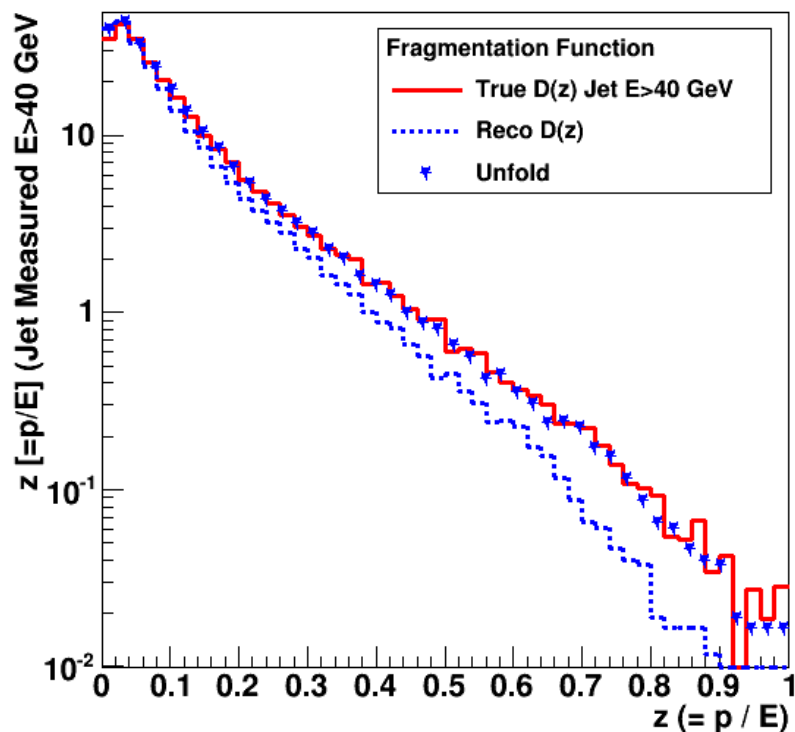


Figure 4.19: The truth distribution of unmodified fragmentation functions for reconstructed jets with energy greater than 40 GeV. Also shown are the sPHENIX projected measurement in 20-weeks of Au+Au data taking at 200 GeV. Finally the unfolded distribution is shown that recovers the original truth distribution.

As an example of measuring the transverse re-distribution of energy, sPHENIX will be able to track charged particles and correlate them in relative angle to the jet axis or direct photon direction. This is particularly appealing as a complement to the dijet measurements. At sufficiently low energy, the background of fake jets for the away-side jet in a dijet analysis becomes problematic. At that same low p_T , one can turn to the excellent tracking capabilities to extend the measurement.

One can use γ +hadron correlations to study the redistribution of energy lost by the opposite going parton, and results from CMS [71] and STAR [63] on jet+hadron correlations indicate that, this energy is spread over a wide angular range. Measurements at RHIC of γ +hadron correlations have not had the statistical precision or the acceptance necessary to make comparable statements about the modification to jet fragmentation. In order to recover the energy using the standard jet reconstruction, one would have to use an extremely wide jet cone, and in a heavy-ion collision this presents a problem, as it exposes the away side jet finder to a very large contamination of energy coming from the underlying event. Precisely because of this difficulty, one could instead use correlations between a trigger γ and an away side hadron.

Figure 4.20 shows γ +hadron correlations for photons with $E_T > 20$ GeV from PYTHIA and PYQUEN in the hadron p_T range of 0.5–4.0 GeV/c. The PYQUEN distributions are broader and have a larger yield at lower p_T , and would be easily measured by sPHENIX.

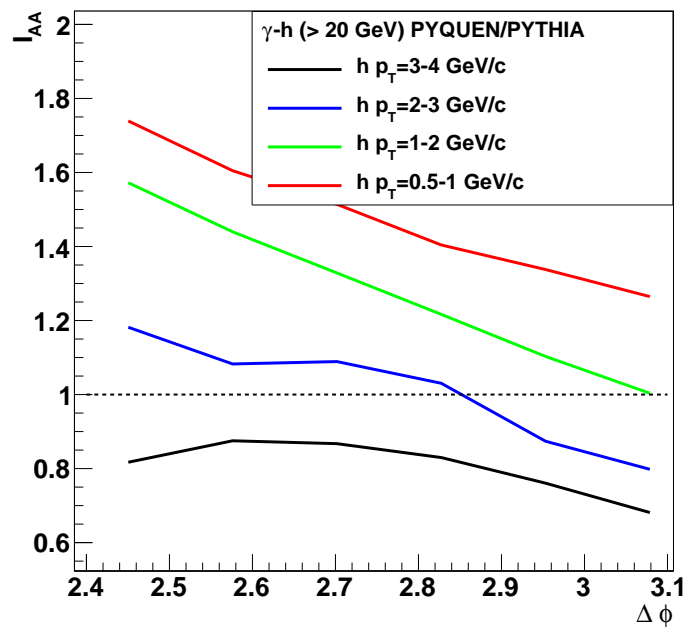
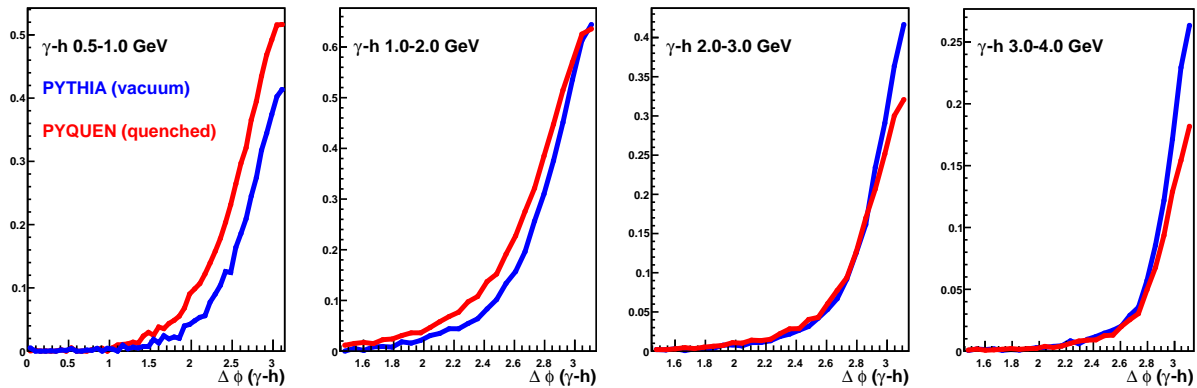


Figure 4.20: A simulation of the γ +hadron angular correlation for PYTHIA and for PYQUEN events for hadron p_T ranges shown in the Figure. These p_T s would be accessible with the current PHENIX silicon tracker. The lower panel shows the nuclear modification I_{AA} between Au+Au central with PYQUEN and $p+p$ with PYTHIA as a function of hadron p_T and $\Delta\phi$.

4.8 Heavy Quark Jets

Heavy quarks traversing the quark-gluon plasma are an excellent test of our understanding of the mechanism for energy loss. Due to the finite velocity in medium there is an expected suppression of radiative energy loss in the forward direction. sPHENIX maintains the inner two pixel ladders and one strip-pixel layer currently in use in PHENIX. Shown in Figure 4.21 is the distance of closest approach performance for the current silicon barrel detector. sPHENIX has the same DCA resolution specification and the pattern recognition is augmented by additional silicon strip tracking layers.

The rates for heavy quark jets shown in Figure 1.27 indicate a substantial number of accepted jets for sPHENIX in the large data samples achievable. With a jet tagged efficiency for beauty jets of order 1%, one would have thousands of beauty jets for energy above 20 GeV and hundreds of thousands above 10 GeV. The tagging of heavy flavor dramatically reduces the “fake” jet background and may allow one to push below the 20 GeV energy range even in central Au+Au events. Detailed GEANT4 studies are at an early stage and require detailed studies to document the full capabilities.

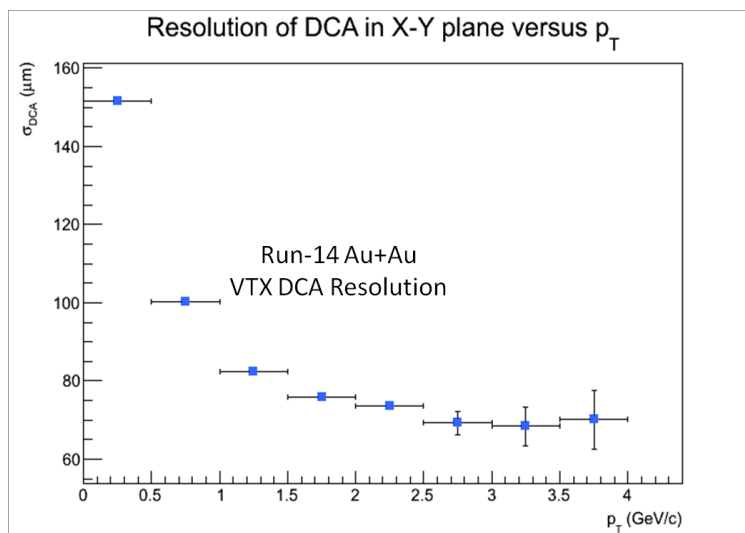


Figure 4.21: Performance of the PHENIX Silicon Vertex Tracker (VTX) in the 2014 Au+Au at 200 GeV run. Note that the ladder-to-ladder adjustments are not finalized and the distance of closest approach (DCA) resolution already significantly exceeds the 100 μm specification.

4.9 Jet Physics Summary

Overall we conclude that a robust jet, dijet, γ -jet, fragmentation function program with high statistics is achievable with the sPHENIX detector upgrade. These observables indicate excellent discriminating ability between scenarios with different medium coupling strengths and jet quenching mechanisms.

4.10 Beauty Quarkonia Performance

Measurements of beauty quarkonia, the Upsilon states, provide critical information by probing the quark-gluon plasma at different length scales determined by the size of the state. Here we detail the sPHENIX measurement capabilities to access this physics with precision.

We first report on the expected yield and line shape of the $Y(1S)$, $Y(2S)$ and $Y(3S)$ signal from decays to dielectrons. The results were obtained with single simulated Y events in a GEANT4 simulation with the reference sPHENIX silicon tracking configuration inside the BaBar solenoid. The sPHENIX acceptance times tracking efficiency for $Y(1S + 2S + 3S) \rightarrow e^+e^-$ decays was found to be 0.34, in the mass window 7–11 GeV/ c^2 .

The baseline $p+p$ cross section for $Y(1S + 2S + 3S)$ of $B_{ee}d\sigma/dy|_{y=0} = 108 \pm 38 \pm 15 \pm 11$ pb is taken from a PHENIX central arm measurement [140]. The rapidity dependence was taken from PYTHIA. The relative yields of the three Y states were taken from CDF measurements at 1.8 TeV [141]. Estimates of the $p+p$ yields in sPHENIX are shown in Table 4.1, along with projected yields of the three Y states for a 20-week long Au+Au run. These projections assume binary scaling and no suppression of any of the Y states.

Species	$\int L dt$	Events	$\langle N_{coll} \rangle$	Y(1S)	Y(2S)	Y(3S)	Y(1S+2S+3S)
$p+p$	18 pb^{-1}	756 B	1	805	202	106	1113
Au+Au (MB)		50 B	240.4	12794	3217	1687	17698
Au+Au (0–20%)		10 B	783.2	8336	2096	1099	11530

Table 4.1: The yield of different Y states obtained in 10 weeks of $p+p$ or 20 weeks Au+Au RHIC running. The numbers for Au+Au in this table are calculated assuming no suppression of any of the Y state yields.

A critical question is whether the proposed tracking system is capable of adequately resolving the $Y(1S)$ from the $Y(2S)$ and $Y(3S)$ states. The reconstructed mass spectrum for dielectron decays is shown in Figure 4.22, including a fit using a Crystal Ball function that accounts for the radiative tail contribution at low invariant mass. This example spectrum contains the number of Upsilon expected in the 0–20% centrality bin if there is no suppression. It can be seen that there are significant low mass tails on the Upsilon mass peaks due to radiative energy loss in the material of the silicon tracker. The radiative tails can be further suppressed with tight track quality cuts, thus eliminating tracks with large kinks, at the expense of some loss in efficiency.

These GEANT4 simulations are performed with the reference configuration with six silicon tracking layers covering 2π in azimuth and two units in pseudorapidity, with specifications

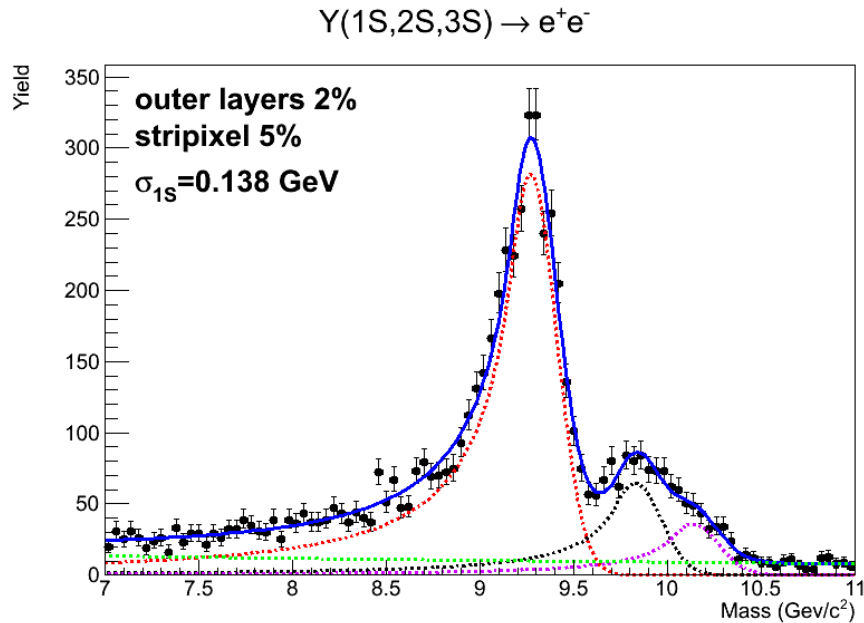


Figure 4.22: The mass spectrum from reconstructed electron decay tracks for the three Upsilon states combined. The yield corresponds to that for the 0–20% centrality bin from 50 billion minimum bias events, assuming no suppression in Au+Au collisions.

given in Table 3.2. We are currently optimizing the performance of the tracking with relevant parameters including the exact outer radial locations for the outer three silicon strip layers, the achievable thicknesses, and the overall project cost.

In both $p+p$ and Au+Au, the background under the Upsilon peaks consists of an irreducible physics background due to dileptons from correlated charm, correlated bottom and Drell-Yan. There is also combinatorial background from misidentified charged pions. The latter can be estimated and removed by like sign or mixed event subtraction. To study the physics background, correlated charm and bottom di-electron invariant mass distributions predicted by PYTHIA were normalized to the PHENIX measured charm and bottom cross-sections in Au+Au collisions. The PYTHIA Drell-Yan di-electron invariant mass distribution was normalized to the theoretical prediction by Vogelsang.

The combinatorial background was studied by generating events with fake electrons due to misidentified pions, using input pion distributions taken from PHENIX measured π^0 spectra in Au+Au collisions. A p_T -independent rejection factor was applied to the $\pi^{+/-}$ spectra to imitate fake electron spectra. For the 0–20% most central Au+Au collisions a rejection factor of 90 is assumed at a single electron track efficiency of 70% (giving a pair efficiency of 49%). The pair efficiency is increased to 95% as Au+Au collisions become more peripheral. The combinatorial background due to misidentified pions is assumed here to be zero in $p+p$ collisions, with an electron matching efficiency of greater than 95%. These rejections are derived from GEANT4 studies of the electromagnetic calorimeter

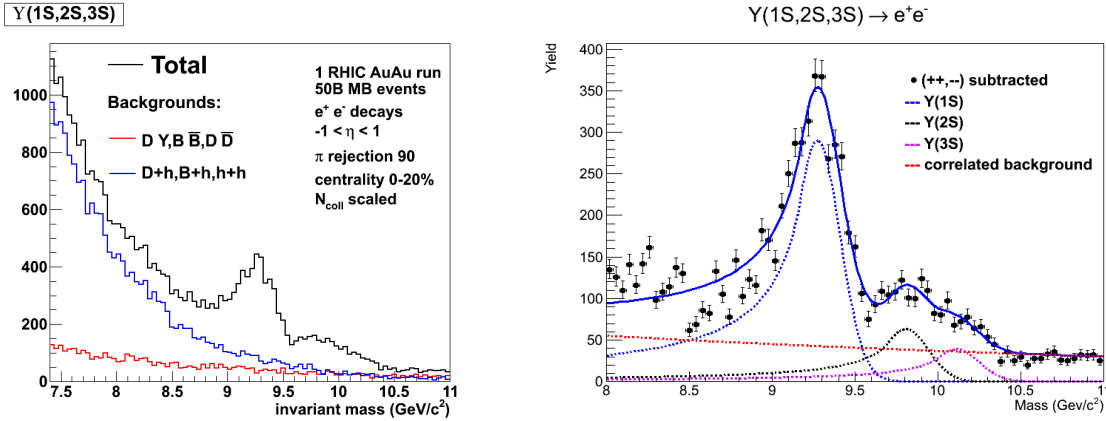


Figure 4.23: (Left) The signal plus background in the Upsilon mass region for ten billion 0–20% central Au+Au events, assuming a pion rejection factor of 90, with the signal reduced by a pair identification efficiency of 49%. The combined backgrounds due to correlated bottom, correlated charm, and Drell-Yan are shown as the red curve. The combined backgrounds due to fake electrons combining with themselves, bottom, and charm are shown as the blue line. (Right) The expected invariant mass distribution for ten billion 0–20% central Au+Au events, after subtraction of combinatorial background using the like-sign method. The remaining background from correlated bottom, charm and Drell-Yan is not removed by like sign subtraction. It must be estimated and subtracted.

response to electrons and charged pions. The efficiencies are obtained by embedding electrons in HIJING events. The rejection and efficiency are still being optimized for the detector configuration relevant for electron identification.

All combinations of fake electrons from misidentified pions were made with each other, and with high p_T electrons from physics sources. The combinatorial background is found to be dominated by the combinatorics of misidentified pions, with only 30% or so coming from combinations of misidentified pions with electrons. The results are summarized in Figure 4.23 (left), which shows the signal + background in the Y mass region for the ten billion 0–20% most central events, along with our estimates of the total correlated physics background and the total uncorrelated combinatoric backgrounds. In Figure 4.23 (right) we show the di-electron invariant mass distribution for ten billion 0–20% central Au+Au events after the combinatorial background has been removed by subtracting all like-sign pairs.

From Figure 4.23 (left) we estimate that without Y suppression the S/B ratios are Y(1S): 1.0, Y(2S): 0.6, and Y(3S): 0.5 for central Au+Au collisions. Using our estimates of the S/B ratio at each centrality as the unsuppressed baseline, we show in Figure 4.24 the expected statistical precision of the measured R_{AA} for 50 billion recorded Au+Au events assuming that the suppression for each state is equal to that from a recent theory calculation [142]. For each state, at each value of N_{part} , both the Y yield and the S/B ratio were reduced together by the predicted suppression level.

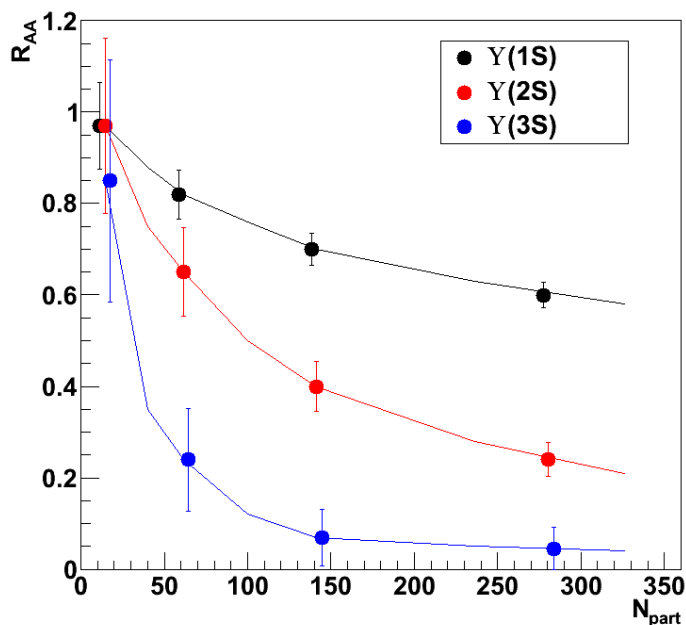


Figure 4.24: Estimate of the statistical precision of a measurement of the Y states using sPHENIX, assuming that the measured R_{AA} is equal to the results of a recent theory calculation [142]. The yields assume 50 billion recorded Au+Au events.

We conclude from these results that the proposed upgrade to the sPHENIX detector would provide an excellent Y measurement, and would have the required mass resolution and S/B to separate the Y(1S) state from the Y(2S) and Y(3S) states. Further, we expect that by fitting a line shape—which could be determined very well from the Y(1S) peak—we could extract the Y(2S) and Y(3S) yields separately with precision.

The expected higher statistics from the LHC experimental measurements of Upsilon over the next decade underscore the need for measurements at RHIC with sufficient statistics to differentiate cold and hot nuclear matters effects. In particular the almost order of magnitude larger acceptance for sPHENIX compared with the STAR MTD enables the precision required in $p+p$ and $p+A$ to test models for the onset of suppression, where CMS already observes differential suppression of the three states.

Appendix A

Evolution to an EIC Detector

The Nuclear Physics QCD community long term plan centers on the realization of an Electron Ion Collider (EIC). Brookhaven National Laboratory is working towards a specific realization of an EIC with a potential turn-on date of 2025 with an electron beam energy up to 21.2 GeV, hadron beam energies up to 255 GeV for protons and 100 GeV/nucleon for gold ions, and design luminosities of $10^{33} \text{ cm}^{-2}\text{s}^{-1}$ for 15.0 GeV on 255 GeV $e+p$ collisions. The EIC detector proposed here, built on the foundation of sPHENIX, will have excellent performance for a broad range of exciting EIC physics measurements, providing powerful investigations not currently available that will dramatically advance our understanding of how quantum chromodynamics binds the proton and forms nuclear matter.

From the beginning, it was realized that the sPHENIX detector design, with its large bore superconducting solenoid, midrapidity calorimetry, open geometry, coupled with the existing investment in infrastructure in the PHENIX interaction region, provides an excellent foundation for an EIC detector. With this in mind, EIC design considerations for the sPHENIX proposal have been incorporated from the start [143].

A full engineering rendering of the proposed detector — showing how it builds upon sPHENIX — is shown in Figure A.1. In addition to fully utilizing the sPHENIX superconducting solenoid and barrel calorimetry, new detectors are added in the barrel and electron-going and hadron-going directions. In the electron-going direction a crystal calorimeter is added for electron identification and precision resolution. A compact time projection chamber, augmented by additional forward and backward angle GEM detectors, provides full tracking coverage. In the hadron-going direction, behind the tracking is electromagnetic and hadronic calorimetry. Critical particle identification capabilities are incorporated via a barrel DIRC, and in the hadron-going direction, a gas RICH and an aerogel RICH.

The physics case for an EIC is documented in depth in the EIC White Paper [144]. An EIC will enable major scientific advances in at least three main areas: 1) Detailed imaging of the spin and momentum structure of the nucleon; 2) Investigation of the onset of gluon saturation in heavy nuclei; and 3) Study of hadronization in cold nuclear matter. In this

document we review each area with a focus on the connection to detector acceptance and performance requirements. We consider each subsystem in sufficient detail to be able to map out the performance using both parametrized and full GEANT4 simulations. We find a broad suite of observables where this EIC detector realization has excellent capabilities.

The EIC detector built around the BaBar magnet and sPHENIX calorimetry capably addresses most all of the physics enabled at this EIC machine. We believe we have struck a strong balance between capabilities and costs for this proposed detector, but there remain clear targets for augmenting those capabilities—for instance, by adding a silicon vertex detector to enable measurements of open charm observables (e.g., F_2^c). In addition, there is a possibility to upgrade eRHIC to even higher energy electron beams at a future date, and we believe EIC detector built around the BaBar magnet and sPHENIX calorimetry provides an excellent base upon which an upgraded detector capable of exploiting the physics potential of those collisions could be built. There is also the potential, if one can realize appropriate instrumentation in the hadron-going direction while $p+p$ and $p+A$ collisions are still available in RHIC, to pursue a rich program of forward physics measurements.

The PHENIX collaboration itself has outstanding detector expertise and technical support as a base for the construction of an EIC detector. Nonetheless, we view EIC detector built around the BaBar magnet and sPHENIX calorimetry being by constructed and operated by a fundamentally new collaboration that would require and welcome the addition of new institutions bringing with them additional detector expertise, physics insights, and scientific leadership.

The PHENIX collaboration was asked to produce a document detailing the capabilities of an EIC detector utilizing electron beams of 5-10 GeV. That document, as submitted in October 2013, is included as the remainder of this Appendix. We note that now higher initial electron beam energies are envisioned and the detector concept is readily being adapted to take full advantage of this additional physics potential.

This Appendix is organized as follows. Section A.1 illustrates the wide spectrum of EIC physics that can be addressed. Section A.4 describes the detector requirements that follow from that physics and which drive this EIC detector design. Section A.5 details the EIC detector concept and shows its performance for key measurements.

A.1 Physics at an Electron-Ion Collider

The 2007 Nuclear Physics Long Range Plan [145] states that the Electron-Ion Collider (EIC) embodies “the vision for reaching the next QCD frontier.” In this Chapter we review the primary physics goals as detailed in the EIC White Paper [144] and the broad physics program that can be carried out with the ePHENIX detector.

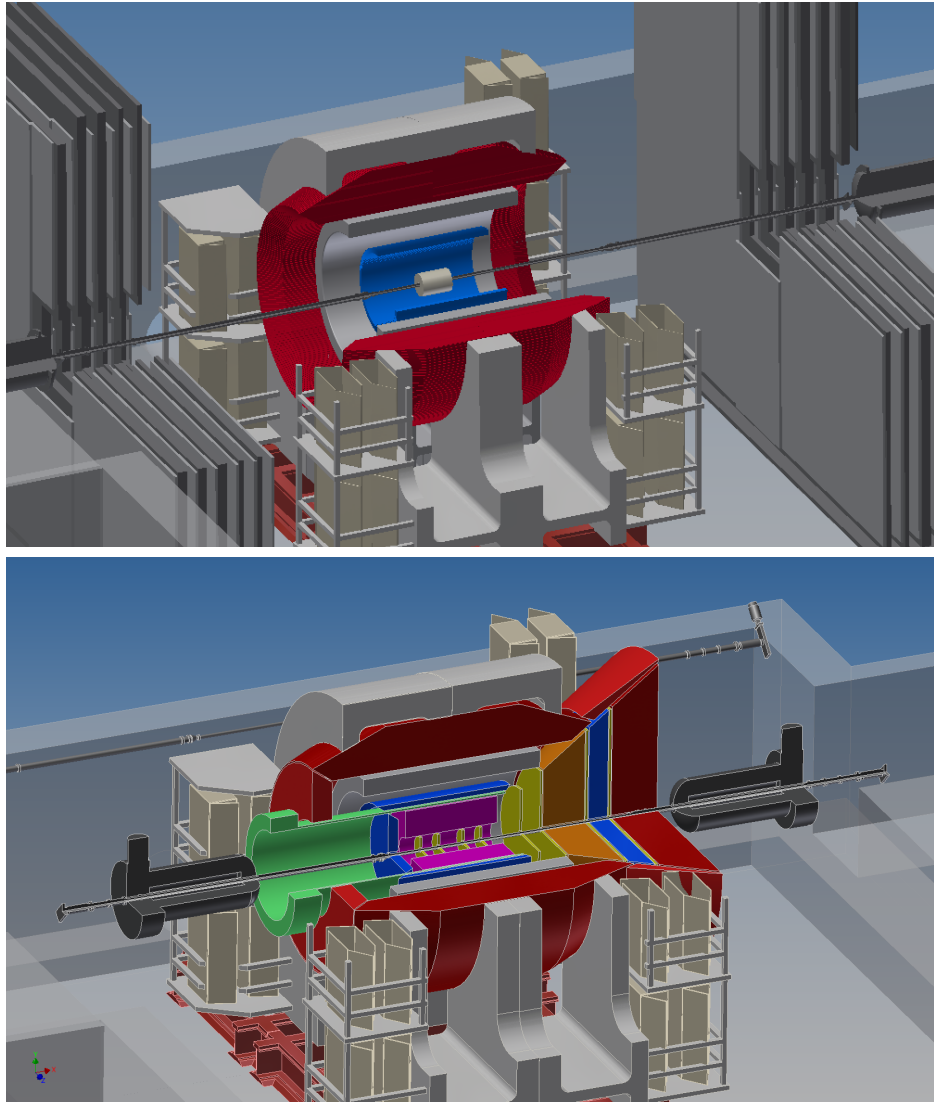


Figure A.1: The evolution of the sPHENIX detector, with its focus on jets and hard probes in heavy-ion collisions, into ePHENIX, with additional capabilities supporting its focus on $e+p$ and $e+A$ collisions. (top) The sPHENIX detector in the existing PHENIX experimental hall. (bottom) The EIC detector, in the same hall, showing the reuse of the superconducting solenoid and the electromagnetic and hadronic calorimeter system. The eRHIC focusing quadrupoles, each located 4.5 m from the interaction point, and the height of the beam pipe above the concrete floor, set the dominant physical constraints on the allowable dimensions of the EIC detector.

A.1.1 Fundamental questions addressed by the EIC

The EIC is designed to address several important question that are described in detail in the recent EIC White Paper [144]. Quoting from the White Paper, these questions are reproduced here:

- **How are the sea quarks and gluons, and their spins, distributed in space and momentum inside the nucleon?** How are these quark and gluon distributions correlated with overall nucleon properties, such as spin direction? What is the role of the orbital motion of sea quarks and gluons in building the nucleon spin?
- **Where does the saturation of gluon densities set in?** Is there a simple boundary that separates this region from that of more dilute quark-gluon matter? If so, how do the distributions of quarks and gluons change as one crosses the boundary? Does this saturation produce matter of universal properties in the nucleon and all nuclei viewed at nearly the speed of light?
- **How does the nuclear environment affect the distribution of quarks and gluons and their interactions in nuclei?** How does the transverse spatial distribution of gluons compare to that in the nucleon? How does nuclear matter respond to a fast moving color charge passing through it? What drives the time scale for color neutralization and eventual hadronization?

The White Paper describes in detail the “golden” measurements in inclusive Deep Inelastic Scattering (DIS), Semi-Inclusive DIS (SIDIS), and exclusive scattering at a future $e+p$ and $e+A$ collider which will address the above questions employing a perfect detector.

A.2 eRHIC: realizing the Electron-Ion Collider

The accelerator requirements for an EIC that can answer the questions listed above are spelled out in the EIC White Paper [144]. Two possible designs are presented based on current facilities: (1) the eRHIC design, which adds a Energy Recovery LINAC to the existing RHIC complex at Brookhaven National Laboratory (BNL) which can accelerate polarized protons up to 250 GeV and ions such as gold up to 100 GeV/nucleon, and (2) the EElectron-Ion Collider (ELIC) design, which uses the 12 GeV Upgrade of CEBAF at Jefferson Laboratory with a new electron and ion collider complex.

As per the charge from the Brookhaven National Laboratory Associate Lab Director, we consider the following eRHIC design parameters:

- A polarized electron beam with energy up to 10 GeV and polarization of 70%,
- A polarized proton beam with energy up to 250 GeV and polarization of 70%,

- An ion beam which can run a range of nuclei from deuteron to gold and uranium with energy up to 100 GeV/nucleon for gold,
- Luminosity with a 10 GeV electron beam of $10^{33} \text{ cm}^{-2}\text{s}^{-1}$ for $e+p$ with 250 GeV proton beam energy, and $6 \times 10^{32} \text{ cm}^{-2}\text{s}^{-1}$ for $e+A$ with 100 GeV ion beams.

A.3 Physics Deliverables

The three fundamental and compelling questions in QCD to be addressed by the EIC discussed in Section A.1.1 can be broken down into five golden measurements suggested in the EIC White Paper [144].

The first three relate to using the proton as a laboratory for fundamental QCD studies.

- **The longitudinal spin of the proton:** With the good resolution calorimetry and tracking in ePHENIX, Inclusive DIS measurements in polarized $e+p$ collisions will decisively determine the gluon and quark spin contributions to the proton spin. Further, planned particle identification capabilities will allow ePHENIX to pin down the spin contributions from the different quark flavors.
- **Transverse motion of quarks and gluons in the proton:** With the excellent particle identification capabilities of ePHENIX and the high luminosity of eRHIC, unparalleled SIDIS measurements will be possible, and enable us to explore and understand how the intrinsic motion of partons in the nucleon is correlated with the nucleon or parton spin.
- **Tomographic imaging of the proton:** The large acceptance of ePHENIX for tracking and calorimetry, far forward proton and neutron detector capabilities, the high luminosity of eRHIC and the phase space accessible in a collider geometry enables ePHENIX to significantly extend the kinematic coverage of exclusive measurements such as Deeply Virtual Compton Scattering (DVCS). With these, detailed images of how (sea) quarks and gluons are distributed in the proton will become possible for the first time.

The following two relate to extending these techniques to the heaviest stable nuclei.

- **Hadronization and its modification in nuclear matter:** With ePHENIX PID and the versatility of eRHIC to collide many different ions, measurements of identified hadrons in $e+p$ and $e+A$ will allow precise study of how quarks hadronize in vacuum and in nuclear matter.
- **QCD matter at extreme gluon density:** ePHENIX will enable measurements of diffractive and total DIS cross-sections in $e+A$ and $e+p$. Since the diffractive cross

section is viewed as a double gluon exchange process, the comparison of diffraction to total cross section in $e+A$ and $e+p$ is a very sensitive indicator of the gluon saturation region. ePHENIX would be an ideal detector to explore and study this with high precision.

Below we discuss each of these points in more detail and with specific details on the ePHENIX capabilities.

The proton as a laboratory for QCD

Deep Inelastic Scattering experiments over the last several decades have greatly enhanced our understanding of the proton substructure. Measurements with colliding beams at H1 and ZEUS at HERA have mapped out the momentum distributions of quarks and gluons, and shown that the gluons carry roughly half of the proton momentum. Fixed target experiments, with polarized nucleons and leptons at SLAC, CERN, DESY and JLab have revealed new surprises about proton structure, finding that only a small fraction of the proton spin comes from the quark spin and that there is significant correlation between the intrinsic motion of quarks and the nucleon spin. Measurements at both fixed target and colliders have started to image the proton through exclusive measurements.

eRHIC will greatly enhance the kinematic coverage for DIS with polarized beams, as shown in Figure A.2. With the capabilities of ePHENIX, we will significantly extend our understanding of the proton. The gluon and flavor dependent sea quark spin contributions to the proton spin will be determined, as will the possible orbital angular momentum contributions. The spatial and momentum distributions of (sea) quarks and gluons can be mapped, giving a multidimensional description of the proton.

Longitudinal spin of the proton The puzzle of the proton spin, to which the quark spin only contributes roughly a third, has spurred two decades of study. Measurements from fixed target polarized DIS have determined the quark contribution, but are less sensitive to the gluon due to the small kinematic coverage. Current RHIC measurements indicate that the gluon spin contribution may be comparable or even larger than the quark spin contribution, but due to the limited coverage at low longitudinal momentum fraction, x , large uncertainty remains, as is shown in Figure A.3 (yellow band).

Determining the gluon longitudinal spin contribution is a primary goal of the EIC and of ePHENIX, and will be possible due to the large reach in x and four-momentum transfer squared, Q^2 . Figure A.3 shows the expected impact from ePHENIX measurements of inclusive DIS on the uncertainty of the gluon helicity distribution as a function of x .

With the ePHENIX particle identification (PID) detectors, measurements of pions and kaons will greatly improve on the determination of the sea quark longitudinal spin distribution as well, including that of the strange quark, Δs , which has been of particular interest in the

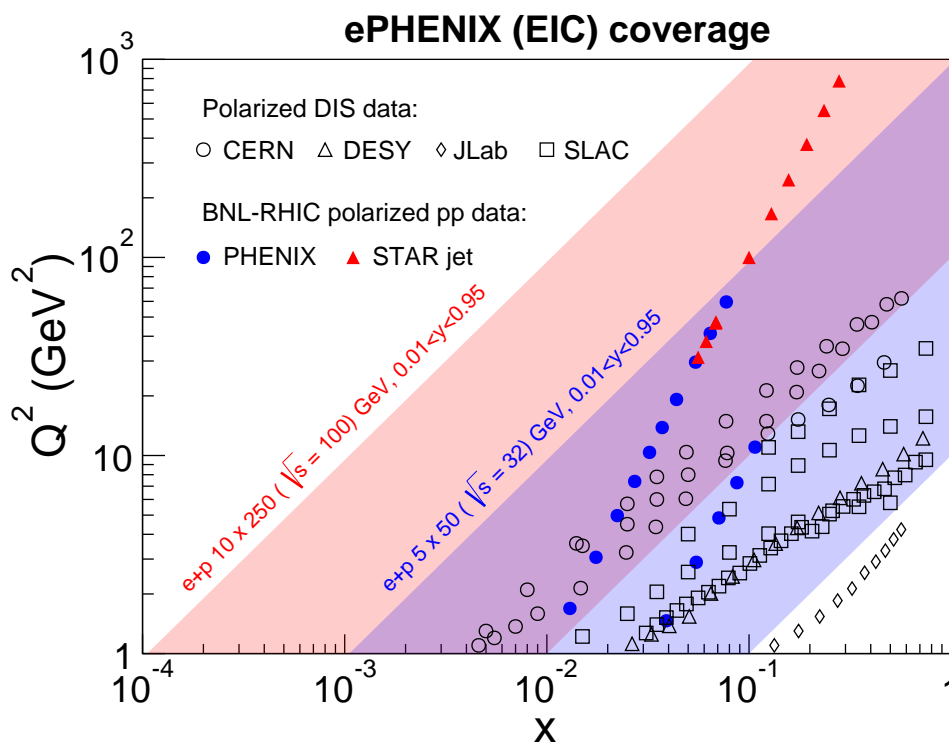


Figure A.2: Kinematic coverage of ePHENIX for two beam energy configurations, 10×250 GeV and 5×50 GeV, which show the range of eRHIC capabilities. Also shown are data from current polarized fixed target DIS experiments and RHIC $p+p$ collisions.

last few decades, because of the contradictory results obtained from different data. Current global analyses use hyperon beta decay to constrain Δs , which indicates a negative value for the full integral over x . Fixed target SIDIS measurements of kaon asymmetries, which directly probe Δs , though at low values of Q^2 and in a limited x range, find a positive contribution for $x > 0.01$. eRHIC provides data over a wide x and Q^2 range. Further, ePHENIX will provide excellent particle ID capability to identify kaons and allow direct measurements of strangeness spin contribution to the nucleon down to $\sim 2 \times 10^{-4}$.

Transverse motion of quarks and gluons in the proton Large transverse spin asymmetries measured in fixed target SIDIS in the past decade have spurred significant theoretical work. These asymmetries relate to the transversity distribution, the correlation between the transverse spin of the proton and a transversely polarized quark in it, and Transverse Momentum Distributions (TMDs), such as the Sivers or Boer-Mulders distributions, which describe correlations between either the proton or quark spin and the quark intrinsic motion, specifically the transverse momentum of the quark. With measurements of identified pions and kaons, these asymmetries give a 2+1 dimensional description of the spin and momentum distributions of different quark flavors in the proton, such as is

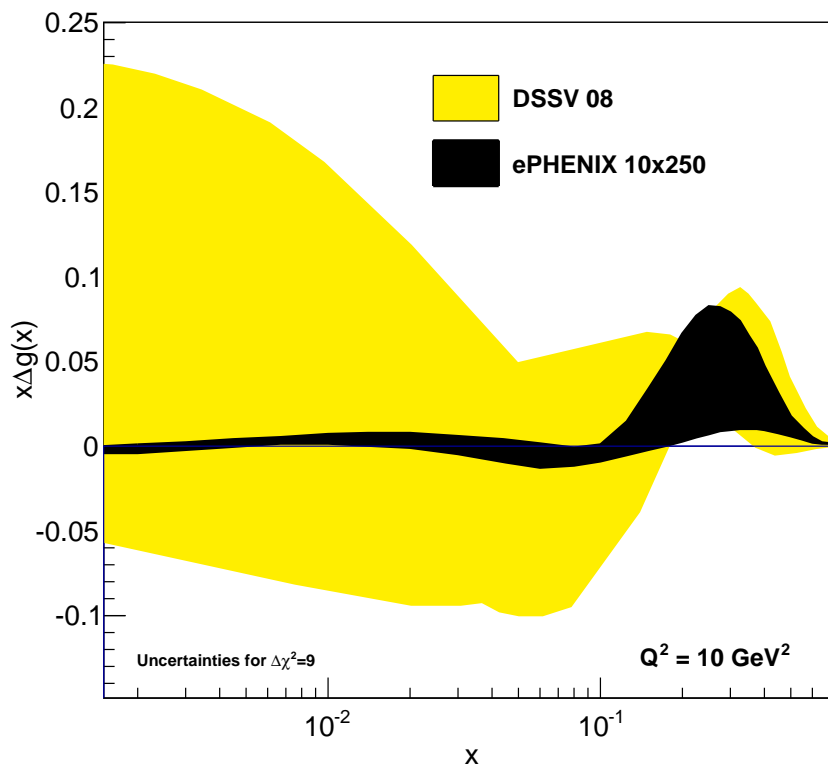


Figure A.3: The projected reduction in the uncertainty (black) on the gluon longitudinal spin distribution based on simulated PYTHIA events corresponding to an integrated luminosity of 10 fb^{-1} at the $10 \text{ GeV} \times 250 \text{ GeV}$ beam energy configuration. A 1% systematic uncertainty in beam and target polarization is applied. The yellow area shows the uncertainty from current data based on the analysis in Ref. [146].

shown in Figure A.4.

Current measurements, however, are only able to probe a small region in x and Q^2 , limiting the description to the valence quark region. Understanding of how the sea quarks and gluons contribute requires a larger kinematic range, such as provided at eRHIC. With the PID capabilities of ePHENIX, asymmetry measurements with transversely polarized nucleons and electrons in SIDIS will enable the study of these TMDs over most of this range, significantly expanding our knowledge of the proton structure. The constraint on the Sivers distributions was discussed in the EIC White Paper [144], with the expectations shown in Figure A.4. For the first time, determination of the Sivers distribution over a wide range in x will be possible, including the low x region where gluons dominate.

The transversity distribution, when coupled with the Collins fragmentation asymmetry, would result in an azimuthal asymmetry in the hadron production. This has been called the Collins effect, and is a measurement that goes to the heart of establishing the transversity

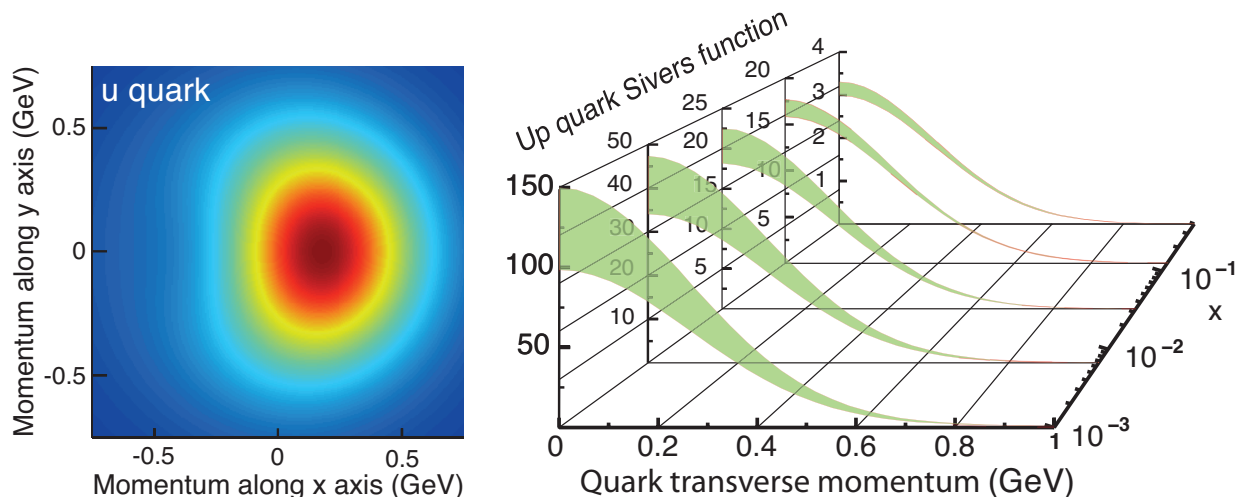


Figure A.4: [Reproduced from Ref. [144].] (left) The transverse-momentum distribution of an up quark with longitudinal momentum fraction $x = 0.1$ in a transversely polarized proton moving in the z -direction, while polarized in the y -direction. The color code indicates the probability of finding the up quarks. (right) The transverse-momentum profile of the up quark Sivers function at five x values accessible with the kinematics available at eRHIC, and corresponding statistical uncertainties.

distribution in a proton [147]. Measurement over the wide kinematic region would not only allow us to measure transversity, but the wide x -coverage possible at eRHIC would afford the first reliable measurement of the tensor charge of the proton (the integral over x of the transversity distribution). No other currently operational or planned facility can do this.

Tomographic imaging of the proton Hard exclusive processes such as the Deeply Virtual Compton Scattering (DVCS) and Deeply Virtual Vector Meson production (DVVM) involve interactions between the virtual photon and the partons in the proton without breaking the proton, resulting in the production of a real photon in DVCS or a vector meson in DVVM processes. Just as elastic lepton-nucleon scattering gives information on the spatial distribution of the electric charge and magnetization in the nucleon, DVCS and DVVM processes probe the transverse distribution of quarks, anti-quarks and gluons. This information is encoded in generalized parton distributions (GPDs), which quantify the distributions of quarks and gluons in terms of their positions in the transverse plane and longitudinal momentum fraction, providing 2+1 dimensional imaging of the nucleon. Measurements with polarized beams enable studies of spin-orbit correlations of quarks and gluons in the nucleon, by correlating the shift in the parton transverse distribution and proton transverse polarization. It is intuitively connected with orbital angular momentum carried by partons in the nucleon and hence of great interest in addressing the nucleon spin puzzle (nucleon spin decomposition) [148].

The existing data on GPDs from fixed target experiments cover only a limited kinematical range of t (the squared momentum transfer to the proton), medium to high x and low Q^2 . The t is connected through the Fourier transform with the impact parameter range probed. While data from HERA collider experiments (ZEUS and H1) covered lower x and a wide range in Q^2 , they are statistically limited. Furthermore, the HERA proton beams were unpolarized, so ZEUS and H1 were not able to study the proton-spin dependence in these measurements. With its large acceptance, excellent detection capabilities, high luminosity and broad range of energies of the polarized proton/helium beams available at eRHIC, ePHENIX will provide high precision data over a wide range of x , Q^2 and t . The wide range in t possible at eRHIC is of crucial importance, and will be achieved by integrating Roman Pot detectors in the accelerator lattice from the outset. Similar measurements performed with ion beams will allow analogous imaging of nuclei, allowing the first look at the parton distributions inside the nuclei.

The EIC White Paper demonstrates the precision that can be achieved in such a program with Deeply Virtual Compton Scattering (DVCS) and exclusive J/ψ production. The detector requirements for such measurements discussed in the White Paper and what we propose as ePHENIX are similar. For such, we expect ePHENIX will be able to make high impact measurements of GPDs.

Nucleus as a laboratory for QCD

Electron scattering interactions from nuclei allow key tests of the modification of parton distribution functions in nuclei of various sizes. The EIC has the unprecedented energy reach to probe deep into the low- x quark and gluon region where there are predictions of significant non-linear evolution effects and possibly the realization of a universal state of the QCD vacuum at high gluon density. In addition, rather than looking at the modified number of deep inelastic scatterings, one can study via SIDIS the changes in the process of a highly virtual struck quark to color neutralize and eventually hadronize when in the presence of a nuclear medium.

Hadronization and its modification in nuclear matter Deep inelastic scattering with heavy nuclear targets provides an effective stop watch and meter stick with which one can measure the color neutralization and hadronization times, and understand important details of partonic interactions with the nucleus. By varying the size of the nuclear target (at eRHIC all the way up to uranium) and changing key DIS parameters (Q^2 , ν , z , p_T^2 , ϕ) one can calibrate this watch and meter stick. Figure A.5 shows the kinematic reach for 5 GeV electrons scattering from 100 GeV/nucleon heavy nuclei in terms of the initial virtuality Q^2 and the energy of the struck quark in the nuclear rest frame ν . Earlier experiments with fixed targets have measured very interesting modifications in apparent fragmentation functions, and yet those results are limited to small values of Q^2 and ν . In the case of the published HERMES results [149] in Fig. A.5, one observes a dramatic decrease in the

number of high- z hadrons (those with a large fraction of the struck quark momentum) in scattering from nuclear targets. There are many possible explanations of the experimental results, including parton energy loss due to multiple scattering in the nucleus and induced gluon radiation — a similar mechanism has been used to explain the “jet quenching” phenomena discovered in heavy ion collisions at RHIC. Other theoretical frameworks predict a strong correlation between a short color neutralization timescale and high- z resulting processes. An excellent review of the various theoretical approaches is given in Ref. [150]. Figure A.5 also shows the expected statistical precision with the ePHENIX PID capabilities over the full ν range in one Q^2 bin.

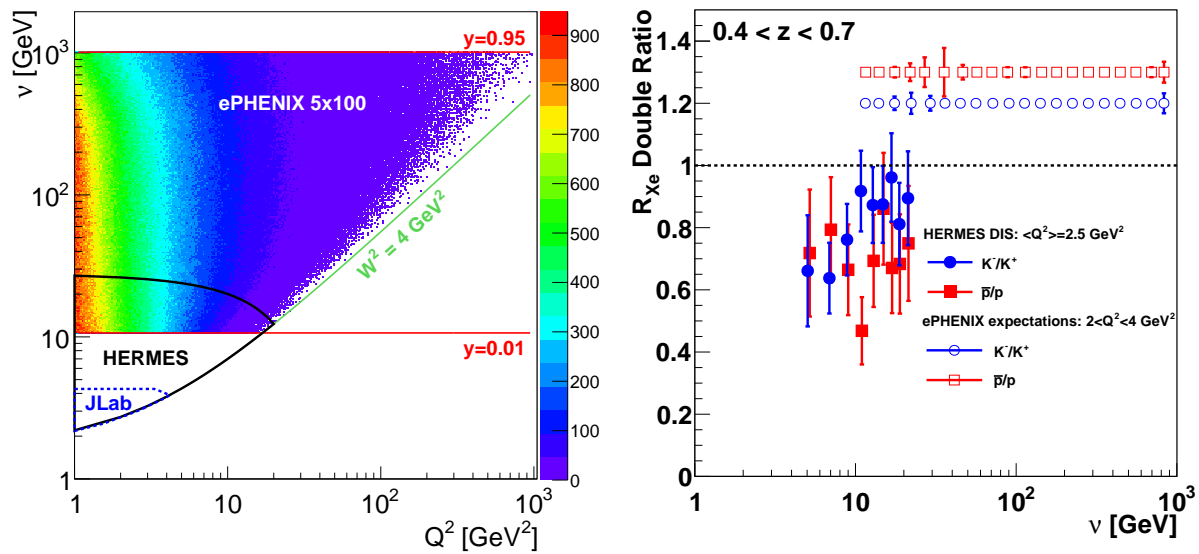


Figure A.5: (left) Shown is the very large virtuality Q^2 and ν coverage for ePHENIX (EIC) measurements with collisions of 5 GeV electrons on 100 GeV/nucleon heavy nuclei. The z -axis color scale shows the relative distribution of events from the PYTHIA event generator. Also shown are the kinematic reach for the CLAS experiment at JLab [151] and for the HERMES results [149]. (right) Experimental data from HERMES [149] on the modified fragmentation from xenon targets (R_{Xe}) in the range $0.4 < z < 0.7$ and with average $\langle Q^2 \rangle = 2.5 \text{ GeV}^2$. The filled points are the double ratio for antiprotons relative to protons (red) and for K^- relative to K^+ (blue). ePHENIX will measure with precision the modified fragmentation distribution with excellent π, K, p particle identification over a very broad range of Q^2 and ν . The open symbols show the expected statistical precision for ePHENIX with its particle identification capabilities for one bin in Q^2 , $2 < Q^2 < 4 \text{ GeV}^2$ based on 2 fb^{-1} at the $5 \text{ GeV} \times 100 \text{ GeV}$ beam energy configuration.

If the struck quark remains an undressed color charge while it traverses the nucleus, one might expect that the ratio of final state hadrons (π^+, K^+, p and their anti-particles) would show the same degree of nuclear modification. Shown in the right panel of Figure A.5 are the double ratios of modifications R_{Xe} with a xenon target for antiprotons to protons and K^- to K^+ . It is notable that there is a larger suppression for the hadrons with a larger cross section with nucleons (e.g. $\sigma_{\bar{p}+N} > \sigma_{p+N}$ and $\sigma_{K^-+N} > \sigma_{K^++N}$). If this is due

to hadronization occurring within the nucleus, then inelastic collisions can result in the differential attenuation. How does this attenuation vary with the energy of the struck quark? The EIC realization has the enormous reach in the energy of the struck quark ν at fixed Q^2 to measure the full evolution with high statistics. As demonstrated in this document, ePHENIX will have excellent π, K, p particle identification to make exactly this measurement with high statistics. In addition, one can vary the virtuality which is also expected to play a significant role in the length scale probed in the nucleus and thus rate of initial radiation.

Tests with charm mesons via displaced vertex measurements are not in the initial suite of ePHENIX capabilities, and could be added with a later inner thin silicon detector. Measurements of the interactions of charm quarks with the nucleus would be quite interesting in the context of suppressed radiation due to the “dead-cone” effect. However, the relation to kinematic variables z and ν may depend on the balance of DIS events from intrinsic charm as opposed to photon-gluon fusion reactions resulting in $c\bar{c}$ pair production.

QCD matter at extreme gluon density A key goal of any future EIC is to explore the gluonic matter at low x , where it is anticipated that the density of gluons will saturate as the rate of gluon recombination balances that of gluon splitting. In fact, there are well known modifications to the quark distribution functions in nuclei that have significant x dependence: high x Fermi motion effects, then the EMC suppression, anti-shadowing enhancement, and finally nuclear shadowing at the lowest x . The ePHENIX detector, combined with the large kinematic reach of an $e+A$ collider, is in an excellent position to map this physics out in the gluon sector.

The lowest x regime with saturated gluon densities is unique to QCD, as gluons carry the QCD charge, “color”, and so interact with themselves. In order to explore this saturation region, one must probe nuclear matter at high center-of-mass energy, so as to reach as low in x as possible while still in the perturbative QCD regime (i.e., $Q^2 > 1 \text{ GeV}^2$). Generally, a saturation scale, Q_s , is defined to indicate the onset of saturation (where the gluon splitting and recombination balance each other), with Q_s falling as x increases. In reality the point at which recombination starts to balance the gluon splitting is a range in x and Q^2 and so making measurements over a wide range in x and Q^2 is necessary to fully understand these effects.

eRHIC will have a significantly lower center-of-mass energy than HERA, and so cannot improve upon the minimum x probed with measurements in $e+p$. However, eRHIC will also be capable of accelerating heavy ions in $e+A$ collisions. As the x probed is related to the resolution of the probe, collisions at the same Q^2 can resolve significantly lower x due to the larger extent of the nucleus: the partons in the highly accelerated nucleus are probed coherently. This effectively reduces the x probed in $e+A$ collisions by a factor of $A^{\frac{1}{3}}$, with A the atomic weight, as this is proportional to the size of the nucleus. At the energies planned for eRHIC, based on measurements in $p(d)+A$, one expects saturation

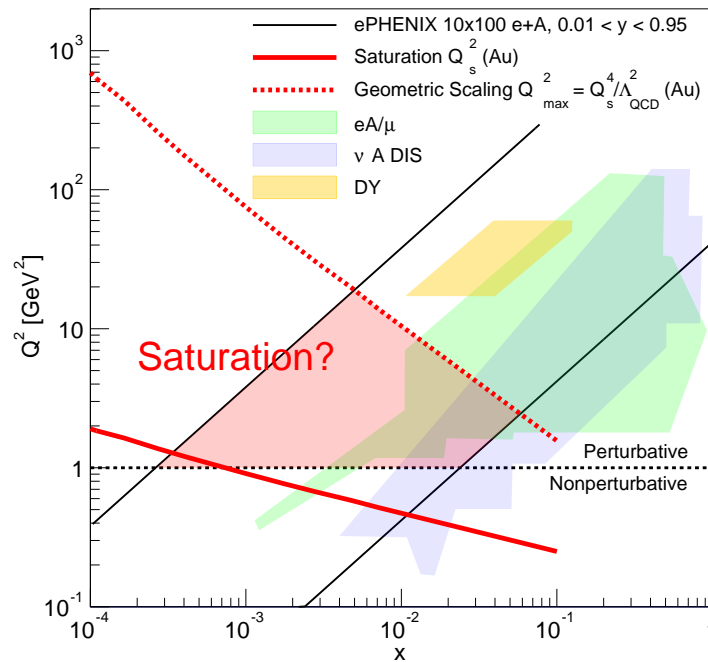


Figure A.6: Shown is the coverage in x and Q^2 for the EIC and the ePHENIX detector for 10 GeV electrons on 100 GeV/nucleon heavy nuclei. The two black lines indicate the kinematic coverage with selections on the inelasticity $0.01 < y < 0.95$ (which might be slightly reduced depending on the final electron purity at low momentum). Also shown are the kinematic coverage by previous experiments in $e+A$ and $\nu+A$ DIS and also Drell-Yan measurements. The red solid line is an estimate of the x dependence for the saturation scale Q_s^2 . The region where this universal saturated matter dictates the physics is estimated to extend over the geometric scaling region up to $Q_{max}^2 = Q_s^4 / \Lambda_{QCD}^2$ shown by the red dashed line [152].

effects in inclusive DIS in $e+A$.

Figure A.6 shows the x and Q^2 coverage of ePHENIX for the 10 GeV \times 100 GeV/nucleon configuration compared with the current fixed target data. Two red lines are drawn, one (solid) showing expectations of Q_s^2 in $e+Au$ and the other (dashed) showing the expected turn on of geometric scaling, which relates to the saturation scale by $Q_{max}^2 = Q_s^4 / \Lambda_{QCD}^2$. The shaded red region is where ePHENIX can search for saturation effects.

As described in the EIC White Paper [144], it can be even more effective to explore this region of dense gluonic matter with diffractive physics, where at least two gluons are exchanged in the interaction. Therefore, a primary measurement to probe saturation effects at eRHIC will be comparing the diffractive-to-total cross-section from $e+p$ and $e+A$. The ratio of these cross-sections will directly relate to the size of any saturation effects. Figure A.7, taken from the EIC white paper [144], shows the prediction of one saturation model for this cross-section ratio with and without saturation, indicating large possible effects. Note that the statistical and systematic uncertainties in this plot are scaled up by

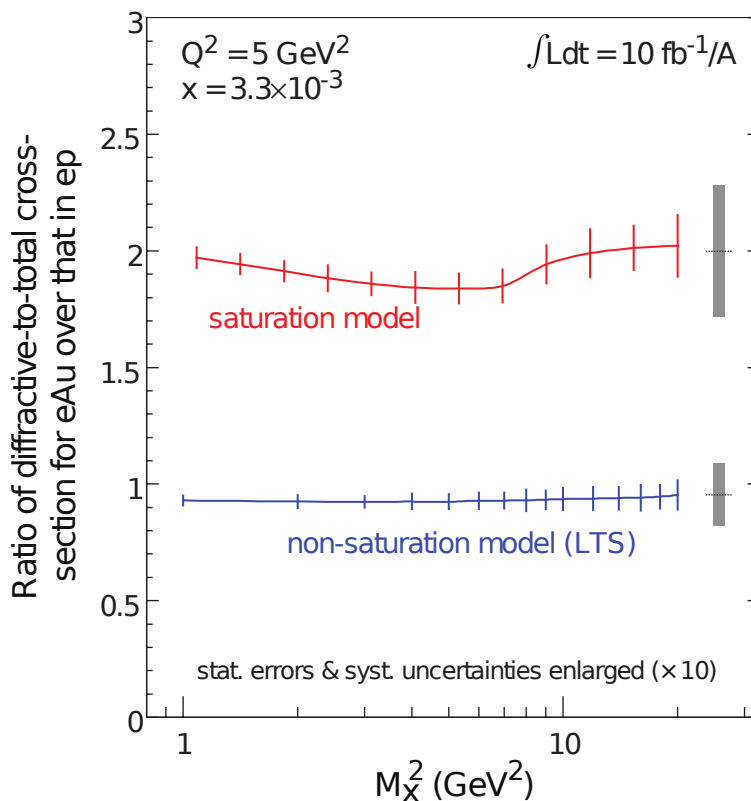


Figure A.7: [Reproduced from Ref. [144].] Ratio of diffractive-to-total cross-section for $e+Au$ normalized to $e+p$ plotted as a function of the squared mass of the hadronic final state, M_X^2 . The expected uncertainties for 10 fb^{-1} are scaled by a factor of 10 to be visible. The ePHENIX detector will have similar capabilities as was assumed for this plot, and will achieve similar precision.

a factor of 10 in order to be visible. This measurement relies on measuring events with a large rapidity gap, which is the signature of diffractive events due to the fact that the hadron remains intact after the scattering (though in the case of ions, the nucleus may still break up). The ePHENIX detector will have wide calorimetric coverage, and so will be able to make a measurement of the ratio of diffractive-to-total cross-sections with comparable precision as shown in Figure A.7.

A.4 Detector Requirements

The detector requirements for Deep Inelastic Scattering measurements are well established by previous DIS experiments (H1, ZEUS, HERMES, COMPASS, etc.) and by EIC group studies [144, 150]. Table A.1 summarizes these basic requirements and how ePHENIX would meet them. After a brief overview of the relevant kinematic variables, detailed

studies are presented in this chapter.

The suggested ePHENIX detector configuration is shown in Figure A.1. It is built around the sPHENIX detector, which is a superconducting solenoid and electromagnetic and hadronic calorimeter in the central region ($-1 < \eta < 1$ for pseudorapidity η). This proposal would add to that detector the following detector subsystems:

electron-going direction ($-4 < \eta < -1$): High resolution Crystal EMCal with GEM tracking.

Barrel ($-1 < \eta < 1$): Compact-TPC for low mass tracking and PID for momentum $p < 4$ GeV/c with DIRC

hadron-going direction ($1 < \eta < 4$): Hadronic and Electromagnetic calorimeters, GEM trackers, and Aerogel-based ($1 < \eta < 2$) and gas-based RICH for PID up to momentum $p \sim 50$ GeV.

Far-Forward in hadron-going direction: Roman Pots and Zero-Degree Calorimeter.

A.4.1 Kinematics

In DIS, a lepton is scattered off a target hadron via the exchange of a virtual boson, which for electron beam energy $E_e < 10$ GeV can always be taken as a virtual photon. Defining the four-momenta of the incoming and scattered electron and the incoming proton as k , k' and p respectively, we can define the following Lorentz invariant quantities:

$$s \equiv (k + p)^2 = 4E_e E_p \quad (\text{A.1})$$

$$Q^2 \equiv -q^2 = -(k - k')^2 = 2E_e E_e' (1 - \cos\theta) \quad (\text{A.2})$$

$$y \equiv \frac{p \cdot q}{k \cdot p} = 1 - \frac{E_e'}{E_e} + \frac{Q^2}{4E_e^2} \quad (\text{A.3})$$

$$x \equiv \frac{Q^2}{2p \cdot q} = \frac{Q^2}{ys} \quad (\text{A.4})$$

$$v \equiv \frac{p \cdot q}{M} = \frac{Q^2}{2Mx} \quad (\text{A.5})$$

where s is the center-of-mass energy squared, q is the 4-momentum transferred from scattered electron and Q^2 is the virtuality of the photon which gives the resolution scale of the scattering, y is the inelasticity of the scattering and x is Bjorken x , the fractional momentum carried by the struck parton. Here, we have also written these in the lab frame in terms of the measured scattering angle, θ and the energies of the proton and incoming and scattered electron, E_p , E_e and E_e' , respectively, under the approximation that the electron and proton mass are small compared to the beam energies.

Table A.1: Detector requirements

Detector requirements	Detector solution
<p>Electron-ID: High purity (99%) identification of the scattered lepton over hadron and photon background <i>Important for electron-going direction and barrel acceptance</i></p>	<p>Electromagnetic Calorimetry and charged particle tracking Minimum material budget before EMCal Good energy and tracking resolution for E/p matching</p>
<p>Resolution in x and Q^2: Excellent momentum and angle resolution of the scattered lepton to provide high survival probability (80%) in each (x, Q^2) bin (important for unfolding) <i>Important for electron-going direction and barrel acceptance</i></p>	<p>High resolution EMCal and tracking in electron-going direction Good (tracking) momentum resolution for $E'_e < 10$ GeV in barrel Good (EMCal) energy resolution for $E'_e > 10$ GeV in barrel</p>
<p>Hadron identification: > 90% efficiency and > 95% purity</p>	<p>In barrel acceptance: DIRC for $p_h < 4$ GeV/c In hadron-going direction: Aerogel for lower momentum and gas RICH for higher momentum</p>
<p>Wide acceptance for leptons and photons in DVCS: Ability to measure DVCS lepton and photon within $-4 < \eta < 4$</p>	<p>EMCal and tracking with good resolution over for lepton and photon measurements covering $-4 < \eta < 4$</p>
<p>Electron/Photon separation: Separate DVCS photon and electron in electron-going direction</p>	<p>High granularity EMCal in electron-going direction</p>
<p>Measurement of scattered proton in exclusive processes</p>	<p>Roman pots in hadron-going direction</p>
<p>“Rapidity gap” measurement capabilities: Measure particles in $-2 < \eta < 4$ for diffractive event identification</p>	<p>Hadronic calorimetry covering $-1 < \eta < 5$, and EMCal covering $-4 < \eta < 4$</p>
<p>Forward Zero-Degree calorimetry: Measure neutrons from nucleus breakup in diffractive $e+A$ events</p>	<p>Zero-Degree calorimeter in hadron-going direction planned, in coordination with CAD</p>

For inclusive DIS, where only the kinematics of the scattered lepton are measured, Eq. A.1–A.5 fully describe the event. For SIDIS, in which a final state hadron is also measured, additional variables are needed. The fraction of the scattered parton’s momentum carried by the hadron is defined as

$$z \equiv \frac{p_h \cdot p}{q \cdot p} \quad (\text{A.6})$$

where p_h is the four-momentum of the measured hadron. Further, we can define $p_{h\perp}$ as the transverse momentum of the hadron w.r.t. the virtual photon, in the center-of-mass frame of the proton (or ion) and virtual photon.

For exclusive processes, in addition to the scattered lepton, the final state photon in DVCS or meson in Deeply Virtual Meson Production as well as the scattered proton are measured. In this case, another kinematic variable is introduced – the squared momentum transfer to the proton, t , defined as

$$t \equiv (p' - p)^2 \quad (\text{A.7})$$

where p' is the four-momentum of the scattered proton.

A.4.2 Inclusive DIS and scattered electron measurements

In inclusive DIS, where only the kinematics of the scattered electron are necessary, the primary requirements of any detector are electron identification and sufficient resolution in x and Q^2 , which in turn mandates good energy and angle resolution for the scattered electron measurements (Eq. A.2–A.4).

Electron Identification

In collider geometry, the DIS electrons are scattered mainly in the electron-going direction and central rapidities (barrel acceptance), see Figure A.8. Central rapidity selects scatterings with higher Q^2 and higher x (due to its correlation with Q^2). The higher the electron beam energy, the more scattering there is in the electron-going direction. The energy of the scattered electron varies in the range from zero up to the electron beam energy and even to higher values for electrons detected in the barrel acceptance, see Figure A.8.

Collider kinematics allow clear separation of the scattered electrons from other DIS fragments — hadrons and their decay products — which are detected preferably in the hadron-going direction, leaving much softer spectra in the central region and the electron-going direction. Figure A.9 shows scattered electron momentum spectra along with photon (mainly from hadron decays) and charged pion spectra. For the 10 GeV electron beam, hadronic and photonic backgrounds are small above ~ 5 GeV/c, but increase rapidly at lower momenta.

The different response of the EMCAL to hadrons and electrons, along with a direct comparison of energy deposited in the EMCAL and momentum measured in the tracking system

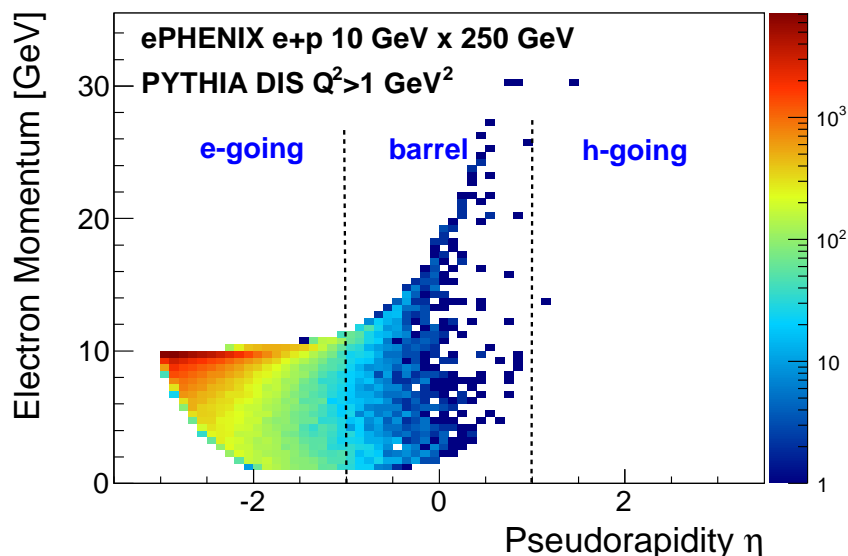


Figure A.8: Shown is the distribution of scattered electrons in pseudorapidity and energy. The results are from PYTHIA DIS simulations for $e+p$ collisions with $10 \text{ GeV} \times 250 \text{ GeV}$ beam energies. The events are selected as DIS with $Q^2 > 1 \text{ GeV}^2$.

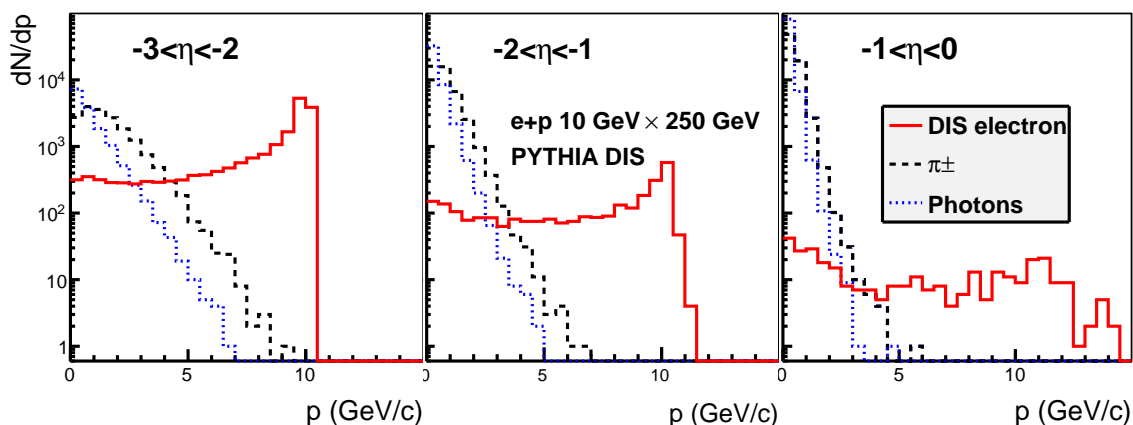


Figure A.9: For $10 \text{ GeV} \times 250 \text{ GeV}$ beam energy configuration: Momentum spectra for scattered electron (red), charged pions (black) and photons (blue).

(i.e., E/p matching) provides a significant suppression of hadronic background in DIS scattered electron measurements: from a factor of 20–30 at momenta near $1 \text{ GeV}/c$ to a factor of greater than 100 for momenta above $3 \text{ GeV}/c$. Figure A.10 shows the effectiveness of electron identification with the EMCAL and tracking, providing high purity for DIS

scattered electron measurements at momenta >3 GeV/ c for the 10 GeV electron beam (and >1.5 GeV/ c for the 5 GeV electron beam). The evaluations above are done with a parametrized response of the EMCAL to hadrons and electrons, and EMCAL and tracking resolutions described in Sections A.5.3 and A.5.2. Further enhanced electron identification is expected from the use of the transverse shower profile. We are also studying possible electron identification improvement with longitudinal segmentation in the crystal calorimeter in the electron-going direction. These are expected to move the detector capabilities for high purity electron identification down to 2 GeV/ c (1 GeV/ c) for 10 GeV (5 GeV) electron beam, which only marginally limits the (x, Q^2) space probed in our measurements, see Figure A.11.

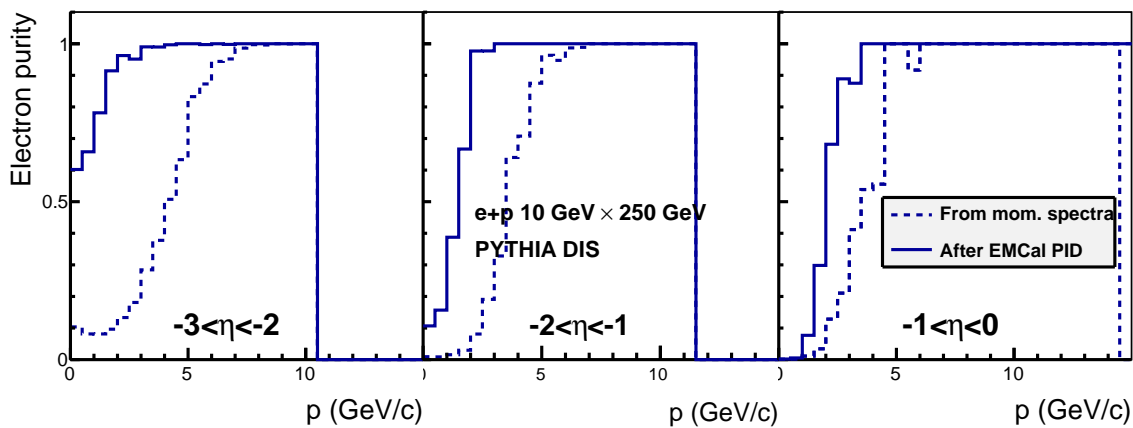


Figure A.10: For 10 GeV \times 250 GeV beam energy configuration: The fraction of charged particles from DIS electrons before electron identification (dotted) and after identification with the EMCAL response and E/p matching (solid).

Photon conversion in material between the collision point and the tracker (mainly beam pipe, with thickness as small as 0.3% of radiation length) is not expected to contribute sizable background. Moreover, conversion electron-positron pairs will be well identified by our tracking system in the magnetic field and additionally suppressed by E/p matching cut. A detailed GEANT simulation study is ongoing to quantify this effect.

Resolution in x and Q^2 and bin survival probability

Measurements of the scattered electron energy and polar angle impact the DIS kinematic reconstruction, Eq. A.2–A.4. Unfolding techniques are generally used to correct for smearing in (x, Q^2) due to detector effects, and the effectiveness of this technique depends on the degree to which events migrate from their true (x, Q^2) bin to another. This migration can be characterized by the likelihood of an event remaining in its true (x, Q^2) bin — the bin survival probability.

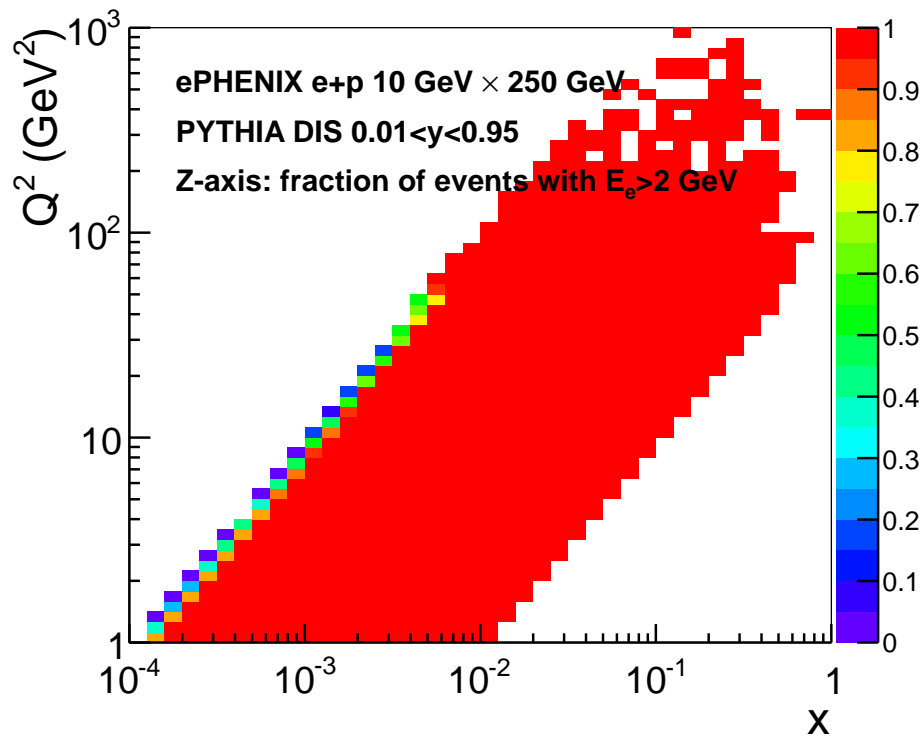


Figure A.11: For 10 GeV \times 250 GeV beam energy configuration: The color axis indicates the fraction of events in (x, Q^2) space surviving after a > 2 GeV energy cut on the DIS scattered electron.

The energy resolution σ_E is directly propagated to σ_{Q^2} , so that $\sigma_{Q^2}/Q^2 = \sigma_E/E$. The EMCAL energy and tracking momentum resolutions will provide excellent precision for Q^2 measurements. Conversely, the σ_x resolution is magnified by a factor of $1/y$ as $\sigma_x/x = 1/y \cdot \sigma_E/E$, and so the energy resolution in this approach effectively defines the limit of our kinematic reach at low y .

Figure A.12 shows the relative resolution in Q^2 and x measurements using the standard “electron” method, in which the scattered electron is measured. While the Q^2 relative uncertainty, σ_{Q^2}/Q^2 , is better than 10% over whole x - Q^2 acceptance, the relative uncertainty on x , σ_x/x , clearly demonstrates its y -dependence (the same y points are on the diagonal, as from Eq. A.4, $Q^2 = syx$). The step in resolution around $Q^2 = 50$ GeV² in these plots corresponds to the transition from the electron-going direction to the barrel acceptance, which differ mainly in the resolution of the different electromagnetic calorimeters covering those two regions of the acceptance. All of this translates to the statistics survival probability in a bin shown in Figure A.13, which is calculated for five bins per decade in each of x and Q^2 . The survival probability is $> 80\%$ for $y > 0.1$ in the electron-going direction and for $y > 0.3$ in the barrel acceptance.

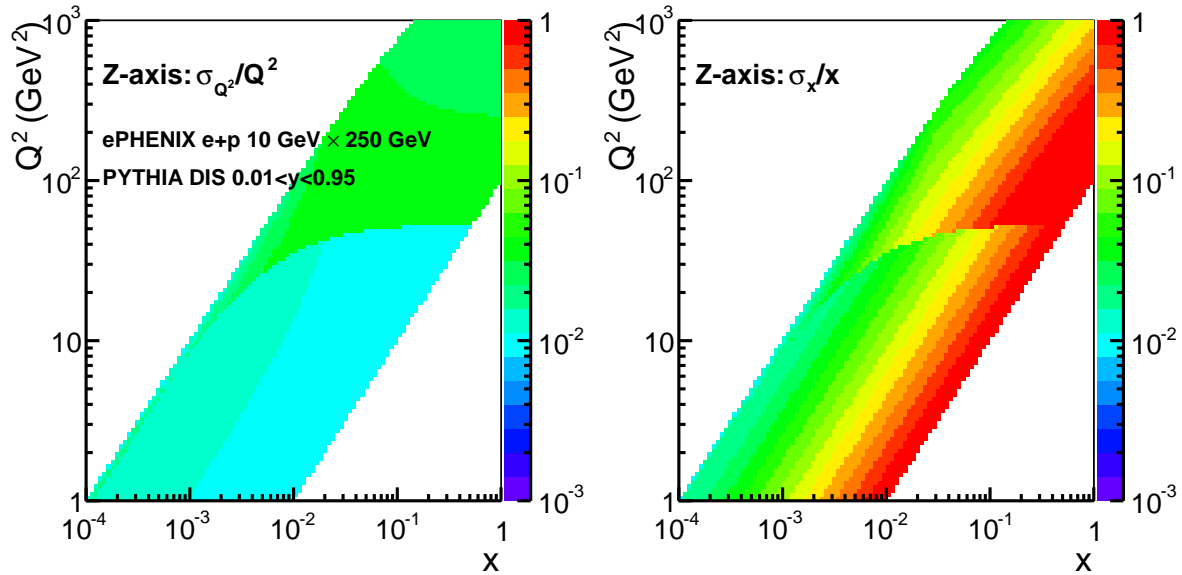


Figure A.12: For 10 GeV \times 250 GeV beam energy configuration: the relative resolution for Q^2 (left) and x (right) as a function of (x, Q^2) .

The effect of the polar angle resolution θ in Eq. A.2–A.4, is the biggest for forward scattering (small θ). It was found that crystal EMCal position resolution (better than 3 mm for > 1 GeV electrons, see Section A.5.3) provides enough precision for scattered electron angle measurements, so that it affects the statistics migration in bins on Figure A.13 only marginally.

The Jacquet-Blondel method using the hadronic final state is an alternative approach to reconstruct DIS kinematics. Its resolution for inelasticity y , and hence for x , is nearly flat, so it provides much better precision for x determination than the “electron” method, in the region with small y . It is also better in the higher Q^2 region corresponding to the barrel acceptance, where the resolution of the “electron” method is limited by the EMCal resolution.

The Jacquet-Blondel method requires the measurement of all final state hadrons produced in $e+p$ or $e+A$ scattering. A study with the PYTHIA generator shows that the precision of this approach does not deteriorate if the hadron detection capabilities are limited to $|\eta| < 4$. This method provides relative precision for the measurement of x of better than 20%, which satisfies the bin statistics migration criteria discussed above. It was found that for $y < 0.3$ the precision of this approach deteriorates only slightly when hadron measurements are limited to the barrel and forward acceptance $-1 < \eta < 4$ (the acceptances we plan to equip with hadron identification capabilities, see Section A.5.5). As was shown above, measurements at higher y are well provided by the “electron” method.

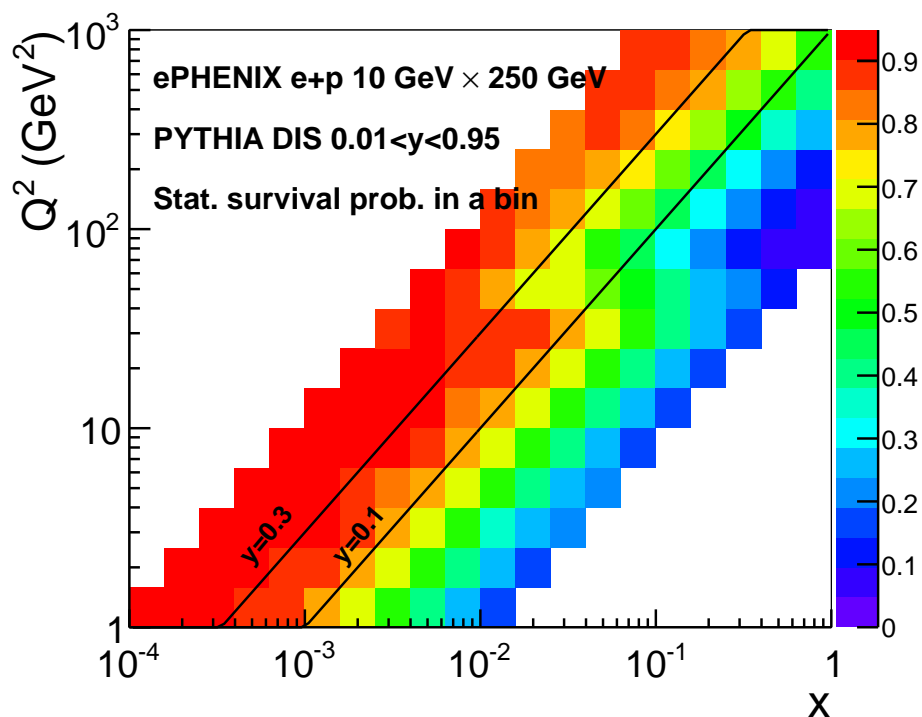


Figure A.13: For 10 GeV \times 250 GeV beam energy configuration: Statistics survivability in (x, Q^2) bins.

Therefore, combining the electron and hadronic final state measurements provides precise determination of basic kinematic variable x , y and Q^2 in the whole kinematical space.

QED radiative effects (radiation of real or virtual photons) are another source of smearing which is usually corrected with unfolding techniques. Unlike energy-momentum resolutions which introduces Gaussian-like smearing, radiative corrections are tail-like. They can be responsible for as much as 10–20% of statistics migrating away from a bin, and dominate over energy-momentum smearing at higher y (compare to Figure A.13).

A.4.3 Semi-inclusive DIS and hadron ID

As was discussed in Chapter A.1, measurements of hadrons in SIDIS events are necessary to determine both the (sea)quark separated helicity distributions and TMDs. It is also important for understanding the hadronization process in nuclear matter. For these measurements, one needs to identify the hadron, particularly in the case of pions and kaons. In this section, we discuss the kinematic ranges of interest for pions, kaons and protons, and in Chapter A.5, we discuss technology choices which can effectively make

these measurements.

Figure A.14 shows the yields of positively charged hadrons as a function of momentum and pseudorapidity for the 10 GeV \times 250 GeV beam configuration. A minimum $z > 0.2$ to remove soft physics effects and beam remnant is applied. For $\eta < 0$, the hadron momenta are limited by the electron beam momentum, while in the hadron-going direction, the hadron momenta extend almost to the full proton beam energy. The results are similar for other beam energy configurations.

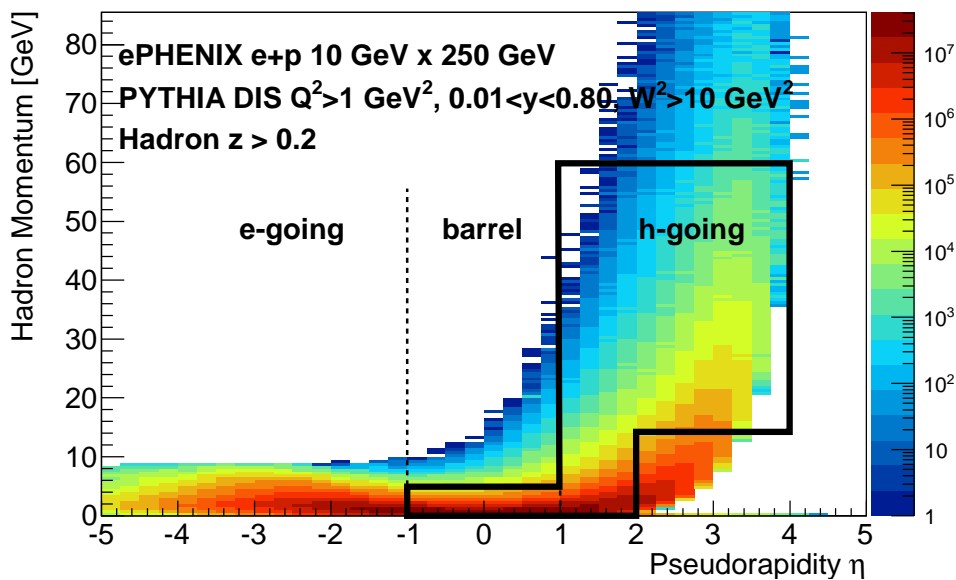


Figure A.14: Shown is the distribution of hadrons from DIS events in $e+p$ as a function of momentum and pseudorapidity, based on PYTHIA simulations of the 10 GeV \times 250 GeV beam energy configuration. The black outline indicates the pseudorapidity and momentum range covered for kaons by the planned PID detectors in ePHENIX.

As was stated above, ePHENIX will have three PID systems: (1) a DIRC covering $|\eta| < 1$ providing π - K separation below 3.5–4 GeV/ c (depending on purity and efficiency requirements), (2) an aerogel based RICH covering $1 < \eta < 2$ providing π - K (K - p) separation below 6 (10) GeV/ c and (3) a gas based RICH covering $1 < \eta < 4$ providing π - K separation for $3 < p < 50$ GeV/ c and K - p separation for $15 < p < 60$ GeV/ c (depending on the balance between efficiency and purity chosen). Based on these numbers, the PID for kaons would cover the η and p region outlined in black in Figure A.14. The resulting ePHENIX x and Q^2 coverage for SIDIS events with an identified kaon is shown in Figure A.15, for low ($0.30 < z < 0.35$) and high ($0.70 < z < 0.75$) z bins, along with lines indicating the accessible DIS y range ($0.01 < y < 0.95$).

Figure A.16 shows the impact on the x and Q^2 coverage of removing one of the three

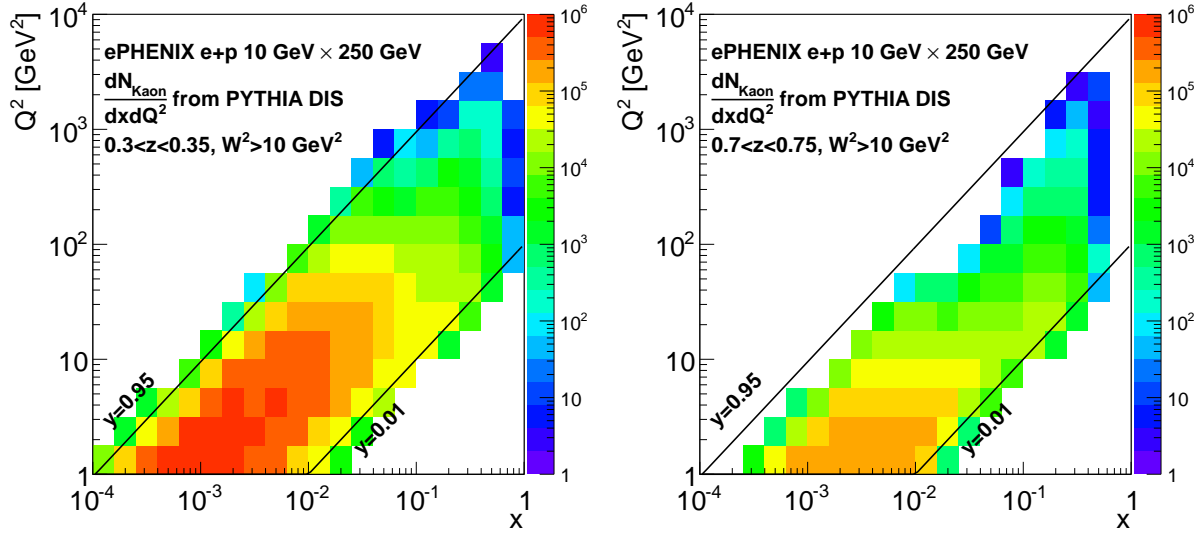


Figure A.15: x and Q^2 distribution of events with kaons which can be identified with the ePHENIX PID detectors in expected binning at (left) low and (right) high z .

PID detectors planned for ePHENIX at low and high z . The plots show the ratio of kaon yields when using only two PID detectors to those with all three detectors (i.e., standard ePHENIX). If the gas-based RICH detector is removed (left), the high x reach, particularly at high Q^2 , is lost. If the aerogel-based RICH is removed (middle), sensitivity to the region of moderate x , Q^2 and y is lost. Finally, if the DIRC is removed, significant kinematic coverage at low x , as well as moderate x and high Q^2 is lost. To achieve a wide x and Q^2 coverage, all three detectors are necessary. Extending the aerogel-based RICH to $\eta > 2$ does not extend the kinematic coverage; the momentum range covered by such a detector corresponds to very low values of y .

A.4.4 Exclusive DIS

Among exclusive processes, Deeply Virtual Compton Scattering (DVCS) is of special interest (see Section A.3). The produced DVCS photon energy versus pseudorapidity distribution is shown in Figure A.17. Most of the photons fall in the electron-going direction and the barrel (central rapidity) acceptance. The photon energy for $-1 < \eta < 1$ varies in the range $\sim 1\text{--}4$ GeV/ c and is nearly independent of the beam energy in the range considered for eRHIC. Photons in the electron-going direction are more correlated with the electron beam and have energy from 1 GeV up to electron beam energy.

Figure A.18 shows the x - Q^2 range covered by DVCS measurements for different rapidity ranges, emphasizing the importance of measurements over a wide rapidity range. Wide kinematical coverage is also important for separating DVCS events from Bethe-Heitler (BH) events (when a photon is radiated from the initial or final state lepton), which share

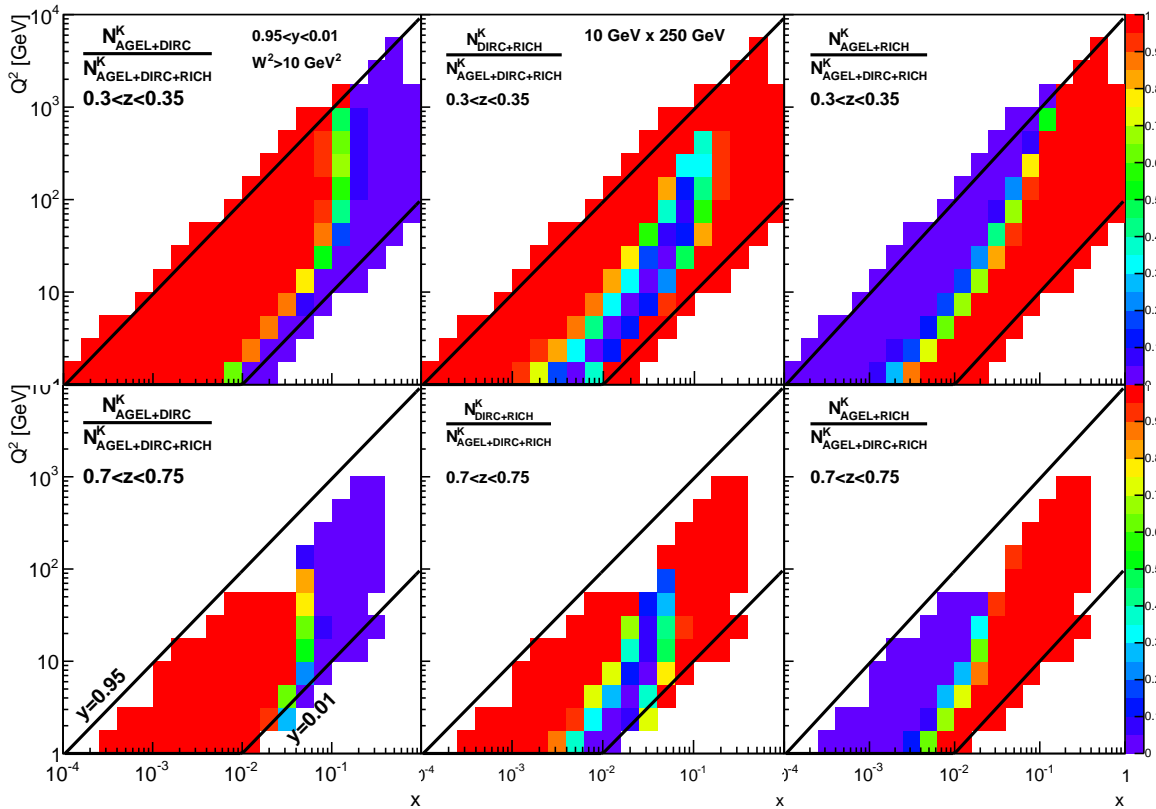


Figure A.16: Efficiency as a function of x and Q^2 of kaon identification when comparing to baseline ePHENIX design with a DIRC, RICH and Aerogel when one of these subsystems is removed. The top three plots are for low z ($0.3 < z < 0.35$) and the bottom three are for high z ($0.7 < z < 0.75$). Also shown are lines indicating different values of y .

the same final state. This can be done by utilizing the different kinematic distributions of DVCS and BH photons (e.g., in rapidity and inelasticity y). The planned EMCal and tracking cover $|\eta| < 4$ (Section A.5.3 and A.5.2) and will provide excellent capabilities for DVCS measurements.

To ensure the reliable separation of electromagnetic showers in the EMCal from the scattered electron and the DVCS photon, sufficient EMCal granularity is necessary. The minimal angle separation between the electron and the photon is reached for electrons with the smallest scattering angle (i.e., the smallest Q^2) and is inversely proportional to electron beam energy. For a 10 GeV electron beam and $Q^2 > 1 \text{ GeV}^2$, the minimum angle is ~ 0.1 rad. The proposed crystal EMCal in the electron-going direction, with granularity ~ 0.02 rad (see Section A.5.3), will provide the necessary electron and photon shower separation.

It is also important to ensure the exclusiveness of the DVCS measurements, and so it is

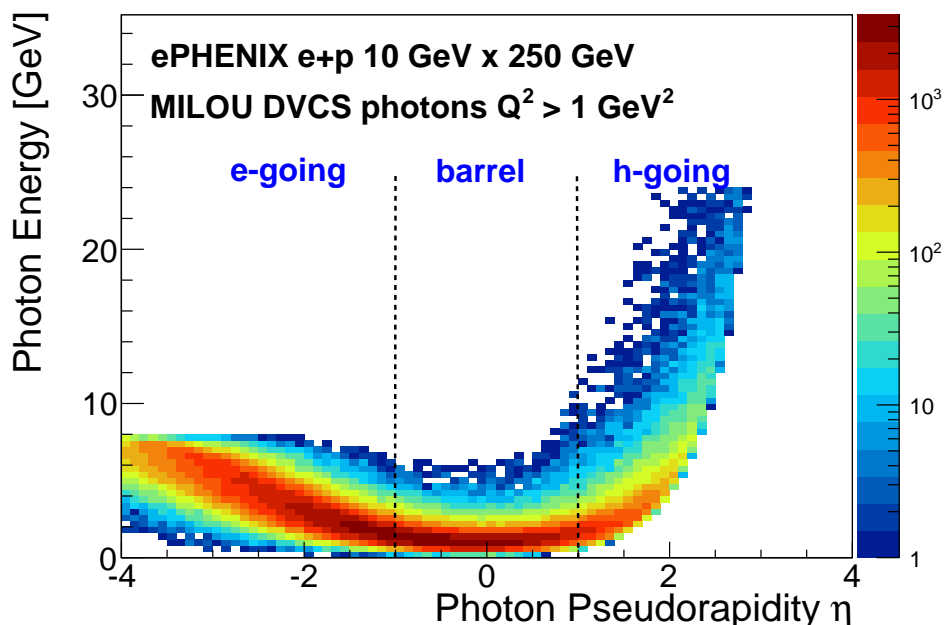


Figure A.17: For the $10 \text{ GeV} \times 250 \text{ GeV}$ beam energy configuration: DVCS photon energy vs pseudorapidity distribution; the z-axis scale shows the relative distribution of events from the MILOU event generator.

highly desirable to reconstruct the scattered beam proton. The proton scattering angle is inversely proportional to proton beam energy and varies from 0 to 5 mrad for 250 GeV proton beam and four-momentum transfer $-t < 1 \text{ GeV}^2$. It can be detected with the planned “Roman Pots” detectors located along the beam line (See Section A.5.6).

A.4.5 Diffractive measurements

Diffractive event measurements play an important role in nucleon and nucleus imaging. They are particularly sensitive to the gluon distribution in nuclei and hence to gluon saturation phenomena. Diffractive events are characterized by a rapidity gap, i.e. an angular region in the direction of the scattered proton or nucleus devoid of other particles. Figure A.19 shows the pseudorapidity distribution for the most forward going particle in DIS events and in diffractive events. Extending the forward acceptance of the detector to $\eta = 4$ and beyond is important if one is to have good capability using the rapidity gap method for detecting diffractive events and to separate them from DIS processes.

The planned ePHENIX EMCal and tracking coverage of $|\eta| < 4$ and hadronic calorimetry coverage of $-1 < \eta < 5$ are expected to provide excellent identification capabilities for diffractive events. In addition, to separate coherent (the nucleus remains intact) and

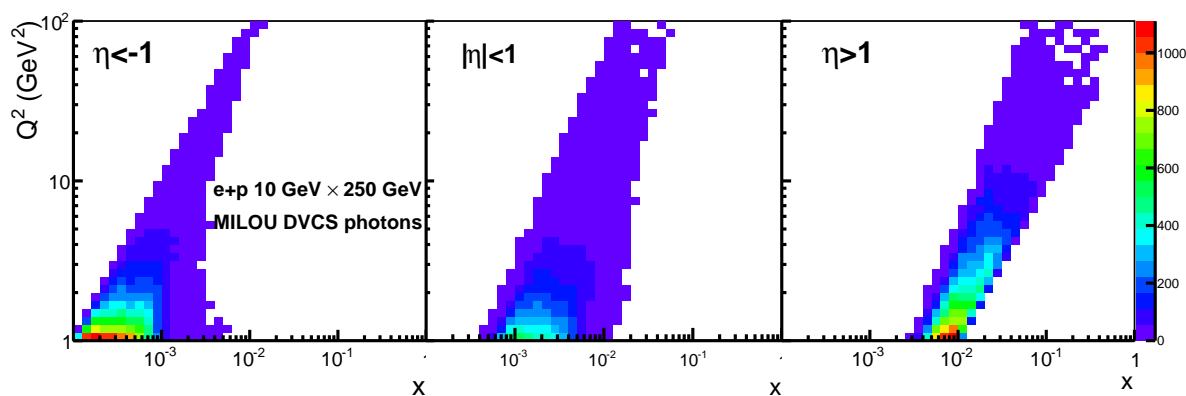


Figure A.18: For 10 GeV \times 250 GeV beam energy configuration: x - Q^2 coverage for DVCS events with photon detected in the electron-going direction, $\eta < -1$ (left), or central rapidities, $|\eta| < 1$ (middle) and hadron-going direction, $\eta > 1$ (right). The z -axis scale shows relative distribution of events from the MILOU event generator.

incoherent (the nucleus excites and breaks up) diffractive events, we plan to place a zero degree calorimeter after the first RHIC dipole magnet (see Section A.5.6), which is expected to be very efficient at detecting nuclear break-up by measuring the emitted neutrons.

A.5 Detector Concept

A full engineering rendering of ePHENIX is shown in Figure A.20. The drawing shows the ePHENIX detector in the existing PHENIX experimental hall and illustrates the reuse of the superconducting solenoid and the electromagnetic and hadronic calorimeter system of sPHENIX. The rendering also shows the final eRHIC focusing quadrupoles, each located 4.5 m from the interaction point (IP). Those magnets and the height of the beam pipe above the concrete floor, set the dominant physical constraints on the allowable dimensions of ePHENIX. This Section will describe the ePHENIX detector concept in terms of its component subdetectors and their expected performance.

The ePHENIX detector consists of a superconducting solenoid with excellent tracking and particle identification capabilities covering a large pseudorapidity range, as shown in Figure A.21. It builds upon an excellent foundation provided by the proposed sPHENIX upgrade [153] detailed in the MIE proposal submitted to the DOE Office of Nuclear Physics by Brookhaven National Laboratory in April 2013. The strong sPHENIX focus on jets for studying the strongly-coupled quark-gluon plasma in $p+p$, $p/d+A$ and $A+A$ is enabled by excellent electromagnetic and hadronic calorimetry in the central region ($|\eta| < 1$).

The C-AD Interaction Region (IR) design at the time the Letter of Intent charge was issued had the final focusing quadrupoles of the accelerator positioned ± 4.5 m from the IP and

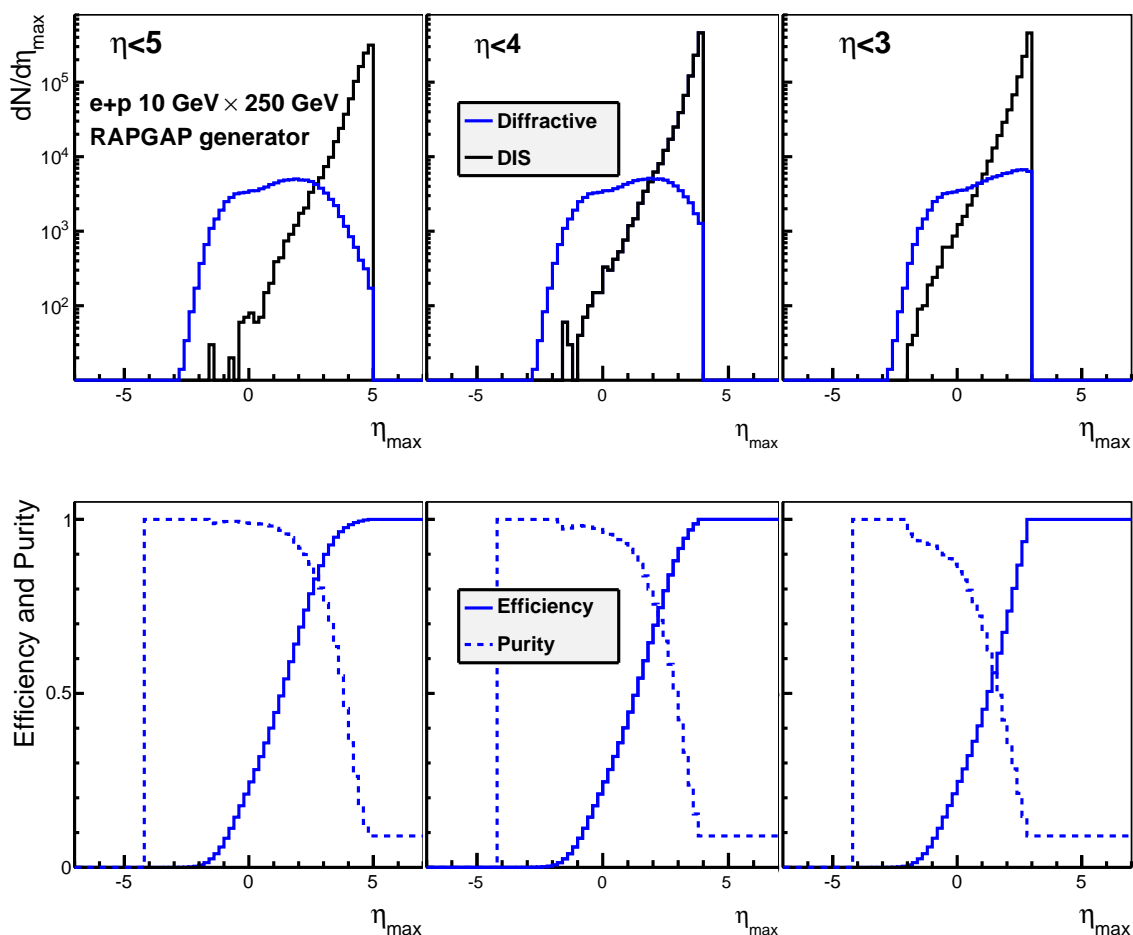


Figure A.19: For the 10 GeV \times 100 GeV beam energy configuration: Top: Pseudorapidity distribution for the most forward going particle in DIS events (black) and in diffractive events (blue); Bottom: Efficiency (dashed) and purity (solid) for diffractive event identification as a function of pseudorapidity cut defining the rapidity gap, for different detector acceptance: $|\eta| < 5$ (left), $|\eta| < 4$ (middle), $|\eta| < 3$ (right). Obtained using the RAPGAP generator developed at HERA and tuned to H1 and ZEUS data.

employed a “crab crossing” to maintain high luminosity while allowing the electron and hadron beams to intersect at an angle of 10 mrad (see Figure A.33). The ePHENIX detector concept shown in Figure A.20 and Figure A.21 respects these constraints. For instance, the hadronic calorimeter in the hadron-going direction fits within the 4.5 m constraint imposed by the accelerator magnets, and the detector is aligned so that the electron beam travels along the symmetry axis of the magnetic field. Clearly, the progress of ePHENIX from concept to final design will be done in close consultation with C-AD to ensure that the design of IR and the design of the detector remain synchronized.

We have an extensive GEANT4 description of the ePHENIX detector, based on the same

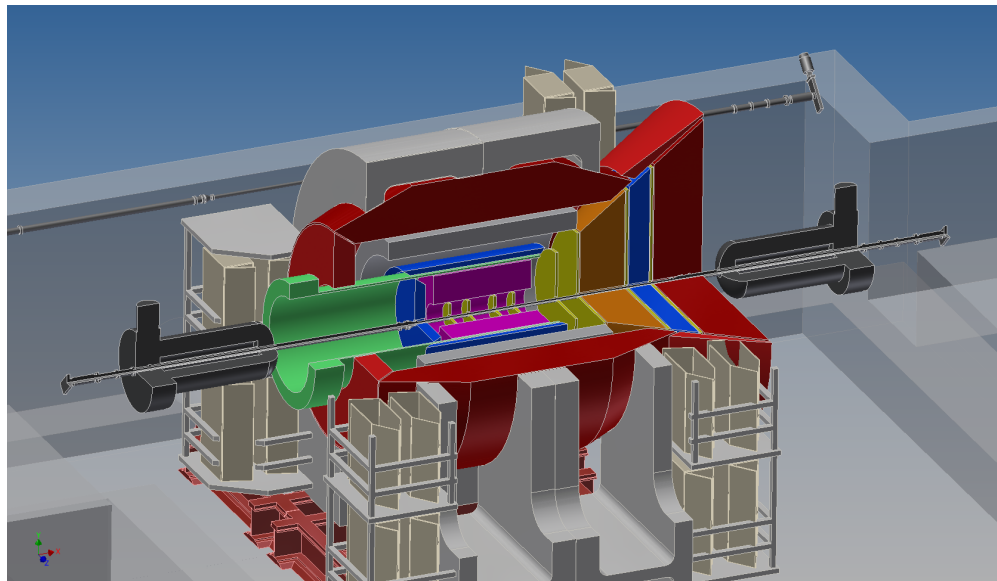


Figure A.20: Engineering rendering of ePHENIX in the PHENIX experimental hall. The drawing shows the location of the final eRHIC focusing quadrupoles as well as the electron bypass beamline behind the detector.

software framework as used in PHENIX and sPHENIX, which enables ready use of many existing PHENIX software analysis tools. An example of running a DIS event through the GEANT4 detector description is shown in Figure A.22.

The DOE funded sPHENIX subsystems which will be reused in ePHENIX are:

Superconducting solenoid: The sPHENIX detector concept reuses the BaBar superconducting solenoid to provide a 1.5 Tesla longitudinal tracking magnetic field. Its field is shaped in the forward directions with an updated yoke design in the ePHENIX detector as discussed in Section A.5.1.

Electromagnetic calorimeter: A tungsten-scintillator sampling electromagnetic calorimeter with silicon photomultipliers (SiPMs) enables a compact barrel calorimeter positioned inside the bore of the superconducting solenoid. The calorimeter system provides full azimuthal coverage for $|\eta| < 1$ with an energy resolution of $\sim 12\%/\sqrt{E}$. The readout is segmented into towers measuring roughly $\Delta\eta \times \Delta\phi \sim 0.024 \times 0.024$.

Hadronic calorimeter: A $5\lambda_{\text{int}}$ -depth hadron calorimeter surrounds the solenoid. An iron-plate and scintillator sampling design provides an energy resolution of better than $\sim 100\%/\sqrt{E}$ with full azimuthal coverage. It also serves as part of the magnetic flux return for the solenoid.

In addition, new subsystems will be added to the ePHENIX detector, which will be further discussed in this Section. These subsystems include:

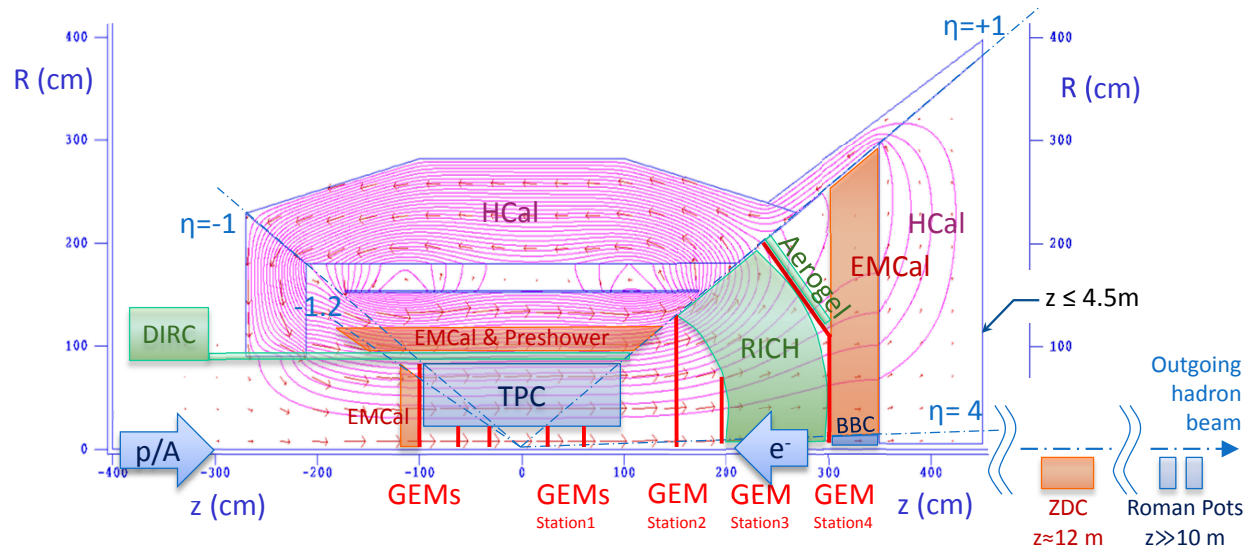


Figure A.21: A cross section through the top-half of the ePHENIX detector concept, showing the location of the superconducting solenoid, the barrel calorimeter system, the EMCal in the electron-going direction and the system of tracking, particle identification detectors and calorimeters in the hadron-going direction. Forward detectors are also shown along the outgoing hadron beamline. The magenta curves are contour lines of magnetic field potential as determined using the 2D magnetic field solver, POISSON.

Electron going direction: GEM detectors [154, 155] and lead-tungstate crystal electromagnetic calorimeters

Central barrel: Fast, compact TPC tracker and DIRC

Hadron going direction: GEM tracking system, gas-based RICH, aerogel-based RICH, beam-beam counter (BBC), electromagnetic and hadron calorimeter

Beam line of hadron-going direction: Roman pot detectors and a zero-degree calorimeter

A.5.1 Magnet system

As with sPHENIX, ePHENIX is based around the BaBar superconducting solenoid [156] with no modifications to its inner structure. The major specifications for its coil are listed in

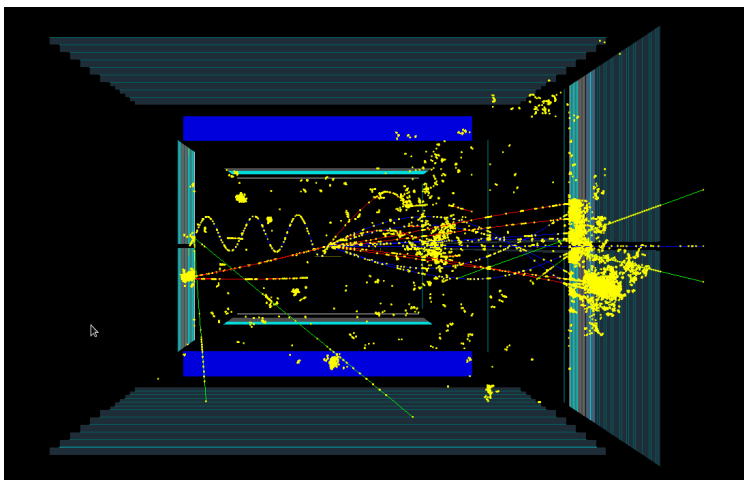


Figure A.22: The response of the ePHENIX detector to a single event, as determined using GEANT4. The field map in this simulation was determined using the 2D magnetic field solver OPERA. These same OPERA calculations were used to verify and validate the calculations underlying the magnetic field lines shown in Figure A.21.

Table A.2: Main characteristics of BaBar solenoid [156]

Central Induction	1.5 T
Winding structure	2 layers, 2/3 higher current density at both ends
Winding axial length	3512 mm
Winding mean radius	1530 mm
BaBar operation current	4596 A, 33% of critical current
Total turns	1067

Table A.2. A notable feature of the BaBar magnet is that the current density of the solenoid can be varied along its length, i.e., lower current density in the central region and higher current density at both ends. This is accomplished by using narrower windings (5 mm) for the last 1 m at both ends. The central winding uses 8.4 mm-width coils [156]. The main purpose of the graded current density is to maintain a high field uniformity in the bore of the solenoid, which is also a benefit for ePHENIX. This design feature enhances the momentum analyzing power in both the electron-going and hadron-going directions.

A magnetic flux return system, consisting of the forward steel/scintillator hadron calorimeter, a flaring steel lampshade, and a steel endcap not only returns the flux generated by the

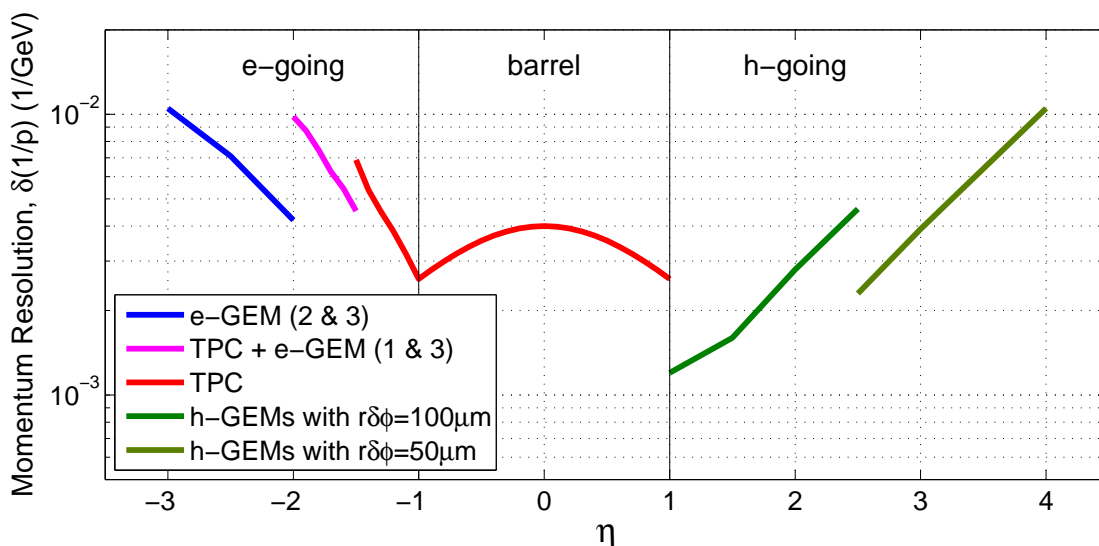


Figure A.23: Momentum resolution over the full pseudorapidity coverage of the planned tracking system in the high momentum limit. Multiple scattering contribution to the relative momentum resolution (not shown on the plot) was studied with GEANT4 simulation, and found to vary from below 1% at low pseudorapidity to $\sim 3\%$ at $|\eta|=3$.

solenoid, but shapes the field in order to aid the momentum determination for particles in the hadron-going and electron-going directions. As shown in Figure A.21, the flux return system consists of the following major components:

- Forward steel/scintillator hadron calorimeter, at $z = 3.5$ to 4.5 m
- Steel flux shaping lampshade, along the $\eta \sim 1$ line
- Barrel steel/scintillator hadron calorimeter, from $r = 1.8$ to 2.8 m
- Steel end cap, at $z = -2.1$ to -2.7 m and $r > 90$ cm

The magnetic field lines were calculated and cross checked using three different 2D magnetic field solvers (POISSON, FEM, and OPERA) and are shown in Figure A.21. In the central region, a 1.5 Tesla central field along the electron beam direction is produced. The field strength variation within the central tracking volume is less than $\pm 3\%$.

A.5.2 Vertex and Tracking

The z -location of the primary event vertex will be determined using a timing system enabling a precision of $\Delta z \leq 5$ mm. The ePHENIX tracking system utilizes a combination of GEM and TPC trackers to cover the pseudorapidity range of $-3 < \eta < 4$. The momentum resolution for the full device is summarized in Figure A.23.

Event vertex measurement

The vertex information is used for the determination of photon kinematics and for assisting the track fitting. Precise vertex information is important for momentum determination in the electron-going direction, where tight space constraints limit the possible number of tracking planes. The location of the vertex will be measured by:

- For non-exclusive processes, we propose to identify the z-location for the vertex using timing information from a BBC detector in the hadron-going direction in coincidence with the electron beam RF timing. The BBC detector covers $\eta = 4\text{--}5$ at $z = 3.0$ m. A timing resolution of 30 ps or better enables the measurement of the vertex with resolution of $\Delta z = 5$ mm. It leads to a sub-dominant error for the momentum determination for the electron-going direction ($\delta p/p = 2\%$). This timing resolution can be provided by the existing technology of Multigap Resistive Plate Chamber (MRPC) [157] or by microchannel plate detectors (MCP) photomultiplier [158] with a thin quartz Čerenkov radiator, a technology which is under active current development.
- We plan to measure the average transverse beam position by accumulating tracking information over the course of a one hour run. The statistical precision for the beam center determination is expected to be much smaller than the distribution of the transverse collision profile ($\sigma_{x,y} \sim 80 \mu\text{m}$), and therefore a negligible contribution to the uncertainty for event-by-event vertex determination.

Tracking in the central region, $-1 < \eta < 1$

A fast, compact Time Projection Chamber (TPC) will be used for tracking in the central region, occupying the central tracking volume of $r = 15\text{--}80$ cm and $|z| < 95$ cm and covering $-1 < \eta < 1$. A TPC will provide multiple high resolution space point measurements with a minimal amount of mass and multiple scattering. The design is based on a GEM readout TPC, similar to a number of TPCs that have either already been built or are currently under design. For example, the LEGS TPC [159] utilized a fine chevron-type readout pattern with a pad size of $2 \text{ mm} \times 5 \text{ mm}$ and achieved a spatial resolution $\sim 200 \mu\text{m}$. The use of such a readout pattern helps minimize the total channel count for the electronics and hence the total cost. The GEM TPC upgrade for ALICE [160, 161] and the large GEM readout TPC for ILC [162, 163] are other examples of large GEM TPCs that have recently been studied.

It is assumed that the TPC will have a single high voltage plane at $z = 0$ cm and be read out on both ends, resulting in a maximum drift distance ~ 95 cm. It will use a gas mixture with a fast drift time, such as 80% argon, 10% CF_4 and 10% CO_2 , which, at an electrical field of 650 V/m, achieves a drift speed $\sim 10 \text{ cm}/\mu\text{s}$, and would result in a maximum drift time of 10 μs . With a position resolution of $\sigma(r\Delta\phi) = 300 \mu\text{m}$ and 65 readout rows, the expected transverse momentum resolution would be $\delta(1/p_T) = 0.4\% / (\text{GeV}/c)$ for high momentum tracks.

Tracking in hadron-going direction, $\eta > 1$

The design of the magnetic flux return enables tracking in the hadron-going direction in the main and fringe fields of the BaBar magnet. Compared to a compact solenoid with no current density gradient, the BaBar magnet system improves the momentum analyzing power for forward tracks by about a factor of four due to two main factors: 1) the BaBar magnet has a length of 3.5 m, which provides a longer path length for magnetic bending; 2) the higher current density at the ends of the solenoid improves the magnetic field component transverse to forward tracks, and therefore provides higher analyzing power.

The tracking system at high η in the hadron-going direction utilizes four stations of GEMs.

- Station 1 consists of two planes with complementary η coverages. They are located at $z = 17$ and 60 cm, respectively, covering a radius of $r = 2$ – 15 cm.
- Stations 2–4 are at $z = 150, 200, 300$ cm, respectively, covering $\eta = 1$ – 4 .

The readout planes for these devices are optimized to preserve high position resolution in the azimuthal direction ($\sim 200 \mu\text{m}$ in $r\delta\phi$ using a chevron-type readout with a pad size similar to the central TPC) and ~ 10 – 100 mm in δr , while minimizing the readout channel cost. However, the r - ϕ resolution can be improved to be better than $100 \mu\text{m}$, even for tracks at larger angles (up to 45 degrees), by the use of mini-drift GEM detectors, in which a small track segment, or vector, is measured for each track at each measuring station. These detectors, which are currently under development [164], would provide improved position resolution with less material and lower cost than multiple stations of planar GEM detectors. For this letter, we assumed that a high resolution GEM readout pattern (1 mm wide chevron-type readout) with a $r\delta\phi \sim 50 \mu\text{m}$ for the inner tracking region ($\eta > 2.5$). For the outer tracking region ($1 < \eta < 2.5$), mini-drift GEM with 2 mm chevron-type readout provide $r\delta\phi \sim 100 \mu\text{m}$. The momentum resolution is estimated in Figure A.23.

It should be noted that the size of the GEM trackers for Stations 2–4 are quite large (~ 5 – 20 m^2). It is currently challenging to produce such large GEM foils and to do so at an affordable cost. However, there has been substantial progress in this area in recent years at CERN due to the need for large area GEM detectors for the CMS Forward Upgrade [165]. CERN has developed a single mask etching technology which allows fabrication of very large area GEMs (up to $2 \text{ m} \times 0.5 \text{ m}$), and they plan to transfer this technology to various commercial partners (such as Tech Etch in the US, which supplied the GEM foils for the STAR Forward GEM Detector). We anticipate being able to procure such large area GEM detectors by the time they are needed for EIC.

Tracking in the electron-going direction, $\eta < -1$

The electron direction tracking is designed to fit in the space limited by the DIRC ($R < 80$ cm) and the electromagnetic calorimeter ($z > -100$ cm). Three GEM tracking stations,

located at $z = 30, 55$ and 98 cm, are used in combination with the TPC and vertex information to determine the momentum vector.

- For $\eta = -1.5$ to -1 , TPC track segment and vertex are used
- For $\eta = -2.0$ to -1.5 , vertex, TPC track segment, GEM station 1 and 3 are used.
- For $\eta = -3.0$ to -2.0 , vertex, GEM station 2 and 3 are used.

Similar to the hadron-going direction, the position resolution for these detectors is $r\Delta\phi$ $50 \mu\text{m}$ for $-3 < \eta < -2$ using 1 mm wide chevron-type readout. For $-2 < \eta < -1$, the mini-drift GEM technology [164] and 2 mm wide chevron-type readout provide $r\delta\phi \sim 100 \mu\text{m}$. The radial resolution is $\delta r = 1$ cm (stations 1 and 2) and $\delta r = 10$ cm (station 3). As shown in Figure A.23, a momentum resolution of $\Delta p/p < 5\%$ can be achieved for tracks of $p < 4$ GeV/ c and $-1 < \eta < -3$, which is sufficient for the calorimeter E - p matching cut for the electron identification. For DIS kinematics reconstruction the tracking radial resolution is not crucial as enough precision for scattered electron polar angle measurements will be provided by the EMCal, see Section A.4.2.

A.5.3 Electromagnetic calorimeters

The ePHENIX detector will have full electromagnetic calorimeter coverage over $-4 < \eta < 4$. The sPHENIX barrel electromagnetic calorimeters will also be used in ePHENIX, covering $-1 < \eta < 1$ with an energy resolution of $\sim 12\%/\sqrt{E}$. In addition, crystal and lead-scintillator electromagnetic calorimeter are planned for the electron-going and hadron-going direction, respectively. Optimization of the design of the barrel and endcap calorimeters will aim for uniform response in the overlap region between $-1.2 < \eta < -1$.

Crystal Electromagnetic calorimeter

The calorimeter on the electron-going side consists of an array of lead tungstate (PbWO_4) crystals (commonly known as PWO), similar to the PANDA endcap crystal calorimeter shown in Figure A.24 [166]. An enhanced light output version of lead tungstate (PWO-II) was chosen to provide high light yield (~ 20 p.e./MeV at room temperature) at a moderate cost ($\sim \text{€}5/\text{cm}^3$). It will provide an energy resolution $\sim 1.5\%/\sqrt{E}$ and position resolution better than $3 \text{ mm}/\sqrt{E}$ in order to measure the scattered electron energy and angle in the electron-going direction down to low momentum with high precision.

The ePHENIX PWO calorimeter will consist of ~ 5000 crystals, compared with 4400 crystals for the PANDA endcap, and will have a similar size and shape to the PANDA crystals. They will be $\sim 2 \text{ cm} \times 2 \text{ cm}$ (corresponding to one R_M^2) and will be read out with four SiPMs. This is different than the PANDA readout, which uses large area ($\sim 1 \text{ cm}^2$)

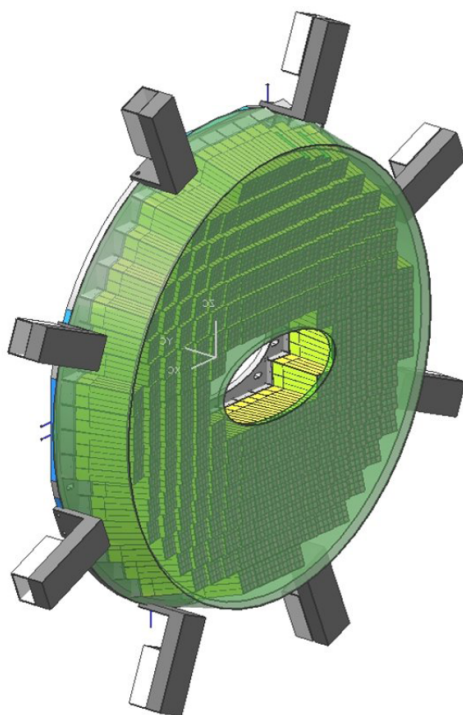


Figure A.24: PANDA Crystal Endcap Calorimeter [166]. The PW0 crystal modules are shown in green color, which is projective towards the target.

APDs. The SiPMs will provide higher gain, thus simplifying the readout electronics, and will utilize the same readout electronics as the other calorimeter systems in sPHENIX. It is also expected that the cost of SiPMs will be less than that of APDs covering the same area by the time they are needed for ePHENIX.

Lead-scintillator electromagnetic calorimeter

The electromagnetic calorimeter in the hadron-going direction consists of a lead-scintillating fiber sampling configuration, similar to the tungsten-scintillating fiber calorimeter in the central sPHENIX detector. Lead is used instead of tungsten in order to reduce the cost, but it is otherwise assumed to be of a similar geometry. It will cover the rapidity range from $1 < \eta < 4$ and have $0.3 X_0$ sampling (2 mm lead plates) with 1 mm scintillating fibers, which will give an energy resolution $\sim 12\%/\sqrt{E}$. The segmentation and readout will also be similar to the central tungsten calorimeter, with $\sim 3 \text{ cm} \times 3 \text{ cm}$ towers (roughly $1 R_M^2$) that are read out with SiPMs. This segmentation leads to $\sim 26\text{K}$ towers. By using the same type of readout as the central calorimeter, the front end electronics and readout system will also be similar, resulting in an overall cost savings for the combined calorimeter systems.

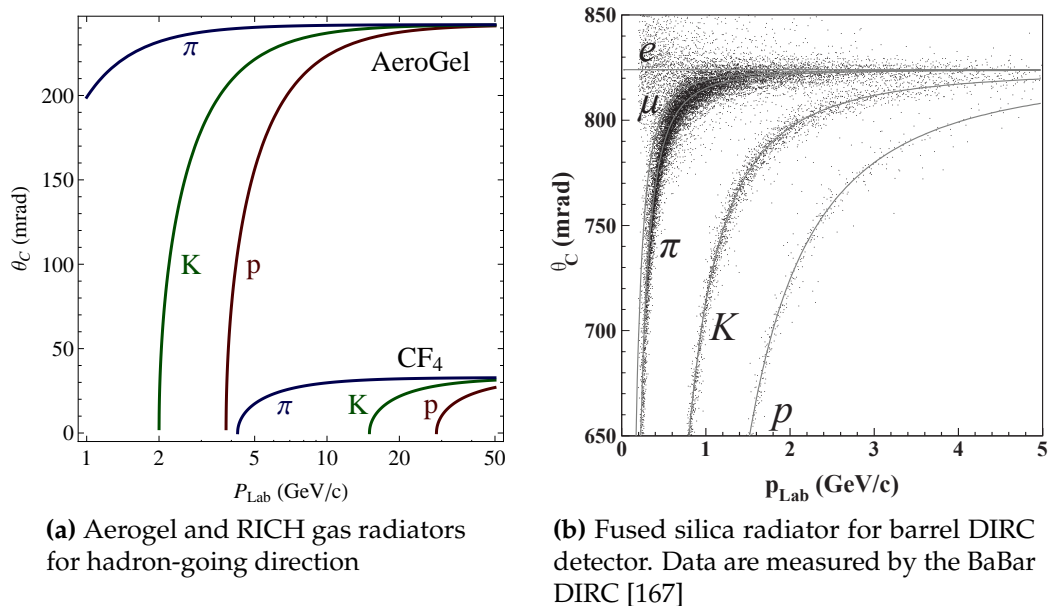


Figure A.25: Čerenkov angle versus momentum for various particle species.

A.5.4 Hadron calorimeter

The hadron calorimeter in the hadron-going direction consists of a steel-scintillating tile design with wavelength shifting fiber readout, similar to the central sPHENIX hadron calorimeter. It will be $\sim 5 L_{abs}$ thick and cover a rapidity range from $1 < \eta < 5$. The steel in the absorber will also serve as part of the flux return for the solenoid magnet. The segmentation will be $\sim 10 \text{ cm} \times 10 \text{ cm}$, resulting in ~ 3000 towers. The readout will also be with SiPMs, similar to the central sPHENIX HCAL, which will again provide an advantage in being able to use a common readout for all of the calorimeter systems.

A.5.5 Hadron PID detectors

Hadron PID is planned for the hadron-going and barrel regions, covering $-1.2 < \eta < 4$. In the hadron-going direction, two PID detectors cover complementary momentum range: a gas-based RICH detector for the higher momentum tracks and an aerogel-based RICH detector for the lower momentum region. As in the BaBar experiment [167], a DIRC detector identifies hadron species in the central barrel. In addition, the TPC detector assists with PID by providing dE/dx information for the low momentum region.

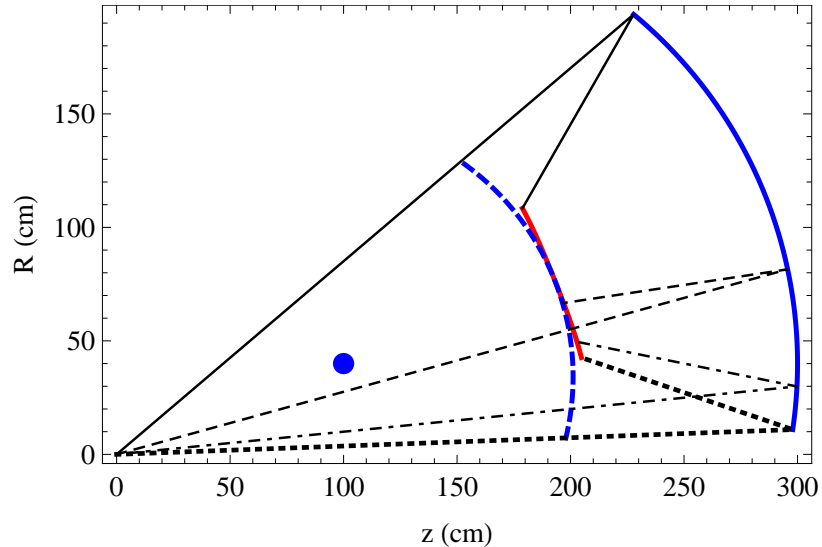


Figure A.26: The cross-section of the gas-based RICH detector in the r - z plane that crosses the mirror center. The interaction point is centered at $(0, 0)$. The geometric center of the mirror is shown as the blue dot at $(r, z) = (40 \text{ cm}, 100 \text{ cm})$. The mirror and RICH entrance window are shown by the solid and dashed blue curves, respectively. Several example tracks and the central axis of their Čerenkov light cone are illustrated by the black lines. The Čerenkov photons are reflected by the mirror to the focal plane, shown in red.

Gas RICH detector

High momentum hadron PID is provided by an optically focused RICH detector using a gas radiator. The main features for this RICH setup are

- One meter of CF_4 gas is used as the Čerenkov radiator. The pion, kaon and proton thresholds are 4, 15 and 29 GeV, respectively.
- Čerenkov photons are focused to an approximately flat focal plane using spherical mirrors of 2 m radius, as shown in Figure A.26. The geometric center of the mirror is at $(r, z) = (40 \text{ cm}, 100 \text{ cm})$, as highlighted by the blue dot.
- There are six azimuthal segmented RICH sextants.
- The photon detector consists of CsI-coated GEM detectors [168], which are installed on the focal plane. The CsI coating converts the Čerenkov photons into electrons which are then amplified by the GEM layers and readout through mini-pads. The photon detector for each RICH sextant assumes a roughly triangle shape and covers an area of 0.3 m^2 .

Two distortion effects were estimated to be sub-dominant in error contributions for most cases:

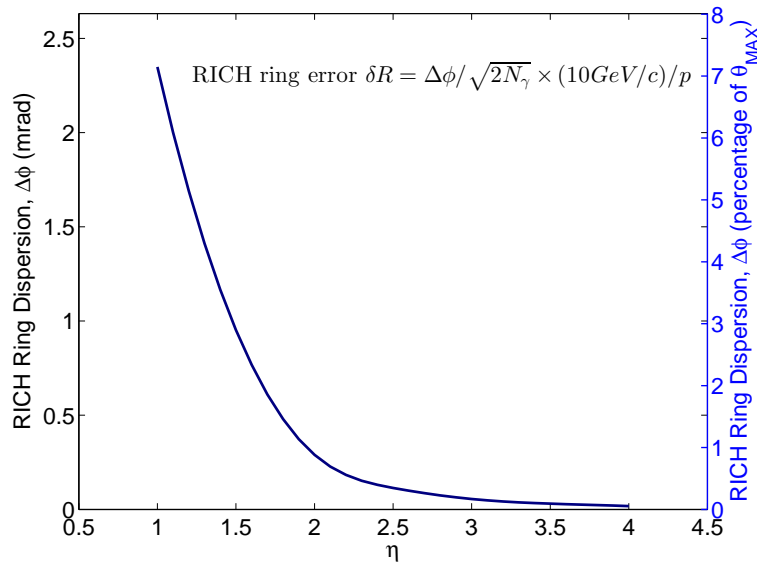


Figure A.27: Azimuthal angular dispersion of gas-based RICH ring due to fringe magnetic field for a $p = 10 \text{ GeV}/c$ track. It is compared to the maximum RICH ring angle as shown on the right vertical axis.

- Strong residual magnetic field (~ 0.5 Tesla) are present in the RICH volume. This field will bend the tracks as they radiate photons, and therefore smear the Čerenkov ring in the azimuthal direction. However, the field design ensures that the field component is mostly parallel to the track inside RICH and therefore this smearing effect is minimized. The RMS size of the smearing, $\Delta\phi$, is evaluated as in Figure A.27. The uncertainty contribution to the RICH ring angular radius is $\delta R = \Delta\phi / \sqrt{2N_\gamma} (10 \text{ GeV}/c) / p$, which is sub-dominant comparing to the photon measurement error for $\eta > 1.5$. The field contribution was included in the RICH performance estimation.
- For tracks that originate from an off-center vertex, their focal point may be offset from the nominal focal plane as shown in Figure A.26. The effect is η dependent. For the most extreme case, that a track of $\eta = 1$ originates from the vertex of $z = 40 \text{ cm}$ (1.5 sigma of expected vertex width), an additional relative error of $5\% / \sqrt{N_\gamma}$ is contributed to the ring radius measurement, which averages over all vertices to below $2\% / \sqrt{N_\gamma}$ contribution. For high η tracks, the difference is negligible comparing to the nominal RICH error.

We simulated the RICH performance with a radiator gas CF_4 (index of refraction 1.00062). We use PYTHIA to generate the momentum distributions for pions, kaons, and protons. For each particle species, we use the momentum resolution and RICH angular resolution, to calculate the particle mass $m(p, \theta_{Crk})$ distribution. For higher momentum tracks the combined information from tracking system and energy deposit in HCal helps to improve

momentum resolution particularly at higher rapidities, where momentum resolution from tracking degrades. For example, at pseudorapidity $\eta=4$, the tracking momentum resolution for 50 GeV/c tracks is $\sim 50\%$ (see Figure A.23), while HCal can provide energy measurements with precision $100\% / \sqrt{50[\text{GeV}]} \sim 14\%$. Our simulation showed that the HCal is very effective in improving the resolution for high momentum track measurements even when this and other tracks (usually with lower momenta) are merged in a single cluster of deposited energy in HCal. In such a case, the contribution of lower energy tracks in HCal can be evaluated and subtracted based on momentum measurements in tracking system.

Figure A.28 shows mass distributions for the most challenging high rapidity region $\eta=4$ for different reconstructed track momenta. We make a symmetric 90% efficiency cut on the mass distributions, and calculate the purity for π, K, p , shown in Figure A.29. One can see high purity for all particle species up to momenta ~ 50 GeV/c. Introducing asymmetric cuts on the mass distributions (and sacrificing some efficiency) extends further our capabilities for high purity hadron identification.

It is notable that the limitation on the mass resolution comes from the estimated 2.5% radius resolution per photon for the RICH from the EIC R&D RICH group. Our calculation includes the effect of the magnetic field distortion mentioned above, which is sub-dominant. This is a somewhat conservative estimate and LHCb and COMPASS have quoted values near 1% per photon. The R&D effort is working towards the best radius resolution, though there are challenges in having the light focus and readout within the gas volume in this configuration compared with LHCb or COMPASS.

Aerogel RICH detector

The aerogel detector will provide additional particle ID for kaons in the momentum range $\sim 3\text{--}15$ GeV/c when used in conjunction with the gas RICH. Pions can be identified by the signal they produce in the gas RICH starting at a threshold of ~ 4 GeV/c, and kaons will begin producing a signal in the aerogel at a threshold ~ 3 GeV. Reconstructing a Čerenkov ring in the aerogel enables one to separate kaons from protons up to a momentum ~ 10 GeV/c with reduced efficiency above that.

Measuring a ring in the aerogel detector is a challenging technical problem for a number of reasons. Due to its relatively low light output, it will require detecting single photons in the visible wavelength range with high efficiency inside the rather strong fringe field of the superconducting solenoid. Also, due to the limited space available, it is difficult to have a strong focusing element in the RICH to focus the light into a ring in a short distance. One possibility for how this might be accomplished has been proposed by the Belle II experiment [169] and is shown in Figure A.30. It uses several layers of aerogel with slightly different indices of refraction to achieve and approximate focusing of the light onto an image plane located behind the radiator. It should be possible to add additional layers of aerogel and optimize their thickness for producing the best quality ring for kaons

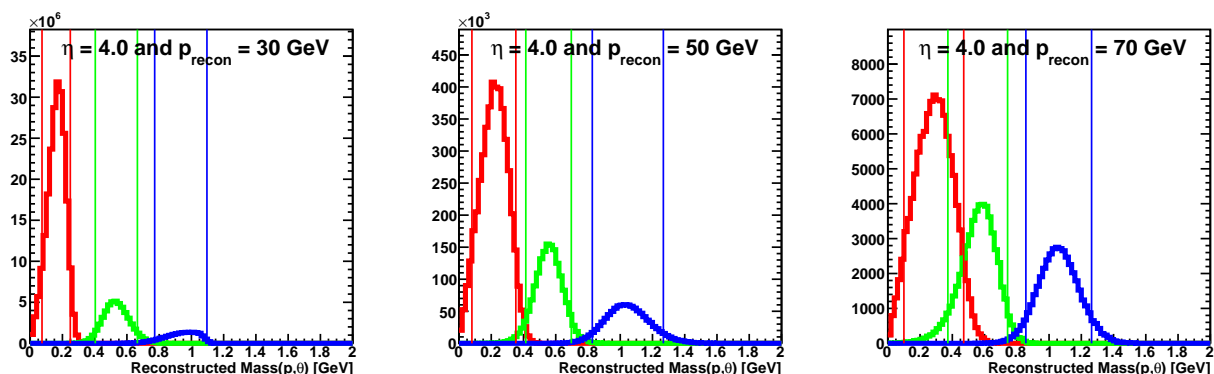


Figure A.28: Reconstructed mass distribution via $m(p, \theta_{Crk})$ at $\eta = 4$ for reconstructed momenta 30 GeV/c (left), 50 GeV/c (middle) and 70 GeV/c (right), for pions (red), kaons (green) and protons (blue), with the parent momentum and particle abundances from the PYTHIA generator. Vertical lines indicate the symmetric mass cuts corresponding to 90% efficiency. Note that particle true momentum is on the average smaller than reconstructed momentum, see Figure A.29.

using this technique, and therefore achieve good kaon-proton separation up to the highest momentum. One possibility for the photon detector would be large area Microchannel Plate detectors (MCPs), such as those being developed by the Large Area Picosecond Photodetector (LAPPD) Collaboration [158]. This effort is based on utilizing flat panel screen technology to produce large area MCPs at very low cost, while also preserving their excellent timing resolution (typically ~ 20 -30 ps). These devices would use multi-alkali photocathodes, which would be suitable for detecting the Cherenov light from aerogel with high efficiency, and also provide high gain for detecting single photoelectrons. The excellent time resolution would also provide additional time of flight capability when used in conjunction with the BBC to further enhance hadron particle ID. While this is still an R&D effort, it has already produced very encouraging results and has substantial support within the high energy physics community, and we feel that this would offer an attractive low cost, high performance readout for the aerogel detector.

DIRC

The main form of particle ID in the central region will be provided by a DIRC (Detection of Internally Reflected Čerenkov Light). The DIRC will be located at a radius of ~ 80 cm and extend ~ 8 -10 cm in the radial direction. As we will be using the BaBar magnet

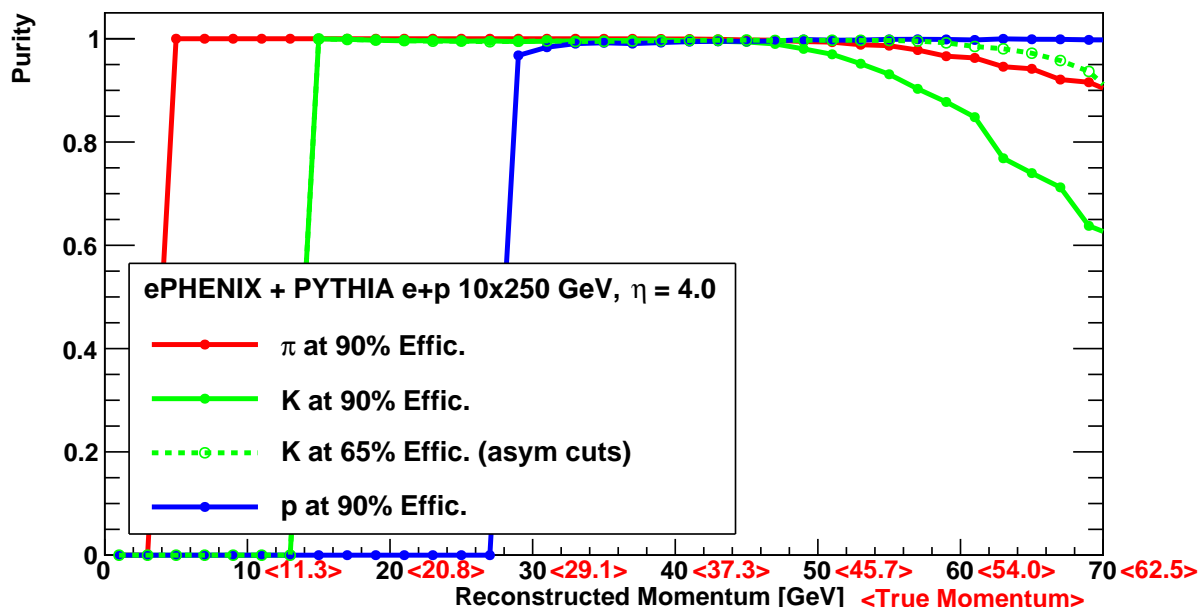


Figure A.29: π, K, p purities at pseudorapidity 4.0 as a function of reconstructed momentum, based on symmetric cut on reconstructed mass corresponding to 90% efficiency (solid lines), and asymmetric cut with stricter selection on the kaons with efficiency 65% (dashed line); Also indicated in angle brackets are the values of the average true momentum at each reconstructed momentum, which are different due to momentum smearing and sharply falling momentum spectra.

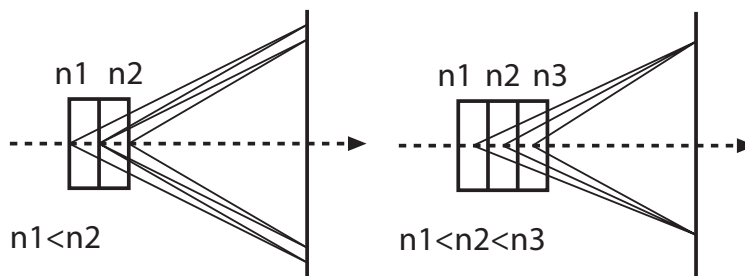


Figure A.30: Approximate focusing method using two (left) and three (right) layers of aerogel with slightly different indices of refraction proposed by Belle II [169]

for ePHENIX, it would be a major benefit to also acquire the BaBar DIRC, which was specifically designed to fit inside this magnet, and would completely satisfy the physics requirements for ePHENIX. However, since it is not certain at this time that the BaBar DIRC will be available for ePHENIX, we consider it more as a model for the type of DIRC that would be required in terms of its construction and performance.

The BaBar DIRC, shown in Figure A.31, consists of 144 precision fabricated quartz radiator bars that collect Čerenkov light produced by charged particles traversing the bars. In

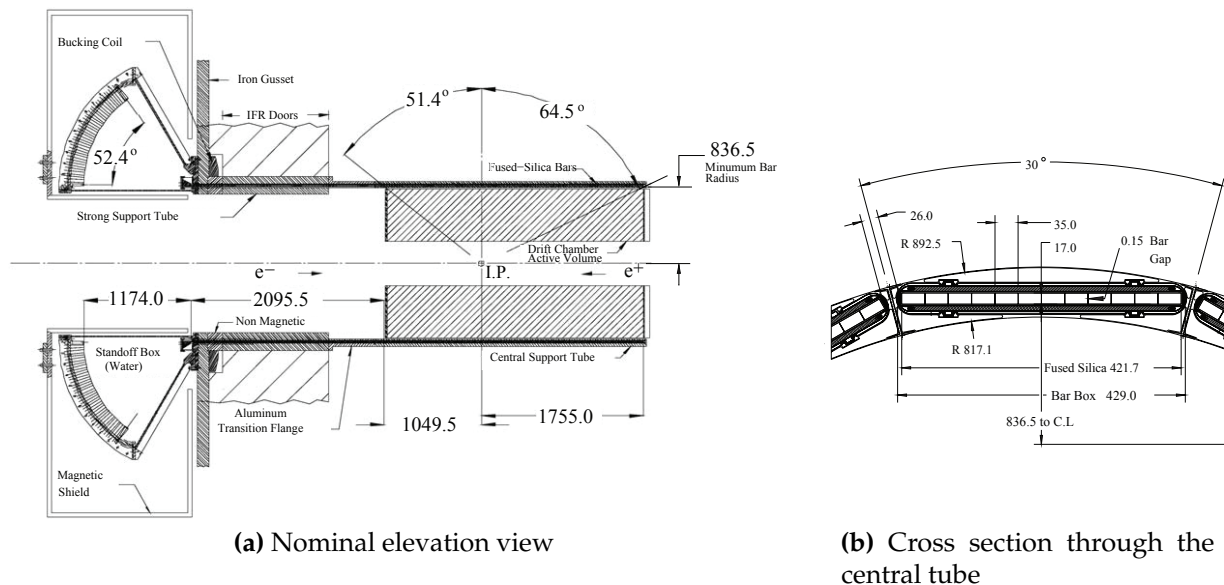


Figure A.31: BaBar DIRC geometry [167]. All dimensions are given in mm.

the BaBar DIRC, the quartz bars were read out on one end utilizing a large water filled expansion volume to allow the light to spread out and be read out using a large number (over 10,000) 28 mm diameter photomultiplier tubes.

The BaBar design, while allowing for a conventional PMT readout without the use of any focusing elements, requires a large expansion volume and this places stringent demands on the mechanical specifications for the detector. After the shutdown of BaBar at SLAC, it was proposed to use the DIRC in the SuperB Experiment in Italy. In doing so, it was also proposed to convert the original DIRC into a Focusing DIRC (FDIRC) [170], which would utilize mirrors at the end of the radiator bars, allowing for a considerable reduction in the size of the expansion region, more highly pixellated PMTs, and an overall expected improvement in performance. We would therefore propose the same modification of the BaBar DIRC for ePHENIX, or would construct a similar FDIRC if the BaBar DIRC were not available.

Similar to the BaBar technique [167], the hadron PID in the barrel will be analyzed using an event likelihood analysis with the DIRC and TPC dE/dx information simultaneously. A dE/dx measurement in the TPC gives very good hadron separation for very low momentum particles. But the ability of that technique to separate $K-\pi$ and $p-K$ drops off quickly around $0.5 \text{ GeV}/c$ and $0.8 \text{ GeV}/c$, respectively. Meanwhile, the pions and kaons exceed their respective DIRC Čerenkov thresholds in this momentum region, as shown in Figure A.25. Therefore, the DIRC sensitivity for $K-\pi$ and $p-K$ turns on sharply. A combined analysis of both pieces of information can give high PID purity up to a few GeV/c , as shown by the BaBar experiment [167]. At higher momenta, the DIRC ring resolution limits the separation capability. As shown in Figure A.32, the $K-\pi$ and $p-K$ separation gradually drops below plateau above momentum of 2 and 5 GeV/c , respectively. A $\sim 20\%$ pion and

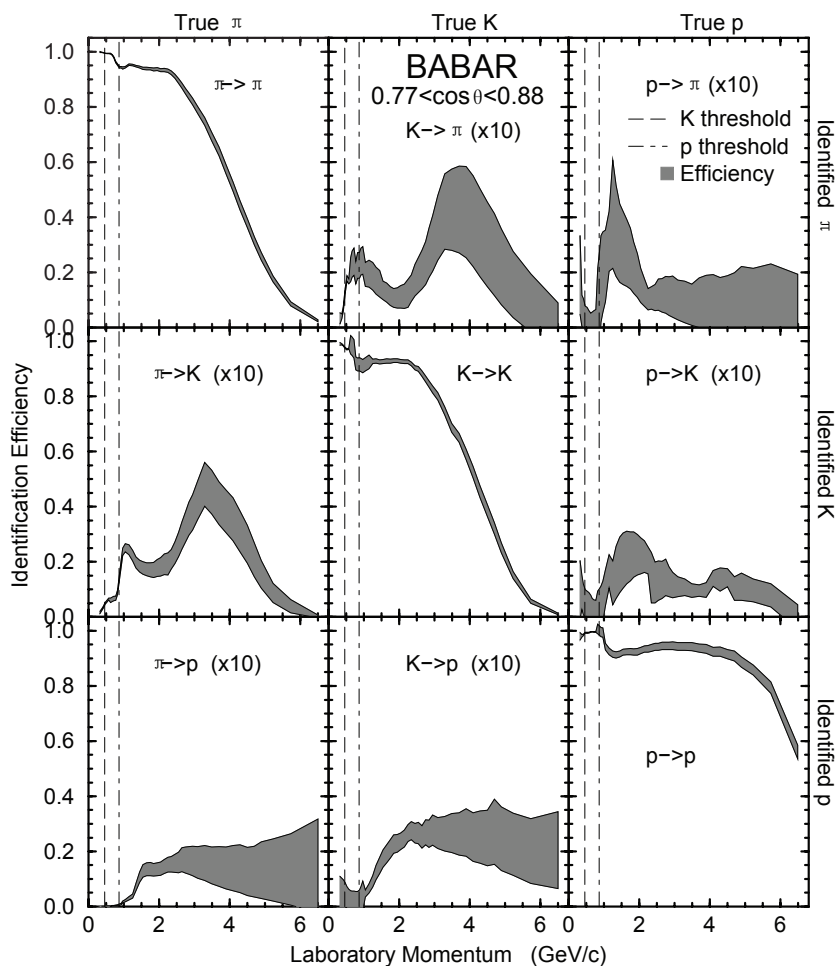


Figure A.32: Simulated PID Efficiency matrix and its uncertainty for $1.0 < \eta < 1.4$ region, utilizing combined information of the BaBar DIRC and dE/dx measured in the tracking detector [167]. Note that the off-diagonal efficiency values are scaled by a factor of 10.

kaon efficiency can still be maintained at 5 GeV/c. The vast majority of hadron kinematics in SIDIS can be covered in the 5×100 GeV/c collisions. In the 10×250 GeV/c collisions, the low to intermediate- z region in SIDIS are still well covered by this design.

A.5.6 Beamline detectors

Two detectors will be installed near the outgoing hadron beam, downstream of the ePHENIX detector. They will be included in the eRHIC machine lattice design [144].

Zero Degree Calorimeter: A Zero Degree Calorimeter (ZDC) is planned for the hadron-going direction for the ePHENIX IP. Consistent with the eRHIC IR design

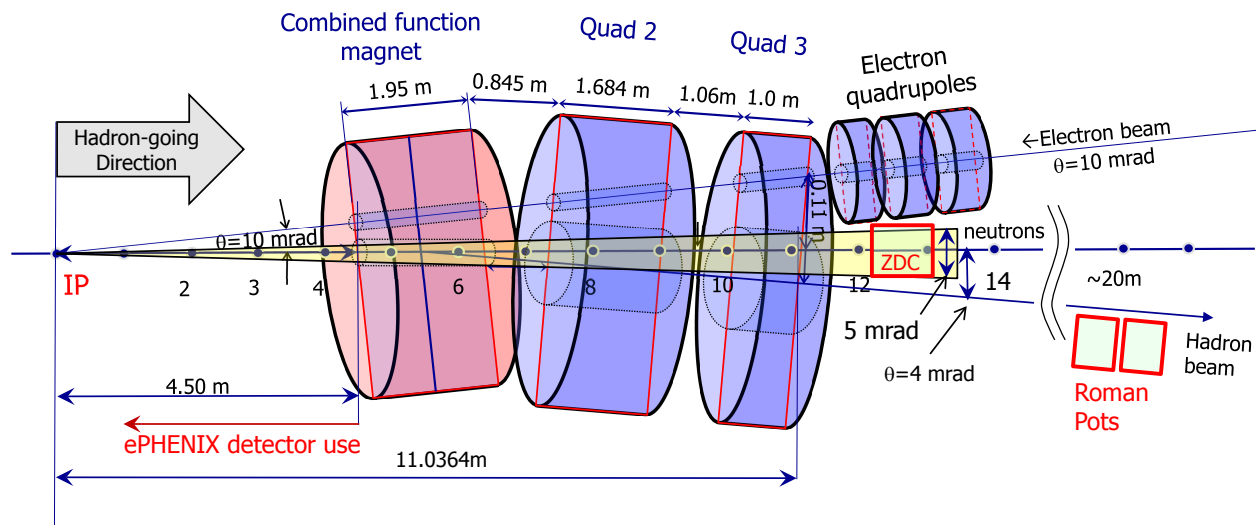


Figure A.33: Floor plan show the locations for ZDC and Roman Pots relative to the ePHENIX interaction point. One layout of the interaction point magnets are also shown [171].

(Figure A.33), the ZDC will be installed about 12 meters downstream of the IP centered on the hadron direction at the IP. A 5 mrad cone opening of the IP is guaranteed by the ePHENIX detector and beam line magnets. The ZDC for the current PHENIX experiment [172] and its design can be reused for this device.

Roman Pots: In exclusive deep inelastic $e+p$ scattering, the final state proton will have a small scattering angle and escape the main ePHENIX detector. Two silicon tracking stations (also called the Roman Pot spectrometer) will be installed close to the beam, inside the beam pipe, downstream in the hadron-going direction to capture such protons. Each of the ePHENIX Roman Pot stations utilizes four tracking modules to cover the full azimuthal angles. Each of the tracking modules can use the design of the existing STAR Roman Pots [173]. Depending on the eRHIC lattice and magnet design, their location will be around 20 meters from the IP. This Roman Pot spectrometer will provide high efficiency for the exclusive DIS events in the $e+p$ collisions.

Appendix B

The PHENIX Collaboration

Abilene Christian University, *Abilene, Texas 79699, USA*

M.S. Daugherty, K. Gainey, D. Isenhower, H. Qu, A. Tate, R. Towell, R.S. Towell*,
T.S. Watson

Department of Physics, *Banaras Hindu University, Varanasi 221005, India*

P. Garg, P.K. Khandai, B.K. Singh, C.P. Singh*, V. Singh

Bhabha Atomic Research Centre, *Bombay 400 085, India*

D.K. Mishra, A.K. Mohanty*, P.K. Netrakanti, P. Sett, P. Shukla

Baruch College, *City University of New York, New York, New York, 10010 USA*

S. Bathe*, J. Bryslawskyj

Collider-Accelerator Department, *Brookhaven National Laboratory, Upton, New York
11973-5000, USA*

M. Bai, K.A. Drees, S. Edwards, Y.I. Makdisi*, A. Zelenski

Physics Department, *Brookhaven National Laboratory, Upton, New York 11973-5000, USA*

B. Azmoun, A. Bazilevsky, S. Boose, M. Chiu, G. David, E.J. Desmond, K.O. Eyser,
A. Franz, P. Giannotti, J.S. Haggerty, J. Jia, B.M. Johnson, H.-J. Kehayias, E. Kistenev,
D. Lynch, E. Mannel, J.T. Mitchell, D.P. Morrison, R. Nouicer, E. O'Brien, R. Pak,
C. Pinkenburg, R.P. Pisani, M.L. Purschke, T. Sakaguchi, A. Sickles, I.V. Sourikova,
P. Steinberg, S.P. Stoll, A. Sukhanov, M.J. Tannenbaum*, C.L. Woody

University of California - Riverside, *Riverside, California 92521, USA*

K.N. Barish*, M. Beaumier, D. Black, K.O. Eyser, T. Hester, R.S. Hollis, A. Iordanova,
D. Kleinjan, M. Mendoza, S.D. Rolnick, K. Sedgwick, R. Seto

Charles University, *Ovocný trh 5, Praha 1, 116 36, Prague, Czech Republic*

M. Finger Jr., M. Finger*, M. Slunečka, V. Slunečkova

Chonbuk National University, Jeonju, 561-756, Korea

J.B. Choi, E.-J. Kim*, K.-B. Kim, G.H. Lee

Science and Technology on Nuclear Data Laboratory, China Institute of Atomic Energy,

Beijing 102413, P. R. China

X. Bai, X. Li*, S. Zhou

Center for Nuclear Study, Graduate School of Science, University of Tokyo, 7-3-1 Hongo,

Bunkyo, Tokyo 113-0033, Japan

R. Akimoto, T. Gunji, H. Hamagaki*, R. Hayano, S. Hayashi, Y. Hori, Y. Komatsu,
S. Masumoto, A. Nukariya, H. Oide, K. Ozawa, Y. Sekiguchi, A. Takahara, H. Torii,
T. Tsuji, Y.S. Watanabe, Y.L. Yamaguchi

University of Colorado, Boulder, Colorado 80309, USA

A. Adare, T. Koblesky, M. McCumber, J.L. Nagle*, M.R. Stone,

Columbia University, New York, New York 10027 and Nevis Laboratories, Irvington, New

York 10533, USA

C.Y. Chi*, B.A. Cole, T. Engelmores, N. Grau, Y.S. Lai, D. Perepelitsa, F.W. Sippach,
E. Vazquez-Zambrano, A. Veicht, D. Winter, W.A. Zajc, L. Zhang

Czech Technical University, Zikova 4, 166 36 Prague 6, Czech Republic

T. Liška, M. Tomášek, M. Virius*, V. Vrba

Debrecen University, H-4010 Debrecen, Egyetem tér 1, Hungary

J. Imrek, P. Tarján*

ELTE, Eötvös Loránd University, H - 1117 Budapest, Pázmány P. s. 1/A, Hungary

M. Csanád*, Á. Kiss, M. Kofarago, M.I. Nagy, M. Vargyas

Ewha Womans University, Seoul 120-750, Korea

K.I. Hahn*, S.Y. Han, D.H. Kim, J. Lee, I.H. Park

Florida State University, Tallahassee, Florida 32306, USA

A.D. Frawley*, J.R. Hutchins, J. Klatsky, D. McGlinchey

Georgia State University, Atlanta, Georgia 30303, USA

C. Butler, H. Guragain, X. He*, M. Jezghani, L. Patel, M. Sarsour, A. Sen

Hanyang University, Seoul 133-792, Korea

B.H. Kang, J.S. Kang, Y.K. Kim*, M.S. Ryu

Hiroshima University, Kagamiyama, Higashi-Hiroshima 739-8526, Japan

K. Homma, T. Hoshino, K.M. Kijima, Y. Nakamiya, M. Nihashi, K. Shigaki,
T. Sugitate*, D. Watanabe

The PHENIX Collaboration

IHEP Protvino, *State Research Center of Russian Federation, Institute for High Energy Physics, Protvino, 142281, Russia*

V. Babintsev, V. Bumazhnov, S. Chernichenko, A. Denisov*, A. Durum, I. Shein, A. Soldatov, A. Yanovich

University of Illinois at Urbana-Champaign, *Urbana, Illinois 61801, USA*

J. Blackburn, I.J. Choi, L. Eberle, F. Giordano, M. Grosse Perdekamp*, D.S. Jumper, Y.-J. Kim, M. Leitgab, C. McKinney, B. Meredith, D. Northacker, J.-C. Peng, E. Thorsland, S. Wolin, R. Yang, E. Zarndt

Institute for Nuclear Research of the Russian Academy of Sciences, *prospekt 60-letiya Oktyabrya 7a, Moscow 117312, Russia*

V. Pantuev*

Institute of Physics, *Academy of Sciences of the Czech Republic, Na Slovance 2, 182 21 Prague 8, Czech Republic*

J. Popule, P. Sicho, L. Tomášek, M. Tomášek, V. Vrba*

Iowa State University, *Ames, Iowa 50011, USA*

S. Campbell, L. Ding, J.C. Hill*, J.G. Lajoie, A. Lebedev, R. McKay, C.A. Ogilvie, J. Perry, M. Rosati, A. Shaver, M. Shimomura, A. Timilsina, S. Whitaker

Advanced Science Research Center, *Japan Atomic Energy Agency, 2-4 Shirakata Shirane, Tokai-mura, Naka-gun, Ibaraki-ken 319-1195, Japan*

K. Imai*, T. Maruyama, H. Sako, S. Sato

Joint Institute for Nuclear Research, *141980 Dubna, Moscow Region, Russia*

S. Afanasiev, A. Isupov, A. Litvinenko*, A. Malakhov, V. Peresedov, P. Rukoyatkin, L. Zolin

Helsinki Institute of Physics and University of Jyväskylä, *P.O.Box 35, FI-40014 Jyväskylä, Finland*

D.J. Kim, F. Krizek, N. Novitzky, J. Rak*

KEK, *High Energy Accelerator Research Organization, Tsukuba, Ibaraki 305-0801, Japan*

Y. Fukao, S. Kanda, M. Makek, T. Mibe, S. Nagamiya, K. Ozawa, N. Saito, S. Sawada*, Y.S. Watanabe

Korea University, *Seoul, 136-701, Korea*

B. Hong*, C. Kim, K.S. Lee, S.K. Park,

Russian Research Center "Kurchatov Institute", *Moscow, 123098 Russia*

D.S. Blau, S.L. Fokin, A.V. Kazantsev, V.I. Manko*, T.V. Moukhanova, A.S. Nyanin, D.Yu. Peressounko, I.E. Yushmanov

Kyoto University, *Kyoto 606-8502, Japan*

H. Asano, S. Dairaku, K. Karatsu, T. Murakami*, T. Nagae, K.R. Nakamura

Laboratoire Leprince-Ringuet, *Ecole Polytechnique, CNRS-IN2P3, Route de Saclay, F-91128, Palaiseau, France*

S. Chollet, A. Debraine, O. Drapier, F. Fleuret*, F. Gastaldi, M. Gonin,
R. Granier de Cassagnac

Lawrence Livermore National Laboratory, *Livermore, California 94550, USA*

I. Garishvili, A. Glenn, R.A. Soltz*

Los Alamos National Laboratory, *Los Alamos, New Mexico 87545, USA*

C. Aidala, M.L. Brooks, J.M. Durham, J. Huang, X. Jiang, J. Kapustinsky, K.B. Lee,
M.J. Leitch, M.X. Liu*, P.L. McGaughey, C.L. Silva, W.E. Sondheim, H.W. van Hecke

Department of Physics, *Lund University, Box 118, SE-221 00 Lund, Sweden*

P. Christiansen, A. Oskarsson*, L. Österman, E. Stenlund

University of Maryland, *College Park, Maryland 20742, USA*

O. Baron, L. D’Orazio, A.C. Mignerey*, E. Richardson, L. Stevens

Department of Physics, *University of Massachusetts, Amherst, Massachusetts 01003-9337, USA*

N. Bandara, D. Kawall*, M. Stepanov

Muhlenberg College, *Allentown, Pennsylvania 18104-5586, USA*

G. Benjamin, A. Carollo, N. Cronin, N. Crossett, B. Fadem*, A. Isinhue,
M. Moskowitz, S. Motschwiller, A. Nederlof, M. Skolnik, S. Solano, A. Tullo,
M. Young, C. Zumberge

Myongji University, *Yongin, Kyonggido 449-728, Korea*

S.J. Jeon, K.S. Joo*

Nagasaki Institute of Applied Science, *Nagasaki-shi, Nagasaki 851-0193, Japan*

T. Fusayasu*, Y. Tanaka

University of New Mexico, *Albuquerque, New Mexico 87131, USA*

B. Bassalleck, J. Bok, S. Butsyk, A. Datta, K. DeBlasio, D.E. Fields*, M. Hoefferkamp,
J.A. Key, I. Younus

New Mexico State University, *Las Cruces, New Mexico 88003, USA*

J. Bok, A. Meles, V. Papavassiliou, S.F. Pate*, G.D.N. Perera, E. Tennant, X.R. Wang,
F. Wei

Department of Physics and Astronomy, *Ohio University, Athens, Ohio 45701, USA*

X. Bing, J.E. Frantz*, D. Kotchetkov, N. Riveli

Oak Ridge National Laboratory, *Oak Ridge, Tennessee 37831, USA*

T.C. Awes, M. Bobrek, C.L. Britton, Jr., V. Cianciolo, Y.V. Efremenko, K.F. Read,
D. Silvermyr, P.W. Stankus*, M. Wysocki

The PHENIX Collaboration

IPN-Orsay, *Universite Paris Sud, CNRS-IN2P3, BP1, F-91406, Orsay, France*
D. Jouan*

PNPI, *Petersburg Nuclear Physics Institute, Gatchina, Leningrad region, 188300, Russia*
V. Baublis, D. Ivanischev, V. Ivanov, A. Khanzadeev, L. Kochenda, B. Komkov,
P. Kravtsov, V. Riabov, Y. Riabov, E. Roschin, V. Samsonov*, V. Trofimov,
E. Vznuzdaev

RIKEN Nishina Center for Accelerator-Based Science, *Wako, Saitama 351-0198, Japan*
Y. Akiba, K. Aoki, H. Asano, S. Baumgart, S. Dairaku, A. Enokizono, Y. Fukao,
Y. Goto, K. Hashimoto, T. Ichihara, Y. Ikeda, Y. Imazu, K. Karatsu, M. Kurosawa,
S. Miyasaka, T. Murakami, J. Murata, I. Nakagawa, K.R. Nakamura, T. Nakamura,
K. Nakano, M. Nihashi, K. Ninomiya, R. Seidl, T.-A. Shibata, K. Shoji, A. Taketani,
T. Todoroki, K. Watanabe, Y. Watanabe*, S. Yokkaichi

RIKEN BNL Research Center, *Brookhaven National Laboratory, Upton, New York
11973-5000, USA*
Y. Akiba*, S. Bathe, K. Boyle, C.-H. Chen, A. Deshpande, Y. Goto, T. Ichihara,
J. Koster, M. Kurosawa, I. Nakagawa, R. Nouicer, K. Okada, J. Seele, R. Seidl,
A. Taketani, K. Tanida, Y. Watanabe, S. Yokkaichi

Physics Department, *Rikkyo University, 3-34-1 Nishi-Ikebukuro, Toshima, Tokyo 171-8501,
Japan*
K. Hashimoto, K. Kurita*, J. Murata, K. Ninomiya, K. Watanabe

Saint Petersburg State Polytechnic University, *St. Petersburg, 195251 Russia*
A. Berdnikov, Y. Berdnikov*, D. Kotov, A. Safonov

Universidade de São Paulo, *Instituto de Física, Caixa Postal 66318, São Paulo
CEP05315-970, Brazil*
O. Dietzsch*, M. Donadelli, M. Kuriyama, M.A.L. Leite, R. Menegasso, E.M. Takagui

Department of Physics and Astronomy, *Seoul National University, Seoul, Korea*
S. Choi, S. Park, K. Tanida, I. Yoon

Chemistry Department, *Stony Brook University, SUNY, Stony Brook, New York 11794-3400,
USA*
N.N. Ajitanand, J. Alexander, X. Gong, Y. Gu, J. Jia, R. Lacey*, A. Mwai, M. Soumya,
S. Radhakrishnan, R. Reynolds, A. Taranenko, R. Wei

Department of Physics and Astronomy, *Stony Brook University, SUNY, Stony Brook, New
York 11794-3400, USA*
N. Apadula, E.T. Atomssa, B. Bannier, K. Dehmelt, A. Deshpande*, A. Dion,
A. Drees, H. Ge, C. Gal, J. Hanks, T.K. Hemmick, B.V. Jacak, J. Kamin,
V. Khachatryan, P. Kline, S.H. Lee, R. Lefferts, B. Lewis, A. Lipski, M. Lynch,
A. Manion, C. Pancake, R. Petti, B. Sahlmueller, E. Shafto, D. Sharma, J. Sun

Accelerator and Medical Instrumentation Engineering Lab, *SungKyunKwan University*,
53 Myeongnyun-dong, 3-ga, Jongno-gu, Seoul, South Korea
J.-S. Chai*

University of Tennessee, *Knoxville, Tennessee 37996, USA*
A. Garishvili, C. Nattrass, K.F. Read, S.P. Sorensen*, E. Tennant

Department of Physics, *Tokyo Institute of Technology, Oh-okayama, Meguro, Tokyo 152-8551*,
Japan
S. Miyasaka, K. Nakano, T.-A. Shibata*

Institute of Physics, *University of Tsukuba, Tsukuba, Ibaraki 305, Japan*
T. Chujo, S. Esumi*, M. Inaba, Y. Miake, S. Mizuno, T. Niida, M. Sano, T. Todoroki,
K. Watanabe

Vanderbilt University, *Nashville, Tennessee 37235, USA*
R. Belmont, S.V. Greene*, S. Huang, B. Love, C.F. Maguire, D. Roach, B. Schaefer,
J. Velkovska

Weizmann Institute, *Rehovot 76100, Israel*
M. Makek, A. Milov, I. Ravinovich, I. Tserruya*

Institute for Particle and Nuclear Physics, *Wigner Research Centre for Physics, Hungarian
Academy of Sciences (Wigner RCP, RMKI) H-1525 Budapest 114, POBox 49, Budapest,
Hungary*
T. Csörgő*, M.I. Nagy, T. Novak, A. Ster, J. Sziklai, R. Vértési

Yonsei University, *IPAP, Seoul 120-749, Korea*
J.H. Do, J.H. Kang*, H.J. Kim, Y. Kwon, S.H. Lim

*PHENIX Institutional Board member

The PHENIX Collaboration

Co-Spokesperson

David Morrison

Brookhaven National Laboratory

Co-Spokesperson

Jamie Nagle

University of Colorado

Deputy Spokesperson

Yasuyuki Akiba

RIKEN Nishina Center for

Accelerator-Based Science

Deputy Spokesperson

John Lajoie

Iowa State University

Operations Director

Ed O'Brien

Brookhaven National Laboratory

Deputy Operations Director for Upgrades

Mike Leitch

Los Alamos National Laboratory

Deputy Operations Director for Operations

John Haggerty

Brookhaven National Laboratory

Bibliography

- [1] C. N. Bo et al. Extracting jet transport coefficients from jet quenching at RHIC and the LHC. 2013. URL: <https://sites.google.com/a/lbl.gov/jetwiki/documents-1/report-on-status-of-qhat>. (document), 1.5, 1.12
- [2] A. Bazavov, T. Bhattacharya, M. Cheng, N. H. Christ, C. DeTar, S. Ejiri, S. Gottlieb, R. Gupta, U. M. Heller, K. Huebner, C. Jung, F. Karsch, E. Laermann, L. Levkova, C. Miao, R. D. Mawhinney, P. Petreczky, C. Schmidt, R. A. Soltz, W. Soeldner, R. Sugar, D. Toussaint, and P. Vranas. Equation of state and qcd transition at finite temperature. *Phys. Rev. D*, 80:014504, Jul 2009. URL: <http://link.aps.org/doi/10.1103/PhysRevD.80.014504>, doi:10.1103/PhysRevD.80.014504. 1, 1.1
- [3] A. Adare et al. Enhanced production of direct photons in Au+Au collisions at $\sqrt{s_{NN}} = 200$ GeV and implications for the initial temperature. *Phys. Rev. Lett.*, 104:132301, 2010. arXiv:0804.4168, doi:10.1103/PhysRevLett.104.132301. 1
- [4] M. Luzum and P. Romatschke. Viscous hydrodynamic predictions for nuclear collisions at the LHC. *Phys. Rev. Lett.*, 103:262302, 2009. arXiv:0901.4588, doi:10.1103/PhysRevLett.103.262302. 1
- [5] A. Adams, L. D. Carr, T. Schaefer, P. Steinberg, and J. E. Thomas. Strongly correlated quantum fluids: ultracold quantum gases, quantum chromodynamic plasmas, and holographic duality. 2012. arXiv:1205.5180. 1
- [6] S. S. Gubser. Using string theory to study the quark-gluon plasma: Progress and perils. *Nucl. Phys.*, A830:657C–664C, 2009. arXiv:0907.4808. 1
- [7] S. S. Gubser, I. R. Klebanov, and A. W. Peet. Entropy and temperature of black 3-branes. *Phys. Rev.*, D54:3915–3919, 1996. arXiv:hep-th/9602135, doi:10.1103/PhysRevD.54.3915. 1
- [8] U. A. Wiedemann. Stepping outside the neighborhood of T(c) at LHC. *Nucl. Phys.*, A830:74C–80C, 2009. arXiv:0908.2294. 1
- [9] G. Aad et al. Measurement of the Azimuthal Angle Dependence of Inclusive Jet Yields in Pb+Pb Collisions at $\sqrt{s_{NN}} = 2.76$ TeV with the ATLAS detector. 2013. arXiv:1306.6469. 1

- [10] G. Aad et al. Measurement of the jet radius and transverse momentum dependence of inclusive jet suppression in lead-lead collisions at $\sqrt{s_{NN}} = 2.76$ TeV with the ATLAS detector. *Phys.Lett.*, B719:220–241, 2013. arXiv:1208.1967, doi:10.1016/j.physletb.2013.01.024. 1, 4.4.1, 4.5
- [11] K. Adcox et al. Formation of dense partonic matter in relativistic nucleus-nucleus collisions at RHIC: Experimental evaluation by the PHENIX collaboration. *Nucl. Phys.*, A757:184–283, 2005. arXiv:nucl-ex/0410003, doi:10.1016/j.nuclphysa.2005.03.086. 1.1
- [12] M. Luzum and P. Romatschke. Conformal relativistic viscous hydrodynamics: Applications to RHIC results at $\sqrt{s_{NN}} = 200$ GeV. *Phys. Rev.*, C78:034915, 2008. arXiv:0804.4015, doi:10.1103/PhysRevC.78.034915. 1.1
- [13] P. Danielewicz and M. Gyulassy. Dissipative phenomena in quark gluon plasmas. *Phys. Rev.*, D31:53–62, 1985. doi:10.1103/PhysRevD.31.53. 1.1
- [14] P. Kovtun, D. Son, and A. Starinets. Viscosity in strongly interacting quantum field theories from black hole physics. *Phys. Rev. Lett.*, 94:111601, 2005. arXiv:hep-th/0405231, doi:10.1103/PhysRevLett.94.111601. 1.1, 1.2
- [15] H. Song and U. W. Heinz. Causal viscous hydrodynamics in 2+1 dimensions for relativistic heavy-ion collisions. *Phys. Rev.*, C77:064901, 2008. arXiv:0712.3715, doi:10.1103/PhysRevC.77.064901. 1.1
- [16] B. Alver, C. Gombeaud, M. Luzum, and J.-Y. Ollitrault. Triangular flow in hydrodynamics and transport theory. *Phys. Rev.*, C82:034913, 2010. arXiv:1007.5469, doi:10.1103/PhysRevC.82.034913. 1.1
- [17] D. A. Teaney. Viscous Hydrodynamics and the Quark Gluon Plasma. 2009. arXiv:0905.2433. 1.1
- [18] B. Schenke, S. Jeon, and C. Gale. Elliptic and triangular flows in 3 + 1D viscous hydrodynamics with fluctuating initial conditions. *J. Phys. G*, G38:124169, 2011. 1.1
- [19] A. Adare et al. Measurements of higher-order flow harmonics in Au+Au collisions at $\sqrt{s_{NN}} = 200$ GeV. arXiv:1105.3928 [hep-ex] (2011). 1.1
- [20] A. Adare et al. Energy loss and flow of heavy quarks in Au+Au collisions at $\sqrt{s_{NN}} = 200$ GeV. *Phys. Rev. Lett.*, 98:172301, 2007. arXiv:nucl-ex/0611018, doi:10.1103/PhysRevLett.98.172301. 1.1
- [21] A. Majumder, B. Muller, and X.-N. Wang. Small shear viscosity of a quark-gluon plasma implies strong jet quenching. *Phys. Rev. Lett.*, 99:192301, 2007. arXiv:hep-ph/0703082, doi:10.1103/PhysRevLett.99.192301. 1.2, 1.1, 1.2

- [22] H. Liu, K. Rajagopal, and U. Wiedemann. Calculating the jet quenching parameter from AdS/CFT. *Phys. Rev. Lett.*, 97:182301, 2006. arXiv:hep-ph/0605178, doi:10.1103/PhysRevLett.97.182301. 1.1, 1.2
- [23] L. Csernai, J. Kapusta, and L. McLerran. On the strongly-interacting low-viscosity matter created in relativistic nuclear collisions. *Phys. Rev. Lett.*, 97:152303, 2006. arXiv:nucl-th/0604032, doi:10.1103/PhysRevLett.97.152303. 1.2
- [24] P. B. Arnold, G. D. Moore, and L. G. Yaffe. Transport coefficients in high temperature gauge theories. 2. Beyond leading log. *JHEP*, 0305:051, 2003. arXiv:hep-ph/0302165. 1.2
- [25] M. Prakash, M. Prakash, R. Venugopalan, and G. Welke. Nonequilibrium properties of hadronic mixtures. *Phys. Rept.*, 227:321–366, 1993. doi:10.1016/0370-1573(93)90092-R. 1.2
- [26] N. Demir and S. A. Bass. Shear-viscosity to entropy-density ratio of a relativistic hadron gas. *Phys. Rev. Lett.*, 102:172302, 2009. arXiv:0812.2422, doi:10.1103/PhysRevLett.102.172302. 1.2
- [27] H. B. Meyer. A calculation of the shear viscosity in SU(3) gluodynamics. *Phys. Rev.*, D76:101701, 2007. arXiv:0704.1801, doi:10.1103/PhysRevD.76.101701. 1.2
- [28] Y. Hidaka and R. D. Pisarski. Small shear viscosity in the semi quark gluon plasma. *Phys. Rev.*, D81:076002, 2010. arXiv:0912.0940, doi:10.1103/PhysRevD.81.076002. 1.2
- [29] P. K. Srivastava and C. P. Singh. Critical Point on the QCD Deconfining Phase Boundary. 2012. 15 pages, 4 figures. arXiv:1201.0445. 1.2
- [30] P. Kovtun, G. D. Moore, and P. Romatschke. The stickiness of sound: An absolute lower limit on viscosity and the breakdown of second order relativistic hydrodynamics. *Phys. Rev.*, D84:025006, 2011. arXiv:1104.1586, doi:10.1103/PhysRevD.84.025006. 1.2
- [31] Charles Gale, Sangyong Jeon, Bjorn Schenke, Prithwish Tribedy, and Raju Venugopalan. Event-by-event anisotropic flow in heavy-ion collisions from combined Yang-Mills and viscous fluid dynamics. *Phys.Rev.Lett.*, 110:012302, 2013. arXiv:1209.6330, doi:10.1103/PhysRevLett.110.012302. 1.2
- [32] H. Song, S. A. Bass, and U. Heinz. Elliptic flow in 200 A GeV Au+Au collisions and 2.76 A TeV Pb+Pb collisions: insights from viscous hydrodynamics + hadron cascade hybrid model. *Phys. Rev.*, C83:054912, 2011. arXiv:1103.2380, doi:10.1103/PhysRevC.83.054912. 1.2
- [33] J. L. Nagle, I. G. Bearden, and W. A. Zajc. Quark-gluon plasma at RHIC and the LHC: perfect fluid too perfect? *New J. Phys.*, 13:075004, 2011. arXiv:1102.0680, doi:10.1088/1367-2630/13/7/075004. 1.2

- [34] H. Niemi, G. S. Denicol, P. Huovinen, E. Molnar, and D. H. Rischke. Influence of the shear viscosity of the quark-gluon plasma on elliptic flow in ultrarelativistic heavy-ion collisions. *Phys. Rev. Lett.*, 106:212302, 2011. arXiv:1101.2442, doi:10.1103/PhysRevLett.106.212302. 1.2
- [35] N. Armesto, B. Cole, C. Gale, W. A. Horowitz, P. Jacobs, et al. Comparison of Jet Quenching Formalisms for a Quark-Gluon Plasma 'Brick'. 2011. arXiv:1106.1106. 1.2
- [36] P. B. Arnold, G. D. Moore, and L. G. Yaffe. Transport coefficients in high temperature gauge theories. 1. Leading log results. *JHEP*, 0011:001, 2000. arXiv:hep-ph/0010177. 1.2
- [37] J. Liao and E. Shuryak. Angular Dependence of Jet Quenching Indicates Its Strong Enhancement Near the QCD Phase Transition. *Phys. Rev. Lett.*, 102:202302, 2009. arXiv:0810.4116, doi:10.1103/PhysRevLett.102.202302. 1.2, 1.3
- [38] K. Rajagopal. International Quark Matter presentation (2011). URL: <http://qm2011.in2p3.fr/node/12>. 1.3
- [39] C. E. Coleman-Smith, G.-Y. Qin, S. A. Bass, and B. Muller. Jet modification in a brick of QGP matter. 2011. arXiv:1108.5662. 1.3, 1.6, 1.18
- [40] C. E. Coleman-Smith, S. A. Bass, and D. K. Srivastava. Implementing the LPM effect in a parton cascade model. *Nucl. Phys.*, A862-863:275–278, 2011. arXiv:1101.4895, doi:10.1016/j.nuclphysa.2011.05.071. 1.3, 1.6, 1.6
- [41] B. Muller. Talk given at RHIC/AGS Users' Meeting, June 2011". 1.4, 1.9
- [42] B. Muller. Parton energy loss in strongly coupled AdS/CFT. *Nucl. Phys.*, A855:74–82, 2011. arXiv:1010.4258, doi:10.1016/j.nuclphysa.2011.02.022. 1.4
- [43] A. Dainese, C. Loizides, and G. Paic. Leading-particle suppression in high energy nucleus-nucleus collisions. *Eur. Phys. J.*, C38:461–474, 2005. arXiv:hep-ph/0406201, doi:10.1140/epjc/s2004-02077-x. 1.10, 1.5
- [44] C. Loizides. High transverse momentum suppression and surface effects in Cu+Cu and Au+Au collisions within the PQM model. *Eur. Phys. J.*, C49:339–345, 2007. arXiv:hep-ph/0608133, doi:10.1140/epjc/s10052-006-0059-8. 1.10, 1.5
- [45] A. Adare et al. Quantitative constraints on the transport properties of hot partonic matter from semi-inclusive single high transverse momentum pion suppression in Au+Au collisions at $\sqrt{s_{NN}} = 200$ GeV. *Phys. Rev. C*, 77:064907, 2008. arXiv:0801.1665, doi:10.1103/PhysRevC.77.064907. 1.10, 1.5
- [46] K. Adcox et al. Suppression of hadrons with large transverse momentum in central Au+Au collisions at $\sqrt{s_{NN}} = 130$ GeV. *Phys. Rev. Lett.*, 88:022301, 2002. arXiv:nucl-ex/0109003, doi:10.1103/PhysRevLett.88.022301. 1.5

- [47] C. Adler et al. Centrality dependence of high p_T hadron suppression in Au+Au collisions at $\sqrt{s_{NN}} = 130$ GeV. *Phys. Rev. Lett.*, 89:202301, 2002. arXiv:nucl-ex/0206011. 1.5
- [48] S. Bass et al. Systematic comparison of jet energy-loss schemes in a realistic hydrodynamic medium. *Phys. Rev.*, C79:024901, 2009. arXiv:0808.0908, doi:10.1103/PhysRevC.79.024901. 1.5, 1.13
- [49] A. Adare et al. Transition in yield and azimuthal shape modification in dihadron correlations in relativistic heavy ion collisions. *Phys. Rev. Lett.*, 104:252301, 2010. arXiv:1002.1077, doi:10.1103/PhysRevLett.104.252301. 1.5
- [50] A. Adare et al. Suppression of away-side jet fragments with respect to the reaction plane in Au+Au collisions at $\sqrt{s_{NN}} = 200$ GeV. *Phys. Rev. C*, 2010. arXiv:1010.1521. 1.5
- [51] J. Adams et al. Distributions of charged hadrons associated with high transverse momentum particles in $p+p$ and Au+Au collisions at $\sqrt{s_{NN}} = 200$ GeV. *Phys. Rev. Lett.*, 95:152301, 2005. arXiv:nucl-ex/0501016. 1.5
- [52] J. L. Nagle. Ridge, bulk, and medium response: how to kill models and learn something in the process. *Nucl. Phys.*, A830:147C–154C, 2009. arXiv:0907.2707. 1.5
- [53] W. A. Horowitz and M. Gyulassy. The Surprising Transparency of the sQGP at LHC. *Nucl. Phys.*, A872:265–285, 2011. arXiv:1104.4958. 1.5
- [54] K. Aamodt and C. A. Loizides. Suppression of charged particle production at large transverse momentum in central Pb–Pb collisions at $\sqrt{s_{NN}} = 2.76$ TeV. *Phys. Lett.*, B696:30–39, 2011. arXiv:1012.1004. 1.5
- [55] X.-F. Chen, T. Hirano, E. Wang, X.-N. Wang, and H. Zhang. Suppression of high p_T hadrons in $Pb + Pb$ Collisions at LHC. *Phys. Rev.*, C84:034902, 2011. arXiv:1102.5614, doi:10.1103/PhysRevC.84.034902. 1.5
- [56] B. G. Zakharov. Variation of jet quenching from RHIC to LHC and thermal suppression of QCD coupling constant. *JETP Lett.*, 93:683–687, 2011. arXiv:1105.2028, doi:10.1134/S0021364011120162. 1.5
- [57] A. Buzzatti and M. Gyulassy. Jet Flavor Tomography of Quark Gluon Plasmas at RHIC and LHC. *Phys. Rev. Lett.*, 108:022301, 2012. 4 pages, 3 eps figures. arXiv:1106.3061, doi:10.1103/PhysRevLett.108.022301. 1.5
- [58] A. Buzzatti and M. Gyulassy. A running coupling explanation of the surprising transparency of the QGP at LHC. *Nucl.Phys.A904-905*, 2013:779c–782c, 2013. arXiv:1210.6417, doi:10.1016/j.nuclphysa.2013.02.133. 1.5

- [59] S. Chatrchyan et al. Study of high-pT charged particle suppression in PbPb compared to pp collisions at $\sqrt{s_{NN}} = 2.76$ TeV. *Eur.Phys.J.*, C72:1945, 2012. arXiv:1202.2554, doi:10.1140/epjc/s10052-012-1945-x. 1.5, 1.11
- [60] A. Adare et al. Azimuthal anisotropy of π^0 production in Au+Au collisions at $\sqrt{s_{NN}} = 200$ GeV: path-length dependence of jet quenching and the role of initial geometry. *Phys. Rev. Lett.*, 105:142301, 2010. arXiv:1006.3740, doi:10.1103/PhysRevLett.105.142301. 1.5, 1.13
- [61] C. Marquet and T. Renk. Jet quenching in the strongly-interacting quark-gluon plasma. *Phys. Lett.*, B685:270–276, 2010. arXiv:0908.0880, doi:10.1016/j.physletb.2010.01.076. 1.5
- [62] S. Wicks, W. Horowitz, M. Djordjevic, and M. Gyulassy. Elastic, inelastic, and path length fluctuations in jet tomography. *Nucl. Phys.*, A784:426–442, 2007. arXiv:nucl-th/0512076, doi:10.1016/j.nuclphysa.2006.12.048. 1.13
- [63] L. Adamczyk et al. Jet-Hadron Correlations in $\sqrt{s_{NN}} = 200$ GeV Au+Au and $p+p$ Collisions. 2013. arXiv:1302.6184. 1.5, 1.14, 4.5, 4.7
- [64] H. Caines. Jets and jet-like Correlations at RHIC. 2011. arXiv:1110.1878. 1.5
- [65] J. Putschke. STAR: Jet reconstruction, direct gamma and multi-hadron correlations: Hard probes of the initial and final state. *Nucl. Phys.*, A855:83–91, 2011. 1.5
- [66] J. Putschke. First fragmentation function measurements from full jet reconstruction in heavy-ion collisions at $\sqrt{s_{NN}} = 200$ GeV by STAR. *Eur. Phys. J.*, C61:629–635, 2009. arXiv:0809.1419. 1.5
- [67] P. M. Jacobs. Background fluctuations in heavy ion jet reconstruction. 2010. arXiv:1012.2406. 1.5
- [68] Y.-S. Lai. Direct jet reconstruction in $p+p$ and Cu+Cu collisions at PHENIX. *Nucl. Phys.*, A855:295–298, 2011. 1.5
- [69] Y.-S. Lai. Probing medium-induced energy loss with direct jet reconstruction in $p+p$ and Cu+Cu collisions at PHENIX. *Nucl. Phys.*, A830:251C–254C, 2009. arXiv:0907.4725. 1.5
- [70] G. Aad et al. Observation of a centrality-dependent dijet asymmetry in lead-lead collisions at $\sqrt{s_{NN}} = 2.76$ TeV with the ATLAS detector at the LHC. *Phys. Rev. Lett.*, 105:252303, 2010. Accepted for publication at Physical Review Letters. arXiv:1011.6182, doi:10.1103/PhysRevLett.105.252303. 1.5, 1.15, 4.2, 4.3.2
- [71] S. Chatrchyan et al. Observation and studies of jet quenching in PbPb collisions at nucleon-nucleon center-of-mass energy = 2.76 TeV. *Phys. Rev.*, C84:024906, 2011. arXiv:1102.1957, doi:10.1103/PhysRevC.84.024906. 1.5, 1.16, 1.6, 4.3.2, 4.7

- [72] X.-N. Wang, Z. Huang, and I. Sarcevic. Jet quenching in the opposite direction of a tagged photon in high-energy heavy ion collisions. *Phys. Rev. Lett.*, 77:231–234, 1996. arXiv:hep-ph/9605213, doi:10.1103/PhysRevLett.77.231. 1.5
- [73] S. Chatrchyan et al. Studies of jet quenching using isolated-photon+jet correlations in PbPb and pp collisions at $\sqrt{s_{NN}} = 2.76$ TeV. 2012. Submitted to Physics Letters B. arXiv:1205.0206. 1.5
- [74] S. Chatrchyan et al. Jet momentum dependence of jet quenching in PbPb collisions at $\sqrt{s_{NN}} = 2.76$ TeV. 2012. arXiv:1202.5022. 1.5, 4.2
- [75] P. Steinberg. Recent Heavy Ion Results with the ATLAS Detector at the LHC. 2011. arXiv:1110.3352. 1.5
- [76] J. Casalderrey-Solana, J. G. Milhano, and U. Wiedemann. Jet quenching via jet collimation. *J. Phys. G*, G38:124086, 2011. arXiv:1107.1964. 1.6
- [77] T. Renk. Energy dependence of the dijet imbalance in Pb-Pb collisions at 2.76 ATeV. 2012. arXiv:1204.5572. 1.6
- [78] T. Renk. Jets in medium: What RHIC and LHC measurements of R_{AA} and I_{AA} can teach about the parton-medium interaction. 2011. arXiv:1111.0769. 1.6
- [79] JET Topical Collaboration. URL: <http://jet.lbl.gov>. 1.6
- [80] K. C. Zapp, J. Stachel, and U. Wiedemann. LPM-effect in Monte Carlo models of radiative energy loss. *Nucl. Phys.*, A830:171C–174C, 2009. arXiv:0907.4304. 1.6
- [81] T. Renk. YaJEM: a Monte Carlo code for in-medium shower evolution. *Int. J. Mod. Phys.*, E20:1594–1599, 2011. arXiv:1009.3740, doi:10.1142/S0218301311019933. 1.6
- [82] C. Young, S. Jeon, C. Gale, and B. Schenke. Monte-Carlo simulation of jets in heavy-ion collisions. 2011. arXiv:1109.5992. 1.6, 1.6
- [83] I. P. Lokhtin, A. V. Belyaev, and A. M. Snigirev. Jet quenching pattern at LHC in PYQUEN model. *Eur. Phys. J.*, C71:1650, 2011. arXiv:1103.1853, doi:10.1140/epjc/s10052-011-1650-1. 1.6
- [84] N. Armesto, L. Cunqueiro, and C. A. Salgado. Monte Carlo for jet showers in the medium. *Nucl. Phys.*, A830:271C–274C, 2009. arXiv:0907.4706. 1.6
- [85] T. Renk. Biased Showers — a common conceptual framework for the interpretation of High p_T observables in heavy-ion collisions. 2012. arXiv:1212.0646. 1.6, 1.17, 4.5
- [86] C. E Coleman-Smith and B. Muller. What can we learn from Dijet suppression at RHIC? 2012. arXiv:1205.6781. 1.18, 1.20, 1.21

- [87] K. Geiger and B. Muller. Dynamics of parton cascades in highly relativistic nuclear collisions. *Nucl. Phys.*, B369:600–654, 1992. doi:10.1016/0550-3213(92)90280-0. 1.6
- [88] C. Wesp, A. El, F. Reining, Z. Xu, I. Bouras, et al. Calculation of shear viscosity using Green-Kubo relations within a parton cascade. *Phys. Rev.*, C84:054911, 2011. arXiv:1106.4306, doi:10.1103/PhysRevC.84.054911. 1.6
- [89] G.-Y. Qin and B. Muller. private communication. 1.22, 1.6, 1.23, 1.24, 4.13, 4.4.2
- [90] G.-Y. Qin and B. Muller. Explanation of Di-jet asymmetry in Pb+Pb collisions at the Large Hadron Collider. *Phys. Rev. Lett.*, 106:162302, 2011. 4 pages, 3 figures, made corrections for numerical inaccuracies, qualitative conclusions unaffected. arXiv:1012.5280, doi:10.1103/PhysRevLett.106.162302. 1.6, 1.6
- [91] B. Schenke, C. Gale, and S. Jeon. MARTINI: Monte Carlo simulation of jet evolution. *Acta Phys. Polon. Supp.*, 3:765–770, 2010. arXiv:0911.4470. 1.6
- [92] B. Schenke, S. Jeon, and C. Gale. (3+1)D hydrodynamic simulation of relativistic heavy-ion collisions. *Phys. Rev.*, C82:014903, 2010. arXiv:1004.1408, doi:10.1103/PhysRevC.82.014903. 1.6
- [93] C. Young, B. Schenke, S. Jeon, and C. Gale. Dijet asymmetry at the energies available at the CERN Large Hadron Collider. *Phys. Rev.*, C84:024907, 2011. arXiv:1103.5769, doi:10.1103/PhysRevC.84.024907. 1.6
- [94] C. Young and B. Schenke. private communication. 1.24
- [95] Y. He, I. Vitev, and B.-W. Zhang. Next-to-leading order analysis of inclusive jet and di-jet production in heavy ion reactions at the Large Hadron Collider. 2011. arXiv:1105.2566. 1.6, 1.25, 4.13
- [96] R. B. Neufeld and I. Vitev. Parton showers as sources of energy-momentum deposition in the QGP and their implication for shockwave formation at RHIC and at the LHC. 2011. 8 pages, 4 figures. arXiv:1105.2067. 1.6, 1.25, 4.13
- [97] I. Vitev and B.-W. Zhang. Jet tomography of high-energy nucleus-nucleus collisions at next-to-leading order. *Phys. Rev. Lett.*, 104:132001, 2010. arXiv:0910.1090, doi:10.1103/PhysRevLett.104.132001. 1.6, 1.25, 4.13
- [98] W. Horowitz and M. Gyulassy. Heavy quark jet tomography of Pb+Pb at LHC: AdS/CFT drag or pQCD energy loss? *Phys. Lett.*, B666:320–323, 2008. arXiv:0706.2336, doi:10.1016/j.physletb.2008.04.065. 1.8
- [99] M. Cacciari. private communication. 1.8, 1.27

- [100] A. Adil and I. Vitev. Collisional dissociation of heavy mesons in dense QCD matter. *Phys. Lett.*, B649:139–146, 2007. arXiv:hep-ph/0611109, doi:10.1016/j.physletb.2007.03.050. 1.8
- [101] R. Sharma, I. Vitev, and B.-W. Zhang. Light-cone wave function approach to open heavy flavor dynamics in QCD matter. *Phys. Rev.*, C80:054902, 2009. arXiv:0904.0032, doi:10.1103/PhysRevC.80.054902. 1.8
- [102] V. Abazov et al. *b*-Jet Identification in the D0 Experiment. *Nucl. Instrum. Meth.*, A620:490–517, 2010. arXiv:1002.4224, doi:10.1016/j.nima.2010.03.118. 1.8
- [103] W. Vogelsang. private communication. 1.29, 1.9, 4.18
- [104] W. Fischer. RHIC Luminosity Upgrade Program. *Conf.Proc.*, C100523:TUXMH01, 2010. 1.9
- [105] RHIC Beam Projections [online]. URL: <http://www.rhichome.bnl.gov/RHIC/Runs/RhicProjections.pdf>. 1.9
- [106] A. Pikin, J.G. Alessi, E.N. Beebe, A. Kponou, R. Lambiase, et al. RHIC EBIS: Basics of design and status of commissioning. *JINST*, 5:C09003, 2010. 1.9
- [107] S. Afanasiev et al. Measurement of Direct Photons in Au+Au Collisions at $\sqrt{s_{NN}} = 200$ GeV. 2012. arXiv:1205.5759. 1.30
- [108] A. Adare et al. Direct-Photon Production in $p + p$ Collisions at $\sqrt{s} = 200$ GeV at Midrapidity. 2012. arXiv:1205.5533. 1.30
- [109] X. Zhao and R. Rapp. Medium Modifications and Production of Charmonia at LHC. *Nucl. Phys.*, A859:114–125, 2011. 7 pages, 9 eps figures. arXiv:1102.2194, doi:10.1016/j.nuclphysa.2011.05.001. 1.10
- [110] R. Arnaldi. J/ψ production in $p+A$ and $A+A$ collisions at fixed target experiments. *Nucl. Phys.*, A830:345c–352c, 2009. arXiv:0907.5004, doi:10.1016/j.nuclphysa.2009.10.030. 1.10
- [111] N. Brambilla, S. Eidelman, B. K. Heltsley, R. Vogt, G. T. Bodwin, et al. Heavy quarkonium: progress, puzzles, and opportunities. 2010. arXiv:arXiv:1010.5827. 1.10, 1.10
- [112] B. Abelev et al. J/ψ production at low transverse momentum in Pb-Pb collisions at $\sqrt{s_{NN}} = 2.76$ TeV. 2012. arXiv:1202.1383. 1.10, 1.31
- [113] M. Calderón de la Barca Sánchez. Dimuon results in PbPb and pp collisions in CMS. 2011. arXiv:1109.1850. 1.10
- [114] C. L. da Silva. Recent heavy flavour and quarkonia measurements by the PHENIX experiment. *J. Phys. G*, G38:124031, 2011. 1.10

- [115] R. Reed. Measuring the upsilon nuclear modification factor at STAR. *J. Phys. G*, G38:124185, 2011. arXiv:1109.3891, doi:10.1088/0954-3899/38/12/124185. 1.10
- [116] B. Muller, J. Schukraft, and B. Wyslouch. First results from Pb+Pb collisions at the LHC. 2012. arXiv:1202.3233. 1.10
- [117] A. Emerick, X. Zhao, and R. Rapp. Bottomonia in the quark-gluon plasma and their production at RHIC and LHC. 2011. arXiv:1111.6537. 1.10
- [118] L. Ruan, G. Lin, Z. Xu, K. Asselta, H. F. Chen, et al. Perspectives of a midrapidity dimuon program at RHIC: a novel and compact muon telescope detector. *J. Phys. G*, G36:095001, 2009. arXiv:0904.3774, doi:10.1088/0954-3899/36/9/095001. 1.10
- [119] O.D. Tsai, L.E. Dunkelberger, C.A. Gagliardi, S. Heppelmann, H.Z. Huang, et al. Results of & on a new construction technique for W/ScFi Calorimeters. *J.Phys.Conf.Ser.*, 404:012023, 2012. doi:10.1088/1742-6596/404/1/012023. 3.2.1
- [120] Tungsten Heavy Powder. URL: <http://www.tungstenheavypowder.com>. 3.2.1
- [121] R. Wigmans. Calorimetry: Energy measurement in particle physics. *Int. Ser. Monogr. Phys.*, 107:1-726, 2000. 3.6
- [122] Inc. Saint-Gobain Ceramics & Plastics. Scintillating optical fibers. 3.3
- [123] Kuraray Co. Ltd. Scintillation materials catalogue. 3.3
- [124] A. Izmaylov, S. Aoki, J. Blocki, J. Brinson, A. Dabrowska, et al. Scintillator counters with WLS fiber/MPPC readout for the side muon range detector (SMRD) of the T2K experiment. *Nucl. Instrum. Meth.*, A623:382-384, 2010. arXiv:0904.4545, doi:10.1016/j.nima.2010.03.009. 3.3
- [125] O. Mineev, A. Afanasjev, G. Bondarenko, V. Golovin, E. Gushchin, et al. Scintillator counters with multi-pixel avalanche photodiode readout for the ND280 detector of the T2K experiment. *Nucl. Instrum. Meth.*, A577:540-551, 2007. arXiv:physics/0606037, doi:10.1016/j.nima.2007.04.161. 3.3
- [126] S. Agostinelli et al. GEANT4: A Simulation toolkit. *Nucl. Instrum. Meth.*, A506:250-303, 2003. doi:10.1016/S0168-9002(03)01368-8. 3.4, 4.1
- [127] CERN SRS Home Page. <https://espace.cern.ch/rd51-wg5/srs/default.aspx>. 3.5.3
- [128] RD51 Collaboration Meeting. <https://indico.cern.ch/conferenceTimeTable.py?confId=176664>, Feb. 2012. 3.5.3
- [129] S. Lochner. Development, optimisation and characterisation of a radiation hard mixed-signal readout chip for LHCb. 2006. 3.5.3

- [130] M. Allen et al. PHENIX inner detectors. *Nucl.Instrum.Meth.*, A499:549–559, 2003. doi:10.1016/S0168-9002(02)01956-3. 3.7
- [131] T. Sjostrand, P. Eden, C. Friberg, L. Lonnblad, G. Miu, et al. High-energy physics event generation with PYTHIA 6.1. *Comput. Phys. Commun.*, 135:238–259, 2001. arXiv:hep-ph/0010017, doi:10.1016/S0010-4655(00)00236-8. 4.1, 4.3.1
- [132] M. Gyulassy and X. Wang. HIJING 1.0: A Monte Carlo program for parton and particle production in high-energy hadronic and nuclear collisions. *Comput. Phys. Commun.*, 83:307, 1994. arXiv:nucl-th/9502021, doi:10.1016/0010-4655(94)90057-4. 4.1
- [133] M. Cacciari and G. P. Salam. Dispelling the N^3 myth for the k_t jet-finder. *Phys. Lett.*, B641:57–61, 2006. arXiv:hep-ph/0512210, doi:10.1016/j.physletb.2006.08.037. 4.1, 4.2
- [134] I. P. Lokhtin and A. M. Snigirev. A Model of jet quenching in ultrarelativistic heavy ion collisions and high-p(T) hadron spectra at RHIC. *Eur. Phys. J.*, C45:211–217, 2006. arXiv:hep-ph/0506189, doi:10.1140/epjc/s2005-02426-3. 4.1, 4.4.3
- [135] J.A. Hanks, A.M. Sickles, B.A. Cole, A. Franz, M.P. McCumber, et al. Method for separating jets and the underlying event in heavy ion collisions at the BNL Relativistic Heavy Ion Collider. *Phys.Rev.*, C86:024908, 2012. arXiv:1203.1353, doi:10.1103/PhysRevC.86.024908. 4.1, 4.4.1
- [136] M. Cacciari, G. Salam, and G. Soyez. The anti- k_t jet clustering algorithm. *JHEP*, 0804:063, 2008. arXiv:0802.1189, doi:10.1088/1126-6708/2008/04/063. 4.2
- [137] Jet Performance in pp Collisions at 7 TeV. URL: <http://cdsweb.cern.ch/record/1279362>. 4.3
- [138] T. Auye. Unfolding algorithms and tests using RooUnfold. 2011. arXiv:1105.1160. 4.3.1
- [139] B. A. Cole. Jet probes of $\sqrt{s_{NN}} = 2.76$ TeV Pb+Pb collisions with the ATLAS detector. *J. Phys. G*, G38:124021, 2011. 4.4.1
- [140] A. Adare et al. Measurement of $Y(1S+2S+3S)$ production in $p+p$ and Au+Au collisions at $\sqrt{s_{NN}} = 200$ GeV. 2014. arXiv:1404.2246. 4.10
- [141] D. Acosta et al. Y production and polarization in $p\bar{p}$ collisions at $\sqrt{s} = 1.8$ TeV. *Phys. Rev. Lett.*, 88:161802, 2002. doi:10.1103/PhysRevLett.88.161802. 4.10
- [142] M. Strickland and D. Bazow. Thermal bottomonium suppression at RHIC and LHC. *Nucl. Phys.*, A879:25–58, 2012. arXiv:1112.2761, doi:10.1016/j.nuclphysa.2012.02.003. 4.10, 4.24

- [143] PHENIX Collaboration. The PHENIX Decadal Plan, 2010. URL: http://www.phenix.bnl.gov/phenix/WWW/docs/decadal/2010/phenix_decadal10_full_refs.pdf. A
- [144] A. Accardi et al. Electron Ion Collider: The Next QCD Frontier - Understanding the glue that binds us all. 2012. arXiv:1212.1701. A, A.1, A.1.1, A.2, A.3, A.3, A.4, A.3, A.7, A.4, A.5.6
- [145] 2007 Long Range Plan: The Frontiers of Nuclear Science, 2007. URL: <http://science.energy.gov/~media/np/nsac/pdf/docs/NuclearScienceHighRes.pdf>. A.1
- [146] D. de Florian, R. Sassot, M. Stratmann, and W. Vogelsang. Extraction of Spin-Dependent Parton Densities and Their Uncertainties. *Phys. Rev.*, **D80**:034030, 2009. arXiv:0904.3821, doi:10.1103/PhysRevD.80.034030. A.3
- [147] M. Anselmino et al. Transversity and Collins functions from SIDIS and e^+e^- data. *Phys. Rev.*, **D75**:054032, 2007. arXiv:hep-ph/0701006, doi:10.1103/PhysRevD.75.054032. A.3
- [148] X.-D. Ji. Gauge invariant decomposition of nucleon spin and its spin - off. *Phys. Rev. Lett.*, **78**:610–613, 1997. arXiv:hep-ph/9603249, doi:10.1103/PhysRevLett.78.610. A.3
- [149] A. Airapetian et al. Hadronization in semi-inclusive deep-inelastic scattering on nuclei. *Nucl. Phys.*, **B780**:1–27, 2007. arXiv:0704.3270, doi:10.1016/j.nuclphysb.2007.06.004. A.3, A.5
- [150] D. Boer et al. Gluons and the quark sea at high energies: Distributions, polarization, tomography. 2011. arXiv:1108.1713. A.3, A.4
- [151] A. Daniel et al. Measurement of the nuclear multiplicity ratio for K_s^0 hadronization at CLAS. *Phys. Lett.*, **B706**:26–31, 2011. arXiv:1111.2573, doi:10.1016/j.physletb.2011.10.071. A.5
- [152] E. Iancu, K. Itakura, and L. McLerran. Geometric scaling above the saturation scale. *Nucl. Phys.*, **A708**:327–352, 2002. arXiv:hep-ph/0203137, doi:10.1016/S0375-9474(02)01010-2. A.6
- [153] C. Aidala et al. sPHENIX: An Upgrade Concept from the PHENIX Collaboration. 2012. arXiv:1207.6378. A.5
- [154] F. Sauli. GEM: A new concept for electron amplification in gas detectors. *Nucl. Instrum. Meth.*, **A386**:531–534, 1997. doi:10.1016/S0168-9002(96)01172-2. A.5
- [155] P. Abbon et al. The COMPASS experiment at CERN. *Nucl. Instrum. Meth.*, **A577**:455–518, 2007. arXiv:hep-ex/0703049, doi:10.1016/j.nima.2007.03.026. A.5

- [156] R. Bell et al. The BaBar superconducting coil: Design, construction and test. *Nucl. Phys. Proc. Suppl.*, 78:559–564, 1999. doi:10.1016/S0920-5632(99)00603-9. A.5.1, A.2
- [157] S. An et al. A 20-ps timing device: A Multigap Resistive Plate Chamber with 24 gas gaps. *Nucl. Instrum. Meth.*, A594:39–43, 2008. doi:10.1016/j.nima.2008.06.013. A.5.2
- [158] B. Adams et al. Measurements of the Gain, Time Resolution, and Spatial Resolution of a 20x20cm MCP-based Picosecond Photo-Detector. *Proceedings of the Vienna Conference on Instrumentation*, 2013. URL: <http://psec.uchicago.edu/library/doclib/documents/222/sendit>. A.5.2, A.5.5
- [159] B. Yu et al. A gem based tpc for the legs experiment. In *Nuclear Science Symposium Conference Record, 2005 IEEE*, volume 2, pages 924–928, 2005. doi:10.1109/NSSMIC.2005.1596405. A.5.2
- [160] L. Musa et al. Letter of intent for the upgrade of the alice experiment. Technical Report LHCC-I-022, CERN, 2012. A.5.2
- [161] B. Ketzer. A Time Projection Chamber for High-Rate Experiments: Towards an Upgrade of the ALICE TPC. 2013. arXiv:1303.6694. A.5.2
- [162] T. Abe et al. The International Large Detector: Letter of Intent. 2010. arXiv:1006.3396. A.5.2
- [163] P. Schade and J. Kaminski. A large TPC prototype for a linear collider detector. *Nucl. Instrum. Meth.*, A628:128–132, 2011. doi:10.1016/j.nima.2010.06.300. A.5.2
- [164] C. Woody. Future Applications of GEM Detectors at BNL. Technical report, 2013. Talk on RD51 Collaboration Meeting. A.5.2, A.5.2
- [165] D. Abbaneo et al. Technical Proposal A GEM Detector System for an Upgrade of the CMS Muon Endcaps. Technical report, 2012. A.5.2
- [166] Technical Design Report for PANDA Electromagnetic Calorimeter (EMC). 2008. arXiv:0810.1216. A.5.3, A.24
- [167] I. Adam et al. The DIRC particle identification system for the BaBar experiment. *Nucl. Instrum. Meth.*, A538:281–357, 2005. doi:10.1016/j.nima.2004.08.129. A.25b, A.5.5, A.31, A.5.5, A.32
- [168] W. Anderson et al. Design, Construction, Operation and Performance of a Hadron Blind Detector for the PHENIX Experiment. *Nucl. Instrum. Meth.*, A646:35–58, 2011. arXiv:1103.4277, doi:10.1016/j.nima.2011.04.015. A.5.5

- [169] T. Iijima et al. A Novel type of proximity focusing RICH counter with multiple refractive index aerogel radiator. *Nucl. Instrum. Meth.*, A548:383–390, 2005. arXiv: physics/0504220, doi:10.1016/j.nima.2005.05.030. A.5.5, A.30
- [170] E. Grauges et al. SuperB Progress Reports – Detector. 2010. arXiv:1007.4241. A.5.5
- [171] D. Trbojevic, 2013. Private communication. A.33
- [172] C. Adler et al. The RHIC zero degree calorimeter. *Nucl. Instrum. Meth.*, A470:488–499, 2001. arXiv:nucl-ex/0008005, doi:10.1016/S0168-9002(01)00627-1. A.5.6
- [173] L. Adamczyk et al. Single Spin Asymmetry A_N in Polarized Proton-Proton Elastic Scattering at $\sqrt{s} = 200$ GeV. *Phys. Lett.*, B719:62–69, 2013. arXiv:1206.1928, doi: 10.1016/j.physletb.2013.01.014. A.5.6